APOE isoform-specific effects in isogenic human iPSC-derived neural cells

Dissertation
zur
Erlangung des Doktorgrades
der Naturwissenschaften
(Dr. rer. nat.)

dem

Fachbereich Pharmazie der
Philipps-Universität Marburg

vorgelegt von

Shadaan Zulfiqar

aus Mumbai

Marburg/Lahn 2019

Erstgutachter: Junior Prof. Dr. Katja Nieweg

Zweitgutachter: Assistant Prof. Dr. Amalia M. Dolga

Eingereicht am 14.08.2019

Tag der mündlichen Prüfung am 28.11.2019

Hochschulkennziffer: 1180

To my dear parents

Erklärung

Ich versichere, dass ich meine Dissertation

„APOE isoform-specific effects in isogenic human iPSC-derived neural cells“

selbständig ohne unerlaubte Hilfe angefertigt und mich dabei keiner anderen als der von mir ausdrücklich bezeichneten Quellen bedient habe. Alle vollständig oder sinngemäß übernommenen Zitate sind als solche gekennzeichnet.

Die Dissertation wurde in der jetzigen oder einer ähnlichen Form noch bei keiner anderen Hochschule eingereicht und hat noch keinen sonstigen Prüfungszwecken gedient.

Marburg, den 14.08.2019

.....

(Shadaan Zulfiqar)

Abstract

Alzheimer's Disease (AD) remains the leading cause of dementia in the elderly, one for which there is still no cure. Efforts in AD drug development have largely focused on treating neuronal pathologies that appear relatively late in the disease. Most of this research is carried out in neuron-focused rodent models that overexpress penetrant human genes known to cause familial AD (FAD), such as *APP*, *PSEN1*, although it constitutes only about 5% of total AD cases, as opposed to sporadic AD which makes up the remaining cases. The consistent ineffectiveness of existing therapeutic approaches which mostly aim at reducing the level of Aβ in the brain has challenged the Aβ-dominated as well as the neurocentric way of viewing the disease.

Meanwhile, due to their complex interplay with neurons, there is greater appreciation for the role of astrocytes in neurodegeneration. The strongest genetic risk factor for sporadic AD is the E4 allele of the *APOE* gene (*Corder et al., 1993*). The APOE protein has 3 isoforms: APOE2 (protective), APOE3 (wild type) and APOE4 (pathogenic) and is primarily produced by astrocytes. Most APOE4-related dysfunctions in the AD brain are described in the context of the Aβ pathway which accumulates with aging, or by the abnormal expression of APOE in neurons, which occurs due to stress conditions possibly brought on with aging or other factors. However, there is a dearth of research on the cell-autonomous effects of APOE4 in astrocytes. Additionally, in order to catch the disease at its earliest, there needs to be greater focus on studying dysfunctions that are known to arise early in susceptible individuals, such as metabolic dysfunctions (*Reiman et al., 2004*) and endocytic abnormalities (*Cataldo et al., 2000*). Also, developing better human-focused disease models is the need of the hour, to avoid artefacts arising as a result of species-specific differences. Therefore, the goal of this study was to develop an isogenic human patient-derived neural cellular model to examine APOE4-isoform specific effects in neurons and astrocytes.

The first step towards that goal was the generation of a series of iPS cells derived from human APOE4 carriers and non-carriers. iPSCs were characterized for pluripotency and chromosomal integrity, by karyotyping. Next. In order to modify the *APOE4/4* genotype of a patient-derived iPSC line to *APOE3/3*, genome editing protocols for precise homology directed repair (HDR) were optimized. The iPSC field suffers from a scarcity of protocols for CRISPR/Cas9

ribonucleoprotein-mediated HDR which is a rare event compared to non-homologous end joining which leads to frameshift mutations. Therefore, protocols were developed for CRISPR delivery, FACS and clonal isolation that would yield a high transfection efficiency, high clonal survival and high rate of HDR. Using these protocols, an isogenic APOE3/3 iPSC line was developed form an APOE4/4 AD patient line. The use of isogenic controls that differ only at a single locus is important when studying a polygenic disease like AD to ensure that subtle phenotypes are not lost due to individual-to-individual genomic background variation. The pair of isogenic lines were then differentiated to cortical neurons. Characterisation of the neurons using cortical markers revealed that cells of both genotypes gave rise to similar neuronal populations. Typical AD-related phenotypes were tested with these neurons. Compared to APOE3/3, APOE4/4 neurons exhibited somatodendritic mislocalisation of phosphorylated tau and increased cell death in response to oxidative stress. There was no significant difference in Aβ42/40 ratio or mean area of endosomes and lysosomes between the genotypes. However, treatment of APOE4/4 neurons with APOE4/4 astrocyte-conditioned medium lead to an increase in Aβ42/40 ratio as well as endosome and lysosome enlargement. Next, to study the contribution of astrocytes to APOE4-associated AD pathology, the isogenic lines were differentiated to astrocytes. Astrocytes were characterized for common astrocytic markers and functional properties. Astrocytes expressed and secreted APOE, were able to take up glutamate, elicit calcium transients in response to glutamate and ATP, and increased chemokine secretion upon exposure to TNFα. In comparison to APOE3/3 astrocytes, APOE4/4 astrocytes exhibit endosome and lysosome enlargement as well as reductions in glycolytic capacity, basal respiration and ATP production. This was accompanied by a decrease in mitochondrial complex expression and an increase in mitochondrial reactive oxygen species (ROS) production.

In summary, this study describes the generation and characterization of isogenic physiologically relevant iPSC-derived neurons and astrocytes that can be used for sporadic AD modelling studies. The neural cells were utilized to highlight early pathologies in AD astrocytes that are understudied, such as metabolic and endolysosomal deficits. The protocols developed for genome editing and differentiation can be used to develop models for other diseases with a genetic component.

Zusammenfassung

Die Alzheimer-Erkrankung (AE) ist nach wie vor die Hauptursache für Demenz bei älteren Menschen, für die es immer noch keine Heilung gibt. Die Bemühungen in der Medikamentenentwicklung konzentrierten sich weitgehend auf die Behandlung von neuronalen Pathologien, die relativ spät in der Erkrankung auftreten. Der größte Teil dieser Forschung wird in neuronenfokussierten Nagetier-Modellen durchgeführt, welche menschliche Gene überexprimieren, die bekanntermaßen die familiäre AE verursachen (wie *APP, PSEN1*). Die familiäre Form der AE betrifft jedoch nur etwa 5% der Patienten, im Gegensatz zur sporadischen AE, die die restlichen Fälle ausmacht. Die Ineffektivität bestehender Therapieansätze, die vor allem darauf abzielen, den Spiegel von Aβ im Gehirn zu senken, hat sowohl die von Aβ dominierte als auch die neurozentrische Sichtweise der Krankheit in Frage gestellt.

Aufgrund ihres komplexen Zusammenspiels mit Neuronen wird der Rolle von Astrozyten bei neurodegenerativen Prozessen eine größere Bedeutung zugemessen. Der stärkste genetische Risikofaktor für die sporadische AE ist das E4-Allel des *APOE*-Gens (*Corder et al., 1993*). Das APOE-Protein hat 3 Isoformen: APOE2 (protektiv), APOE3 (wildtypisch) und APOE4 (pathogen) und wird hauptsächlich von Astrozyten produziert. Die meisten APOE4-bezogenen Dysfunktionen im AE-Gehirn wurden bisher vor allem angesichts von Aβ-basierten Prozessen, die sich im Alter anhäufen oder vor dem Hintergrund abnormaler Expression von APOE in Neuronen, bedingt durch zellulären Stress, aufgrund von Alterungsprozessen oder anderen Faktoren, beschrieben. Es fehlt jedoch an Erkenntnissen über die zellautonomen Wirkungen von APOE4 in Astrozyten. Um die Krankheit frühestmöglich zu erkennen, muss der Fokus zudem stärker auf das Studium von Dysfunktionen gelegt werden, von denen bekannt ist, dass sie bei prädisponierten Personen frühzeitig auftreten. Dazu gehören metabolische Dysfunktionen (*Reiman et al., 2004*) und endozytische Anomalien (*Cataldo et al., 2000*). Auch die Entwicklung besser auf den Menschen ausgerichteter Krankheitsmodelle ist dringend notwendig, um Artefakte zu vermeiden, die durch artspezifische Unterschiede entstehen. Daher ist das Ziel dieser Studie, ein isogenes, vom menschlichen Patienten abgeleitetes neurales Zellmodell zu entwickeln, um APOE4-isoformspezifische Effekte in Neuronen und Astrozyten zu untersuchen.

Der erste Schritt zu diesem Ziel war die Generierung einer Reihe von iPS-Zellen, die aus menschlichen APOE4-Trägern und Nicht-Trägern gewonnen wurden. iPSZ wurden dann hinsichtlich ihrer Pluripotenz und chromosomalen Integrität charakterisiert. Um den *APOE4/4*-Genotyp einer patientenabgeleiteten iPSZ-Linie zu *APOE3/3* zu konvertieren, wurden *Genome-editing* Protokolle für eine präzise homologieorientierte Reparatur (HR) optimiert. Das iPSZ-Feld leidet unter einem Mangel an effizienten Protokollen für CRISPR/Cas9 Ribonukleoprotein-vermittelte HR. Daher wurden optimierte Protokolle für die zelluläre Transfektion der notwendigen *editing* Komponenten, eine hohe Rate an HR, zelluläre Selektion mittels FACS und klonale Isolierung für iPSZ entwickelt. Unter Verwendung dieser Protokolle wurde eine isogene APOE3/3 iPSC-Linie aus einer APOE4/4 AE-Patientenlinie entwickelt. Die Verwendung von isogenen Kontrollen, die sich nur an einem einzigen genomischen Ort unterscheiden, ist wichtig, wenn man eine polygene Erkrankung wie AE untersucht. Dadurch kann sicher gestellt werden, dass marginale Phänotypen nicht durch Individuums bedingte Variabilität verloren gehen. Das Paar isogener Linien wurde dann zu kortikalen Neuronen differenziert. Die Charakterisierung der Neuronen mit kortikalen Markern ergab, dass iPSZ beider Genotypen ähnliche neuronale Populationen hervorbrachten. Typische AE-bezogene Phänotypen wurden an diesen Neuronen untersucht. Im Vergleich zu APOE3/3 zeigten APOE4/4-Neuronen eine somatodendritische Fehllokalisierung des phosphorylierten Tau und einen erhöhten Zelltod als Reaktion auf oxidativen Stress. Es gab keinen signifikanten Unterschied im Verhältnis Aβ42/40 oder der Größe von Endosomen und Lysosomen zwischen den Genotypen. Die Behandlung von APOE4/4-Neuronen mit APOE4/4 Astrozyten-konditioniertem Medium führte jedoch zu einem Anstieg des Verhältnisses Aβ42/40 sowie zu einer Vergrößerung von Endosom und Lysosom. Als nächstes, um den Beitrag der Astrozyten zur APOE4-assoziierten AE-Pathologie zu untersuchen, wurden die isogenen Linien zu Astrozyten differenziert. Die Astrozyten wurden durch gängige astrozytische Marker und funktionelle Untersuchungen charakterisiert. Die Astrozyten zeigten APOE Expression und Sekretion und waren in der Lage, Glutamat aufzunehmen, Kalziumtransienten als Reaktion auf Glutamat und ATP hervorzurufen und die Chemokin-Sekretion durch Exposition von TNFα zu erhöhen. Im Vergleich zu APOE3/3 Astrozyten weisen APOE4/4 Astrozyten eine Endosomen- und Lysosomenvergrößerung sowie eine Verringerung der glykolytischen Kapazität, der basalen Atmung und der ATP-Produktion

auf. Dies ging einher mit einer Reduktion der Expression mitochondrialer Komplexproteine und einem Anstieg der Produktion von mitochondrialen reaktiven Sauerstoffspezies.

Zusammenfassend beschreibt diese Studie die Erzeugung und Charakterisierung iPSZ-abgeleiteter isogener, physiologisch relevanter Neurone und Astrozyten, die für sporadische AE-Modellierungsstudien verwendet werden können. Mit Hilfe dieser Zellen konnten frühe pathologische Prozesse in AE-Astrozyten, wie metabolische und endolysosomale Defizite die in dieser Form bisher nicht bekannt waren, gezeigt werden. Die für das *Genome-editing* und die Zell-Differenzierung entwickelten Protokolle können zukünftig genutzt werden, um Modelle für andere Krankheiten mit einer eindeutigen genetischen Komponente zu entwickeln.

Table of contents

1. Introduction

1.1 Alzheimer's Disease

Alzheimer's Disease (AD) is the most common cause of dementia in the elderly. It is a neurodegenerative disorder with a long prodromal period, clinically characterized by short-term memory loss, followed by a progressive loss of long-term memory, as well as reduced language skills and personality changes.

The estimated cost of AD worldwide was calculated to be over $600 billion in the year 2010 alone. It is estimated to affect nearly 24 million people worldwide and this number is expected to double every 20 years (*Reitz et al., 2011*), which puts the number of sufferers at approximately 95 million by the year 2050 (*Qiu & Fratiglioni, 2017*). Needless to say, this disease places an enormous financial and emotional burden on sufferers, caregivers and society.

1.1.1 Types of AD, symptoms and diagnosis

AD is characterized by cognitive (language difficulties, disorientation, memory loss, visuospatial problems) and non-cognitive (depression, delusions, mood swings) symptoms. It can broadly be classified based on the age of onset into early-onset and late-onset AD. In early onset AD, also called Familial AD (FAD), patients develop symptoms before the age of 65. This is due to the inheritance of penetrant mutation in the genes *APP, PSEN1* or *PSEN2* in an autosomal dominant manner. Only about 5% of all AD cases can be classified as FAD. The more prevalent form of AD is the late onset form, also called sporadic AD (SAD), which can be caused by several genetic, epigenetic and environmental factors.

It was in 1906 that Alois Alzheimer first described its histopathological hallmarks: extracellular amyloid plaques composed of misfolded Aβ protein and intracellular neurofibrillary tangles (NFT) which are aggregates of hyperphosphorylated tau protein (*Hippius et al., 2003*) (Figure 1.1B). These, in turn, trigger activation of astrocytes and microglia, followed by neuroinflammation and oxidative injury, ending in synapse and neuron loss. Increase in disease severity is accompanied by cortical thinning and decreased hippocampal volume, which predict conversion from mild cognitive impairment (MCI) to AD (Figure 1.1A).

Due to the high degree of inter-patient heterogeneity in disease progression, there is no single definitive method of diagnosing AD. Cognitive decline followed by the post-mortem observation of plaques and tangles were the traditional confirmatory test of AD. Today, tests like the Mini-Mental State Examination (MMSE) (*Tombaugh & McIntyre, 1992*) and Clinical Dementia Rating (CDR) are used to gather an idea about the cognitive status of a patient which includes making clinical assessments of memory retention, changes in behavior and the ability to carry out daily tasks independently. Biochemically, measurements of Aβ and tau protein in the cerebrospinal fluid are made, since these proteins are components of amyloid plaques and neurofibrillary tangles, respectively.

Brain imaging analyses such as functional magnetic resonance imaging (fMRI) to measure functional changes in the brain, computed tomography (CT) to study structural changes and positron emission tomography (PET) to allow imaging of Aβ using PiB compound, also aid in diagnosis.

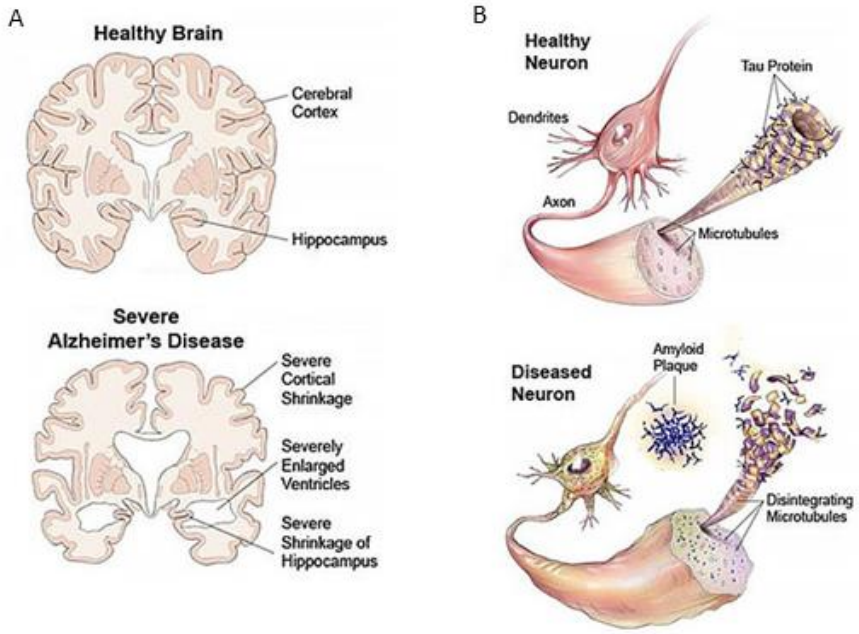

Figure 1.1 Alzheimer's Disease hallmarks: A) Compared to a healthy brain, an AD brain shows cortical thinning, enlarged ventricles and loss of hippocampal volume. B) Neuropathologically, the AD brain is characterized by the presence of extracellular amyloid plaques and intracellular neurofibrillary tangles. (Adapted from *www.brightfocus.org/alzheimers-disease/infographic/progression-alzheimers-disease*)

1.1.2 Mechanistic hypotheses for Alzheimer's Disease

Several hypotheses have attempted to explain the mechanistic basis of AD, with the most well studied one being the amyloid hypothesis, which posits that the extracellular accumulation of Aβ protein is the initiating cause of the disease. Aβ is a 37-49 amino acid peptide generated by cleavage of the transmembrane Amyloid Precursor Protein (APP) by 3 enzymes (α-, β- or γ-secretases) (*Zolezzi et al., 2014*). Sequential cleavage of APP by α-secretase followed by γ-secretase is called non-amyloidogenic processing and yields soluble end products. Here, APP is first cleaved by α-secretase to yield the extracellular sAPPα and intracellular C-terminal fragment α (CTFα). CTFα is further cleaved by γ-secretase to AICD and p3 peptide. On the other hand, the amyloidogenic pathway begins with APP cleavage by the rate-limiting enzyme β-secretase to give extracellular sAPPβ and the membrane-bound CTFβ. CTFβ is further cleaved by γ-secretase to intracellular AICD and extracellular Aβ peptide. Aβ peptide of 42 amino acids length (Aβ42) is neurotoxic *(Klein et al., 2006*) and has a tendency to form oligomers, fibrils and plaques (*Burdick et al., 1992*). Results from animal models suggest that non-fibrillar Aβ oligomers are more toxic than the insoluble Aβ fibrils found in amyloid plaques (*Kayed et al., 2013*).

It is presumed that accumulation of amyloid aggregates leads to the hyperphosphorylation and misfolding of the tau protein (*Zheng et al., 2002*), which aggregate to form neurofibrillary tangles (NFT) and are also neurotoxic. Traditionally, tau has been believed to function mainly in stabilizing microtubules, and that hyperphosphorylation and aggregation of the protein leads to a loss-of-function in AD (*Morris et al., 2011*). However, recent studies have demonstrated that tau plays a role in the distribution of synapse-related signaling molecules, thus regulating excitatory neurotransmission (*Sotiropoulos et al., 2017*). When abnormally phosphorylated, it can aggregate in dendritic spines and interfere with synaptic transmission (*Hoover et al., 2010*). Studies have also shown that a large part of the toxic effect of Aβ occurs through tau, and tau reduction can also reduce the pathogenic effects of Aβ (*DeVos et al., 2018*). Additionally, it is NFTs and not plaques, which ultimately correlate with the severity of cognitive impairment (*Augustinack et al., 2002*).

Besides the amyloid and tau hypothesis, there are other hypotheses, like the cholinergic deficit hypothesis, which postulates that the loss of cholinergic neurons is the primary event of AD (*Craig et al., 2011*). Based on studies from mouse models and human brains, loss of cholinergic neurons

was correlated with cognitive decline. A wide range of cholinergic abnormalities including alterations in acetylcholine release, transport of choline and function of α7 nicotinic acetylcholine receptors have been observed in several brain regions (*Liu et al., 2009*). These receptors are known to regulate synaptic plasticity (*Jurgensen et al., 2010*).

The glutamatergic hypothesis relies on the activation of NMDA receptors by Aβ (*Roberson et al., 2007*). Excitatory glutamatergic neurotransmission through NMDA receptors plays a critical role in regulating synaptic plasticity as well as survival of neurons. However, excessive activation of these receptors causes exaggerated calcium influx, leading to excitotoxicity and cell death (*Texidó et al., 2011*). Since astrocytes are critically involved in the uptake of glutamate by excitatory amino acid transporters (EAATs) and are believed to be capable of releasing glutamate to modulate neuronal activity, impairments in their functions can also lead to a disturbance in the physiological levels of extracellular glutamate.

The oxidative stress/ neuroinflammation hypothesis focuses on the fact that the brain is particularly vulnerable to oxidative stress. Several groups have reported decreased mitochondrial complex IV (cytochrome c oxidase, COX) activity in AD patients, which increased reactive oxygen species (ROS) and decreased ATP levels. The AD brain is shown to have increased lipid peroxidation as well. In connection with the amyloid hypothesis, Aβ is known to interact with mitochondrial complexes leading to dysfunction (*Bobba et al., 2013*). This further results in increased oxidative stress as well as a reduced antioxidant defenses. Ultimately, this leads to activation of microglia and astrocytes, which are responsible for most of the immune responses in the brain. Inflammation, which is an innately protective response to microorganism or cellular debris, if compromised, can disturb the brain microenvironment and expedite pathological processes. Reactive astrocytes can secrete a variety of chemokines, cytokines and inflammatory mediators. The extracellular molecules secreted by astrocytes can be neuroprotective (e.g. cytokines like interleukin-6 (IL-6)) or neurotoxic (e.g. tumor necrosis factor α (TNFα)) (*Sofroniew et al., 2009*). *Liddelow et al., 2017* proposed a novel classification of reactive astrocytes where A1 astrocytes are of the neurotoxic phenotype and A2 are neuroprotective. A1 astrocytes have been shown to be predominant in AD brains and neuroinflammation is often considered central to the AD disease process. Astrocyte reactivity is known to correlate with the severity of AD (*Simpson et al., 2010*). In particular, the

concentration of TNF-α has a close correlation with disease progression. *Holmes et al, 2009* reported that over a six-month period, a two-fold increase in serum TNFα was associated with a two-fold rate of cognitive deterioration.

1.1.3 Etiology of Alzheimer's Disease: GWAS studies

AD is caused by a combination of genetic, epigenetic and environmental factors. Aging is the most important non-genetic risk factor. Other environmental risk factors include diabetes, obesity, head trauma and low education levels. Studies on human brain samples have revealed that AD is associated with epigenetic dysregulation such as abnormal DNA methylation and histone modifications. (*Chouliaras et al., 2010*).

With the advent of genome-wide association studies (GWAS) and next-generation sequencing, over two dozen AD susceptibility genes have been identified. In addition to *APP, PSEN1* and *PSEN2* which lead to FAD, genes that impart risk for sporadic AD include *TREM2, CLU, PICALM, BIN1, CD33, SORL1, ABCA7, EPHA1* etc. Of these, the strongest genetic risk factor that has been verified in different populations across the world with high confidence has been the *APOE4* allele (*Bertram et al., 2010*).

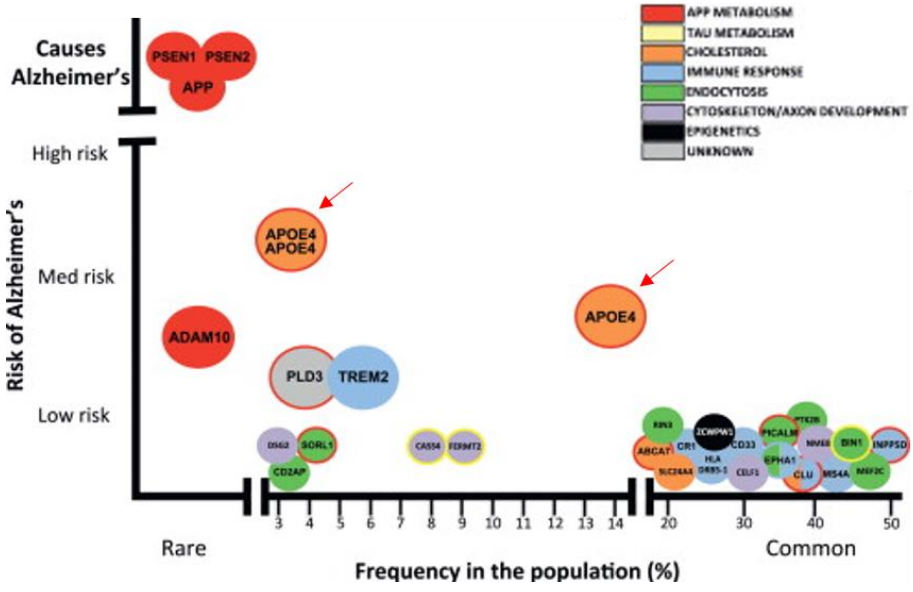

Figure 1.2: AD susceptibility genes: Early-onset AD is caused by penetrant mutations in *APP, PSEN1* or *PSEN2* while a large number of susceptibility genes with smaller effect sizes can increase risk for late-onset AD. The *APOE*4 allele is unique in imparting a medium to high risk for disease while being fairly common in the population. (*Adapted from Yu et al., 2014*)

concentration of TNF-α has a close correlation with disease progression. *Holmes et al, 2009* reported that over a six-month period, a two-fold increase in serum TNFα was associated with a two-fold rate of cognitive deterioration.

1.1.3 Etiology of Alzheimer's Disease: GWAS studies

AD is caused by a combination of genetic, epigenetic and environmental factors. Aging is the most important non-genetic risk factor. Other environmental risk factors include diabetes, obesity, head trauma and low education levels. Studies on human brain samples have revealed that AD is associated with epigenetic dysregulation such as abnormal DNA methylation and histone modifications. (*Chouliaras et al., 2010*).

With the advent of genome-wide association studies (GWAS) and next-generation sequencing, over two dozen AD susceptibility genes have been identified. In addition to *APP, PSEN1* and *PSEN2* which lead to FAD, genes that impart risk for sporadic AD include *TREM2, CLU, PICALM, BIN1, CD33, SORL1, ABCA7, EPHA1* etc. Of these, the strongest genetic risk factor that has been verified in different populations across the world with high confidence has been the *APOE4* allele (*Bertram et al., 2010*).

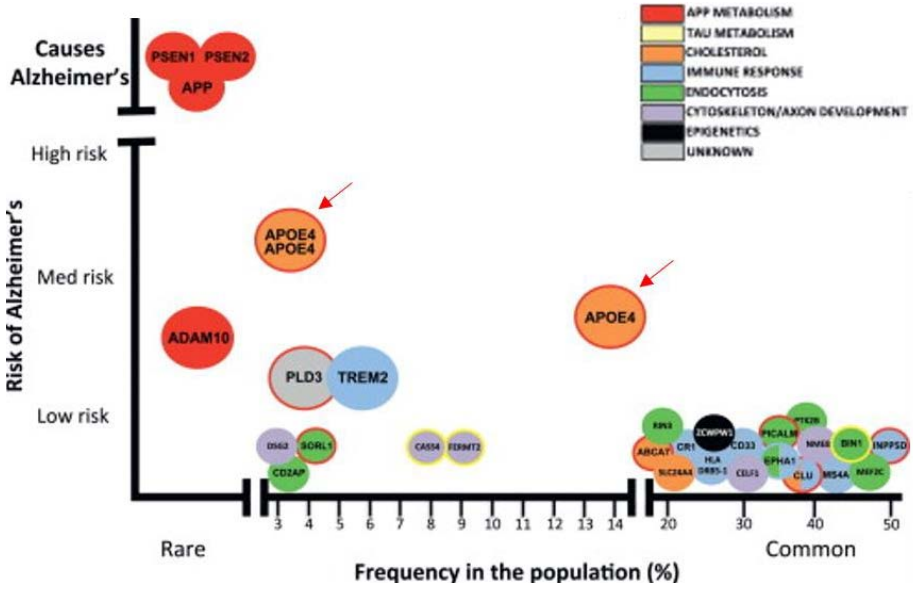

Figure 1.2: AD susceptibility genes: Early-onset AD is caused by penetrant mutations in *APP, PSEN1* or *PSEN2* while a large number of susceptibility genes with smaller effect sizes can increase risk for late-onset AD. The *APOE*4 allele is unique in imparting a medium to high risk for disease while being fairly common in the population. (*Adapted from Yu et al., 2014*)

APOE encodes Apolipoprotein E and has 3 isoforms: APOE2, APOE3 and APOE4. APOE4 is found in about 15% of the general population, but about 40% of AD patients are carriers (*Farrer et al., 1997*). *APOE4* homozygotes have up to 15-fold increased risk of developing AD as compared to non-carriers (*Farrer et al., 1997*). Meanwhile, *APOE2* has been shown to have a protective effect.

1.1.4 Current treatment

Despite decades of active research, there are no disease-modifying treatments for AD, to help slow down the progression of the disease. Available treatments are symptomatic in nature and help to improve the quality of life. Since impairment in cholinergic transmission has been observed in AD, acetylcholinesterase inhibitors which allow the extended presence of acetylcholine in the synaptic cleft help to alleviate symptoms of moderate AD. These include drugs like donepezil, galantamine and rivastigmine. Drugs like memantine which antagonize NMDA glutamate receptors in order to prevent excitotoxicity are also used.

However, the approved treatments show variable effectiveness in patients and are often given in combination for greater impact. A large number of patients also face undesirable side effects from these drugs. Moreover, the effectiveness of these drugs is greatest if the disease is diagnosed and treatment is started early on. Therefore, several early events in the disease such as endosome enlargement and reduction in cerebral glucose metabolism are interesting subjects of study.

1.2 APOE

1.2.1 Structure and function

Apolipoprotein E (APOE), a 34 kDa protein was first identified in the 1970s in triglyceride-rich lipoproteins (*Shore et al., 1973*). APOE is a component of plasma lipoproteins in lipid transport between different cell types and tissues, such as astrocytes to neurons. In the CNS, after neuronal death or degeneration, APOE takes up cholesterol and lipids from the dying cells and redistributes them to surrounding cells which require the lipids for membrane repair or myelination of growing axons (*Hauser et al., 2011*). In 1993, *Corder et al*. identified *APOE4* as a major genetic risk factor for AD. GWAS studies have revealed several other loci as susceptibility factors, but these have

much lower odds ratios compared to *APOE4* (with the exception of *TREM2*). Additionally, APOE4 is more common in the population than the other SNPs, thus having a much higher population-attributable risk (*Guerreiro et al., 2013*).

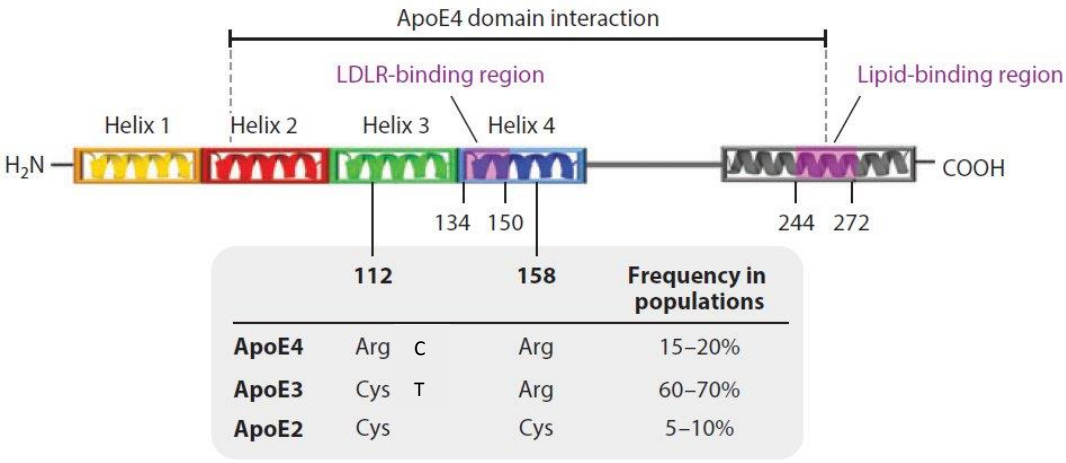

	112		158	Frequency in populations
ApoE4	Arg	C	Arg	15–20%
ApoE3	Cys	T	Arg	60–70%
ApoE2	Cys		Cys	5–10%

Figure 1.3: APOE structure: A linear diagram of the human APOE protein with an N-terminal receptor binding domain and C-terminal lipid-binding domain connected by a hinge region. *APOE3* is the most common allele, followed by *APOE4*, the 'pathogenic' allele and *APOE2*, which is protective. The difference between *APOE4* and *APOE3* is a single base pair change at amino acid 112. (*Adapted from Yu et al., 2014*)

The human *APOE* gene is located on chromosome 19q13 and encodes a 299 amino acid lipoprotein. It shows the highest expression in liver, followed by the brain, where it is mainly expressed by astrocytes. Structurally, it has 2 domains separated by a hinge region: a C-terminal lipid binding domain and an N-terminal receptor binding domain, which allows it to bind to APOE receptors (LDLR- Low Density Lipoprotein Receptor family). These receptors mediate endocytosis of ligands and are recycled back to the membrane. The APOE protein has 3 main isoforms: APOE2, APOE3 and APOE4. They differ from each other at residues 112 or 158. APOE2 has cysteines and APOE4 has arginines at both positions, while APOE3 has a cysteine and an arginine respectively. This single amino acid change affects the tertiary structure and function of the folded protein. The Arg112 of the N-terminal domain reorients the Arg61 side chain such that it can interact with Glu255 of the C-terminal domain, thus resulting in the interaction between the N- and C-terminal domains (*Zhong & Weisgraber, 2009*). Although a lot is still not known about the mechanism of pathogenesis of APOE4 in AD, there are some popular hypothesis, which are described below:

1.2.2 Amyloid β-dependent role of APOE in AD

There are a couple of ways by which APOE4 results in an increased amount of Aβ in the system. Firstly, it might affect APP processing itself. It has been shown in cultured neuronal cells that exogenously applied APOE4 results in greater Aβ production by increasing LRP1-mediated APP endocytosis (*Ye et al., 2005*). This effect was abolished by blocking APOE4 domain interaction using a small molecule. Secondly, APOE4 shows an isoform-specific effect on Aβ aggregation. PET imaging in cognitively normal (*Reiman et al., 2009*) and prodromal AD patients (*Villemagne et al., 2011)* has shown an increased amyloid burden in the brains of APOE4 carriers. These effects have been replicated using APOE transgenic animal models which show increased Aβ plaque deposition in APOE4 animals (*Bales et al., 2009*). Thirdly, sporadic AD is characterized by impaired Aβ clearance (*Mawuenyega et al., 2010*). APOE is known to bind to Aβ and affect its clearance through several pathways: through microglia, astrocytes, via the blood-brain barrier or through enzymatic degradation. APOE4 knock-in mice show impaired clearance of Aβ from the brain and into the periphery, as compared to APOE3 (*Castellano et al., 2011*).

1.2.3 Amyloid β-independent role for APOE in AD

In addition to Aβ, APOE4 has also been shown to affect the other major AD hallmark, tau pathology. In APOE4-carrying AD patients, higher amounts of total and phosphorylated tau have been observed (*Vemuri et al., 2010*). These observations have been replicated using animal models; 3X TG-APOE4 mice also show tau mislocalization to the somatodendritic compartment (*Bennett et al., 2013*). APOE4 has also been shown to increase phosphorylated tau levels by regulating GSK3, a tau-phosphorylating kinase (*Hoe et al., 2006*). P301S tau transgenic mice with human APOE4 knock-in show greater somatodendritic tau redistribution as well as higher levels of neuroinflammation (*Shi et al., 2017*).

As there has been a recent resurgence in interest in the role of neuroinflammation in AD, the effects of APOE4 on neuroninflammation seem even more interesting. While APOE3 has been shown to suppress neuroinflammation, APOE4 has been associated with a proinflammatory immune response (*Keene et al., 2011*). In line with this finding, anti-inflammatory treatments for AD show a greater response in APOE4 carriers compared to non-carriers (*Szekely et al., 2008*). Being a lipid-

carrier, APOE also plays a role in synaptic plasticity (*Klein et al., 2010*). *Chung et al., 2010* report the contribution of APOE in synapse pruning by astrocytes. APOE4 was shown to decrease the phagocytosis of synapses, thus increasing the accumulation of senescent synapses exposed to complement-mediated degeneration. *Korwek et al., 2009* also demonstrated the isoform-specific effects of APOE on long term potentiation (LTP) using APOE targeted replacement mice.

Among some of its very early effects, APOE4 carriers show a predisposition for AD through metabolic and structural alterations. Dean et al., 2004 showed that APOE4-carrying infants have decreased cortical gray matter volume in areas typically affected in AD. Similarly using FDG PET imaging, reduced glucose metabolism can be found in APOE4 carriers as young as 20-30 years old, decades before any symptoms appear (*Reiman et al., 2004*). In relation to metabolic changes, mitochondrial dysfunction seems to aggravate AD pathology. As mentioned before, in the brain, APOE is primarily produced by astrocytes, but it can also be expressed by neurons in conditions of stress *(Mahley et al., 2006*). However, when expressed by neurons, it is more prone to proteolytic degradation. These proteolytic fragments have proven to be neurotoxic, with the APOE4 (1-272) fragment binding to mitochondrial complexes subunits and disrupting their activity (*Nakamura et al., 2009*). This potentially strong role of APOE in AD-related pathology makes a case for studying the cell type that highly expresses APOE in the brain- the astrocytes.

1.3 Why study astrocytes in the context of AD

Historically considered accessory cells to neurons, there is increasingly greater interest in the role of astrocytes in normal and pathological conditions. Astrocytes are involved in neurotransmitter recycling, antioxidant supply, ion buffering and neuroinflammation i.e. a lot of the same pathways that go astray in Alzheimer's Disease (AD). This is due to the close symbiotic relationship between neurons and astrocytes

1.3.1 The indispensable neuron-astrocyte relationship

Astrocytes, one of the most numerous cell types in the brain, were first named so in 1893 by Michael von Lenhossek due to their star-shaped appearance. They form contiguous, non-overlapping domains interconnected with other astrocytes by gap junctions. They extend radially arranged processes: fine perivascular processes that ensheathe the synapses, and larger vascular

endfeet that contact the blood vessels. Astrocytes demonstrate considerable morphological and functional diversity depending on the region. Morphologically, astrocytes have endfeet positioned at the intraparenchymal capillaries that allow them to function as gatekeepers of glucose entry into the brain. Astrocytes can sense synaptic activity and energy requirement, and accordingly modulate cerebral blood flow (*Magistretti et al., 2006*). In addition to being derived from the blood, glucose is also stored in the form of glycogen in the brain, almost exclusively in astrocytes, and the greatest concentrations of glycogen are found in regions of highest synaptic density (*Sagar et al., 1987*). Not only does breakdown of this glycogen help to support neurons in conditions of hypoglycemia, but it has been found to be very important in learning and memory formation.

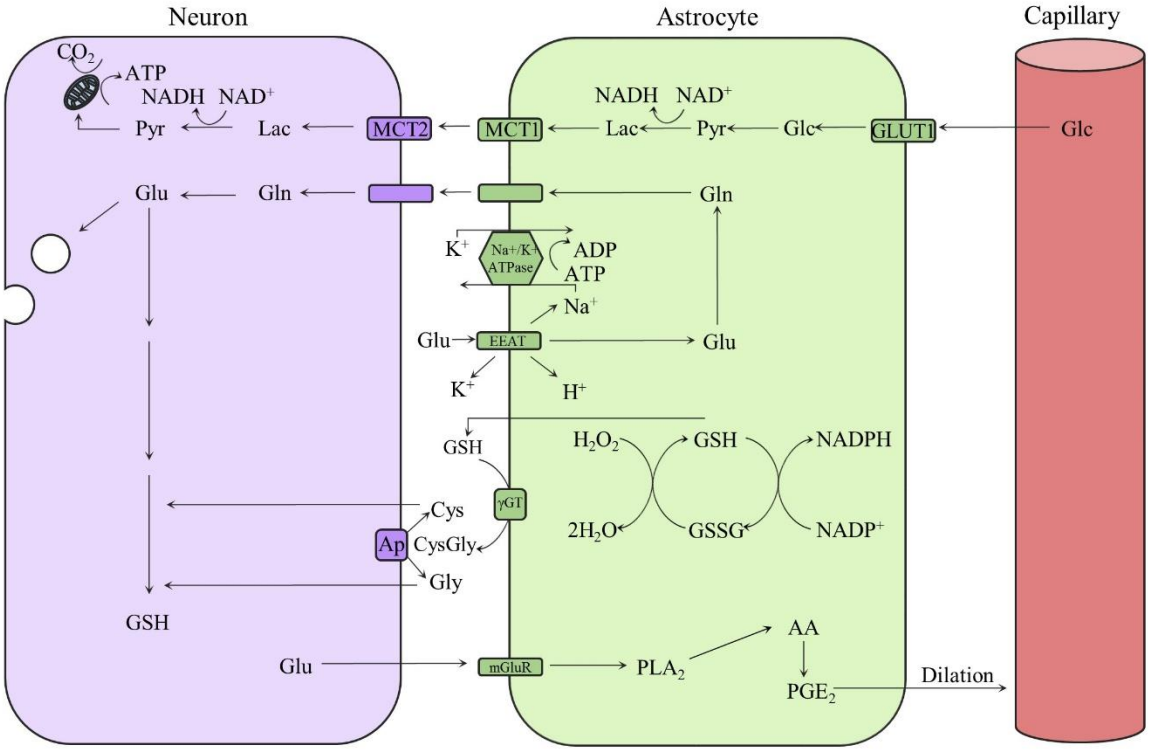

Figure 1.4: Astrocyte function in brain homeostasis. (i) Astrocyte-neuron lactate shuttle: In response to neuronal activity, astrocytes take up glucose (Glc) from the blood vessels through glucose transporter GLUT1. This triggers the conversion of glucose to lactate (Lac) by anaerobic glycolysis. The lactate is shuttled to neurons through monocarboxylate transporters MCTs, where it is utilized by the mitochondria for energy production. (ii) Glutamate (Glu) released by neurons into the synaptic space is taken up by astrocytes through Na+-dependent excitatory amino acid transporters (EAATs). The Na+/K+ ATPase pump consumes ATP to extrude the Na+. The glutamate is converted to glutamine (Gln) by Glutamine synthetase and shuttled into the neurons where it is converted again to glutamate by the action of Glutaminase. (iii) Astrocytes provide neurons with the antioxidant glutathione (GSH), which is cleaved in the extracellular space by ectoenzyme γ-glutamyl transpeptidase (γGT). The resulting CysGly is cleaved by the neuronal ectopeptidase to give rise to cysteine (Cys) and glycine (Gly) which serve as precursors for neuronal GSH

synthesis. GSH detoxifies ROS like hydrogen peroxide (H2O2). The oxidized glutathione (GSSG) is recycled back to GSH using NADPH as a reducing equivalent. (iv) Activation of metabotropic glutamate receptors (mGluR) by glutamate causes calcium transients in astrocytes. This leads to the activation of cytosolic phospholipase A2 (PLA2), which produces arachidonic acid (AA). AA can generate prostaglandins like PGE2 which have a vasodilatory effect on blood vessels, thus, regulating cerebral blood flow.

Astrocytes also help to protect neurons against oxidative stress which is a result of excess reactive oxygen species (ROS) production. ROS arise due to a high OxPhos in neurons. Superoxides are detoxified by molecules and enzymes like glutathione (GSH), glutathione peroxidase, catalase and heme oxygenase. These enzymes are more abundant in astrocytes. The reduction of peroxides is catalyzed by glutathione peroxidase which results in GSH being oxidized to glutathione disulphide (GSSH). GSH can be regenerated from GSSG by glutathione reductase, using NADPH as a reducing equivalent (*Fillenz et al., 2005*). Both NADPH and GSH are found in high abundance in astrocytes. Neurons are also dependent on astrocytes for the precursor amino acids for GSH synthesis.

Among their other support functions, astrocytes are also involved in K^+ ion, pH and water buffering. Increased neuronal activity results in decreases in extracellular water volume and K^+ ion efflux due to opening of potassium channels. In order to avoid altering neuronal activity, excess extracellular K^+ ions are taken up by astrocytes through inward rectifier K^+ channels present on perisynaptic processes (*Kofuji et al., 2004*). Osmotic balance is maintained by the water transport through aquaporin channels found on astrocytic endfeet and perisynaptic processes (*Simard et al., 2004*).

Astrocytes further control signaling in the brain by removal of GABA and glutamate from the synapse. Glutamate uptake is carried out by astrocyte-specific glutamate transporters excitatory amino acid transporter 1 and 2 (EAAT1 and EAAT2). Astrocytes convert the glutamate to glutamine through glutamine synthetase (*Martinez-Hernandez et al., 1977*). Nontoxic glutamine is transported to the extracellular space where it is taken up by neurons and used as a precursor to replenish stores of GABA and glutamate. This glutamate-glutamine shuttle controls glutamate overstimulation and excitotoxicity.

Additionally, astrocytes and microglia are responsible for most of the immune responses in the brain. Astrocytes have graded responses to different kinds of damage and upon activation, change

their morphological and functional properties. Reactive astrocytes can secrete a variety of chemokines, cytokines and inflammatory mediators. The extracellular molecules secreted by astrocytes can be neuroprotective (e.g. cytokines like interleukin-6 (IL-6)) or neurotoxic (e.g. tumor necrosis factor α (TNFα)) (*Sofroniew et al., 2009*). Reactive astrocytes are known to surround Aβ deposits in the AD brain and internalize them.

1.3.2 A role for astrocytes in AD pathological mechanisms

The diverse functions that astrocytes have in the survival and maintenance of neurons, puts them in a central position to the development of AD pathology (Figure 2). These could include a gain of function (such as the production of proinflammatory cytokines) or loss of their neuroprotective functions.

AD is characterized by a presymptomatic reduction in cerebral glucose metabolism (CMRglc) of 21-28% when compared to normal elderly controls (*de Leon et al., 1983*). This decline is more significant in the regions known to be affected early in AD such as the posterior cingulate and frontal cortex. Glucose hypometabolism represents a misregulation of nutrient transporters, metabolic enzymes and mitochondrial complexes. Postmortem AD brain studies show that astrocytic GLUT1 and neuronal GLUT3 (both responsible for uptake of glucose) have reduced levels (*Simpson et al., 1994*). This reduction has also been observed in astrocyte cultures derived from transgenic arcAβ mice (mice overexpressing human APP695 with Swedish and Arctic mutations leading to amyloid pathology in brain parenchyma and vasculature) which also show a reduction in lactate transporters (*Merlini et al., 2011*). In addition to impaired uptake of glucose, the activities of glycolytic enzymes are altered in AD patients. This includes an increase in the activity of lactate dehydrogenase and pyruvate kinase in the frontal and temporal cortex and a decrease in the activity of glucose 6-phosphate dehydrogenase, the rate-limiting pentose phosphate pathway (PPP) enzyme, in the hippocampus (*Bigl et al. 1999; Yun and Hoyer 2000*). This breakdown in glycolytic function has been confirmed in iPSC-derived PSEN1ΔE9 astrocytes which show reduced glycolysis, lactate secretion and neuronal support function compared to control astrocytes (*Oksanen et al., 2017*).

Mitochondria are severely altered in AD neurons at a structural and functional level. Genes encoding components of the TCA cycle are underexpressed in AD, particularly in the posterior cingulate cortex and hippocampus. Complex IV is reduced in the AD brain (*Parker et al., 1994*). Electron transport chain defects lead to ROS formation and further damage to mitochondria. *Volobueva et al., 2007* have shown that when astrocytic mitochondrial function is inhibited by fluorocitrate, they failed to protect co-cultured neurons from glutamate toxicity. Furthermore, astrocytes have been shown to help with mitochondrial quality control by taking up and degrading damaged neuronal mitochondria in astrocytic lysosomes through a process known as transmitophagy (*Chung-ha et al., 2014*). Using an iPSC derived model, astrocytes have been shown to completely restore mitochondrial function in dopaminergic neurons by co-culture (*Du et al., 2018*).

Glucose hypometabolism not only results in decline of brain energy homeostasis but also leads to an oxidative stress condition in the brain. Increased ROS production can damage mitochondrial membranes and DNA and thus further damage mitochondrial function. Increased oxidative stress has also been shown to increase Aβ production. (*Li et al., 2004; Moreira et al., 2007*). Oxidative stress and Aβ act as agents of injury to induce a senescence-associated secretory phenotype (SASP), which is characterized by a proinflammatory microenvironment. At the same time, astrocytes tend to gather around amyloid plaques in the brain and undergo reactive astrogliosis. This includes overexpression of structural proteins like GFAP and vimentin, hypertrophy and secretion of proinflammatory cytokines like TNFα, IL-1β, MCP-1 etc.

Astrocytes are also an important factor in the amyloid pathway as they are able to influence Aβ production and deposition, which are considered the key histopathological features of AD. Astrocytic metabolic dysfunction can affect Aβ pathology by modifying APP processing and influencing digestion or clearance of Aβ from the brain. Downregulation of glycolysis by pharmacological inhibition of its key regulator PFKFB3 results in Aβ accumulation within and around astrocytes (*Fu et al., 2015*). Meanwhile, treatment of an AD mouse model with 2-DG improves astrocytic energy metabolism, as a result leading to increased α-secretase and reduced γ-secretase expression, thus limiting the buildup of Aβ and slowing the progression of pathology (*Yao et al., 2011*). While BACE1 is normally expressed mainly in neurons (*Roßner et al., 2001*),

inflammation in the AD brain induces activity of BACE1 in reactive astrocytes (*Zhao et al., 2011*). Astroglial BACE1 was found around Aβ plaques in AD transgenic mouse models as well (*Hartlage-Rubsamen et al., 2003; Roßner et al., 2001*). Amyloid buildup occurs when the Aβ production and clearance mechanisms are not balanced. Astrocytes are found in the vicinity of Aβ plaques in the brain and have the ability to degrade amyloid by phagocytosis. However this sequestration ability has been found to be defective in astrocytes from APP transgenic mice (*Wyss-Coray et al., 2003*).

Astrocytes play a key role in the uptake of extracellular glutamate and its conversion to glutamine, to provide neurons with a precursor for GABA and glutamate production. Depletion of the glutamate transporter EAAT1 in astrocytes results in abnormal neuronal excitation and leads to tau pathology (*Kilian et al., 2017*). Other hallmarks of AD like Aβ42 have been shown to decrease the expression of EAAT1 and EAAT2 in cultured astrocytes via adenosine A2A receptors (*Matos et al., 2012; de Vivo et al., 2010*). At the same time, Aβ can also induce astrocytic glutamate release, leading to extrasynaptic NMDA receptor activation (*Talantova et al., 2013*).

As mentioned in Section 1.2, APOE, the strongest known genetic risk factor for AD, is primarily produced in the brain by astrocytes. Animal, human and patient iPSC studies have suggested several ways by which APOE4 exerts its pathogenic effect. Mice expressing human APOE3 develop fewer plaques than mice expressing APOE4 (*Holtzman et al., 2000*) and APOE3 astrocytes were more effective in clearing amyloid deposits (*Simonovitch et al., 2016*). Using APOE4 sporadic AD patient-derived astrocytes, Jones et al., 2017 demonstrated their atrophic profile compared to control astrocytes. Further, APOE4 astrocytes show reduced ability to deal with the oxidative stress arising from increased free radical production. APOE4-conditioned medium showed reduced protection of B12 cells from H_2O_2 cytotoxicity (*Miyata et al., 1996*). In general, as *Zhao et al., 2017* illustrated, that when co-cultured with iPSC-derived neurons, APOE4 astrocytes are less effective in supporting neuronal survival and function than APOE3 astrocytes.

1.4 Animal models for AD and their limitations

Most studies on AD mechanisms have been carried out using mouse models. In order to recapitulate amyloid or tau pathology in these transgenic animals, overexpression of the dominant

mutation of human early onset AD (EOAD)-causing genes (*APP, PSEN1, PSEN2*) was carried out. However, these mice show learning and memory deficits without another important characteristic of AD i.e. neuron loss (*Schaeffer et al., 2011*). Also, in many cases, no tau pathology was seen without expression of human tau mutations, mutations which are normally seen in Frontotemporal Dementia and not AD patients. Moreover, these models may represent the EOAD system, which only account for about 1-5% of total AD cases. In order to study APOE4-mediated mechanisms in late onset AD (LOAD), better rodent models are required.

Since mouse APOE exists as only one isoform, structurally similar to APOE3, mouse models expressing human APOE have been generated. The Holtzman group generated APOE knock-in mice expressing human APOE3 or APOE4 under the human GFAP promoter (*Sun et al., 1998*). However, this led to differences in copy number and expression level of both the isoforms, which can confound interpretation of mechanistic studies. *Mann et al. 2004* then generated APOE2, APOE3 and APOE4 mice by knocking in human APOE2, APOE3 or APOE4 cDNA in frame at the mouse APOE site and disrupting it. Since all isoforms are expressed under the endogenous mouse APOE promoter, this ensures that expression levels between the different isoforms can be compared (*Mann et al., 2004*). However, this model proved to have limited utility as no differences in Aβ or cholesterol levels could be detected. For most studies however, targeted replacement mice generated by the Maeda lab are used. Human *APOE2*, *APOE3* and *APOE4* exon and introns were inserted in place of a mouse *APOE* site (*Sullivan et al., 1998, Sullivan et al., 1997, Knouff et al., 1999).* These mice show isoform-specific differences and have been the most popular model for APOE mechanistic studies. However, despite the wide usage of these models, it has not translated in health benefits for human patients. This may be due to species-specific differences in the functions of identical genes and the non-physiological effects of human transgene overexpression.

Regarding the role of astrocytes in AD research, the question of using suitable model systems is even more crucial. Most studies on astrocytes in AD have either used post-mortem brain tissues, with already reactive or dystrophic astrocytes, or rodent models of AD. Here, it is important to note that human astrocytes differ from their rodent counterparts, in that they are about 2.6 times larger and more complex. They have 10 times the number of processes and cover about 20-fold more synaptic contacts (*Oberheim et al., 2006*). Thus, human neural cells obtained by

differentiating induced pluripotent stem cells (iPSCs) promise to be important tools in AD research.

1.5 Induced pluripotent stem cells (iPSCs)

1.5.1 iPSCs for disease modelling

In order to bring therapies from mouse models to humans, better physiological models of the disease are required. Since human brain tissues are inaccessible, induced pluripotent stem cell (iPSC)-derived neural cells are increasingly being used for basic studies. These can be obtained uninvasively, can be propagated indefinitely and differentiated to various cell types of the brain. After an egg is fertilized and a zygote is formed, it divides along several planes to give rise to the ball-like morula. This further develops into the blastocyst, which consists of an outer layer and an inner cell mass. The inner cell mass contains pluripotent stem cells. Pluripotent stem cells are characterized by the property of self-renewal and the ability to give rise to cells of the three germ layers- ectoderm, mesoderm and endoderm.

Waddington's epigenetic landscape model depicts the differentiation of a cell as a ball rolling downhill. (Figure 1.5) It was believed for a long time that the acquisition of a cell fate can occur only in one direction, i.e. from an undifferentiated to a differentiated state. A series of landmark experiments showed that cell fate can be reversed to a pluripotent state as well, i.e. by the ball climbing uphill past a series of epigenetic thresholds. In the 1960s, John Gurdon (*Gurdon, 1962*) showed that by transferring the nucleus of a somatic cell to an enucleated egg, an embryo can be formed. Thus, the process of SCNT (somatic cell nuclear transfer) was able to demonstrate that somatic cells retain all genetic information and can be manipulated to enter a pluripotent state. In 1981, Evans et al. generated self-renewing embryonic stem cell (ESC) lines from pre-implantation embryos. This was followed by reports of several cloned animals like sheep and mice, using SCNT (*Wilmut et al., 1997*). Studies showing direct conversion of one cell type to another by a single transcription factor, highlighted the prospect of cell fate conversion by ectopic expression of transcription factors, e.g. MYOD-mediated conversion from mouse fibroblasts to myoblasts.

Building on these seminal discoveries, *Takahashi et al., 2006* narrowed down 24 candidate reprogramming factors, selected for their high and specific expression in stem cells, to just 4

factors that were sufficient to generate mouse iPSCs from fibroblasts. The process of reprogramming was repeated in human iPSCs using the same four factors (*Takahashi et al., 2007*). The four factors, commonly called Yamanaka's factors delivered by retroviral transduction were OCT3/4, SOX2, KL4 and MYC (OSKM). At the same time, James Thompson's lab (*Yu et al., 2007*) also generated human iPSCs with 4 factors, where the KLF4 and MYC were replaced by LIN28 and Nanog. However, a lingering issue with reprogramming has been low reprogramming efficiencies.

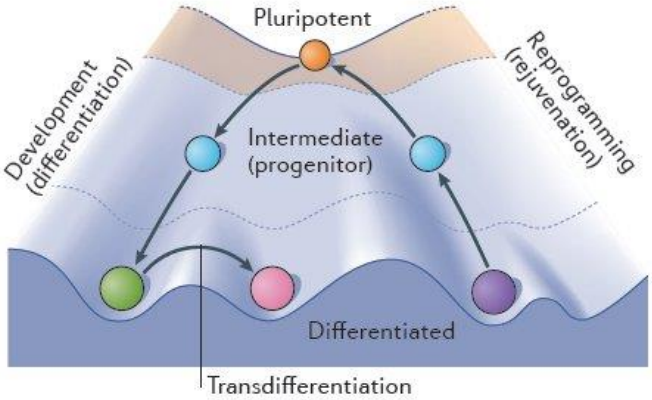

Figure 1.5: Conrad Waddington's model of development: Waddington's model depicts the acquisition of cell fate as a ball rolling down a mountain from an undifferentiated to a differentiated state. Landmark experiments in the field have demonstrated that this process is reversible as well, where cells can be reverted to an undifferentiated state through the process of reprogramming. Conversion of one cell type to another by the ectopic expression of tissue-specific transcription factors is also possible through the process of transdifferentiation that can be depicted as the ball travelling from one valley to another past an epigenetic threshold. *(Adapted from Takahashi et al., 2016)*

Somatic cell reprogramming is thought to occur in 2 phases: an early phase and a late phase (Figure 1.6). After transduction and expression of the reprogramming factors in the cell, the first 'early' stage of reprogramming includes suppression of somatic genes, mesenchymal-to-epithelial transformation and metabolic switch from oxidative phosphorylation to a glycolysis-based metabolism. The 'late' stage of reprogramming includes expression of late pluripotency factors, silencing of transgenes and a complete epigenetic resetting (*Takahashi et al., 2016*). Once both stages take place, complete reprogramming to iPSCs has occurred. However, based on the stochastic model of reprogramming, not all cells are able to complete both stages of reprogramming, and hence remain incompletely reprogrammed. This results in reduced efficiency of reprogramming. Additionally, a combination of high levels of OCT3/4 and low levels of SOX2 are essential to elicit mesendodermal features and this stoichiometry is especially important to complete the early stage of reprogramming (*Papapetrou et al., 2009*).

Another issue with early reprogramming protocols was the use of retroviruses or lentiviruses to deliver the transcription factors to the cells of interest. These vectors integrate into the genome of the host and thus run the risk of disrupting an important gene or reactivation of the reprogramming factors themselves. This is especially problematic in the case of KLF4 and c-Myc which are reported to have high oncogenic potential (*Dang, 2012*). In order to generate integration-free iPSCs, several alternate methods of reprogramming factor delivery have been employed such as episomal plasmids, recombinant proteins, mRNAs and Sendai viruses. Additionally, in order to facilitate iPSC use for transplantation studies, xeno-free substrates and culture media have been developed in order to carry out defined culture and eliminate usage of animal-derived products. Further, to eliminate the need for transfection, small molecule-based protocols have been developed by which certain small molecules mimic the functions of OSKM by blocking certain signaling cascades and epigenetic modifiers (*Takahashi et al., 2016*). One or two of these small molecules can also be used in conjunction with transfection of OSKM factors to improve reprogramming.

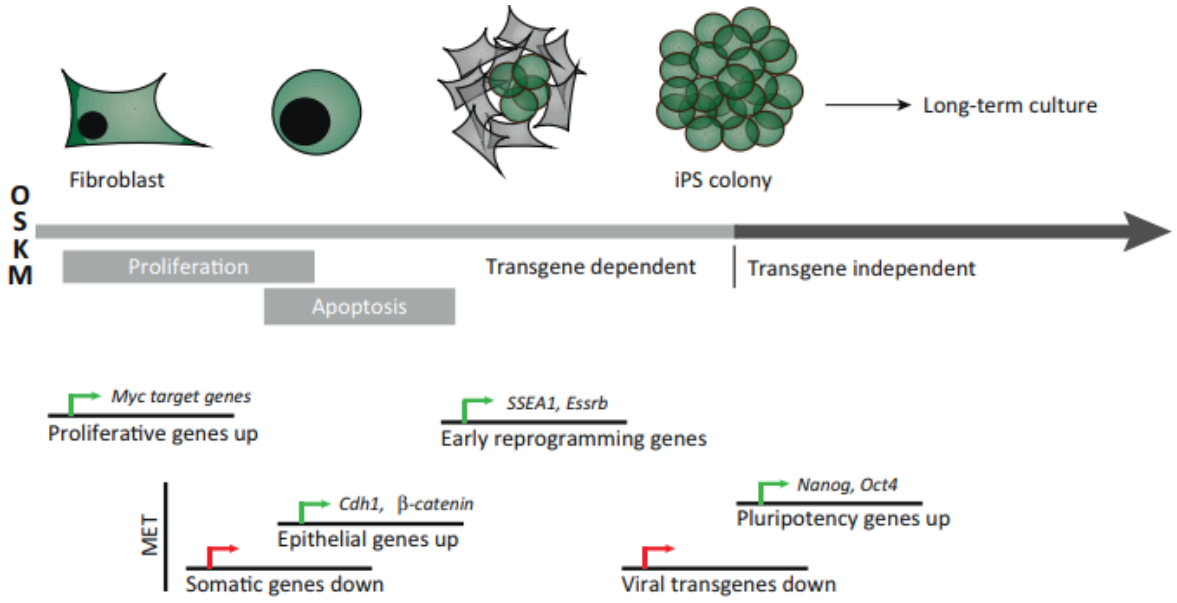

Figure 1.6: Somatic cell reprogramming phases: Reprogramming of somatic cells occurs in 2 stages: early and late. According to the stochastic model of reprogramming, not all the cells make it through both stages. Soon after exogenous OSKM expression in the cell, somatic gene expression is repressed while epithelial gene expression increases as part of the mesenchymal-to-epithelial transition (MET). Early reprogramming genes start to express and widespread apoptosis is observed at this stage. The early reprogrammed cells proliferate rapidly, start assuming a stem cell-like appearance, and form small clusters. As the expression of pluripotency genes in the cells rises, the core pluripotency network is re-activated and eventually cell pluripotency is transgene-independent *(modified from Federation et al., 2014).*

iPSCs can not only be generated from patient-derived somatic cells, but can also be genome edited at specific loci to yield isogenic cell lines, that enable the study of single disease-causing polymorphisms in isolation. In addition to studying disease mechanisms, iPSC-derived cultures can also be used for toxicity testing. Since the cells can be expanded in relatively short amount of time and differentiated to various cell types, they can be used to test candidate drugs before applying them to animal models or humans. Since autologous iPS cells can be generated from a patient's somatic cells, it reduces the risk of infection and immune rejection upon transplantation (Figure 1.7)

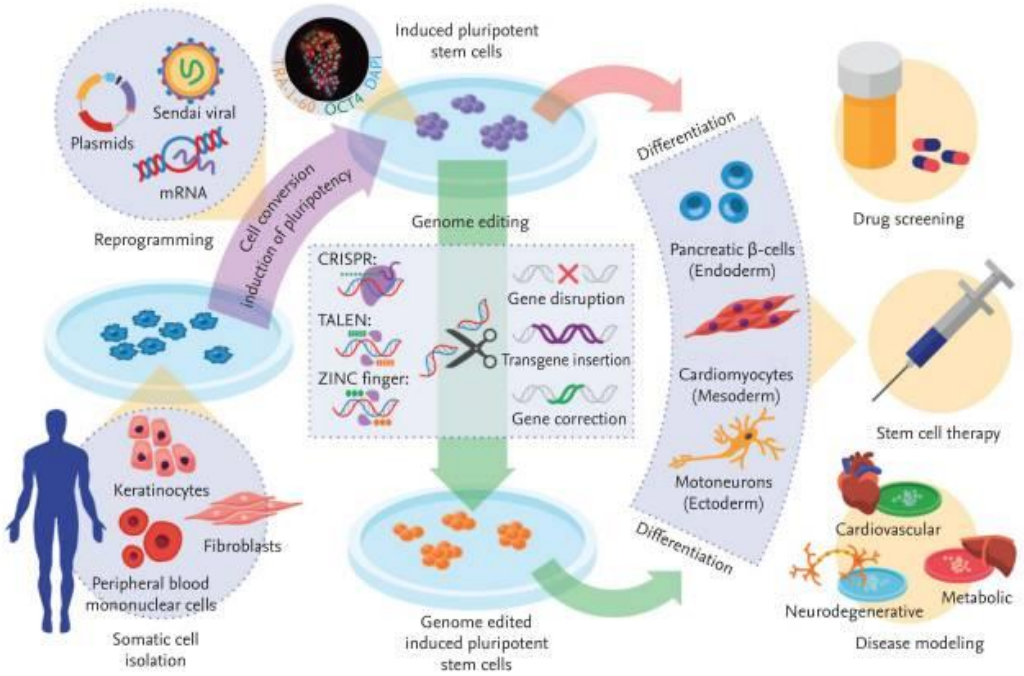

Figure 1.7: Applications of iPSCs: Somatic cells derived from patient or control individuals can be reprogrammed by transfection with pluripotency factors using plasmid, virus, protein or mRNA-based methods. The genome of these iPS cells can be edited using tools like CRISPR, TALEN or ZFN to generate isogenic lines. iPSCs can then be differentiated to several different cell types from the three germ layers. These cells types can be used as model systems to study disease mechanisms, or can be utilized for drug and toxicity testing. They can also help to push personalized medicine ahead by generating autologous cells for transplantation, to replace cells lost or damaged in disease. *(Adapted from Diecke et al., 2014)*

1.5.2 Differentiating hiPSCs to neurons

Progress in the study of human nervous system development and disease mechanisms has been hampered by inaccessibility of brain tissue. At the same time, human transgene overexpression animal models have been inadequate to study multifactorial and polygenic diseases like AD. iPSC technology has allowed the generation of patient-derived neural cells which enables the study of

the individual's unique genetic landscape. Using genome editing technologies, this genetic background can be tweaked to address specific questions. Protocols to differentiate iPSCs to neural cells types have been aided by landmark studies on the molecular programs involved in neural lineage commitment and regionalization.

The human nervous systems starts to develop when the stem cells of the inner cell mass start to proliferate and differentiate into the three germ layers: the endoderm, mesoderm and ectoderm. At the gastrula stage, the ectodermal cells become specialized to follow a neural fate. This is called neural induction. The activation of FGF and inhibition of WNT and BMP results in neuroectoderm specialization. Both these pathways converge onto SMAD signalling. The neuroectoderm further extends caudally to form the neural plate, which folds along a median hinge point and fuses to form the neural tube rostrally and caudally. The neural precursors (NPC) in different domains of the neural tube are patterned by a set of anterior-posterior (WNTs, FGFs, Retinoic Acid) and dorsal-ventral (WNTs, BMPs, SHH) morphogens. Different morphogens at specific concentrations confer positional identity onto the NPCs. These patterned NPCs give rise to different subsets of neurons. Once neurites are formed, neurotransmitter release guides dendrite development and aids in maturation of cells to enable formation of neural networks.

Zhang et al., 2001 were the first to report neural differentiation from human ES cells. They first switched ESCs from self-renewing conditions and generated embryoid bodies (EBs) by lifting hESC colonies and culturing them in suspension for a short duration in a medium free of mitogens. The EBs were then transferred to adherent culture in a defined medium containing N2 supplement and bFGF, giving rise to rosettes. A neural rosette is a two-dimensional correlate of a neural tube. The neural progenitor cells constituting this stage have a capacity for limited self-renewal and multipotency. Different neuronal subtypes can then be generated from these NPCs by following in vivo morphogen and mitogen cues. E.g. NPCs similar to those found in the hippocampus dentate gyrus have been obtained by treating EBs with antagonists of SHH pathway and with anti-posteriorizing factors like DKK1 and Noggin which block WNT, BMP and TGFβ pathways (*Yu et al., 2014*).

Chambers et al., 2009 described one of the most commonly used and robust protocols to generate dorsal forebrain neurons by 'dual SMAD inhibition' of adherent hESCs with Noggin and SB431542. This results in forebrain NPCs committed to both deep and upper layer fate. For experiments requiring very pure cultures of neuronal cells, immunopanning using neuronal markers can be carried out, such as described in *Nieweg et al., 2015*. Immunopurification entails gentle resuspension of the cell layer to single cells followed by selection with a neuron-specific antibody adsorbed onto the surface of a petri dish. In order to overcome the limitations of two-dimensional cultures, three-dimensional cerebral organoids, specific to different brain regions can better recapitulate human brain development.

1.5.3 Differentiating hiPSCs to astrocytes

Most AD studies thus far have been conducted using neuron-focused models, following leads from genetic studies. The consistent ineffectiveness of existing therapeutic approaches which mostly aim at reducing the level of Aβ in the brain has challenged the Aβ-dominated as well as the neurocentric way of viewing the disease. Rather, increasing evidence of the multitude of astrocyte-mediated homeostatic functions has highlighted the central role of glial cells in the disease etiology.

In recent years, rodent disease models have been used to uncover the role of astrocytes in neurodegeneration. However, crucial differences between human and rodent astrocytes cannot be ignored. Human astrocytes are about 2.6 times larger and far more complex (*Oberheim et al., 2006*). They also propagate Ca^{+2} waves far quicker (*Oberheim et al., 2006*), show more robust responses to glutamate (*Oberheim et al., 2009*) and specifically express about 600 human-enriched genes identified by RNA transcriptomics (*Zhang et al., 2016*). In fact, chimeric mice that received human astrocyte precursor transplants showed improved learning and memory, and enhanced long-term potentiation (*Han et al., 2013*).

Like hiPSC differentiation to neurons, *in vitro* astrocyte differentiation protocols have also evolved from developmental cues seen *in vivo*. However, astrocyte development is comparatively understudied in humans as compared to mice. For a long time, astrocytes were considered a very homogenous population of cells, but research over the past few years has shown that they are

functionally and regionally quite heterogeneous (*Miller et al., 2018*). Thus, a potential issue is agreeing on a definition for astrocytes. Another major issue has been developing reliable markers to characterize the derived astrocytes. The most frequently used astrocytic markers for *in vitro* studies have been S100β and GFAP. However, neural progenitors like radial glia also express these markers and can thus be mistaken for astrocytes.

Differentiation of astrocytes and other neural cells begins at E8.5 in mice with the neutralization of the ectoderm. The neuroepithelial layer first gives rise to radial glia which act as precursors to neurons, astrocytes and neural progenitor cells (NPCs). Radial glia are structurally characterized by their long processes that stretch from the ventricular zone all the way to the marginal zone (*Sild et al., 2011).* These cells divide to give rise to the NPCs which then travel along the radial glia processes to occupy different layers of the cortex (*Noctor et al., 2001*). Once neuronal differentiation and migration is complete, radial glia and NPCs give rise to astrocyte progenitors which differentiate to astrocytes in the early prenatal and late postnatal stages in mice. This process of astrogliogenesis relies on the activation of the BMP/SMAD and JAK/STAT pathways (*Yang et al., 2013*) by growth factors secreted by early neurons, like ciliary neurotrophic factor (CNTF) and leukaemia inhibitory factor (LIF). These induce the formation of SMAD1-STAT3 complex and activation of transcription factors like NF1A which promote the expression of astrocyte-related proteins like S100β and GLAST (*Hong et al., 2014; Deneen et al., 2006*). Furthermore, over the course of several weeks, with the aid of neuronal signaling, these immature astrocyte grow out processes that elongate. The maturation process also includes expression of glutamate and innate immune receptors to give rise to mature functional astrocytes.

In general, protocols to differentiate iPS cells to astrocytes include 4 key steps: (1) neural induction, (2) neural patterning, (3) gliogenic switch and (4) terminal differentiation (Figure 1.8). The neural induction step works similarly to that used for neuronal differentiation protocols, with dual SMAD inhibition being the most common approach. Pluripotency genes are downregulated and neural stem cell markers like Pax6 and Nestin are acquired. Neural rosette formation can be observed and the NPCs can be cultured as a monolayer. The newly generated NPCs are then regionally patterned along the anterior-posterior or dorsal-ventral axes using morphogens described in Section 1.5.2. It has been shown that the regional identity acquired by patterning is

retained also in the late stages of astrogliogenesis by the expression of homeodomain-specific transcription factors (*Krencik et al., 2011; Roybon et al., 2013*). As described above, astrogliogenesis follows neurogenesis *in vivo*. Similarly, *in vitro*, when NPCs are expanded, they switch developmental programs to generate astrocyte progenitors at a temporally defined time. This is known as the gliogenic switch and involves Notch signaling as a major element (*Morrison et al., 2009*), which mediates the simultaneous inhibition of proneural bHLH factors and activation of astrogliogenic JAK-STAT pathway. A wave of demethylation of astrocyte-specific genes is able to make this switch possible (*Namihira et al., 2009*). At this astrocyte progenitor or immature astrocyte stage, the cells are still proliferative. Cytokines like CNTF and LIF can be added at this stage to induce terminal differentiation of the astrocytes, so that they exit the cell cycle.

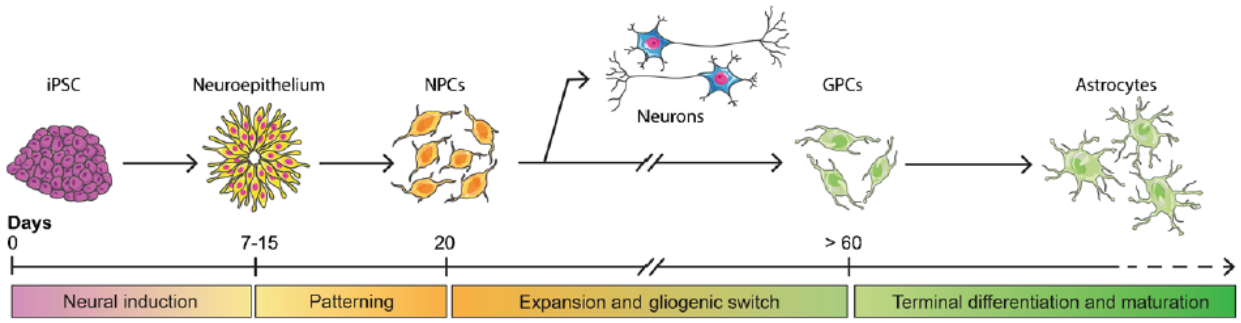

Figure 1.8: iPSC differentiation to astrocytes: The *in vitro* process of astrocyte differentiation goes through many intermediate stages and the entire process can take up to 120-180 days. These stages include neural induction of iPSCs to generate the neuroepithelium, followed by regional patterning of NPCs. Expansion of NPCs leads to a gliogenic switch yielding glial precursor cells (GPCs) after more than 8 weeks *in vitro.* These upon terminal differentiation and maturation yield astrocytes. *(Adapted from Tyzack et al., 2016)*

As astrocytes continue to mature, their gene expression profile changes, particularly involving functions like ion homeostasis, synaptogenesis, cell adhesion and fatty acid metabolism (*Sloan et al., 2017*). This hints that astrocytes change and acquire functions as they mature. However, so called classical astrocytic functions including the ability to uptake glutamate, immune reactivity, propagation of Ca^{+2} waves can be detected in a broad window of astrocyte maturation stages. Interestingly though, human astrocytes, in contrast to rodent astrocytes seem to respond to glutamate by eliciting cytoplasmic calcium elevations only upon reaching a mature stage (*Zhang et al 2016*). Listed in the table below are some of the commonly used astrocyte differentiation protocols. They vary widely in duration of the protocol, as well as efficiency or astrocyte yield. Moreover, protocols for astrocyte generation from iPSCs likely yield cultures with a mix of developmental stages. Since most of these protocols lack co-culture with neuronal cells, there is a

lack of developmental cues from neurons as well. Regarding the issue of overlapping expression of markers and functions between radial glia and astrocytes, it remains difficult to identify the maturity stage of the obtained astrocytes and it therefore becomes difficult to compare astrocyte phenotypes described in different disease modelling studies.

Table 1.1: Comparison of astrocyte differentiation protocols:

Study	GFAP +ve cells	Duration (days)	Growth factors	Astrocyte markers	Functional assays
Krencik et al., 2011	90%	120	EGF, FGF2, CNTF/LIF	CD44, NF1A, GFAP, S100β	Ca^{+2} wave propagation, Glutamate uptake
Emdad et al., 2012	70%	35	EGF, FGF2, CNTF	A2B5, GFAP, S100β	Migration assay
Roybon et al., 2013	70%	90	AA, BDNF, CNTF, FGF2, GDNP, IGF, RA	CD44, NF1A, S100β, CX43, Vimentin, ALDOC, AQP4, EAAT1, EAAT2	Ca^{+2} wave propagation, Glutamate uptake, IL-6 release
Serio et al., 2013	90%	49	EGF, LIF, FGF2, CNTF	CD44, NF1A, S100β, Vimentin, EAAT1	Glutamate uptake, Synaptogenic properties
Shaltouki et al., 2013	70%	42	FGF2, CNTF, NRG1β1	CD44, NF1A, S100β, GFAP, EAAT1	Glutamate uptake, Synaptogenic properties
Mormone et al., 2014	55%	35	EGF, FGF2, CNTF	GFAP, EAAT2, ALDOC	Migration assay

1.6 iPSC-based models to study AD

Most studies for AD cellular pathologies have been carried out using rodent models of disease which show important species-specific differences when compared to post-mortem AD patient brain tissue, which represents end-of-disease pathology, and misses a lot of the early druggable events. Some studies were also carried out using non-neural somatic cells like fibroblasts which suffer from cell-type specific differences. With the advent of iPSC technology in 2007, scientists now had a patient-specific system which could be differentiated to the neural cell types typically affected in AD. These patient-derived cell lines can be used to study molecular mechanisms of disease pathology, or can be used for screening of candidate drugs.

Most of the early studies modeling AD using iPS cells used familial AD patient cells and/or cells with mutations in familial AD-related loci, such as *APP* or *PSEN* (*Yagi et al., 2011*). These studies were able to recapitulate the *in vivo* differences in tau phosphorylation and APP processing. Most

of the studies relied on neuronal differentiation protocols developed around the same time, however a few worked with glia as well. These new human platforms were able to complete and in some cases, contradict the information gathered from rodent models. Most studies used sex- and age-matched controls to compare the patient lines to control lines. An important development was the use of isogenic cell lines generated by gene editing that allowed the recording of subtle phenotypes related to disease that would otherwise be lost in the noise of individual-to-individual variation, especially for a polygenic disease like AD.

With the advent of 3D modeling such as organoids or matrix-embedded cultures, interactions of multiple cells types in a disease state, and the resulting phenotypes can be studied in a more physiological way (*Choi et al., 2014*). Since neurons differentiated from iPSCs represent neonatal neurons, a lingering problem in the field has been the attempt to mature the neurons to study an ageing-related disease like AD. Some groups rely on applying oxidative stress to simulate ageing. Compared to models representing familial AD, relatively fewer groups have studied sporadic AD or APOE isoforms using iPSC-based lines. A summary of these studies can be found in Table 1.2

Table 1.2: Studies on APOE isoform-specific effects using iPSC-derived neural cells

Study	Genotypes tested and diagnosis	Cell type analyzed	Phenotype observed
Duan et al., 2014	*E3/E4* (sporadic AD) Control individuals	Neurons (basal forebrain cholinergic)	AD-APOE3/4 patients showed increased Aβ42/Aβ40 ratios APOE3/4 neurons also exhibited increased vulnerability to glutamate-mediated cell death APOE3/4 neurons showed increased intracellular free calcium upon glutamate exposure
Zhao et al., 2017	*E3/E3* *E4/E4* (both cognitively normal)	Astrocytes	APOE4 lipoprotein particles less lipidated APOE4/4 astrocytes less effective in supporting neurotrophic functions
Jones et al., 2017	*E4/E4* (sporadic AD) Healthy controls	Astrocytes	Reduced morphological heterogeneity compared with healthy cells Atrophy in astrocyte size and morphology S100β localized exclusively at the nucleus compared to control
Kim et al., 2017	Human mut-APP-expressing *E3/E4* and *E3/E3*	Induced neurons	Tendency for increased tau phosphorylation and production of Aβ42

Wang et al., 2018	*E4/E4* *E3/E3* (isogenic)	Neurons	APOE4 increased Aβ production in human, but not in mouse, neurons APOE4-expressing neurons had higher levels of tau phosphorylation APOE4-expressing cells displayed GABAergic neuron degeneration
Lin et al., 2018	*E3/E3* (unaffected control) *E4/E4* (isogenic)	Neurons Astrocytes Microglia Organoids	APOE4 neurons exhibited increased synapse number and elevated Aβ42 secretion APOE4 astrocytes displayed impaired Aβ uptake and cholesterol accumulation APOE4 microglia-like cells exhibited altered morphologies, which correlated with reduced Aβ phagocytosis Increased levels of Aβ and p-tau in APOE4 iPSC-derived cerebral organoids
Wadhwani et al., 2019	*E4/E3 (patient)* *E3/E3 (isogenic)*	Neurons (forebrain excitatory)	E3 neurons were less susceptible to ionomycin-induced cytotoxicity E4 cells exhibited increased tau phosphorylation E4 cells exhibited increased ERK1/2 phosphoactivation E4 neurons released increased amounts of phosphorylated tau extracellularly

1.7 CRISPR/Cas9- Challenges of applying genome editing to iPSCs

iPSC technology has been a major step forward in the study of monoallelic as well as complex polygenic diseases in the physiological context of patient-derived cell lines. The most common method of studying these cells, is to differentiate patient-derived iPSCs as well as age- and sex-matched control iPSCs to cell types of interest, followed by phenotypic comparison. However, a major caveat of using this approach, is the variation that exists between the individual cell lines to differentiate into cell types of a given lineage. While highly penetrant SNPs may possibly show major phenotypic differences, this phenomenon complicates the interpretation of mild phenotypic differences arising out of the study of partially penetrant mutations. In addition to this, one must also consider the variation arising out of the differences in the genetic background of the cases and controls, which may include low effect size SNPs across the genome. Thus, in such cases, using isogenic iPSC controls that differ only at the SNP of study, could help reduce unpredictable variations due to genomic variability.

More than two decades ago, experiments in mammalian cells revealed that a double stranded break (DSB) generated by a site-specific nuclease (SSN) at a site of interest, can stimulate the cell's DNA repair machinery to repair the break either by the error-prone non-homologous end joining

(NHEJ) pathway or the more precise homology-directed repair (HDR) when an exogenous repair template is provided (*Rouet et al., 1994a, 1994b*) (Figure 1.9). Importantly, if a DSB triggered HDR by several orders of magnitude as compared to when only a repair template is delivered. NHEJ repair typically results in small insertions or deletions that result in frameshift mutations and subsequent knockout of protein-coding genes. Precise modifications such as single nucleotide switch or insertion of reporter genes is achieved by co-delivering SSNs with repair templates.

SSNs typically comprise a customizable site-specific DNA binding domain fused to a non-specific nuclease domain. The first SSNs successfully used for genome editing in human iPSCs were zinc finger nucleases (ZFNs) (*Hockemeyer et al., 2009*). The first clinical trials to disrupt CCR5 in the T cells of HIV patients using ZFN are already underway (*Tebas et al., 2014*). However, ZFNs are relatively challenging to engineer and thus, their use remains limited. In 2009, an alternative SSN called transcription activator-like effector nuclease (TALEN) was discovered in plants (*Boch et al., 2009*). It consists of a TALE DNA-binding domain fused to a FokI nuclease domain. However, like the ZFNs, each DNA-binding domain of the TALEN requires precise engineering. Less than a decade ago, the CRISPR/Cas9 system was derived from bacteria (*Jinek et al., 2012*) and has been used to great success in iPSCs. This comparatively easy-to-use system has advantages and disadvantages compared to TALENs. While they show equivalent HDR efficiency in human iPSCs (*Yang et al., 2013*), hypermethylated DNA loci are more efficiently targeted by CRISPRs (*Hsu et al., 2013*). However, TALENs have less stringent design rules and show less tolerance to mismatches compared to the CRISPR/Cas9 system (*Miller et al., 2011, 2015*).

The clustered regularly interspaced short palindromic repeats (CRISPR)/Cas9 (CRISP- associated protein) is an adaptive immune system in bacteria and archaea. DNA fragments from invading bacteriophages are acquired and integrated into the host CRISPR loci between crRNA repeats. Upon the next infection, these ‘spacer’ sequences are transcribed and processed into mature crRNAs which are then recognized and bound by Cas proteins. The spacer sequence helps to recognize the invading genome while the crRNA repeats and tracrRNA help to recognize and bind the Cas9 proteins. The Type II CRISPR/Cas9 systems have been widely repurposed for use in genome editing and regulation of mammalian cells. This system consists of the chimeric guide RNA (gRNA), composed of a usually 20bp customizable sequence, and fused crRNA-tracRNA

sequence that can bind to the Cas9 nuclease protein. This 20bp region can be customized to bind to a target site of interest, and must always be followed by a PAM site on the genomic loci, e.g. in SpCas9 system, it is the NGG trinucleotide sequence. While this NGG sequence is present on average every 8 bp in the human genome (*Cong et al., 2013*), it is a comparatively restrictive feature as opposed to TALENs which can theoretically be used to target any site of interest.

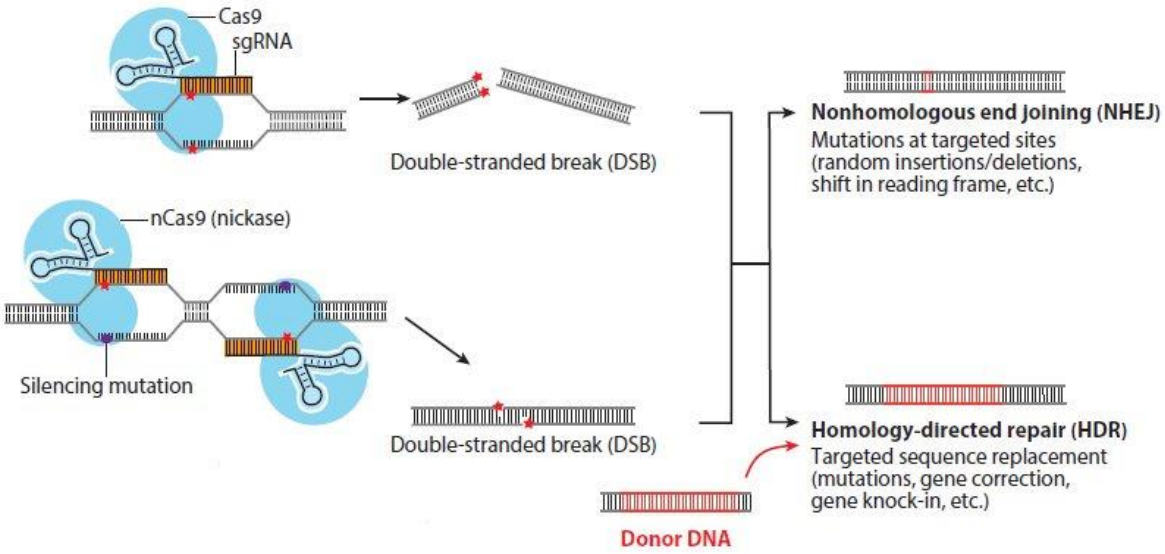

Figure 1.9: CRISPR/Cas9 system and DNA repair: Cas9 delivered as either wild type or nickase causes double stranded breaks (DSB) at the site of interest. This triggers the cell's repair pathways to fix the DSB using either the error prone non-homologous end joining (NHEJ) or if a donor sequence is present, by homology-directed repair (HDR). *(Adapted from Wang et al., 2015)*

While the CRISPR/Cas9 can be customized to target any site in the genome, this system is tolerant to mismatches i.e. promiscuous binding to off-target sites can lead to unwanted modifications. These off-target effects can especially limit clinical use of the modified cells. Engineered versions of the CRISPR/Cas9 system can be used to reduce off-target effects, such as Cas9 nickases (Cas9n). These are Cas9 variants that include a mutation in one of the two Cas9 domains- HNH, the domain that cleaves the target strand-complementary to the gRNA and Ruv-C like domain that cleaves the non-target strand. A nickase cleaves only one strand of DNA that can be repaired in an error-free way. Two adjacent nicks created by a pair of nickases will lead to a DSB, thus increasing the specificity of the system. Using a pair of D10A nickases, with gRNAs targeted to opposite strands created 50- to 1500-fold fewer off targets compared to using wild type Cas9 (*Ran et al., 2013b*). Several other variants of Cas9 exist with different, rarer PAM sites, thus helping to increase the specificity of gRNA binding e.g. Cpf1 which uses a TTTN PAM site. In addition to

naturally occurring variants of Cas9, several rationally engineered high-fidelity variants of Cas9 also exist, for e.g. the HiFi Cas9 which reduces off-target editing while retaining the high on-target activity of Cas9 (*Vakulskas et al., 2018*). Off-target effects can also be predicted and reduced by careful selection of the gRNA, design of the exogenous single stranded oligonucleotide (ssODN) donor sequence, and mode of delivery of Cas9 into the cells.

Converting the *APOE4* allele to *APOE3* in patient iPSCs to generate isogenic controls, involves changing a single base pair in the codon for amino acid 112 (as shown in Figure 1.3) by HDR. Although the HDR:NHEJ ratio induced by genome-editing is inherently influenced by gene locus and cell type (*Miyaoka et al., 2016*), HDR rates can be increased and off targets reduced by modifying key steps in the genome editing process. The various steps of this process includes delivering gRNA, Cas9 and exogenous donor to the cell, followed by selecting the successfully transfected cells, culturing these cells as clones, isolating DNA to perform a preliminary genotype screen and then performing Sanger sequencing to confirm the change of interest. This is generally followed by characterizing the positive clones and testing for off targets.

gRNA sequences must be chosen after careful consideration of the potential off target sites, by using several widely available softwares (e.g. Benchling). Ideally, gRNA sequences must be chosen such that the cut site is within 50 bp of the site of the SNP. Beyond this, the rate of HDR drops dramatically (*Yang et al., 2013*). Efficiency of a gRNA sequence to induce editing can be tested in easily transfected cells such as HEKs, followed by analysis using in silico methods like TIDE (tracking of indels by decomposition). Meanwhile, the choice of donor sequence depends on the size of sequence to be integrated. For small sequences and SNPs, single stranded oligonucleotides (ssODNs) are used instead of plasmids, with at least 40 bp of homology on either side of the SNP. Sequence divergence between the repair template homology arms and genomic locus must be less than 2% to ensure high levels of HDR (*Elliot et al., 1998*). Hence, the site of interest in each cell line must be sequenced before designing the ssODN. It must include a mutation in the gRNA PAM site or gRNA sequence itself, in order to ensure that the site is not recut by the Cas9 after successful integration into the genome. Richardson et al., 2016 have demonstrated an enhancement in HDR using rationally designed asymmetric ssODNs. Additionally, delivery of Cas9 as mRNA or protein has been successfully used in hPSCs, and has been associated with a

reduction in off target indels (*Kim et al., 2014, Zuris et al., 2015).* Several studies have shown an improvement in HDR rates by actively inhibiting NHEJ using small molecule inhibitors SCR7 (*Song et al., 2016, Chu et al., 2015*) and transfection of iPSCs in the G2/M phase (*Yang et al., 2016*). *Guo et al., 2018* suggest 'cold shocking' the cells by culturing at 32ºC after transfection for 24-48 hours in order to improve HDR by two fold in iPSCs.

Performing successful genome editing by HDR in iPSCs is fraught with complications due to several reasons. Firstly, human iPSCs tend to be resilient to gene targeting approaches due to cell intrinsic-features like the preference for repair of a DSB by NHEJ rather than HDR (*Chapman et al., 2012*). Furthermore, iPSCs are particularly hard to transfect and also show poor survival as single cells, thus preventing their clonal culture. They also show poor survival after FACS. Thus, before attempting genome editing with iPSCs, there must be robust protocols in place for iPSC transfection, FACS and clonal culture.

1.8 Aim of the study:

The goal of this study was to develop an isogenic human patient-derived neural cellular model to examine APOE4-isoform specific effects in neurons and astrocytes.

The first part of this study was thus, to generate and characterize a set of iPS cells derived from human APOE4 carriers and controls. The greatest advantage of using patient-derived cells is that they would accurately represent the patient's unique genetic background. Since these iPSCs are derived from adult somatic cells, they circumvent the ethical issues associated with embryonic stem cells, they are obtained rather non-invasively, can divide indefinitely and can be differentiated to different cell types. After generation, the iPSCs had to be characterized for pluripotency and for chromosomal integrity, by karyotyping.

Second, CRISPR/Cas9 protocols had to be optimized to generate isogenic APOE3 controls from the APOE4 patient iPS cells. The use of isogenic controls is especially important to study a polygenic disease like AD so that subtle phenotypes are not lost in the noise of cell line-to-cell line variation. This included optimizing a Cas9 delivery system for a hard-to-transfect cell like iPSCs.

Third, the APOE3 and APOE4 isogenic iPS cells were differentiated to neurons using the protocol established by *Nieweg et al., 2015*. Typical AD-related phenotypes were tested such as Aβ processing, tau phosphorylation, response to oxidative stress, size of endosomes and lysosomes, mitochondrial function, and expression of mitochondrial complexes.

Finally, the APOE3 and APOE4 isogenic iPS cells were differentiated to astrocytes. Since astrocytes develop and mature relatively late in human neurodevelopment, the differentiated cells were characterized for functionality and hence, for their relevance in the study. Further, the astrocytes were used to study AD-related APOE isoform-specific differences in endosome and lysosome enlargement, energy metabolism and mitochondrial function.

2. Materials and Methods

2.1 List of plasticware for cell culture

Item	Catalog no.	Supplier
10 ml Steripipette	4488	Corning
60 mm dish	353004	BD Falcon
100 mm dish	83.1802	Sarstedt
100 mm dish for panning	351029	BD Falcon
0.2 µm filter	28145-477	VWR
6 well plate	83.3920.005	Sarstedt
12 well plate	83.3921	Sarstedt
24 well plate	83.3922.005	Sarstedt
96 well plate	83.392.005	Sarstedt
96 well plate for BCA assay	655101	Greiner
1500 µL microfuge tubes	72.706	Sarstedt
2000 µL microfuge tubes	30120.09	Eppendorf
15 ml falcon tubes	188271	Greiner
50 ml falcon tubes	227261	Greiner
T25 flasks	83.1810.002	Sarstedt
Cryovials	377267	Thermo Scientific
Glass slides		Engelbrecht

2.2 List of plasmids

Plasmid name	Addgene ID	Purpose/Protein expressed
pCXLE-hOCT3/4-shp53-F	Plasmid #27077	human OCT3/4
		shRNA against p53
pCXLE-hSK	Plasmid #27078	human SOX2
		KLF4
pCXLE-hUL	Plasmid #27080	human L-MYC
		LIN28

Plasmid name	Addgene ID	Purpose/protein expressed
PX458 (pSpCas9(BB)-2A-GFP)	Plasmid #48138	Cas9 from S. pyogenes with 2A-EGFP (driven by CBh promoter) and cloning backbone for 1 sgRNA
PX461 (pSpCas9n(BB)-2A-GFP)	Plasmid #48140	Cas9n (D10A nickase mutant) from S. pyogenes with 2A-EGFP (driven by CBh promoter), and cloning backbone for 1 sgRNA
PX461i		Cas9n (D10A nickase mutant) from S. pyogenes with 2A-EGFP (driven by CBh promoter), and cloning backbone for 2 sgRNAs
PX461i-CAG		Cas9n (D10A nickase mutant) from S. pyogenes with 2A-EGFP (driven by CAG promoter), and cloning backbone for 2 sgRNAs
PX461i-PGK		Cas9n (D10A nickase mutant) from S. pyogenes with 2A-EGFP (driven by PGK promoter), and cloning backbone for 2 sgRNAs

2.3 List of commercial cell lines

Cell line	Cell type	Catalog no.	Source
SZ01	Fibroblast	ATCC-SCRC-1041	ATCC
SZ02	Fibroblast		GlobalStem
10984	LCL	AG10984	Coriell Institute
11001	LCL	AG11001	Coriell Institute
10987	LCL	AG10987	Coriell Institute
11368	Fibroblast	AG11368	Coriell Institute
B3/3	iPSC	BIONi010-C-2	EBiSC
B4/4	iPSC	BIONi010-C-4	EBiSC

2.4 Antibodies list

2.4.1 List of primary antibodies

Antibody	Species reactivity	Catalogue no.	Supplier	WB	ICC
Cas9	Ms	#14697	CST	1:1000	1:800
Cas9-PE	Ms	#35193	CST	-	1:50 (FACS)
α/β-tubulin	Rb	#2148	CST	1:10000	-
OCT4	Rb	#9656	CST	-	1:300
SOX2	Rb	#9656	CST	-	1:300
SSEA4	Ms	#9656	CST	-	1:300
TRA1-81	MS	#9656	CST	-	1:300
PAX6	Ms	#AB 528427	Developmental Studies Hybridoma Bank	-	1:100
GATA4	Rb	#A303-503A	CST	-	1:200
FOXC1	Rb	#A303-520A	Bethyl Laboratories inc.	-	1:100
Nestin	Ms	MAB1259	R&D Systems	-	1:200
TBR1	Rb	ab31940	Abcam	-	1:500
SATB2	Ms	ab51502	Abcam	-	1:50
CTIP2	Rat	Ab18465	Abcam	-	1:500
GAD67	Ms	MAB5406	Millipore	-	1:250
S100β	Rb	Ab52642	Abcam	1:2000	-
GFAP	Rb	Z0334	Dako	1:10000	1:2000
S100β	Ms	S2532	Sigma	-	1:500
GLAST	Ms	130-095-822	Miltenyi	-	1:100

Antibody	Species reactivity	Catalogue no.	Supplier	WB	ICC
ALDH1L1	Ms	H00010840-M01	Abnova	1:500	- -
GAPDH	Ms	G8795	Sigma	1:10000	-
AT8	Ms	MN1020	Thermo	1:500	1:300
PHF1	Ms			1:2000	1:500
APOE	Rat	MAB41441	R&DSystems	1:1000	-
MAP2	Ch	ab92434	Abcam	-	1:2500
EEA1	Rb	#07-1820	Millipore	-	1:500
LAMP2	Ms	H4B4	Developmental Studies Hybridoma Bank	-	1:40
OXPHOS Complexes	Ms	Ab110411	Abcam	1:500	-

2.4.2 List of secondary antibodies:

Antibody	Catalogue no.	Supplier	Dilution
Goat anti mouse Alexa Fluor 488	AG11001	Invitrogen	1:1000
Goat anti mouse Alexa Fluor 555	A21424	Invitrogen	1:1000
Goat anti rabbit Alexa Fluor 488	A11034	Invitrogen	1:1000
Goat anti rabbit Alexa Fluor 555	A21429	Invitrogen	1:1000
HRP conjugated anti-mouse IgG	sc-2005	Santacruz Biotechnology	1:4000
HRP conjugated anti-rabbit IgG	sc-2054	Santacruz Biotechnology	1:4000
HRP conjugated anti-rat IgG	sc-2065	Santacruz Biotechnology	1:4000

2.5 Molecular biology kits

Reagent	Catalog no.	Supplier
Human APOE ELISA Kit	EHAPOE	Thermo Scientific
Human Aβ40 ELISA Kit	KHB3481	Invitrogen
Human Aβ42 Ultrasensitive ELISA Kit	KHB3544	Invitrogen
BD Cytometric Bead Array Human Chemokine Kit	552990	BD Biosciences
QIAamp DNA Blood Mini Kit	51104	Qiagen
EndoFree Plasmid Maxi Kit	12362	ZymoResearch
Zyppy Plasmid Miniprep	D4036	Qiagen
QIAquick Gel Extraction Kit	28704	Qiagen
BCA kit	23228	Thermo Scientific

2.6 List of primers

Name	Purpose	Annealing temperature	Sequence (5' to 3')
D7S796 FP	DNA fingerprinting	55°C	TTTTGGTATTGGCCATCCTA
D7S796 RP	DNA fingerprinting	55°C	GAAAGGAACAGAGAGACAGGG
D10S1214 FP	DNA fingerprinting	55°C	ATTGCCCCAAAACTTTTTTG
D10S1214 RP	DNA fingerprinting	55°C	TTGAAGACCAGTCTGGGAAG
EBNA-1 FP	EBNA1	55°C	ATCGTCAAAGCTGCACACAG
EBNA-1 RP	EBNA1	55°C	CCCAGGAGTCCCAGTAGTCA
OriP FP	OriP	55°C	TTCCACGAGGGTAGTGAACC
OriP RP	OriP	55°C	TCGGGGGTGTTAGAGACAAC
APOENickase_OT1_FP	Off target 1 for A3/3 line	51°C	GAGTACCGAGAAACTGCAGATG
APOENickase_OT1_RP	Off target 1 for A3/3 line	51°C	CCTGAGAGTGGTATCTGTCTTG
APOENickase_OT2_FP	Off target 2 for A3/3 line	53°C	GGATCAAACACCAAGCCATGTG
APOENickase_OT2_RP	Off target 2 for A3/3 line	53°C	GCTTCCTTGATGTCCACTCAGAG
APOENickase_OT3_FP	Off target 3 for A3/3 line	59°C	GTGGGCGTTCGACACTGTGC
APOENickase_OT3_RP	Off target 3 for A3/3 line	59°C	CTGCAGCCTCAGCGGTGGG
APOENickase_OT4_FP	Off target 4 for A3/3 line	51°C	GACGACGTAGAGAGTTAAGCTC

Name	Purpose	Annaling temperature	Sequence (5’ to 3’)
APOENickase_OT4_RP	Off target 4 for A3/3 line	51°C	GACGGACTCATGGTTCCCATG
APOE-R	APOE PCR for RFLP	60°C	ACAGAATTCGCCCCGGCCTGGTACACTGCC
APOE-F	APOE PCR for RFLP	60°C	TAAGCTTGGCACGGCTGTCCAAGGA
Px462+iFP	Seq primer to check gRNA integration	-	GAGGGCCTATTTCCCATGATTC
SET2 APOE FP5	APOE PCR for sequencing	61°C	CAGTCTCTCACACTCGTCCTGGC
Set2 APOE RP5new	APOE PCR for sequencing	61°C	AGCCTGCACCTTCTCCACCA
APOEnick1seq1	Seq primer to check for nickase gRNA integration	-	GAGGGCCTATTTCCCAT
RP_seq-Prom462i	Seq primer to check promoter integration		GATCCTTGTAGTCTCCGTCGT

2.7 List of gRNAs and ssODNs

Name	Description	Sequence (5' to 3')
Apoe4_Site3_20bp_ Bbs_top	Site 3 forward gRNA for PX458 and PX461i (with BbSI restriction ends) top strand	CACCGCGGACATGGAGGACG TGCG
Apoe4_Site3_20bp_Bbs_bottom	Site 3 forward gRNA for PX458 and PX461i (with BbSI restriction ends) bottom strand	AAACCGCACGTCCTCCATGTC CGC
Apoe4_Site2_20bp_Bbs_top	Site 2 forward gRNA for PX458 and PX461i (with BbSI restriction ends) top strand	CACCGGAGGACGTGCGCGGC CGCC
Apoe4_Site2_20bp_Bbs_bottom	Site 2 forward gRNA for PX458 and PX461i (with BbSI restriction ends) bottom strand	AAACGGCGGCCGCGCACGTCC TCC
Apoe4_Nicksite_20bp_Sap_top	Nickase site reverse gRNA for PX458 and PX461i (with SapI restriction ends) top strand	ACCGCTGCGCCGCCTGCAGCT CCT
Apoe4_Nicksite_20bp_Sap_bottom	Nickase site reverse gRNA for PX458 and PX461i (with SapI restriction ends) bottom strand	AACAGGAGCTGCAGGCGGCG CAGC
Apoe4_Site2_20bp_crRNA	crRNA to bind Site 2	rGrGrArGrGrArCrGrUrGrCrGrCr GrGrCrCrGrCrCrGrUrUrUrUrArGr ArGrCrUrArUrGrCrU
Apoe4_Site3_20bp_crRNA	crRNA to bind Site 3	rGrCrGrGrArCrArUrGrGrArGrGr ArCrGrUrGrCrGrGrUrUrUrUrArG rArGrCrUrArUrGrCrU

Name	Description	Sequence (5' to 3')
Apoe4_Nicksite_20bp_crRNA	crRNA to bind Nickase Site	rCrUrGrCrGrCrCrGrCrCrUrGrCrA rGrCrUrCrCrUrGrUrUrUrUrArGr ArGrCrUrArUrGrCrU
Apoe4_WT_NTSYM_Site3_125bp	125 bp non-target symmetric ssODN for WT Cas9 with a silent mutation to prevent recutting on gDNA at Site 3	CACGGCTGTCCAAGGAGCTGC AGGCGGCGCAGGCCCGGCTG GGCGCGGACATGGAGGATGT GTGCGGCCGCCTGGTGCAGTA CCGCGGCGAGGTGCAGGCCAT GCTCGGCCAGAGCACCGAGG AG
Apoe4_Nick_NTSYM_Site3_bothmut_124bp	124 bp non-target symmetric ssODN for D10A Cas9 with 2 silent mutations to prevent recutting on gDNA at Site 3 & Nickase Site	CCCCGGTGGCGGAGGAGACG CGGGCACGGCTGTCTAAGGAG CTGCAGGCGGCGCAGGCCCG GCTGGGCGCGGACATGGAGG ATGTGTGCGGCCGCCTGGTGC AGTACCGCGGCGAGGTGCAG GC
Apoe4_WT_TSYM_Site3_125bp	125 bp target symmetric ssODN for WT Cas9 with silent mutation to prevent recutting on gDNA at Site 3	CTCCTCGGTGCTCTGGCCGAG CATGGCCTGCACCTCGCCGCG GTACTGCACCAGGCGGCCGCA CACATCCTCCATGTCCGCGCC CAGCCGGGCCTGCGCCGCCTG CAGCTCCTTGGACAGCCGTG
Apoe4_WT+Nick_TASYM_Site3_127bp	127 bp target asymmetric ssODN for WT Cas9 with silent mutation to prevent recutting on gDNA at Site 3	CAGGTGGGAGGCGAGGCGCA CCCGCAGCTCCTCGGTGCTCT GGCCGAGCATGGCCTGCACCT CGCCGCGGTACTGCACCAGGC GGCCGCACACATCCTCCATGT CCGCGCCCAGCCGGGCCTGCG CC
Apoe4_Nick_TSYM_Site3_bothmut_124bp	124 bp target asymmetric ssODN for D10A Cas9	GCCTGCACCTCGCCGCGGTAC TGCACCAGGCGGCCGCACACA

	with 2 silent mutations to prevent recutting on gDNA at Site 3 & Nickase Site	TCCTCCATGTCCGCGCCCAGC CGGGCCTGCGCCGCCTGCAGC TCCTTAGACAGCCGTGCCCGC GTCTCCTCCGCCACCGGGG
Apoe4_WT_NTSYM_Site2_125bp	125 bp non-target symmetric ssODN for WT Cas9 with a silent mutation to prevent recutting on gDNA at Site 2	CACGGCTGTCCAAGGAGCTGC AGGCGGCGCAGGCCCGGCTG GGCGCGGACATGGAGGACGT GTGCGGCCGGCTGGTGCAGTA CCGCGGCGAGGTGCAGGCCAT GCTCGGCCAGAGCACCGAGG AG
Apoe4_Nick_NTSYM_Site2_site2mut_124bp	124 bp non-target symmetric ssODN for D10A Cas9 with a silent mutation to prevent recutting on gDNA at Site 2	CCCCGGTGGCGGAGGAGACG CGGGCACGGCTGTCCAAGGA GCTGCAGGCGGCGCAGGCCC GGCTGGGCGCGGACATGGAG GACGTGTGCGGCCGGCTGGTG CAGTACCGCGGCGAGGTGCA GGC
Apoe4_Nick_NTSYM_Site2_both mut_124bp	124 bp non-target symmetric ssODN for D10A Cas9 with 2 silent mutations to prevent recutting on gDNA at Site 2 & Nickase Site	CCCCGGTGGCGGAGGAGACG CGGGCACGGCTGTCTAAGGAG CTGCAGGCGGCGCAGGCCCG GCTGGGCGCGGACATGGAGG ACGTGTGCGGCCGGCTGGTGC AGTACCGCGGCGAGGTGCAG GC
Apoe4_Nick_NTSYM_Site3_site3mut_124bp	124 bp non-target symmetric ssODN for D10A Cas9 with a silent mutation to prevent recutting on gDNA at Site 3	CCCCGGTGGCGGAGGAGACG CGGGCACGGCTGTCCAAGGA GCTGCAGGCGGCGCAGGCCC GGCTGGGCGCGGACATGGAG GATGTGTGCGGCCGCCTGGTG CAGTACCGCGGCGAGGTGCA GGC

2.8 Cell culture media and supplements

LCL medium

Reagent	Catalog no.	Supplier	Stock concentration	Volume
RPMI	RPMI-A	Capricorn	1X	83 ml
Fetal Bovine Serum	A15-751	PAA Labs.	1X	15 ml
Glutamax	35050-038	Invitrogen	100X	1 ml
Pen/Strep	15140-122	Invitrogen	100X	1 ml

Fibroblast medium

Reagent	Catalog no.	Supplier	Stock concentration	Volume
High Glucose DMEM	11965092	Gibco	1X	88 ml
Fetal Bovine Serum	A15-751	PAA Labs.	1X	10 ml
Glutamax	35050-038	Invitrogen	100X	1 ml
Pen/Strep	15140-122	Invitrogen	100X	1 ml

E8 medium

Reagent	Catalog no.	Supplier	Stock concentration	Volume
DMEM/F-12	31330-095	Invitrogen	1X	98 ml
NaHCO3	S3817	Sigma	34.3 mg/ml	1 ml
Ascorbic acid	A8960	Sigma	221 mM	100 µl
ITS		Refer 2.7	50X	2 ml
Pen/Strep	15140-122	Invitrogen	100X	1 ml
bFGF	100-18B	Peprotech	20 µg/ml	500 µl
TGFβ	AF100-15	Peprotech	20 µg/ml	100 µl

Medium for differentiation to germ layers

Reagent	Catalog no.	Supplier	Stock concentration	Volume
Knockout DMEM	10829018	Gibco	1X	80 ml
Fetal Bovine Serum	A15-751	PAA Labs.	1X	20 ml
Glutamax	35050-038	Invitrogen	100X	1 ml
Pen/Strep	15140-122	Invitrogen	100X	1 ml

N2B27 medium

Reagent	Catalog no.	Supplier	Stock concentration	Volume
DMEM/F-12	FG4815	Biochrom	1X	50 ml
Neurobasal	21103	Invitrogen	1X	50 ml
N2		Refer 2.7	50X	1 ml
B27 w/o RA	12587-010	Invitrogen	50X	1 ml
Glutamax	35050-038	Invitrogen	100X	0.5 ml
Heparin	H3149	Sigma	10 mg/ml	30 µl
β-mercaptoethanol	31350-010	Invitrogen	50 mM	200 µl
Pen/Strep	15140-122	Invitrogen	100X	1 ml

NSC medium

Reagent	Catalog no.	Supplier	Stock concentration	Volume
DMEM/F-12	FG4815	Biochrom	1X	50 ml
N2		Refer 2.7	50X	1 ml
B27 w/o RA	12587-010	Invitrogen	50X	1 ml
Glutamax	35050-038	Invitrogen	100X	0.5 ml
MEM-NEAA	11140-050	Invitrogen	100X	0.5 ml
Heparin	H3149	Sigma	10 mg/ml	25 µl
Pen/Strep	15140-122	Invitrogen	100X	1 ml
bFGF	100-18B	Peprotech	20 µg/ml	50 µl
EGF	AF100-15	Peprotech	20 µg/ml	50 µl

2.9 Cell culture supplements

Pan PBS

Reagent	Catalog no.	Supplier	Stock concentration	Volume
PBS	PBS-1A	Capricorn	1X	500 ml
Glucose	1083371000	Merck	33.3%	1.5 ml
Na-Pyruvate	11360	Invitrogen	100 mM	1.6 ml

ITS

Reagent	Catalog no.	Supplier	Stock concentration	Volume
DMEM/F-12	31330-095	Invitrogen	1X	90.2 ml
Insulin	I1882	Sigma	10 mg/ml	9.99 ml
Holo-transferrin	616424	Calbiochem	20 mg/ml	2.76 ml
Sodium selenite	S5261	Sigma	1.4 mg/ml	51.5 µl

N2

Reagent	Catalog no.	Supplier	Stock concentration	Volume
DMEM/F-12	FG4815	Biochrom	1X	79 ml
Insulin	I1882	Sigma	10 mg/ml	20 ml
Holo-transferrin	616424	Calbiochem	20 mg/ml	20 ml
Sodium selenite	S5261	Sigma	0.52 mg/ml	80 µl
Progesterone	P8783	Sigma	0.62 mg/ml	80 µl
Putrescine	P5780	Sigma	161 mg/ml	900 µl
BSA	A4919	Sigma	10 mg/ml	40 ml

SATO

Reagent	Catalog no.	Supplier	Stock concentration	Volume
Neurobasal	21103	Invitrogen	1X	33.8 ml
Insulin	I1882	Sigma	10 mg/ml	10 ml
Holo-transferrin	616424	Calbiochem	20 mg/ml	10 ml
Sodium selenite	S5261	Sigma	0.4 mg/ml	400 µl
BSA	A4919	Sigma	20 mg/ml	20 ml
Putrescine	P5780	Sigma	161 mg/ml	400 µl
Progesterone	P8783	Sigma	0.62 mg/ml	400 µl

2.10 Additional reagents for cell culture

Reagent	Catalog no.	Supplier	Stock concentration
Accutase	A6964	Sigma	1X
BSA (for panning)	15260-037	Gibco	7.5%

CNTF	450-13	Peprotech	10 µg/ml
CryoStor	C2874	Sigma	1X
DMSO	D4540	Sigma	100%
DPBS	PBS-1A	Capricorn	1X
Laminin	L2020	Sigma	1 mg/ml
LDN-193189	S2618	Selleckchem	2.5 mM
LIF	300-05	Peprotech	20 µg/ml
Matrigel	354277	BD Bioscience	9.9 mg/ml
mTESR medium	05852	StemCell Tech.	1X
NCAM antibody	VIN-IS-53	DSHB	
Poly L-ornithine	P3655	Sigma	1 mg/ml
ROCK inhibitor	1254	Tocris	10 mM
Secondary Antibody (for panning)	115-005-068	Jackson Labs	10 µg/ml

2.11 Buffers and solutions

2.11.1 Buffers for immunocytochemistry

4% PFA

Reagent	Catalog no.	Supplier	Concentration	Volume
PFA	18814	Polysciences	16%	10 ml
PBS	P0436500	Pan Biotech	1X	30 ml

Permeabilisation buffer

Reagent	Catalog no.	Supplier	Concentration	Volume
Glycine	50045	Sigma	1M	600 µl
Triton X-100	X100	Sigma	10%	150 µl
PBS	P0436500	Pan Biotech	1X	5.25 ml

Antibody buffer

Reagent	Catalog no.	Supplier	Concentration	Volume
Sucrose	10176871000	Merck	50%	600 µl
BSA	A3059	Sigma	20%	600 µl
PBS	P0436500	Pan Biotech	1X	4.8 ml

Blocking buffer

Reagent	Catalog no.	Supplier	Concentration	Volume
Normal goat serum	16210064	Invitrogen	100%	300 µl
Antibody Buffer			1X	700 µl

Additional reagents

Reagent	Catalog no.	Supplier	Concentration
Hoechst 33342	382065	Calbiochem	10 µg/ml
Fluorsave mounting medium	345789	Calbiochem	1X

2.11.2 Buffers for calcium imaging

HEPES-Ringer buffer (Loading and Imaging Buffer)

Reagent	Catalog no.	Supplier	Concentration
$CaCl_2$	HN04.1	Roth	1.5 mM
KCl	HN02.1	Roth	5 mM
NaCl	S5886	Sigma	140 mM
$MgCl_2$	HN03.1	Roth	0.75 mM
NaH_2PO_4	S8282	Sigma	1.25 mM
Glucose	G70021	Sigma	20 mM
HEPES	HN77.3	Roth	15 mM
NaOH	22.146-5	Sigma	Adjust to pH 7.4

1M NaOH was used to adjust the pH to 7.4, followed by filter-sterilization using a 0.2 µm filter.

Additional reagents for calcium imaging

Reagent	Catalog no.	Supplier	Concentration
DMSO	D4540	Sigma	1X
Fluo 4-AM	F14201	Invitrogen	5 µM
ATP	A2383	Sigma	100 µM
L-Glutamate	G6150	Sigma	100 µM

2.11.3 Buffers for protein isolation and western blot

Cell lysis buffer

Reagent	Catalog no.	Supplier	Concentration
RIPA Buffer	R0278	Sigma	1X (10ml)
PhosSTOP	0490845001	Roche	1 tablet
Complete ultra mini	05892970001	Roche	1 tablet

Reagents for protein estimation

Reagent	Catalog no.	Supplier	Concentration
BSA	23228	Thermo Scientific	2 mg/ml
RIPA Buffer	D4540	Sigma	1X
BCA Kit	23228	Thermo Scientific	

Sample loading buffer

Reagent	Catalog no.	Supplier	Concentration	Volume
Tris-HCl pH6.8	H5143	Promega	1.5 M	2 ml
SDS	75746	Sigma		1 g
Glycerol	G8773	Sigma	100%	5 ml
Bromophenol Blue	11439-1	Aldrich	1%	500 µl
DTT	D9779	Sigma	2M	

DTT is added fresh at a final concentration of 40 mM just before use

4X Stacking gel buffer (0.5 M Tris, pH 6.8)

Reagent	Catalog no.	Supplier	Concentration
Tris	0188.2	Roth	0.5 M
HCl	4625.2	Roth	Set pH to 6.8
MilliQ water			

4X Resolving gel buffer (1 M Tris, pH 8.8)

Reagent	Catalog no.	Supplier	Concentration
Tris	0188.2	Roth	1 M
HCl	4625.2	Roth	Set pH to 8.8
MilliQ water			

Additional reagents for gel casting

Reagent	Catalog no.	Supplier	Concentration
SDS	75746	Sigma	10%
Acrylamide/Bis	A9926	Sigma	40%
APS	A0834.0250	AppliChem	10%
TEMED	A1148.0100	AppliChem	100%

Gel running buffer

Reagent	Catalog no.	Supplier	10X Concentration
Tris	0188.2	Roth	250 mM
Glycine	50046	Sigma	1.9 M
SDS	75746	Sigma	1%
MilliQ Water			

Composition of resolving gel

Reagent	8% (ml)	10% (ml)	12% (ml)
MilliQ water	2.645 ml	2.395 ml	2.145 ml
0.5 M Tris pH 6.8	1.25 ml	1.25 ml	1.25 ml
Acrylamide/Bis	1 ml	1.25 ml	1.5 ml

10%SDS	50 µl	50 µl	50 µl
10% APS	50 µl	50 µl	50 µl
TEMED	5 µl	5 µl	5 µl

Composition of stacking gel (4%)

Reagent	Volume
MilliQ water	2.695 ml
0.5 M Tris pH 6.8	1.25 ml
Acrylamide/Bis	500 µl
10%SDS	50 µl
10% APS	50 µl
TEMED	5 µl

Transfer buffer

Reagent	Catalog no.	Supplier	10X Concentration
Tris	0188.2	Roth	250 mM
Glycine	50046	Sigma	1.9 M
MilliQ Water			
Ethanol	5054.5	Roth	

Ethanol added to 1X transfer buffer at a final concentration of 20%

10X TBS

Reagent	Catalog no.	Supplier	Amount
Tris	0188.2	Roth	24.2 g
NaCl	S5886	Sigma	80 g
MilliQ Water			1 L

Blocking buffer

Reagent	Catalog no.	Supplier	Volume
Milk	T145.3	Roth	5g
1X TBST			100 ml

1X TBST

Reagent	Catalog no.	Supplier	Concentration	Volume
TBS			10X	100 ml
Tween-20	P1379	Sigma	10%	10 ml
MilliQ Water				890 ml

Additional reagents for blotting

Reagent	Catalog no.	Supplier
PVDF membrane	10600021	GE Healthcare
Protein ladder	27-2110	PeqLab
WesternBright Quantum ECL	541015	Biozym

2.11.4 Buffers for glutamate uptake assay

HBSS without NaCl

Reagent	Catalog no.	Supplier	Concentration
$CaCl_2$	HN04.1	Roth	2 mM
KCl	HN02.1	Roth	143 mM
$MgCl_2$	HN03.1	Roth	1 mM
Glucose	G70021	Sigma	23 mM
HEPES	HN77.3	Roth	15 mM
NaOH	22.146-5	Sigma	Adjust to pH 7.4

1M NaOH was used to adjust the pH to 7.4, followed by filter-sterilization using a 0.2 μm filter.

HBSS with NaCl

Reagent	Catalog no.	Supplier	Concentration
$CaCl_2$	HN04.1	Roth	2 mM
KCl	HN02.1	Roth	3 mM
NaCl	S5886	Sigma	140 mM
$MgCl_2$	HN03.1	Roth	1 mM
Glucose	G70021	Sigma	23 mM

HEPES	HN77.3	Roth	15 mM
NaOH	22.146-5	Sigma	Adjust to pH 7.4

1M NaOH was used to adjust the pH to 7.4, followed by filter-sterilization using a 0.2 μm filter.

Additional reagents for calcium imaging

Reagent	Catalog no.	Supplier	Concentration
Glutamate determination kit	GLN-1	Sigma	
L-Glutamate	G6150	Sigma	50 μM
L-trans-2,4-PDC	298	Tocris	1 mM

2.11.5 Buffers for molecular biology (5X KCM Buffer for bacterial transformation)

Reagent	Catalog no.	Supplier	Concentration	Volume
KCl	HN02.1	Roth	1 M	25 ml
$CaCl_2$	HN04.1	Roth	1 M	7.5 ml
$MgCl_2$	HN03.1	Roth	1 M	12.5 ml
MilliQ Water				5 ml

2.12 List of reagents (for molecular biology and other assays)

Reagent	Catalog no.	Supplier
Neon transfection 10μL kit (device, tips, cuvette, E & R Buffer)	MPK1025	Thermo Fisher
Sodium Butyrate	B5887	Sigma
Hydrocortisone	H0888	Sigma
Recombinant Human TNFα	300-01A	Peprotech

Reagent	Catalog no.	Supplier
Thermopol Buffer	B9004S	New England Biolabs
dNTP	U151B	Promega
DMSO	F515	Thermo Fisher

Taq Polymerase	M0273S	New England Biolabs
T4 Ligation Buffer	B0202S	New England Biolabs
T4 PNK	M0201S	New England Biolabs
Tango Buffer	B45	Thermo Fisher
DTT	R0861	Thermo Fisher
ATP	E3101K	Epicentre Technologies
T4 Ligase	M0202S	New England Biolabs
PlasmidSafe Buffer	E3101K	Epicentre Technologies
PlasmidSafe Exonuclease	E3101K	Epicentre Technologies
Cutsmart Buffer	B7204S	New England Biolabs
AgeI HF	R3552S	New England Biolabs
BbsI	FD1934	Thermo Fisher
HhaI	R644A	Promega
KpnI HF	0524	Thermo Fisher
SapI	FD1014	Thermo Fisher
XbaI	R0145S	New England Biolabs
Duplex Buffer	11-01-03-01	IDT
Ethidium Bromide	15585011	Thermo Fisher
CM-H2DCF	D399	Invitrogen
Mitosox	M36008	Invitrogen
TMRE	9103	Immuno Chemistry Tech
QuickExtract solution	QE09050	Epicentre Technologies
KaryoMAX Colcemid	15212012	Thermo Fisher
Giemsa solution	T862.1	Roth
Methanol	4627.5	Roth
Acetic acid	7332.1	Roth
Euparal	7356.1	Roth
Calcein Green AM	C3100MP	Molecular Probes
EthD-1	E1169	Molecular Probes
Seahorse Assay Medium	102353	Agilent Technologies
Oligomycin		Agilent Technologies

FCCP		Agilent Technologies
Rotenone		Agilent Technologies
Antimycin A		Agilent Technologies
ATTO550-tracRNA	1075927	IDT
Alt-R Cas9 Nuclease	1081058	IDT
Alt-R Cas9 HiFi	1081060	IDT
Alt-R Cas9 D10A Nickase	1081062	IDT
RS-1	553510	Calbiochem
SCR7	S7742	Selleckchem
4% Trypan Blue	T8154	Sigma

2.13 Cell culture

2.13.1 LCL culture and maintenance

LCLs (AG10984, AG10987, AG11001- all APOE4/4 Alzheimer's Disease patient-derived cell lines) were obtained from Coriell Institute for Medical Research. Cells were cultured in LCL Medium (Table 2.6) in T25 flasks with vented lids. Cells were maintained at 37 ºC and 5% CO_2 and medium was changed every 72 hours. Medium was replaced, by first pooling the cell suspension and centrifuging at 118g for 3 min. Supernatant was discarded and the cell pellet was resuspended in fresh medium. Healthy growing cells tend to form clumps.

Cells were split depending on the growth rate of the cell line, roughly about once in 7 days. The process for splitting was similar. Cells were centrifuged at 118g for 3 min, supernatant was discarded and the pellet resuspended in fresh medium to yield about 250,000 cells per ml.

LCLs were cryopreserved in LCL Medium supplemented with 10% DMSO. At least 1 million cells were pooled before freezing. LCLs were thawed by swirling the cryovial in a water bath set at 37°C. The cells were transferred to 6 volumes of warm LCL medium and centrifuged at 118g for 3 min. The supernatant was discarded and the cell pellet was resuspended in 4ml of LCL medium and transferred to a T25 flask.

2.13.2 Fibroblast culture and maintenance

Fibroblasts (AG11368- an APOE4/4 Alzheimer's Disease patient-derived fibroblast) were obtained from Coriell Institute for Medical Research. Cells were cultured in Fibroblast Medium (Table 2.6) in T25 flasks with vented lids. Cells were maintained at 37 ºC and 5% CO_2 and medium was changed every 48 hours.

Cells were split when ~90% confluent. The attached fibroblasts were first washed with DPBS-/- to remove all the medium. 1.5ml of Trypsin-EDTA was added per T25 to cover the bottom of the flask, followed by incubation at 37 ºC and 5% CO_2 for 3 min. Cells were observed for detachment, followed by neutralization of the Trypsin with at least 6 ml of Fibroblast Medium. Cells were pooled into a Falcon tube and spun at 118g for 3 min. Supernatant was discarded, the cell pellet was resuspended in Fibroblast Medium and the cells were counted using a haemocytometer. 500,000-750,000 fibroblasts were plated onto each T25.

Fibroblasts were cryopreserved in Fibroblast Medium supplemented with 10% DMSO. At least 1 million cells were pooled before freezing. Fibroblasts were thawed by swirling the cryovial in a water bath set at 37°C. The cells were transferred to 6 volumes of warm Fibroblast medium and centrifuged at 118g for 3 min. The supernatant was discarded and the cell pellet was resuspended in 4ml of Fibroblast Medium and transferred to a T25 flask.

2.13.3 Maintenance, freezing and thawing of iPS cells

Human iPS cell lines (SZ01 reprogrammed from human neonatal foreskin fibroblasts (HFF1, ATCC), SZ02 from human neonatal foreskin fibroblast (NuFF1, GlobalStem), 11368 from AG11368 fibroblasts (Coriell Institute for Medical Research), A4/4 from AG10984 LCLs (Coriell Institute for Medical Research), 11001 from AG11001 LCLs (Coriell Institute for Medical Research), A3/3 generated by genome editing A4/4, B4/4 (BIONi010-C-4, EBiSC), B3/3 (BIONi010-C-2, EBiSC)) were maintained in feeder-free conditions using a protocol modified from *Chen at al., 2011*. They were cultured on 0.5 mg/ml Matrigel at 37 ºC and 5% CO_2, in E8 medium (Table 2.6). Matrigel was coated onto the plates for at least 1 hour at room temperature

prior to the split. Medium was changed daily, and spontaneously differentiated cells were removed using a flame-pulled Pasteur pipette under a microscope before splitting.

Cells were split once a week by first washing with DPBS without calcium and magnesium ions (DPBS-/-), followed by incubation in 1ml DPBS-/- per well of a 6-well dish for 10 min. 1 ml of E8 medium was added after removal of DPBS-/- and cells were collected by scraping with a spatula (Biochrom 99010). Cell suspension was centrifuged at 118g for 1 min. The cells were resuspended in fresh E8 medium containing 5 μM ROCK Inhibitor and replated at appropriate density onto Matrigel-coated 6-well dishes. Medium was replaced after 24 hours with plain E8 medium.

The iPSCs were cryopreserved using CryoStor and stored in cryotubes in liquid nitrogen. iPSCs were thawed by swirling the cryovial gently in a water bath at 37°C till only a small piece of ice remained. The cell suspension was quickly transferred to at least 6 volumes of warm E8 medium and centrifuged at 118g for 3 min. The supernatant was discarded and cells were resuspended in E8 medium supplemented with 5 μM ROCK Inhibitor. Cells were plated onto a well of a 6-well dish pre-coated with Matrigel, followed by incubation at 37 ºC and 5% CO_2. Medium was replaced 24 hours later with plain E8 medium. Fresh iPSC stocks of lower passage numbers were thawed, after cells in culture exceeded passage 30 for self-made and passage 60 for commercial iPSC lines.

2.13.4 Reprogramming LCLs and fibroblasts to iPSCs

LCLs were reprogrammed by transfecting them with OriP/EBNA-1-based episomal plasmids encoding OCT3/4, SOX2, KLF4, L-MYC, LIN28, and shRNA of p53 (*Okita et al., 2011*) using the Neon transfection system.

To prepare for the electroporation, desired number of wells of a 24-well dish were coated with 0.5 mg/ml Matrigel at room temperature for at least 1 hour. E and R buffer from the Neon kit were brought to room temperature and the components of the kit including Neon tips, tubes, pipette and pipette station were exposed to UV light for 30 minutes. The pipette station was then connected to the transfection device and an electroporation tube placed in the pipette station as demonstrated in the instrument manual. 3 ml of E Buffer was added to the tube.

LCLs were first triturated to single cells by gentle pipetting and counted using a haemocytometer. 200,000 cells in culture medium were transferred to a falcon tube (per well of a 24-well dish to be plated. All components of the protocol can be linearly scaled up if more wells need to be plated) and centrifuged at 118g for 3 min. The supernatant was discarded and the pellet resuspended in 1 ml DPBS-/-. The cells in PBS were spun again at 118g for 2 min. Ideally, the cells should stay in PBS for as short a duration as possible, in order to improve post-electroporation viability.

Meanwhile, a plasmid mix is made in a 1.5ml Eppendorf tube, containing 1 µl each of the plasmids pCXLE-hOCT3/4-shp53-F, pCXLE-hUL, pCXLE-hSK (all the plasmids are at 1 µg/ml concentration). PBS was removed from the cell pellet as much as possible and they were resuspended in 7 µl of R Buffer, to ensure 10 µl final volume. The cell suspension was transferred to the plasmid mix and the tube tapped gently. A Neon 10 µl tip was attached to the Neon pipette and the cells were taken into the tip. The pipette was fitted into the pipette station and the cells were zapped at 1100 Volts for 2 pulses of 30 ms each. The electroporated cells were then transferred to a Matrigel-coated well of a 24-well dish containing E7 Medium (E8 Medium without TGFβ), supplemented with 100 µM sodium butyrate for 3 days. Medium was changed once every 3 days, after first allowing the cells to attach. After 15-17 days, iPSC colonies started to appear and when they reached a sufficient size, were manually cut and picked using a needle (Sterican) and a pipette tip and were plated onto Matrigel coated dishes, in complete E8 medium.

Fibroblasts were treated with 1 µM of hydrocortisone for 24h before and until 72h after electroporation to promote their growth, and were reprogrammed in the same way except that they were electroporated at 1350 Volts for 2 pulses of 20 ms each. After use, the Neon tips and tube were cleaned with 70% ethanol and sterile distilled water and allowed to dry under the hood.

2.13.5 Embryoid body formation and differentiation to different germ layers

Cells of different germ layers were obtained from iPSCs through spontaneous differentiation as embryoid bodies (EBs). EBs were generated by dissociating iPSCs to single cells using Accutase and suspending them as single drops of 3000 cells per 20 µl of E8 medium (supplemented with 4 mg/ml polyvinyl alcohol and 5µM ROCK Inhibitor) on lids of petri dishes. 24 hours later, EBs were transferred to a non-adherent dish and cultured in suspension for 10 days, replacing E8

medium every 2 days. EBs were then plated on 167 μg/ml Matrigel (BD Bioscience) coated dishes and treated with Knockout Medium (Gibco) supplemented with 20% FBS for 10 days, with media change every 3 days. After 10 days, the cells were fixed and immunostained for markers of the different germ layers (Table 2.3), as mentioned in the immunocytochemistry protocol (Section 2.16).

2.13.6 NSC generation

Neural stem cells (NSCs) were generated from the iPSC lines A3/3 (internal ID 181), its isogenic counterpart A4/4 (internal ID 10984), B3/3 (internal ID C2), its isogenic counterpart B4/4 (internal ID C4). Further details about the origin of the lines can be found in Section 2.3.

The iPS cells were first grown to confluence for about 6 days in E8 medium. On day 7, induction of neural lineage by dual SMAD inhibition protocol was initiated as described in Section 2.13.8: cells were treated with 6 μM SB-431542 and 0.3 nM LDN193189 in N2B27 medium (Table 2.6) for 7 days with a medium change in between. On day 14, EBs were prepared with these cells as described in Section 2.13.8. The EBs were kept in suspension in N2B27 medium for 5 days. On day 19, they were plated onto dishes pre-coated with 0.167 mg/ml Matrigel. The plates were observed for 2-3 days for the appearance of rosette structures representing the neuroepithelial stage. On day 21-22, rosettes were picked under the microscope and cultured in suspension in NSC medium (Table 2.6) containing 10 ng/ml FGF and 10 ng/ml EGF. Twice a week for 2 weeks, the neurospheres were dissociated gently and plated on plastic to allow the non-neural cells with a tendency to attach to the culture dish, to be separated from the neural cells. Neurospheres were then plated onto 0.085 mg/ml Matrigel in NSC medium supplemented with 10 ng/ml FGF and 10 ng/ml EGF to expand the NSCs.

NSCs were cryopreserved at the early passages to maintain early NSC stocks. They were dissociated using Accutase and cryopreserved in 10% DMSO in NSC medium. The cells were revived by thawing the vial in a 37ºC water bath. The cell suspension was transferred to a Falcon tube containing at least 6 ml of NSC medium. Cells were centrifuged at 118g for 3 min, followed by resuspension of the cell pellet and plating of the cells in NSC medium supplemented with 20 ng/ml FGF and 20 ng/ml EGF on 0.085 mg/ml Matrigel coated dishes. Cells were cultured at 37ºC

and 5% CO_2. Medium was changed once in 3 days and cells were passaged when ~80% confluent. After enough passages were cryopreserved, NSCs were differentiated to astrocyte progenitors as described in Section 2.13.7.

2.13.7 Astrocyte differentiation

Astrocyte progenitor cells (APCs) were first differentiated from NSCs and expanded, before terminal differentiation to astrocytes. After sufficient vials of NSCs were cryopreserved (Passage 3-6), cells were redissociated to single cells with Accutase treatment and plated in T25 flasks in NSC-/- Medium supplemented with 20 ng/ml LIF and 20ng/ml EGF (NSC EL20). The lack of an attachment substrate allows neurospheres to form. EGF and LIF co-application in the absence of bFGF promotes astroglial specification of NSCs. Cells were cultured in suspension as neurospheres for 4 weeks with complete media changes every 3 days. If the spheres grew too large, they were mechanically dissociated to a smaller size (protocol modified from *Serio et al., 2013*). After 4 weeks, cells were redissociated and plated onto 167 µg/ml Matrigel-coated dishes in NSC-/- medium supplemented with 20 ng/ml EGF and 20 ng/ml bFGF (NSC EF20). Complete media change was performed every 3 days and if the cells grew too dense, they were passaged. After 4 weeks in monolayer culture, these APCs were expanded and cryopreserved.

In order to terminally differentiate APCs to astrocytes, 150,000 APCs were plated in a 35 mm dish in NSC EF20 medium. The next day, media was changed to NSC-/- medium supplemented with 20ng/mL CNTF. Every 3 days, a complete media change was performed. After 14 days of treatment with CNTF, cells were lysed for Western blotting or redissociated with Accutase and replated at the necessary cell numbers for immunocytochemistry or other assays.

2.13.8 Neuronal differentiation

Human iPSCs were first grown to confluence in 6-well dishes. Induction of neural lineage by dual SMAD inhibition protocol was initiated (*Chambers et al., 2009)* by treating cells with inhibitors of the Tumor Growth Factor beta (TGFβ) and Bone Morphogenetic Protein (BMP) signaling cascades respectively: 6 µM SB-431542 and 0.3 nM LDN193189 in N2B27 medium (Table 2.6) for 7 days, with a medium change in between. This allows rapid differentiation of confluent hiPSC cultures into early neuroectoderm. On day 7, treated cells were washed and incubated with DPBS-

/- for 5 minutes. As they start to detach, DPBS-/- treatment was stopped by adding N2B27 medium. Cell aggregates were scraped and collected in N2B27 medium, followed by centrifugation at 66g for 1 min. Supernatant was discarded and the pellet was resuspended gently in N2B27 medium and plated onto uncoated T25 flasks. It was incubated at 37°C and 5% CO_2 for 2 weeks, with media change once a week, to obtain round embryoid bodies (EBs). On day 21, the EBs were transferred to 0.167 mg/ml Matrigel-coated 100mm dishes in N2B27 medium and incubated at 37°C and 5% CO_2 with weekly media changes. A few days after plating, processes from differentiated cells start to appear. 6 weeks after plating, the cells were used for neuronal enrichment by an immunopanning protocol.

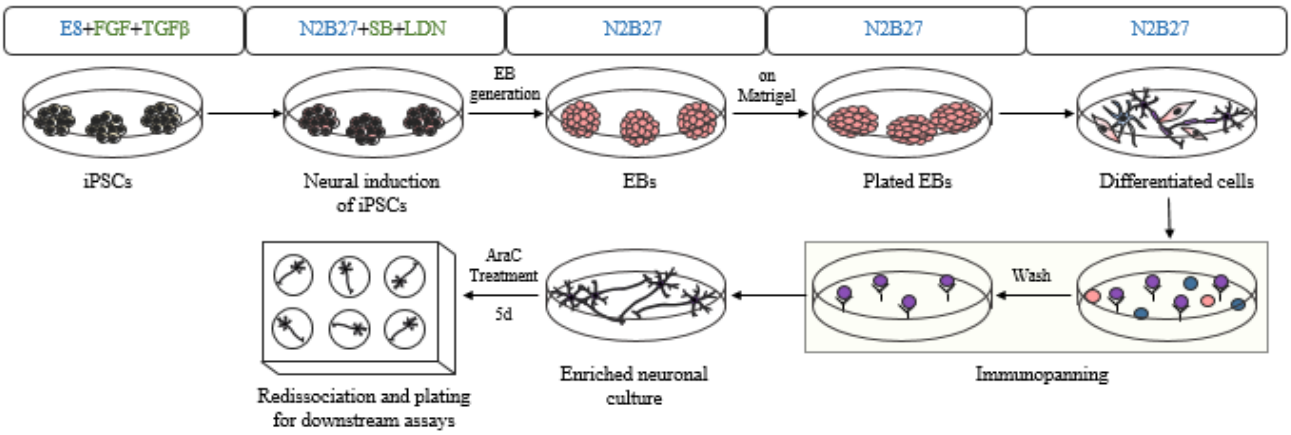

Figure 2.1: Neuronal differentiation

2.13.9 Immunopanning and redissociation of hiPSC-derived neurons

In order to purify neuronal cells from the non-neuronal cells in the mixture, an immunopurification procedure with neural cell adhesion molecule (NCAM) antibody was performed. This results in an enriched population of neurons, with about 90% MAP2-positive cells (*Nieweg et al., 2015*).

First, antibody-coated plates were prepared by incubating bacterial-quality 100cm dishes with secondary goat anti-mouse IgG and IgM antibody in 50mM Tris/HCl, pH 9.5 overnight at 4°C. The next day, antibody solution was removed and plates were washed with 1X PBS. Further, plates were incubated with VIN-IS-53 NCAM antibody solution in 0.2% BSA at 4°C overnight to allow primary antibody to attach to the secondary antibody.

Just before beginning the immunopanning, NCAM antibody solution was collected in a falcon tube and stored at 4°C. Plates were washed thrice with 1X PBS and incubated with 0.2% BSA in PanPBS (Table 2.7) to allow blocking of non-specific areas. Meanwhile, cells were washed with 1X PBS and regions containing neuronal cells were flushed out and placed in a falcon which was centrifuged at 223g for 2 min. The cell pellet was once again washed with 1X PBS and then incubated with Accutase for 20 minutes at 37°C to allow dissociation of neuronal clumps Accutased cells were centrifuged at 223 g for 2 min. Accutase was aspirated out and clumps were triturated gently in 0.2% BSA in PanPBS with a P1000 pipette tip. The cell suspension was centrifuged at 30g for 1 min to allow settling down of cell clumps and collection of single cells from the supernatant into another tube. Similar procedure was followed after triturating cells with a P200 and P10 pipette tip, and collecting the single cells at each step. The falcon tube containing single cells was centrifuged at 149 g for 13 min, supernatant was aspirated and cell pellet was resuspended in 0.02% BSA in PanPBS. Meanwhile 0.2% BSA from the panning plate was also replaced with 0.02% BSA in PanPBS. The single cell suspension was distributed onto the panning plate and incubated for 8-10 minutes to allow attachment of NCAM-expressing neurons to the plates. After the incubation, unbound cells were removed and the plate was washed by swirling with PanPBS 15-20 times, until as few unbound cells are found floating, as possible. The bound cells were then removed from the plate by flushing with 0.02% BSA in PanPBS, till all the cells came off. These cells were collected, a small aliquot loaded onto a haemocytometer for counting and the rest centrifuged at 149g for 13 min. The neuron-enriched cell pellet obtained, was resuspended in Panning medium (Table 2.6) at a density of 5000 cells/µL and plated onto Poly-L-ornithine (1 mg/mL) and Laminin (10 µg/mL) coated coverslips. After about 30 minutes, once the cells have attached, Panning medium was added. 24 hours later, 5 µM AraC was added to the cells to further eliminate proliferating non-neuronal cells. The araC treatment was performed for a total of 5 days, after which the neurons was redissociated and plated for the intended assays.

To redissociate the cells, araC-treated neurons were incubated with Accutase for 10 min at 37°C. Once all the cells had detached, the supernatant was collected and the wells were flushed with 1% BSA in PanPBS to neutralize the Accutase. The collected cells were centrifuged at 223g for 1 minutes. The supernatant was discarded and the cell pellet was triturated through a P200 pipette tip, in 4ml of 0.2% BSA in PanPBS. 10 µL of the cell suspension was loaded onto a

haemocytometer for counting. To the bottom of the tube, 1% BSA in PanPBS was released slowly. The tube was centrifuged at 118g for 8 min. Once the supernatant was discarded, neurons were resuspended in Panning medium at the desired density and replated onto Poly-L-ornithine/Laminin-coated glass or plastic surfaces.

2.13.10 Astrocyte-conditioned media preparation

In order to prepare APOE-containing astrocyte-conditioned medium to treat neurons with, 150000 APCs of B3/3 and B4/4 were plated per well of a 167 µg/ml Matrigel-coated 6-well dish in NSC EF20 medium. 24 h later, medium was changed to NSC-/- medium supplemented with 20 ng/ml CNTF. Medium was changed completely every 3 days. After 14 days of treatment, medium was changed to NSC-/- medium. The resulting astrocytes were kept in this medium for 14 more days with media changes every 3 days. On the 14th day, medium was replaced with Neuronal medium (without growth factors). After 72 hours, medium was collected into 15 ml falcon tubes and replaced with fresh neuronal medium for further treatment. The collection tubes were centrifuged at 1660g for 2 min to eliminate cellular debris. The supernatant was transferred into another falcon tube and stored at -80°C until use or for APOE quantification by ELISA. Once the desired amount of conditioned medium was collected, the cells were lysed using RIPA Buffer and subjected to BCA assay for protein quantification. Before APOE ELISA was performed with the collected medium, the different batches of media were first pooled. ELISA was performed with a small batch, while the rest was frozen into smaller aliquots. (B3/3 yielded 8.69 ng/ml APOE and B4/4 yielded 10.55 ng/ml). Hence, all neurons were treated with 8.69 ng/ml of either APOE genotype-conditioned medium by adjusting the volume with fresh medium. Immunopanned, AraC-treated, redissociated and plated neurons were allowed to grow out for 7 days in dishes and cell numbers suited for the assay of interest. From the 8th day, neurons were treated with conditioned medium for a total of 5 days. After 2 days of treatment, there was a complete media change. For Aβ ELISA experiments, it was this 72 h medium that was collected and analyzed.

2.14 Karyotyping

Karyotyping is a technique to generate a karyotype (or snapshot of chromosomes) of a cell. This is achieved by first arresting the cells at metaphase using a spindle inhibitor like colchicine, followed by swelling of the cells using a hypotonic solution, fixing them and then impacting the

chromosomes onto a glass slide. The chromosomes are then stained with Giemsa dye to generate the characteristic banding pattern of each chromosome (G-Banding).

iPSCs were split 48-72 h before the experiment. They were treated with 0.1ug/ml or 0.2ug/ml Colcemid depending on the cell line. After 3h or 1h respectively, the cells were treated with Accutase for 8 min to ensure single cells in suspension. Cells were centrifuged at 122g for 5 min. 5 ml of 0.56% KCl was added dropwise, while flicking the tube to ensure no cell clumping occurs. Cells were incubated at 37°C for 15 min. 1 ml of Carnoy's fixative (3:1 Methanol: Acetic Acid) was added dropwise while flicking the tube. Cells were spun at 122g for 10 min without breaks. Supernatant was discarded. 5ml of fixative was added before incubation at -20°C overnight. The next day, cells were spun at 122g for 10 min. Supernatant was aspirated. Only 1-2 ml of fixative was retained in the tube depending on the size of the pellet. Cells were triturated. 3 drops of the cell suspension was dropped onto a cold wet slide at an angle of 45°, from a height of ~10 cm. The slides were immediately placed on a wet tissue kept on a hot plate set to 37°C. Once dry, the slides were aged at room temperature for 3-4 days and kept at 60°C for 30 min preceding staining.
Slides were exposed to Trypsin solution in a Coplin jar for 10 sec, 70% ethanol for 10 sec, PBS for 10 sec, Giemsa solution for 10 min and washed with water for 10 sec. Cells were kept at 60°C to dry before mounting with Euparal. Metaphases were imaged using a Zeiss Axioskop, 60×, and analyzed by Dr. Barbara Fritz using Ikaros software (Metasystems). At least 20 metaphases were

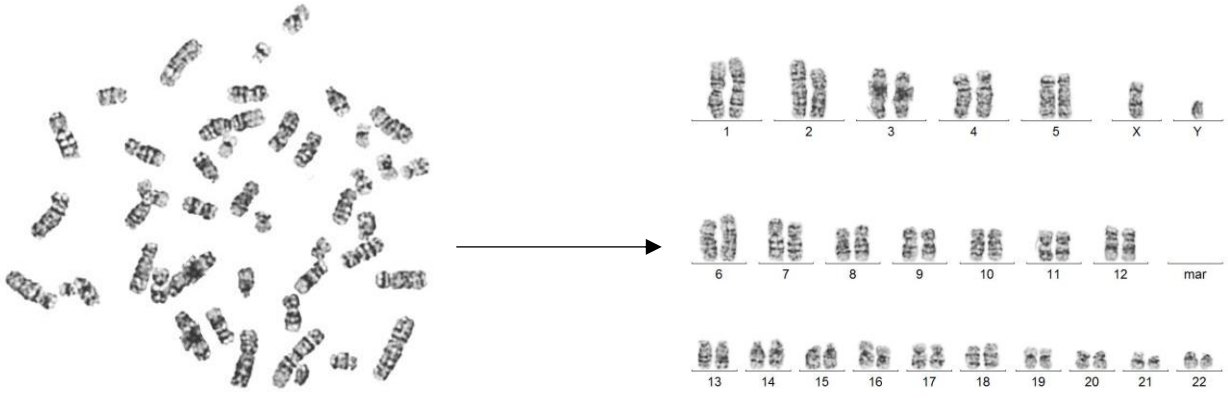

Metaphase of iPSC line SZ02

Karyotype generated using Metasystems Ikaros software

Figure 2.2: Representative image of metaphase spreads

2.15 Western Blotting

2.15.1 Protein isolation

Cells to be lysed were washed once with 1X PBS and 100 µl of RIPA Buffer (containing protease and phosphatase inhibitors) was added per 35mm dish. Lysis buffer was spread uniformly over the surface and the plate was kept on ice for 5 min. Cells were scraped off using a cell scraper and the lysate was collected in a microfuge tube. Tube was vortexed well for 2 min and then stored at -80°C until use.

2.15.2 Protein Estimation by BCA Assay

Protein concentration in cell lysates was determined by the detergent-compatible BCA assay, which consists of 2 reagents containing bicinchoninic acid and copper sulphate. The principle of the method is based on the ability of proteins to reduce Cu^{2+} to Cu^{1+} in an alkaline solution, which results in a purple color formation by bicinchoninic acid. The amount of reduction and color produced is proportional to the amount of protein present, and thus, is measurable colorimetrically.

The kit was used according to the manufacturer's instructions. BSA protein standards were prepared in RIPA buffer. After thawing, protein samples were centrifuged at 13000g for 3 minutes and protein was estimated from the supernatant.1 µL of standard or sample was pipetted to 1.5 ml microfuge tubes and 100 µL of 1:50 Reagent B: Reagent A mix was added to the tubes. Each standard or sample was prepared in duplicates. The tubes were incubated at 60°C for 30 minutes. The samples were then transferred to each well of a Nunc 96-well plate and absorption was measured at 590 nm using a microplate reader (Fluostar OPTIMA, BMG Labtech). The values of the standards were first plotted to generate a standard curve and the linear regression line was used to calculate the protein content in the samples.

2.15.3 SDS-PAGE, blotting and developing

Sodium dodecyl sulfate polyacrylamide gel electrophoresis (SDS-PAGE) was performed to separate proteins on the basis of molecular weight under the effect of an electrical field. The gel bands were then blotted onto a membrane and probed with antibodies against the protein of interest by Western Blotting.

8-15 µg of protein was appropriately diluted in RIPA buffer and mixed with 4X loading dye (supplemented with DTT at a final concentration of 50 mM). Samples were heated to 95°C for 5 minutes and loaded onto a 4% stacking and separated in a resolving gel whose percentage varied depending on the protein of interest. The gel was run in running buffer (Table 2.9.3) at 80V until the sample entered the resolving gel and thereafter run at 120V till the samples reached the bottom of the resolving gel.

After electrophoresis, the samples were transferred onto a PVDF membrane. The PVDF membrane was first activated in methanol for a few minutes. After completely wet, it was placed in transfer buffer (containing 20% ethanol), taking care not to allow the membrane to dry for the rest of the protocol. The sandwich for the transfer was prepared with sponges and Whatmann filter paper on either sides of the gel and PVDF membrane. The transfer was carried out in transfer buffer (which was kept cold and stirring) at 100V for 90 min. Blocking of the membrane in 5% milk in TBST was performed to reduce non-specific binding. Primary antibodies were prepared in the appropriate dilutions in the blocking buffer and were incubated with the membrane shaking overnight at 4°C. The next day, membranes were washed thrice for 10 min each with 1X TBST. HRP-conjugated secondary antibody (1:4000) were prepared in the blocking buffer and incubated with the membrane for an hour at RT with gentle shaking. The membrane was again washed thrice with 1X TBST and once with distilled water just before developing. Luminescence was induced with Advansta Western Bright Quantum ECL reagent according to manufacturer's instructions and measured on a BioRad GelDoc apparatus. Several different exposure times from seconds to minutes, were used for the same blot. Analysis was performed using the Gel macro in Fiji, with appropriate background subtraction. All bands were normalized to an appropriate housekeeping protein like GAPDH or α/β Tubulin.

2.16 Immunocytochemistry

Immunostaining of cells was carried out to determine the presence of certain proteins or antigens in the cells of interest by fluorescence microscopy. Cells were briefly washed with 1X PBS followed by fixation in 4% PFA for 13 minutes at RT. PFA was removed and cells were washed thrice with 1X PBS. Cells were permeabilized using permeabilization buffer as mentioned in Table

2.9.1, with gentle shaking. (In the case of membrane proteins, the permeabilization step was skipped and for LAMP2 & EEA1 staining, 0.1% Triton X-100 in PBS was used instead). Cells were incubated in blocking buffer for 1 h at RT to block non-specific binding of the antibody (Blocking buffer in the case of LAMP2 and EEA1 staining was 5% BSA+ 1%NGS in PBS). Cells were then incubated with primary antibody (Table 2.3) overnight at 4°C. The next day, cells were washed thrice with 1x PBST, followed by incubation with the secondary antibody (Table 2.3) for 1 h at RT. Secondary antibody was removed and cells washed thrice with 1X PBST (0.1% Tween in PBS). At this step, if needed, cells were incubated with Hoechst 33342 (1:1000) for 10 min to stain the nucleus. Cells were washed once with 1X PBS and once with ddH_2O before mounting the coverslips on glass slides using FluorSave mounting reagent. Coverslips were dried overnight before imaging. 3-4 regions were imaged per coverslip, keeping the exposure time and intensity constant between coverslips.

Imaging was carried out using a Zeiss Axiovert 200M inverted epifluorescence microscope, attached to a 12-bit CoolSNAP ES2 CCD Camera (Photometrics). A 10X or 20X objective was used in most cases. For AT8, PHF1, EEA1, LAMP2 imaging, a Zeiss LSM700 confocal microscope with a 63X, 1.4 NA oil objective was used. Maximum intensity projections, background subtractions, cell counting and vesicle size analysis were carried out using Image J-1.46r (NIH, U.S.A).

2.17 Designing gRNA and ssODN

gRNA and donor sequences were designed using Benchling. The APOE locus was imported into the software and gRNAs were chosen using the CRISPR guide design tool. gRNAs with a cut site within 20 bp of the SNP were considered and successful genome editing for A3/3 generation was carried out using a gRNA (site 3) with the cut site a single bp away from the SNP. Ideally, the gRNA chosen does not have a high off-target rate (i.e. low off target score).

ssODN donor sequences were generated using the same tool. The polymorphism at the SNP site was made, but also another silent mutation at the PAM site was generated to prevent recutting of the repaired locus with Cas9. If a silent mutation of the PAM site was not possible, 2 strategic mutations in the gRNA site on the ssODN were made, to prevent recognition of the repaired strand

with a gRNA. For silent mutations, a replacement codon with the closest codon adaptation index (CAI) was chosen. For the symmetric ssODNs, homology arms of 50 bp were chosen for generation of A3/3. For asymmetric ssODN, the rules in *Richardson et al., 2016* were followed. For experiments optimizing HDR rates in iPSCs, longer homology arms were used so that asymmetric and symmetric ssODNs had similar lengths and could be easily compared.

2.18 Generation of a Cas9 nickase plasmid with a second gRNA insertion site

In order to improve genome editing rates using a Cas9 nickase plasmid, a modified version of the PX461 plasmid was generated which included another U6 promoter-driven site for gRNA insertion as well as tracRNA scaffold. This would allow both gRNAs to be inserted into a single plasmid, and hence transfection of the hard-to-transfect iPS cells with a single ~9.6kb plasmid. The gRNA insertion site can be cleaved by a Type II restriction enzyme (BbSI) which then allows insertion of the gRNA of interest with appropriately designed ends (Fig 2.4). A second gRNA site was designed with another Type II restriction enzyme (SapI), so the gRNA ends must be designed accordingly.

The PX461 and PIDTSMART-AMP plasmid containing the U6 promoter-driven site for gRNA insertion and tracRNA scaffold, were cleaved with KpnI and XbaI to generate sticky ends upstream of the Cas9 sequence and cleave out the site of interest respectively.

	pIDTMSART-AMP	PX461
Plasmid DNA	4 µl	15 µl
10X Cutsmart Buffer	1 µl	2 µl
Water	4 µl	2 µl
KpnI	0.5 µl	0.5 µl
XbaI	0.5 µl	0.5 µl

Mixes were incubated at 37°C for 1h. Samples were loaded onto a 1.2% gel. The bands of interest were cut out (341 bp and 9283 bp respectively). DNA fragments were extracted from the gel pieces using a Qiagen Gel Extraction kit according to the manufacturer's instructions. Concentration of

the samples was determined by nanodrop and a ligation was set up with 1:5 molar ratio of the vector:insert.

Component	Amount (µl)
Vector	100ng
Insert	56 ng
10X T4 Ligase Buffer	2 µl
T4 DNA Ligase	0.75 µl
(0.5) PEG 4000	2 µl
Water	up to 20 µl

The mix was incubated at 22°C for 2 h. Competent cells were then transformed with 2 µl of the mix and cultured in the presence of Ampicillin. Plasmid DNA from the resultant clones was isolated and Sanger sequencing was performed to confirm correct insertion of the second gRNA site.

2.19 Insertion of different promoters into the nickase plasmid Px461i

Genome editing in this project was first attempted in the patient-derived fibroblasts and LCLs. Since Cas9-GFP expression was found to be low in fibroblasts and LCLs, the CBh promoter that drives Cas9 in the PX461i plasmid was replaced with a CAG or PGK promoter to test if this improves the Cas9 expression.

The CAG-containing plasmid, PGK gBlock and PX461i were cleaved with KpnI and AgeI enzymes to generate sticky ends to aid insertion into the linearized PX461i with the CBh promoter cut out.

	CAG plasmid	PGK gBlock	PX461i
DNA	500 ng	150 ng	500 ng
10X Cutsmart Buffer	2.5 µl	1.2 µl	2.5 µl
AgeI HF	0.3 µl	0.15 µl	0.3 µl
KpnI HF	0.3 µl	0.15 µl	0.3 µl
Water	up to 25 µl	up to 15 µl	up to 25 µl

The mixes were incubated at 37°C for 2h and then run on 2% gel. The bands of interest (596 bp, 502 bp, 8828 bp respectively) were cut out and extracted from the gel using a Qiagen Gel Extraction kit according to the manufacturer's instructions. Concentration of the samples was determined by nanodrop and a ligation was set up with 1:6 molar ratio of the vector:insert.

	PX461iCAG	PX461iPGK
Linearised vector	50 ng	50 ng
Insert	20.2 ng	17 µl
10X T4 Ligase Buffer	3 µl	3 µl
T4 DNA Ligase	0.45 µl	0.45 µl
(50%) PEG 4000	1.5 µl	1.5 µl
Water	up to 30 µl	up to 30 µl

The tubes were incubated at 22°C for 2 h. Competent cells were then transformed with 2 µL of the mixes each and cultured in the presence of Ampicillin. Plasmid DNA from the resultant clones was isolated and Sanger sequencing was performed to confirm replacement of the CBh promoter with the CAG or PGK promoter. Following are the sequences ordered for CAG and PGK promoters (ordered from Genewiz as a plasmid and a gBlock respectively flanked by KpnI and AgeI at the 5' and 3' ends respectively):

CAG:

ggtaccGCGTTACATAACTTACGGTAAATGGCCCGCCTGGCTGACCGCCCAACGACCCC
CGCCCATTGACGTCAATAATGACGTATGTTCCCATAGTAACGCCAATAGGGACTTTC
CATTGACGTCAATGGGTGGAGTATTTACGGTAAACTGCCCACTTGGCAGTACATCAA
GTGTATCATATGCCAAGTACGCCCCCTATTGACGTCAATGACGGTAAATGGCCCGCC
TGGCATTATGCCCAGTACATGACCTTATGGGACTTTCCTACTTGGCAGTACATCTAC
GTATTAGTCATCGCTATTACCATGGTCGAGGTGAGCCCCACGTTCTGCTTCACTCTCC
CCATCTCCCCCCCCTCCCCACCCCCAATTTTGTATTTATTTATTTTTTAATTATTTTGT
GCAGCGATGGGGGCGGGGGGGGGGGGGGGCGCGCGCCAGGCGGGGCGGGGCGG
GGCGAGGGGCGGGGCGGGGCGAGGCGGAGAGGTGCGGCGGCAGCCAATCAGAGCG
GCGCGCTCCGAAAGTTTCCTTTTATGGCGAGGCGGCGGCGGCGGCCCTATAAA
AAGCGAAGCGCGCGGCGGGCGaccggt

PGK:

ggtaccGGGTAGGGGAGGCGCTTTTCCCAAGGCAGTCTGGAGCATGCGCTTTAGCAGCC
CCGCTGGGCACTTGGCGCTACACAAGTGGCCTCTGGCCTCGCACACATTCCACATCC
ACCGGTAGGCGCCAACCGGCTCCGTTCTTTGGTGGCCCCTTCGCGCCACCTTCTACT
CCTCCCCTAGTCAGGAAGTTCCCCCCCGCCCCGCAGCTCGCGTCGTGCAGGACGTGA
CAAATGGAAGTAGCACGTCTCACTAGTCTCGTGCAGATGGACAGCACCGCTGAGCA
ATGGAAGCGGGTAGGCCTTTGGGGCAGCGGCCAATAGCAGCTTTGCTCCTTCGCTTT
CTGGGCTCAGAGGCTGGGAAGGGGTGGGTCCGGGGGCGGGCTCAGGGGCGGGCTCA
GGGGCGGGGCGGGCGCCCGAAGGTCCTCCGGAGGCCCGGCATTCTGCACGCTTCAA
AAGCGCACGTCTGCCGCGCTGTTCTCCTCTTCCTCATCTCCGGGCCTTTCGaccggt

Following is the sequence of an insert (ordered from IDT as part of a pIDTSMART-AMP plasmid, with the sequence of interest flanked by KpnI and XbaI):

ggtaccAAAAAGCACCGACTCGGTGCCACTTTTTCAAGTTGATAACGGACTAGCCTTAT
TTTAACTTGCTATTTCTAGCTCTAAAACGGAAGAGCTCGCTCTTCCGGTGTTTCGTCC
TTTCCACAAGATATATAAAGCCAAGAAATCGAAATACTTTCAAGTTACGGTAAGCAT
ATGATAGTCCATTTTAAAACATAATTTTAAAACTGCAAACTACCCAAGAAATTATTA
CTTTCTACGTCACGTATTTTGTACTAATATCTTTGTGTTTACAGTCAAATTAATTCCA
ATTATCTCTCTAACAGCCTTGTATCGTATATGCAAATATGAAGGAATCATGGGAAAtc
taga

Sticky ends can be created in both the sequence of interest and the receiving plasmid and ligated, before bacterial transformation and cloning. Final plasmids were confirmed by Sanger sequencing.

2.20 gRNA insertion into Cas9 plasmids and subsequent bacterial transformation

2.20.1 gRNA insertion:

In order to insert the chosen guide RNAs (gRNAs) into the PX458 (WT Cas9-GFP plasmid) or PX461i (D10A Cas9-GFP with 2 gRNAs plasmid), the protocol detailed in *Ran et al., 2013* was followed.

First, the desalted oligo gRNAs (obtained from IDT) were resuspended to 100 µM in TE Buffer (10mM Tris, 0.1 mM EDTA, pH 8.0). The top (A) and bottom (B) strands of oligos for each gRNA were then annealed and the ends were phosphorylated as follows:

Component	Amount (µl)
Oligo A	1
Oligo B	1
T4 ligation Buffer	1
T4 PNK	1
ddH_2O	up to 10

The mixture was placed in a thermocycler using the following parameters: 37°C for 30 min; 95°C for 5 min; ramp down to 25 °C at 5 °C min^{-1}, and cool down to 4°C. The annealed and phosphorylated oligo duplex were diluted 1:200 in room temperature water. The gRNA oligos were cloned into the Cas9 plasmid in a combined restriction-ligation step. For the Px458 gRNA and Px461i Forward (F) gRNA, BbSI was used for digestion. For the Px461i Reverse (R) gRNA, SapI was used for digestion. The digestion-ligation mix was prepared as follows:

Component	Amount (µl)
Px458 or Px461i	100 ng
Diluted oligo duplex	2
10X Tango Buffer	2
10 mM DTT	2
25 mM ATP	0.8
BbSI	1
T4 Ligase	0.5
ddH_2O	up to 25

The reaction was incubated for 6 cycles of 37°C for 5 min and 21°C for 5 min. The ligation reaction was then optionally treated with PlasmidSafe exonuclease to digest any linearized DNA as follows:

Component	Amount (µl)
Ligation reaction from the above step	11
10X PlasmidSafe Buffer	1.5
25 mM ATP	0.6
PlasmidSafe exonuclease	1
Water	up to 15

The PlasmidSafe reaction was incubated at 37 °C for 30 min, followed by and 70°C for 30 min. This reaction mixture has the gRNA-containing Cas9 plasmid and can be used for bacterial transformation.

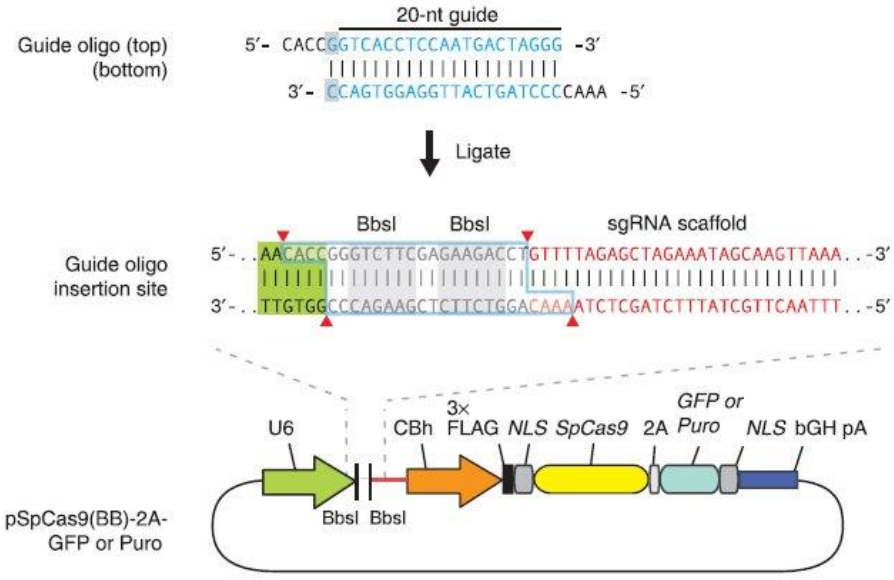

Figure 2.3: Methodology of gRNA insertion into PX461 or PX458 (adapted from *Ran et al. 2013*)

2.20.2 Bacterial transformation:

Chemically competent DH5α *E.coli* cells were transformed with the plasmid mixture by preparing the following mixture in a 1.5 ml Eppendorf tube:

Component	Amount (µl)
5X KCM Buffer	20
ddH_2O	80
PlasmidSafe-treated plasmid mixture	2
DH5α competent cells	100

Competent cells should only be kept on ice and never be thawed by hand. (All transformation and subculturing steps were performed aseptically in a bacterial hood). The above transformation mix was incubated on ice for 20 min, followed by a 10 min 'heat shock' incubation at RT. After the incubation, 1 ml of LB medium was added to the tubes and they were incubated on a shaker at 37°C for 50 minutes at 850 rpm. The cells were then centrifuged at 10,000g for 3 minutes. The cell pellet was resuspended in 110 µl LB medium and mixed. 10 µl and 100 µl each were plated on 2 LB-agar plates containing 100 µg/ml Ampicillin. The plates were incubated at 37°C overnight. By the next day, bacterial colonies containing the plasmid of interest appeared. Colonies well-separated from one another were chosen for expansion, to avoid false positives arising from satellite colonies. Colonies were picked with a sterile 200 µl tip into a falcon tube containing LB medium supplemented with 100 µg/ml Ampicillin. The tubes were incubated overnight at 37°C, shaking.

2.20.3 Plasmid miniprep, maxiprep and glycerol stock preparation:

The next day, plasmid miniprep was performed with part of the bacterial suspension, following the kit instructions. Glycerol stocks were also prepared for storage of the bacterial clones by mixing the bacterial suspension 1:1 with sterile 40% glycerol in 2 ml Eppendorf tubes and immediately storing at -80°C. The DNA obtained from the prep was sent for Sanger sequencing using primer 'Px462+i FP' to ensure correct integration of gRNA. At this stage, in the case of Px461i (D10A) plasmid, the entire process was repeated for the Reverse (R) gRNA insertion.

Once the clones with correctly integrated gRNA were identified, the respective glycerol stocks were thawed out into 200 ml of LB medium containing 100 µg/ml Ampicillin and incubated shaking at 37°C overnight. The next day, endotoxin-free maxiprep was performed following the kit instructions. The concentration of the plasmid thus obtained, was determined using nanodrop and could be used for electroporations.

2.21 Preparation and electroporation of Cas9 RNP and plasmid

In order to determine the most effective CRISPR-Cas9 strategy to generate homology-directed recombination (HDR) in iPSCs, they were electroporated with different combinations of gRNAs, Cas9 types and ssODN donor sequences. This was followed by genomic DNA (gDNA) isolation.

In certain key experiments mentioned in the results, electroporation was followed by FACS before DNA was isolated from the fluorescently labelled tracRNA-positive cells. The gDNA in both cases were then subjected to deep sequencing to determine the on-target and off-target rates for each combination. Mentioned here, is a typical protocol for a single electroporation of 600,000 iPS cells with a 10 µL Neon electroporation tip (for Cas9 delivered as RNP or as plasmid).

6-well dishes were coated with 500 µg/ml Matrigel and incubated at RT for 1 hour. Meanwhile, the laminar hood was UVed for 30 min with the Neon electroporation tips, pipette, cuvette and pipette station. Fresh TESR medium (supplemented with 5µM Rock Inhibitor) was prepare and warmed along with E8 medium (supplemented with 5µM Rock Inhibitor). E and R Buffer were warmed to 37 °C. First the crRNA-tracRNA complex (Mix A) was made as follows:

Component	Amount (µl)
200 µM crRNA	0.253 µl
200 µM tracRNA-ATTO550	0.253 µl
Duplex Buffer	0.62 µl
Total	1.125 µl

Heat at 95°C for 5 min. Allow to cool to RT for 5 min.
Next, Cas9 (Mix B) was diluted with R Buffer:

Component	Amount (µl)
61 µM Cas9	0.675 µl
R Buffer	0.45 µl
Total	1.125 µl

RNP complex was then prepared as follows:

Component	Amount (µl)
Mix A	0.75 µl
Mix B	0.75 µl
Total	1.5 µl

The components were mixed and incubated at RT for 15 min. Meanwhile, iPSCs were dissociated by incubating with Accutase for 8 minutes. Accutase was neutralized with E8 medium and cells were pooled into a falcon tube. Cells were centrifuged at 118g for 3 min. Supernatant was discarded and cells were resuspended in E8 (supplemented with RI), followed by counting the cells. 600,000 cells were added to a falcon tube and centrifuged at 118g for 3 min. This was followed by a wash with 1X PBS. To the cell pellet, 8 µL of R buffer was added and the cell suspension was transferred to the following electroporation mix:

Component	Amount (µl)
RNP mix	1 µl
10 µM Electroporation enhancer	1 µl
10 µM ssODN	1 µl
Cell suspension	8 µl
Total	11 µl

The pipette station was connected to the powerpack, cuvette was inserted into the pipette station and loaded with 3 ml of E Buffer. The electroporation mix was loaded onto a 10 µl electroporation tip and placed in the cuvette. 1 pulse of 1300V of 30ms duration was applied and the cells were transferred to a Matrigel-coated dish containing TESR medium (supplemented with 5 µM Rock Inhibitor, 7.5 µM RS-1 and 1 µM SCR7). 12 hours after electroporation, cells were redissociated for FACS and subsequent gDNA isolation. For D10A electroporation, 2 separate RNP complexes, each bound to one partner of the crRNA pair were prepared and mixed in equimolar ratio in the electroporation mix.

In the case of standardization experiments (Fig 3.8-3.11), there were some small changes. ssODN was not added to the electroporation mix, non-fluorescent tracRNA was used, and D10A was delivered bound to a single crRNA. Also, SCR7 and RS1 were excluded from the plating medium.

For delivery of Cas9 as plasmid, the apparatus and cells were prepared in the same way, however the electroporation mix consisted of 3 µg Cas9 plasmid (PX458 or PX461i) per 600,000 cells. Apart from plasmid, the remaining volume of the cell suspension was made up to 10 µL with R Buffer. Cells were electroporated with 1 pulse of 1000V of 30ms duration. FACS and subsequent

gDNA isolation for Cas9-plasmid transfected cells was carried out 24 hours after the electroporation. Since Deep sequencing and GUIDE-Seq data are being generated, they have not been presented in this thesis.

2.22 APOE RFLP assay

Genotyping for the APOE status was carried out by an RFLP based assay as described in *Hixson et al., 1990*. Genomic DNA was first amplified by PCR as follows:

Component	Amount (µl)
Genomic DNA	100ng
10X Thermopol Buffer	2.5 µl
10mM dNTP mix	0.7 µl
10 µM APOE Forward primer	1.25 µl
10 µM APOE Reverse primer	1.25 µl
DMSO	2.5 µl
Water	Up to 25 µl

The PCR product of interest was amplified by placing the above mix in a thermocycler set at the standard PCR conditions mentioned in Section 2.23, with an annealing temperature of 56°C. The PCR product thus obtained was then digested with the restriction enzyme HhaI as follows:

Component	Amount (µl)
PCR product	25 µl
10X Buffer C	2.7 µl
10mg/ml BSA	0.2 µl
10U/µLHhaI	0.5 µl

The digestion mix was incubated at 37°C for 2 hours. Digestion products were mixed 1:5 with 6X loading dye and run on a 2.5% agarose gel with EtBr. Gel was run at 80 V for about 45 minutes and imaged using a BioRad ChemiDoc. Different allele combinations of APOE yield different banding patterns on the gel, as seen in *Figure 2* from *Hixson et al., 1990*:

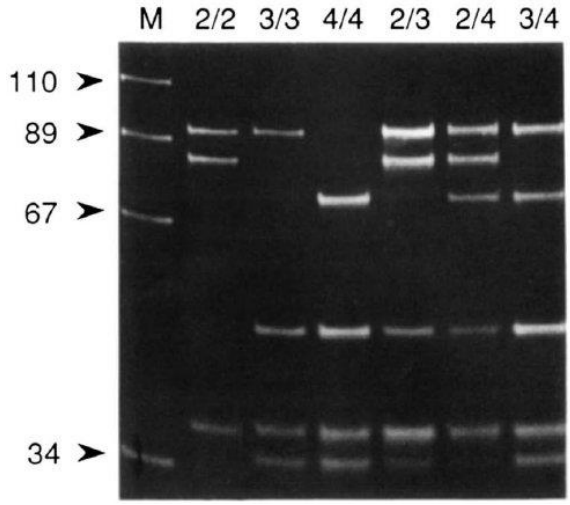

Figure 2.4: Representative gel of APOE RFLP as seen in *Hixson et al., 1990*

2.23 PCR conditions

The typical cycling conditions for PCRs are described below. The annealing temperature used for each PCR is mentioned in Table 2.3

Initial denaturation	94°C	10 min	
Denaturation	94°C	30 sec	32 cycles
Annealing	x°C	30 sec	
Elongation	72°C	1 min	
Final elongation	72°C	5 min	
Cooling	4°C	∞	

2.24 Sanger sequencing

Sanger sequencing is a method of DNA sequencing that relies on the incorporation of labelled dideoxynucleotides during *in vitro* DNA replication. Sanger sequencing was carried out to ensure that gRNA or promoters were inserted properly into plasmids, to sequence the APOE site of different cell lines and off target sites of CRISPR- transfected cells. All Sanger sequencing reactions were carried out by the Tubeseq services at Eurofins Genomics. Each figure indicates whether forward or reverse primer was used.

2.25 Flow sorting transfected iPSC and clonal isolation

In order to obtain almost a 100% Cas9-transfected cell population (to compare editing by DNA sequencing, or for culturing Cas9-positive clones), flow sorting of Cas9-transfected iPSCs was performed. iPSCs were electroporated with Cas9 RNP or Cas9 plasmid as described in Section 2.21. 12 h later (for RNP) and 24 h later (for plasmid), the transfected cells were flow sorted. RNP-transfected cells were sorted for ATTO550 (which was tagged to the tracRNA) and plasmid-transfected cells were sorted using GFP (tagged to the Cas9). Before cells could be sorted, they were washed once with 1X PBS, then treated with Accutase for 5-6 minutes. Accutase was neutralized with Rock Inhibitor-supplemented TESR medium, cells were collected into a Falcon tube and centrifuged at 118g for 3 minutes. Cells were further washed well with 1X PBS by triturating and centrifuged again. Once, the supernatant was discarded, cells were resuspended in FACS buffer (1% BSA in 1X PBS). The cells were then sorted using a Beckman Coulter MoFlo Astrios and sorted cells were collected into 500 µg/ml Matrigel-coated 100 cm dishes if they were to be cloned (5000-10,000 cells per 100cm dish). Alternately, if gDNA was to be isolated, the cells were directly collected in a 1.5 ml Eppendorf tube containing Lysis Buffer provided with the gDNA isolation kit.

In the case of clonal isolation of iPSCs, transfected cells were collected post-sorting at 10,000 cells per 100cm dish. In cases where cells were not sorted, 24 hours after electroporation, they were redissociated and plated at 10,000 cells per 10 cm dish. Cells were grown in complete TESR medium supplemented with 5 µM Rock Inhibitor, with complete medium changes every 2 days. Cells were observed every day to mark colonies growing from single cells as opposed to several cells that clump together. 10-14 days later, when the colonies were large enough, they were picked up with a pipette tip and transferred clonally to Matrigel-coated 96-well dishes. Medium was switched to E8 medium. Once the colonies further grew in size, they were passaged into 24 well dishes, by treating the colonies with 1X PBS for 5 min and scraping to transfer the cells into 24 well dishes. The cells were grown to confluency and then $1/4^{th}$ of the cells were passaged for subculture while genomic DNA was isolated from the remaining cells using QuickExtract solution, following the manufacturer's instructions. Briefly, the cells were pelleted down and 50 µL QuickExtract solution was added. Cells were vortexed for 15 sec. Cells were transferred to a heating block set at 65°C and incubated for 6 min. The tubes were vortexed for 15 secs and

transferred to 98°C. After 2 minutes of incubation, the tubes were removed and stored at -20°C until needed. The clones were first screened for genome editing by APOE RFLP assay. 1.5 µL of the gDNA solution per sample was used to set up the APOE PCR.

2.26 Flow cytometry for Cas9 staining

Immunostaining of electroporated cells against Cas9 was performed 4 hours and 24 hours after electroporation in the case of RNP and plasmid respectively. The wells were first washed gently with 1X PBS to remove dead cells and debris. Cells were treated with Accutase for 7-8 minutes at 37°C. Dish was tapped gently, if the cells did not come off easily. Accutase was diluted with E8 medium and cells were collected in a 1.5 ml Eppendorf tube.

The cells were centrifuged at 600g for 5 minutes. It is necessary to be mindful at each centrifugation and wash step that not too many cells are being lost to the supernatant. The supernatant was then removed carefully with a tip and cells were washed with 0.5ml of 1X PBS by tapping the tube to disperse the cells. Tubes were centrifuged again at 600g for 5 minutes and the supernatant was discarded. The pellet was again resuspended in 300 µl of 1X PBS and cells were gently triturated through a 200 µl tip to ensure that they are well-dispersed and not in the form of clumps before the fixation step. To fix the cells, 100 µl of 4% PFA was added with the tip inside the PBS, and mixed by gentle tapping. The tubes were kept on ice for 10 min, after which the cells were centrifuged again at 700g for 6 min. The supernatant was discarded, ensuring the removal of as much of the PFA solution as possible. Immediately, 400 µl of 100% methanol was added for permeabilization and the cells were again carefully resuspended with a 200 µl tip to ensure cell clumps do not form. The tubes were incubated at -20°C overnight. The next day, the fixed cells were centrifuged at 700g for 6 min. Since fixed cells tend to form diffuse or fluffy pellets, the cells may be centrifuged again with higher force (up to 2000g for 1 min) from this step on, to ensure that cells are not being lost at each step. The pellet was then washed twice with a blocking solution of 0.5% BSA in PBS. About 0.6 ml of BSA solution was added at each step, but this amount may be reduced if the pellet is too small, to avoid loss of cells. After the second centrifugation at 700g for 6 minutes, as much of the supernatant as possible, was removed. Cell pellet was resupended in at least 75 µl of antibody mix (0.5% BSA containing 1:50 PE-conjugated Cas9 mouse mAb). The tubes were covered and incubated with gentle shaking at room temperature

for 1 hour. After the incubation, the tubes were centrifuged again at 700g for 6 min (or up to 2000g for 1 min). This was followed by a washing step with 0.6 ml 0.5% BSA. After another centrifugation at 700g for 6 min (or up to 2000g for 1 min), supernatant was completely removed and the cells were resuspended in at least 300 µl of 1XPBS and triturated with a 200 µl tip, as well as mildly vortexed before FACS to ensure there are single cells only, and to avoid clogging the FACS machine. The tubes are immediately kept on ice until ready for measurement by FACS.

2.27 Viability measurement for Cas9-electroporated cells

Percentage surviving cells after Cas9 plasmid or RNP were determined by performing a cell viability test by trypan blue exclusion method 24 hours after electroporation with Cas9 RNP or plasmid, surviving cells were washed with 1X PBS. Cells were redissociated by treatment with 700 µl Accutase per well of a 6 well dish. After 7-8 minutes of incubation at 37°C, E8 medium was added to stop the reaction and remove cells from the plate. The cells were collected into a 1.5 ml Eppendorf tube and centrifuged at 900g for 3 min to pellet down the cells. After the supernatant was discarded, the cells were resuspended well in E8 medium with the volume depending on the size of the pellet obtained. 20 µl of the cell suspension was mixed with 20 µl of 0.4% Trypan blue solution and incubated for 2 minutes. The mix was loaded onto a haemocytometer and 8 counts were obtained. As Trypan blue is excluded by live cells, dark blue cells were counted as dead cells. Percentage surviving cells was calculated as (live cells counted/ total number of cells electroporated)*100.

2.28 ELISA for APOE quantification in astrocyte conditioned medium

In order to treat neurons with defined quantities of APOE, conditioned media from B3/3 and B4/4 astrocytes was subjected to an ELISA to determine APOE content. Thermo Scientific Human ApoE ELISA kit was used according to the manufacturer's instructions.

First, all reagents were brought to RT. Fresh assay diluent and wash buffer were prepared by diluting in MilliQ water. Biotinylated antibody and streptavidin-HRP reagent was diluted to the working concentration just before application. Lyophilized standard was diluted to 400 ng/ml with assay diluent. This stock solution was further serially diluted in neuronal medium to yield standards in the range of 1.64 to 50 ng/ml. Aliquots of the samples to be assayed were brought to

RT and immediately, 100 µl of samples and standards were loaded into the ELISA plate wells in duplicate. The plate was incubated rocking at 4°C overnight. The next day, the solutions in the wells were discarded by tapping into a discard and then onto a tissue paper. Wells were then washed 4 times with 300 µl wash buffer to each well. 100 µl of biotinylated antibody was added to each well and incubated at RT shaking for 1 h. The wells were again washed 4 times with wash buffer and 100 µl of streptavidin-HRP agent was added to the wells. After 45 minutes of incubation with shaking at RT, the wells were washed 4 times with wash buffer and 100 µl of TMB substrate was added. The plate was incubated for 30 min at RT in the dark. The reaction was stopped using 50 µl of stop solution per well. The wells were measured at 450 nm with a spectrophotometer within 30 min of adding the stop solution.

The standard curve values were plotted and APOE content in samples was determined from the linear regression line.

2.29 ELISA for Aβ40 and Aβ42 quantification in neuronal conditioned medium

Aβ42/40 ratio of neurons treated with or without astrocyte-conditioned medium was compared to observe the effect of the APOE genotype on Aβ production. Astrocyte-conditioned neuronal medium and unconditioned neuronal medium was used to treat neuronal cells for 72 hours. This medium was collected and Aβ40 and Aβ42 ELISA was performed with the Invitrogen Human Aβ40 ELISA kit and Invitrogen Human Aβ42 Ultrasensitive ELISA kit according to the manufacturer's instructions.

Aβ40 and Aβ42 lyophilized standards were reconstituted in Reconstitution Buffer (55 mM sodium bicarbonate, pH 9.0) to 10,000 and 100,000 pg/ml respectively. The Aβ40 and Aβ42 standards were serially diluted in neuronal medium to yield standards in the range of 7.81 to 250 ng/ml and 1.52 to 50 ng/ml respectively. Meanwhile, samples to be tested were thawed to RT and 50 µl of standards and samples were added to the respective ELISA plates in duplicates. Then, 50 µl of the Aβ40 or Aβ42 detection antibodies were added to the respective plates and the covered plates were incubated shaking at 4°C overnight. The next day, wash buffer and secondary anti-rabbit IgG HRP solution was diluted freshly to the working concentration and all the wells were washed 4 times with wash buffer. 100 µl of the secondary antibody was added to each well and incubated shaking

at RT for 30 min. The wells were again washed 4 times with wash buffer and 100 µl of the provided stabilized chromogen was added to each well and incubated for 30 min in the dark at RT. 100 µl of stop solution was added to each well and the wells were measured at 450 nm using a spectrophotometer. The standard curve values were plotted and Aβ40 and Aβ42 content in samples was determined from the linear regression line.

2.30 Live-dead assay for viability of neurons

In order to assess viability of neurons after oxidative stress induction, live-dead assay using Calcein Green AM and Ethidium homodimer-1 (EthD-1) was performed. The cell permeant Calcein Green AM is virtually non-fluorescent. By the action of intracellular esterases, it is converted to fluorescent calcein, thus marking the live cells with green fluorescence (ex/em ~495 nm/~515 nm). Meanwhile, EthD-1 is excluded by live cells, but can enter cells with damaged membranes and upon binding to DNA, produces red fluorescence (ex/em ~495 nm/~635 nm) in dead cells.

The treatment of cells was carried out as follows. Immunopanned and AraC-treated neurons of all 4 lines (A3/3, A4/4, B3/3, B4/4) were redissociated and plated (50,000 cells per 10ul drop) on a polyornithine-laminin-coated coverslip. 2 weeks later, one coverslip of each line was kept as control for live-dead staining while the other was treated for 24 hours with 50µM hydrogen peroxide in conjunction with 5µM ferric chloride, to catalyze the production of reactive oxygen species. Both the control and treated cells were stained with Hoechst 33342 (1 µg/ml) to stain the nucleus, Calcein Green AM (1 µM) to stain the live cells and EthD-1 (2 µM) to stain the dead cells. Staining was carried out without fixation for 30 minutes at 37ºC in neuronal medium. Medium was then gently removed and replaced with HEPES-Ringer buffer. Cells were imaged using an inverted fluorescence microscope (Leica DMI6000B) using a 20X objective. Living cells were determined by counting Hoechst and Calcein Green-co-stained cells whereas dead cells were co-stained with Hoechst and EthD-1. Cells were counted using ImageJ and Live:Dead cell ratio was calculated for all the lines.

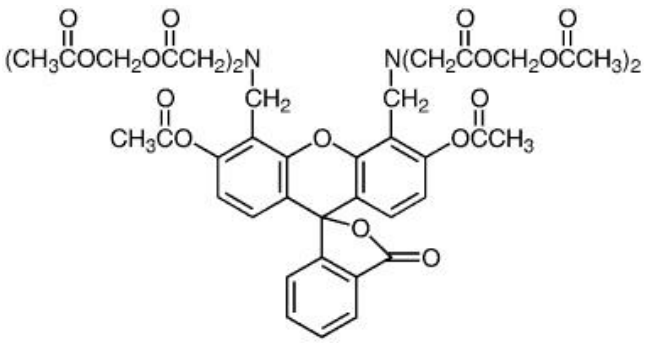

Figure 2.5: Calcein Green AM

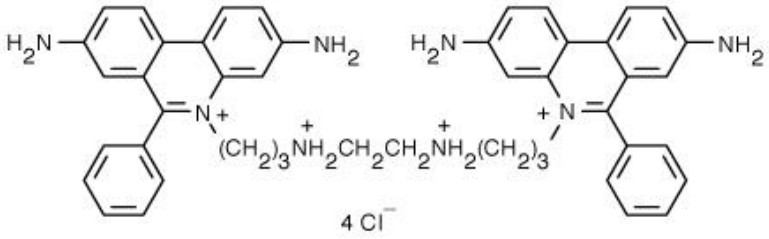

Figure 2.6: Ethidium Homodimer-1

2.31 Calcium imaging of astrocytes

Calcium imaging was performed in astrocytes using Fluo-4 acetoxymethyl ester (Fluo-4 AM) dye. It is a highly permeant dye, with a large dynamic range and a $K_d(Ca^{2+})$ of 345 nM (*Gee et al., 2000*). Inside the cell, it is hydrolyzed by endogenous esterases which allows it to bind calcium, thus increasing its fluorescence emission intensity by 100-fold.

Astrocytes cultured on glass coverslips were prepared by first washing with HEPES-Ringer Buffer containing freshly added 0.1% BSA and placing them in a 24 well dish. Next, the cells were incubated with 0.3 ml of the same buffer containing 5 μM Fluo-4 AM for 30 minutes. At the end of the incubation, the dye was removed, and warm buffer was added again to allow esterification to occur for 30 minutes. The coverslip was transferred to the imaging dish in fresh HEPES-Ringer buffer and placed in the imaging chamber which was heated to 37°C. Fluorescent images were captured at 488 nm, every 500 ms (using a Zeiss Axiovert 200M inverted epifluorescence microscope). For the first 2 min, baseline activity was recorded. At 2 min, ATP (100 μM) or L-Glutamate (100 μM) was added to the cells and recorded for 4 more minutes.

For data analysis, first the maximum projection of all the images was obtained using the ImageJ-Fiji Z-Project tool. The max projection image was thresholded using 'Triangle' thresholding. The image was processed further by applying median and minimum filtering of 1 pixel. Next, the Biovoxxel toolbox plugin was used to watershed irregular features. The ROIs thus obtained were added to ROI manager by 'Analyzing particles'. The selected ROIs were applied to the original image stack and 'Multimeasure' feature was used to obtain fluorescence intensities of the different ROIs for each image in the stack. The data was imported to Microsoft Excel for further analysis. ΔF/F for each ROI was calculated. A cell was counted as positive if it showed a response in the 4 minutes after adding ATP or Glutamate.

2.32 Glutamate uptake assay

The glutamate uptake property of astrocytes was assayed by using the Glutamine/Glutamate determination kit (Sigma). The assay spectrophotometrically measures the conversion of NAD+ to NADH that is accompanied by and is proportional to the amount of L-Glutamate oxidized to α-Ketoglutarate and ammonium ions, under the action of Glutamic dehydrogenase (GLDH) enzyme (*Lund P, 1986*).

A4/4 astrocytes (differentiated from APCs by 14 days of CNTF treatment) were equilibrated in HBSS for 10 min at 37 ºC and 5% CO_2. HBSS was replaced by the following in 3 separate wells for each condition: (i) HBSS + L-Glutamate (50 μM), (ii) HBSS + L-Glutamate (50 μM) + L-*trans*-Pyrrolidine-2,4-dicarboxylic acid (PDC- 1 mM), (iii) HBSS (without Na^+) + L-Glutamate (50 μM). Cells were incubated with the above for 30 min, 60 min and 120 min at 37 ºC, 5% CO_2. At the end of these time points, extracellular solution was collected and centrifuged at 1100rpm at 4ºC for 4 min and supernatant collected in order to remove debris. Meanwhile, cells were washed with 1X PBS and lysed using RIPA buffer (supplemented with protease inhibitor cocktail). At each time point, the centrifuged and collected supernatant was stored at 4ºC until the assay was performed.

To perform the assay, first standards were prepared from 1 mM L-Glutamate main stock as follows:

H2O (µL)	1mM stock Glutamate (µl)	Final Glutamate concentration (µM)
89	0.0	0.0
86.5	2.5	12.5
84	5	25
81.5	7.5	37.5
79	10	50
76.5	12.5	62.5
74	15	75
71.5	17.5	87.5
69	20	100
66.5	22.5	112.5
64	25	125

To a 96-well plate, 89 µL of each standard and sample was added. All samples were assayed in duplicates. Further, 111 µL of the following mix was added to each well (100 µl of Tris-EDTA Hydrazine buffer + 10 µl of NAD + 1 µl of ADP). The background signal was immediately measured at 340 nm using a Tecan Spark 20M plate reader. 2 µl of L-GLDH was immediately added to each well, covered and incubated at room temperature with gentle agitation for 40 minutes. The signal was measured again at 340 nm.

The signal from the protein standards was used to plot a standard curve and the values of unknown samples were extrapolated from the equation of the linear regression line. The value obtained is the amount of glutamate left in the extracellular solution. Subtracting this value from 50 (which was the µM of glutamate added to the cells) gives the amount of glutamate taken up by the cells. Since glutamate uptake is influenced by the cell density, the total protein in the cell lysates was quantified by BCA assay (as described in Section 2.15.2) and the total glutamate taken up by the cells was divided by the total protein in the cell lysate. This yielded the final µM of L-Glutamate/µg cellular protein -uptake by the astrocytes. Percentage inhibition of glutamate uptake by PDC and Na^+ free buffer was calculated with respect to the 'only glutamate added' condition.

2.33 Cytometric bead assay for chemokine secretion from astrocytes

Chemokine secretion upon stimulation with TNFα was tested in iPSC-derived astrocytes using the BD Cytometric Bead Array Human Chemokine Kit. Assay was carried out as recommended in the kit manual.

Briefly, A4/4 astrocytes were treated with 50 ng/ml TNFα (Peprotech) for 48 hours. Medium was then collected for the assay. Capture beads specific for CXCL8, CCL5, CXCL9, CCL2, and CXCL10 were mixed in equal volumes and vortexed well. 50 µl of the bead mix was incubated with 50 µl of PE-conjugated detection antibodies and 50 µl of collected medium (or provided standards for the standard curve), for 3 hours. This mix was then washed with the wash buffer. Subsequently, standards and TNFα treated sample were measured using a Guava Easycyte Flow Cytometer and analysed using Guavasoft 3.1.1 software.

For analysis, the singlet bead population was first gated from the Forward scatter vs. Side scatter plot. Capture beads for each chemokine have a distinct fluorescence intensity in the red channel. Thus, each cluster on the Red vs. Yellow fluorescence dot plot represents a specific chemokine population and was gated separately. The mean intensity of each cluster was calculated for the Yellow fluorescence (arising due to PE detection antibody), representing the amount of that cytokine. From these values, a standard curve was plotted and used to extrapolate the values of samples.

2.34 Seahorse assay

In order to understand the basal energy metabolism and responses to stress between the isogenic neurons and astrocytes, the Seahorse XF96 system was used, which provides information about the different parameters of glycolytic activity and mitochondrial respiration, in real-time and in response to different inhibitors of the electron transport chain and uncouplers of the proton gradient.

Oxygen consumption rate (OCR):
Oxygen consumption rate (OCR) was measured using the Seahorse XF Cell Mito Stress Test to detect respiratory parameters. The Mito Stress Test measure the consumption of oxygen in

response to modulators of the electron transport chain (ETC). Oligomycin, FCCP, and a mix of rotenone and antimycin were injected serially to measure ATP production, maximal respiration, and nonmitochondrial respiration, respectively.

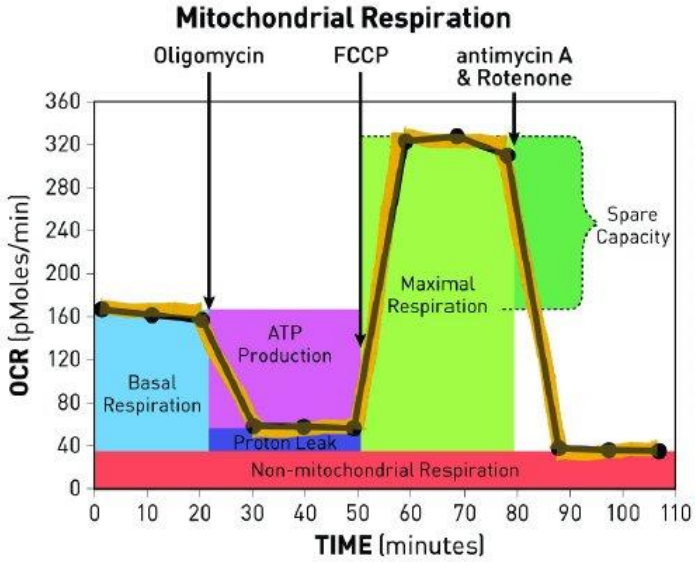

Figure 2.7: Mito Stress Test profile of the key parameters of mitochondrial respiration (adapted from *Agilent Technologies*)

ETC modulators show the following effects:

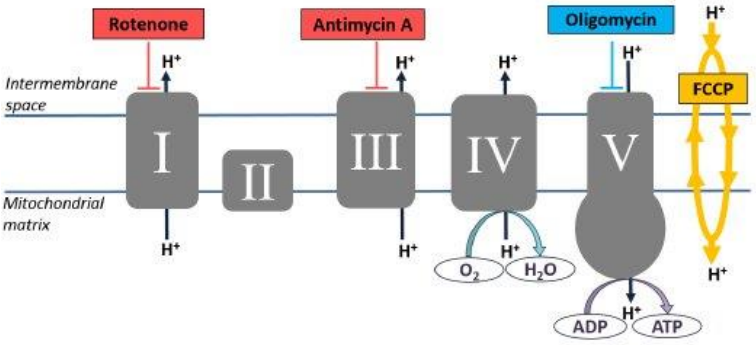

Figure 2.8: ETC modulators and their effects (adapted from *Agilent Technologies*)

Oligomycin inhibits ATP synthase (Complex V), leading to increased proton gradient and reduced oxygen consumption. This decrease in OCR corresponds to mitochondrial respiration associated with ATP production. Carbonyl cyanide-4-(trifluoromethoxy) phenylhydrazone (FCCP) is an uncoupling agent that collapses the proton gradient, by transporting hydrogen ions through the membrane before they can be used to provide energy for oxidative phosphorylation. This mimics a 'physiological energy demand' and the immediate increase in OCR represents the maximal

respiration. The combined application of rotenone and antimycin A, inhibitors of Complex I and Complex III respectively, completely shuts down mitochondrial respiration.

Extracellular acidification rate (ECAR):

The Seahorse XF Cell Glycolysis Stress Test occurs in parallel to the OCR measurement. Glucose is utilized by the cell to produce pyruvate (through glycolysis), which is further converted to lactate and secreted by the cells together with protons, thus decreasing the pH. The ECAR is, thus used to calculate parameters of glycolysis such as basal glycolysis rate, glycolytic capacity, glycolytic reserve and non-glycolytic acidification. This is achieved by first measuring the ECAR in glucose-free medium, and then after the addition of glucose and ETC modulators.

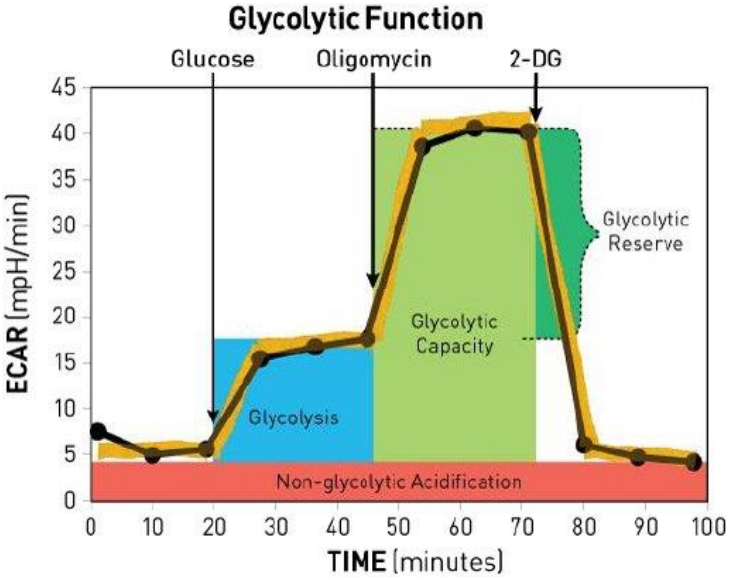

Figure 2.9: Glycolysis Stress Test profile of the key parameters of glycolytic function (adapted from *Agilent Technologies*)

For the measurement of iPSC-derived astrocytes, 96-well XF-plates were coated with 0.167 µg/ml Matrigel for 1h at RT. 24 hours before the experiment, 60000 cells were plated per well in NSC-/- medium and incubated at 37°C, 5% CO_2. To each well of the cartridge, 200 µL of Calibrant was added and incubated overnight at 37°C. The next day, culture medium was replaced with 180 µl of Seahorse assay medium (DMEM containing 4.5 g/L glucose, 2 mM L-Alanyl-L-glutamine, 1 mM Na-pyruvate, pH 7.35) and kept at 37 °C, 5% CO2 for 1 hour. Meanwhile the cartridge was prepared as follows:

Port	Substance	Volume	Stock Concentration	Final concentration
Port A	Glucose	25 µl	200 mM	25 mM
Port B	Oligomycin	25 µl	9 µM	1 µM
Port C	FCCP	25 µl	7.5 µM	0.75 µM
Port D	Rot/AA	25 µl	11 µM/11 µM	1 µM/1 µM

The cartridge was then loaded for calibrating. Meanwhile, the cells were washed twice, very gently with the Seahorse assay medium and finally 180 µl of the medium was added to each well and loaded on the machine. Three baseline OCR and ECAR measurements were recorded, followed by successive injections of Port A-D, with three measurements after the application of each substance (3 min of mixing, then 3 min of measurement).

For the measurement of iPSC-derived neurons, immunopanned neurons treated with AraC for 5d, were redissociated and plated onto Polyornithine and Laminin-coated 96-well XF-plates, at 80000 cells were plated per well. 2 days later, medium was replaced in the untreated wells with Neuronal medium (+BDNF) and in the APOE- treated wells, with astrocyte conditioned medium containing 8.7 ng/ml APOE. Medium was again changed in the same way after 2 days. 3 more days later, Seahorse measurement was carried out. One night before the experiment, to each well of the cartridge, 200 µl of Calibrant was added and incubated overnight at 37°C. The next day, culture medium on the cells was replaced with 180 µl of Seahorse assay medium and kept at 37 °C, 5% CO2 for 1 hour. Meanwhile the cartridge was prepared as follows:

Port	Substance	Volume	Stock Concentration	Final concentration
Port A	Glucose	25 µl	200 mM	25 mM
Port B	Oligomycin	25 µl	18 µM	2µM
Port C	FCCP	25 µl	0.25 µM	0.025 µM
Port D	Rot/AA	25 µl	11 µM/11 µM	1 µM/1 µM

The cartridge was similarly loaded for calibrating and the cells were washed gently twice with the Seahorse assay medium and finally 180 µl of the medium was added to each well and loaded on the machine. Same as for the astrocytes, three baseline OCR and ECAR measurements were recorded, followed by successive injections of Port A-D, with three measurements after the application of each substance. (3 min of mixing, then 3 min of measurement).

At the end of the Seahorse measurement, buffer from the wells was removed and cells were washed very gently with PBS. They were then lysed with 50 µl Lysis Buffer (10mM Tris+0.1% Triton X-100) and shaken at 4°C for 30 min. BCA solution was added and performed as described in Section 2.15.2. Assay values were normalized to protein content. Data was analyzed using Agilent Seahorse Wave software.

2.35 MitoSOX (ROS detection assay)

Flow cytometry:

Flow cytometry is a quantitative technique that allows us to study a heterogeneous population of cells based on their light scattering properties and detection of fluorescent proteins or bound dyes. For flow cytometry measurements, the Guava EasyCyte 6-2 L Benchtop Flow Cytometer (Merck Millipore) was used. Astrocytes were dissociated with 5 minutes of Accutase (Sigma) treatment and seeded in a 24-well format at a density of 40,000 cells per well and kept at 37°C for 24 hours, before treatment with the chosen dye/indicator. Neurons were dissociated as described in Section 2.13.9 and seeded in a 48-well format at a density of 100,000 cells per well. The cells were incubated at 37°C, 5% CO_2 and 80-90% humidity for 5 days before treatment with the chosen dye. Cells were analyzed for specific parameters and data was collected for at least 5,000 cells per cell line or treatment. For analysis, the GuavaSoft InCyte Software package was used.

MitoSOX staining: Mitochondrial ROS:

MitoSOX Red is a live-cell permeable fluorescent dye that acts as a sensor for mitochondrial reactive oxygen species (ROS). MitoSOX rapidly localizes to the mitochondria and upon oxidation specifically by superoxides, shows increased emission at ~580 nm wavelength.

Cells were stained with 2.5 µM MitoSOX solution in NSC-/- medium (for astrocytes) or neuronal medium (for neurons) at 37°C for 30 min. Astrocytes were harvested by Accutase treatment for 5 min. Neurons were harvested by the redissociation protocol described in Section 2.13.9. Cell pellets were resuspended in 300-350 µl of PBS and placed on ice until the measurement.

For MitoSOX flow cytometry, fluorescence was excited with a 488 nm laser (blue) and emission recorded with a 690/50 nm filter (red).

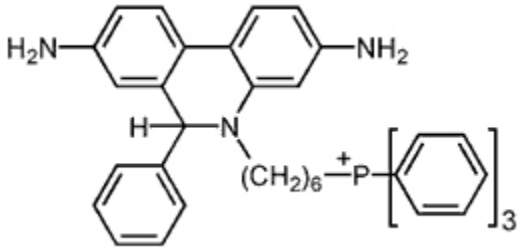

Figure 2.10: MitoSOX

2.36 TMRE staining for mitochondrial membrane potential

Tetramethylrhodamine ethyl ester (TMRE) is a live-cell permeable, lipophilic, positively-charged dye that readily accumulates in active mitochondria due to their relative negative charge. Depolarized or inactive mitochondria have reduced membrane potential and thus, fail to accumulate TMRE. Therefore, reduced emission at ~574 nm wavelength in TMRE stained cells can be used to detect loss of mitochondrial membrane potential.

Cells were stained with 400 nM TMRE solution in NSC-/- medium (for astrocytes) or neuronal medium (for neurons) at 37°C for 30 min. Astrocytes were harvested by Accutase treatment for 5 min. Neurons were harvested by the redissociation protocol described in Section 2.13.9. Cell pellets were resuspended in 300-350 µl of PBS and placed on ice until the measurement.

For TMRE flow cytometry, fluorescence was excited with a 488 nm laser (blue) and emission recorded with a 690/50 nm filter (red).

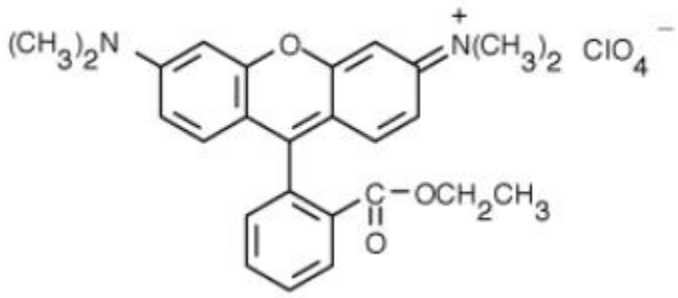

Figure 2.11: TMRE

2.37 Macro for determining sizes of (EEA1 and LAMP2-stained) vesicles

```
@ File (label = "Input directory", style = "directory") input

processFolder(input);

function processFolder(input) {
	list = getFileList(input);
	list = Array.sort(list);
	for (i = 0; i < list.length; i++) {
		processFile(input, list[i]);
	}
}

function processFile(input, file) {
	open(input + File.separator + file);

	run("Split Channels");

	selectWindow("C1-" + file);
	close();

	selectWindow("C2-" + file);
	setAutoThreshold("MaxEntropy dark");
	run("Convert to Mask");
	run("Save", "save=[/" + input + File.separator + "mask_" + file + ".tif]");
	run("Set Measurements...", "area redirect=None decimal=6");
	run("Analyze Particles...", "size=0-Infinity show=Nothing display clear");
	saveAs("Results", input + File.separator + file + ".xls");

	close();

}
```

2.38 Statistical analysis and softwares used

Data collection and analysis was performed in Microsoft excel and statistical tests were carried out with GraphPad Prism 6. Statistical tests used for each figure are mentioned in the respective figure legends. Experiments comparing the partner cell lines of an isogenic pair and between pairs were tested with one-way ANOVA followed by Sidak's post hoc test to correct for multiple comparisons.

Plotted bar graphs signify arithmetic means of the data and error bars represent standard errors of the mean (SEM). p-value < 0.05 was considered statistically significant. One, two and three asterisks denoted p-values smaller than 0.05, 0.01 and 0.001 respectively. Details of the softwares used for specific experiments are mentioned in the respective methods section.

Immunocytochemistry and calcium imaging data acquisition was performed using ZEN software and imported into ImageJ for further analysis.

Agarose and PAGE gels were captured, and Western blot membranes developed using the BioRad ChemiDoc-XRS software. FACS data was stored & analyzed using Summit v6.3 software. Flow cytometry and chemokine assay data was captured, analyzed using Guavasoft 3.1.1 software. Seahorse data was captured & analyzed using Seahorse Wave Desktop software. G-Banding analysis for karyotyping was performed using Metasystems Ikaros software. Metaphase spreads were counted using ImageJ. Plasmid design, restriction digests were planned using ApE. gRNAs and ssODNs were designed using Benchling and MIT CRISPR design tool.

3. Results

3.1. Experimental plan

As detailed in Section 1.4 of the introduction, better human-derived models are required for the study of the isoform-specific effects of APOE. Figure 3.1A represents our experimental approach towards that direction. The first step was to generate a panel of iPS cells from APOE4/4 carrying AD patients. Somatic cells of these patients were sourced from the Coriell Institute for Medical Research. These included patient fibroblasts (AG11368) as well as lymphoblastoid cell lines (LCLs- AG10984, AG10987, AG11001). In addition to these, iPS cells were generated also from human neonatal foreskin fibroblasts to be used as controls in a few experiments. iPS cells from AG10984 (henceforth referred to as A4/4) were then genome edited using a CRISPR/Cas9 system to its isogenic *APOE3/3* counterpart (A3/3). Genome editing at the *APOE4/4* SNP required optimization of the CRISPR/Cas9 tool for use in iPSCs. After the isogenic iPSCs were obtained, they were characterized for their pluripotency and integrity. Additionally, an isogenic pair of *APOE3/3* (B3/3) and *APOE4/4* (B4/4) iPSCs were obtained from the European Bank of induced pluripotent Stem Cells (EBiSC). These cells are derived from a cognitively normal 18 year-old APOE3/4 carrier (*Schmid et al., 2019*). Further details of the cell lines are mentioned in Figure 3.1B. Using cells derived from an *APOE4/4* AD patient as well as a young *APOE3/4* individual allowed untangling of APOE4-induced phenotypes independent of the initial cellular source. Neural cell types differentiated from the pluripotent cells were first characterized for cell type-specific markers and functional properties and then subjected to various assays aiming to screen for well-described cellular AD phenotypes.

A

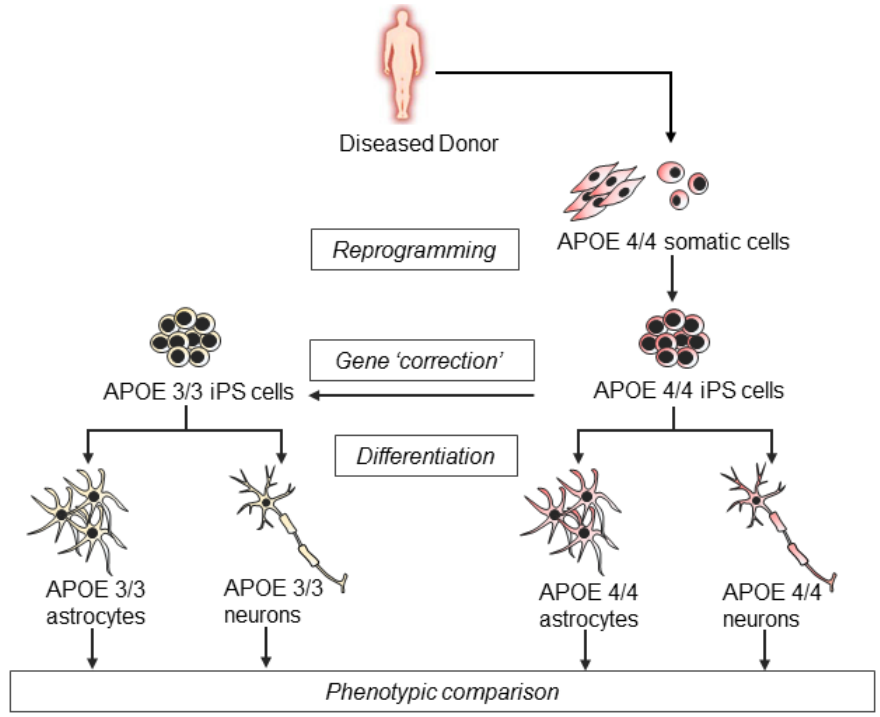

B

Name of line	Diagnosis	Gender, Age at onset	Genotype	Parental line for gene editing	Source	Cell line ID at source
A4/4	Alzheimer's Disease	Female, 68y	APOE4/4	-	Coriell Institute	AG10984
A3/3			APOE3/3	A4/4		
B4/4*	Undiagnosed	Male, 18y	APOE4/4	BIONi010-C (3/4)	EBiSC	BIONi010-C4
B3/3*			APOE3/3	BIONi010-C (3/4)	EBiSC	BIONi010-C2

Figure 3.1: Experimental plan for the study (A) Somatic cells from *APOE4/4* AD patients were reprogrammed to iPS cells followed by genome editing to isogenic *APOE3/3* iPS cells. They were then differentiated to astrocytes and neurons for phenotypic comparisons between the two genotypes. (B) Table of isogenic cell lines used for phenotypic comparisons

3.2 Generation and characterization of patient-derived iPS cells

In order to generate integration-free iPS cells from different somatic cell types using an episomal approach, these cells need to be transfected with plasmids containing Yamanaka's reprogramming factors. An episomal plasmid-based method provides a viral and transgene integration-free approach to reprogramming, which is especially preferred when preparing cells for cell therapy and clinical applications. First, this required selection of optimal electroporation conditions using the Neon transfection system (Life Technologies). Electroporation affords some advantages over

chemical transfection methods such as wide applicability and avoiding the use of toxic chemicals. At the same time, it is technically simpler and faster to use than viral transfection methods. In the Neon system, cells are transfected in a tip, as opposed to in a cuvette, thus improving survival. As compared to the Amaxa nucleofector device (Lonza), it offers the flexibility to modulate different electroporation parameters like voltage (V), pulse width (ms) and number of pulses, depending on the cell type. Optimal electroporation conditions for delivering nucleic acids to human LCLs, fibroblasts, neural stem cells and iPSCs were empirically tested by transfecting the cells with the pCXLE-EGFP plasmid (an episomal plasmid expressing EGFP under the chicken β-actin promoter), followed by microscopy-based quantification. These parameters were used for all subsequent electroporations. (Figure 3.2).

A

Cell type	Electroporation condition	Transfection efficiency
Lymphoblastoid cells (LCLs)	1100 V, 30 ms, 1 pulse	~ 21.51% ± 1.4%
Neural stem cells (NSCs)	1400 V, 20 ms, 2 pulses	~ 77.6% ± 5.7%
Human fetal fibroblasts (HFFs)	1650 V, 10 ms, 3 pulses	~ 19.16% ± 3.4%
Induced pluripotent stem cells (iPSCs)	1250 V, 30 ms, 1 pulse	~ 47.5% ± 13.5%

B

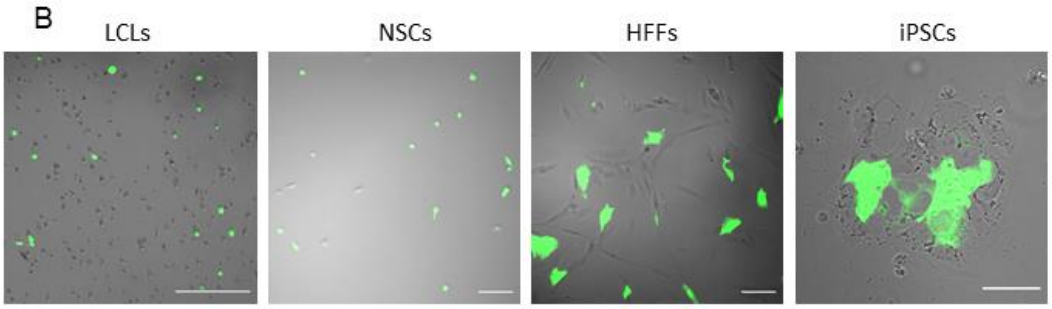

Figure 3.2: Optimizing electroporation conditions for somatic cells (A) Table enlisting electroporation conditions and transfection efficiencies for somatic cell types using a Neon electroporation device. (B) Merge of phase contrast and fluorescent images of the different cell types 24 hours after electroporation with the pCXLE-EGFP plasmid. Green colour represents GFP fluorescence. Scale bar = 100 µm. (n=2, n=1, n=2, n=2).

Patient-derived LCLs or fibroblasts were reprogrammed using a feeder-free protocol modified from *Chen et al., 2011* (Figure 3.3A). Somatic cells were electroporated with episomal plasmids carrying Yamanaka's reprogramming factors (OCT3/4 (octamer-binding transcription factor 4), SOX2 (sex determining region Y-box 2), KLF4 (Krüppel like factor 4), L-MYC, along with LIN28, and shRNA of p53) as described in *Okita et al., 2011*. The culture medium was changed and supplemented with growth factors as the cells go through the different stages of reprogramming. The growth medium was also supplemented with sodium butyrate, an HDAC inhibitor, since it has been shown to enhance reprogramming by promoting epigenetic remodeling *(Mali et al., 2010)*. By about day 22-25, one could observe colonies with typical stem cell-like morphology (Figure 3.3B). However, the efficiency of this process is fairly low at 0.01% (i.e. one iPSC colony obtained per 10,000 cells electroporated).

One reason for this could be the specific stoichiometric and temporal levels of OCT4 and SOX2 expression required for effective reprogramming. High OCT3/4 and low SOX2 expression has been known to lead to the highest efficiency of reprogramming *(Papapetrou et al., 2009)*. Alternatively, co-expression of essential factors might be a limiting parameter. As both, OCT3/4 and SOX2 were delivered by different plasmids, co-expression of both in electroporated APOE4/4 patient LCLs was investigated by immunostaining with antibodies against OCT4 and SOX2. Only a few cells showed expression of both factors with varying expression levels (Figure 3.3 C). Hence, most of the transfected cells could possibly be in potentially incompletely reprogrammed states.

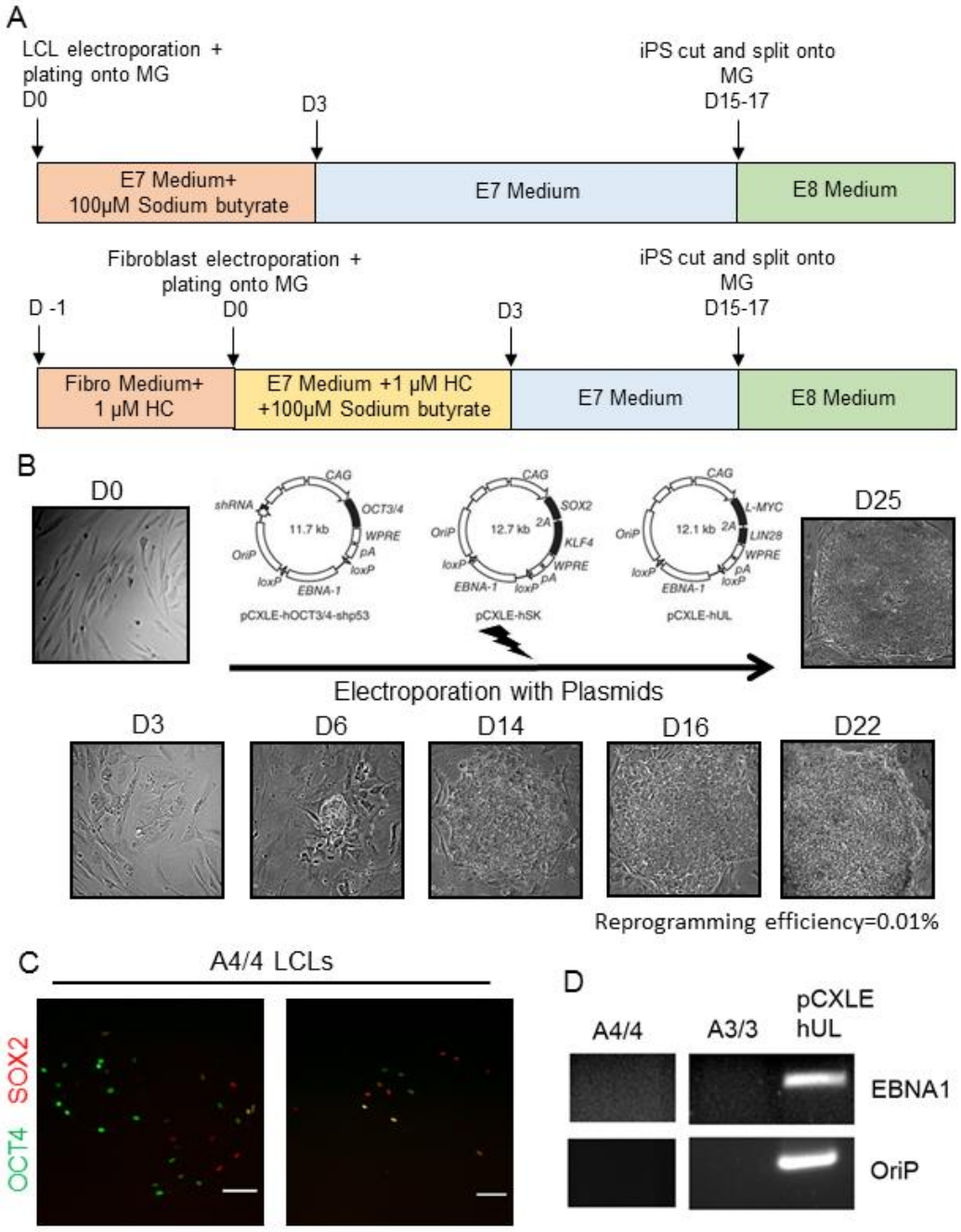

Figure 3.3: iPSC generation from somatic cells (A) Protocols and timeline detailing the generation of iPS cells from patient-derived LCLs and fibroblasts. (B) A series of phase contrast images following human fibroblasts after electroporation with episomal plasmids containing Yamanaka's reprogramming factors. Approximately 22-25 days after electroporation, iPSC colonies appear with typical stem cell morphology. (C) LCLS were electroporated with episomal plasmids containing human OCT3/4, SOX2, followed by immunostaining for OCT4, SOX2 24 hours later. Scale bar = 100 µm. (D) PCR performed for EBNA1, OriP (present on the episomal plasmid backbone) with DNA isolated from iPS cells 7-8 passages old, run on an agarose gel. PCR products of an episomal plasmid itself were run as a positive control.

As opposed to normal fertilization, reprogramming to iPS cells is a relatively long process and thus may result in a heterogeneous culture with cells at different developmental potentials. Therefore, putative iPS cells, selected according to morphological criteria and manually picked were analyzed for the expression of well-established pluripotency markers after 7-8 passages. At the same time, loss of the transient episomal plasmids was investigated. iPSC colonies obtained were immunostained for OCT4, SSEA4, SOX2 and TRA1-60 and most of the cells were found to be positive (Figure 3.4A). PCR performed for EBNA1 and OriP, which are elements of the episomal plasmid backbone, showed that the plasmids were lost from the iPS cells. Thus, one can conclude that the cells expressed their own reprogramming factors as opposed to being expressed from the plasmids.

The differentiation potential of the iPSCs can be tested by allowing them to undergo spontaneous differentiation. Their developmental capacity can then by tested by immunostaining for markers of all three germ layers: PAX6 (for endoderm), GATA4 (for endoderm) and FOXC1 (for mesoderm). By culturing A4/4 iPSCs in serum-containing media as embryoid bodies, they demonstrated the ability to differentiate into all three germ layers (Figure 3.4C). The reprogramming process as well as long-term culture of hESCs and iPSCs has been associated with the accumulation of karyotypic abnormalities. ~13% of hiPSC and ESC culture have been estimated to bear aberrant karyotypes, with gains in chromosomes 12, 17, 20 and X being the most recurrent *(Lund et al., 2012)*. Thus, A4/4 iPSCs were karyotyped and at least 20 chromosomal spreads were counted. G-Banding analysis confirmed that the cells retained a normal karyotype (Figure 3.4B).

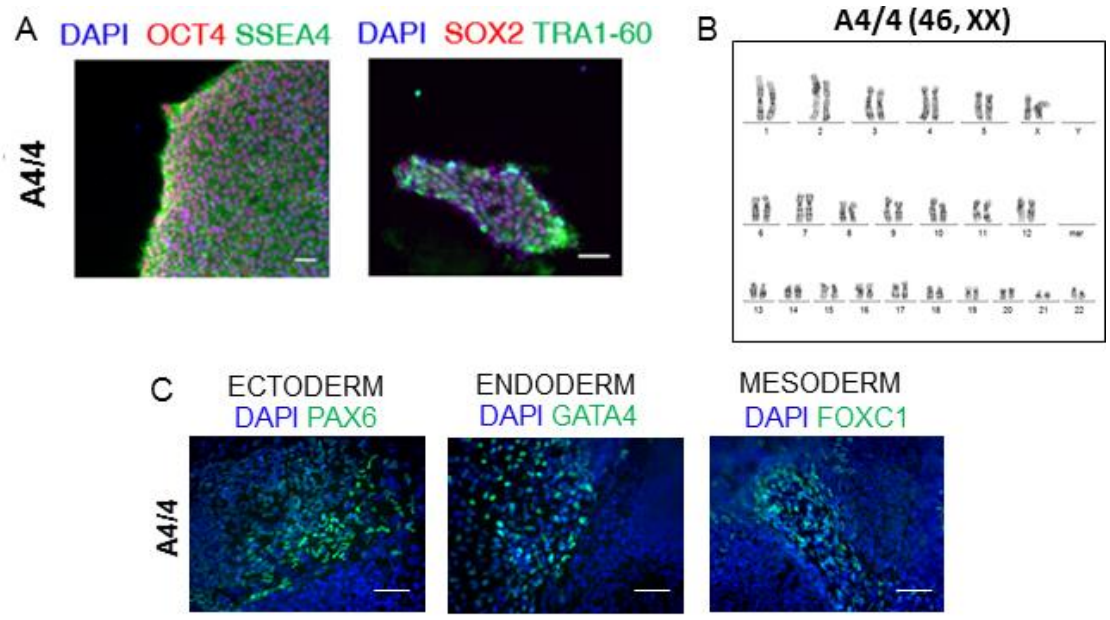

Figure 3.4: Characterisation of patient-derived A4/4 iPSCs (A) A4/4 iPSCs were immunostained for pluripotency markers OCT4, SSEA4, SOX2 and TRA1-60. Nuclei were stained with DAPI (blue). Scale bar = 100 µm. (B) A4/4 iPSC karyotype. At least 20 chromosomal spreads were counted and 7 were analyzed (C) Immunocytochemistry for germ layer markers PAX6 (ectoderm), GATA4 (endoderm) and FOXC1 (mesoderm) after spontaneously differentiating the iPSCs. Nuclei were stained with DAPI (blue). Scale bar = 100 µm.

3.3 Optimizing the CRISPR/Cas9 system to perform HDR in iPS cells

3.3.1. Generating a multiplex CRISPR plasmid toolkit

While attempting to perform HDR-based genome editing in hard-to-transfect cells like iPSCs that show resilience to HDR modifications, it was necessary to first optimize several parameters of the CRISPR/Cas9 process that would increase HDR, while also having low off-target rates. This includes optimizing transfection conditions that result in high efficiency as well as good survival rates, Cas9 delivery approaches and designing gRNAs and ssODNs to also achieve low off-target rates.

The panel of CRISPR/Cas9 plasmids used for this study are PX458 (Cas9-GFP), PX459 (Cas9-Puro), PX461 (Cas9nickase-GFP), PX462 (Cas9nickase-Puro) *(Ran et al., 2013)*. All subsequent data will be shown for PX458 and PX461, although most modification have been performed on the PX459 and PX462 plasmids as well. These are plasmids with a Cas9 or Cas9 nickase connected by a 2A self-cleaving peptide to a GFP gene or Puromycin resistance gene, expressed under a CBh promoter. Each plasmid also contains a customizable site where a single gRNA of interest can be

inserted after digestion with Type II endonuclease, BbsI. The expression of the gRNA is driven by human U6 promoter. Further details about these plasmids are mentioned in Figure 2.4.

Using wild type Cas9 with a single gRNA results in high cutting rates, but *Ran et al., 2013b* have shown that using a D10A nickase with a pair of gRNAs created 50-1500 fold fewer off-targets without sacrificing the on-target rates. However, the two gRNAs must be chosen such that there is -4 to 20bp distance from the ends of each other on opposite strands, to result in optimal targeting (*Ran et al., 2013b*). Since co-transfection of two ~10kb plasmids in hard-to transfect iPS cells would further reduce the efficiency of the process, we generated PX461 and PX462 plasmids with an additional insert that would allow insertion of a second gRNA into the same plasmid after digestion with another Type II endonuclease, SapI, thus allowing multiplexed gRNA expression. These plasmids are henceforth referred to as PX461i and PX462i. (Figure 3.5A). The chosen gRNAs of interest were successfully cloned into the insertion sites for both PX458 (Figure 3.5B) and PX461i (Figure 3.5C) as confirmed by Sanger sequencing.

Initial tests for Cas9 plasmid transfection and expression showed very low efficiency (evidenced by low GFP expression and low resistance to Puromycin). Thus, in an attempt to improve Cas9 expression, we generated nickase plasmids with the CBh promoter driving Cas9 expression replaced with stronger and more universal promoters like CAG and PGK. The plasmids were Sanger sequenced to verify correct promoter insertion and were referred to as PX461i-CAG and PX461i-PGK (Figure 3.5D). The plasmids were then tested for Cas9 expression efficiency in patient and control lymphoblastoid cells (LCLs) and neural stem cells (NSCs) respectively- the cell types originally intended for genome editing. However, no significant difference in transfection efficiency was observed between promoter types (Figure3.5E, F). They were also tested on neonatal foreskin fibroblasts (NFFs) but did not show a strong difference in transfection efficiency, however, more replicates would be needed to confirm this.

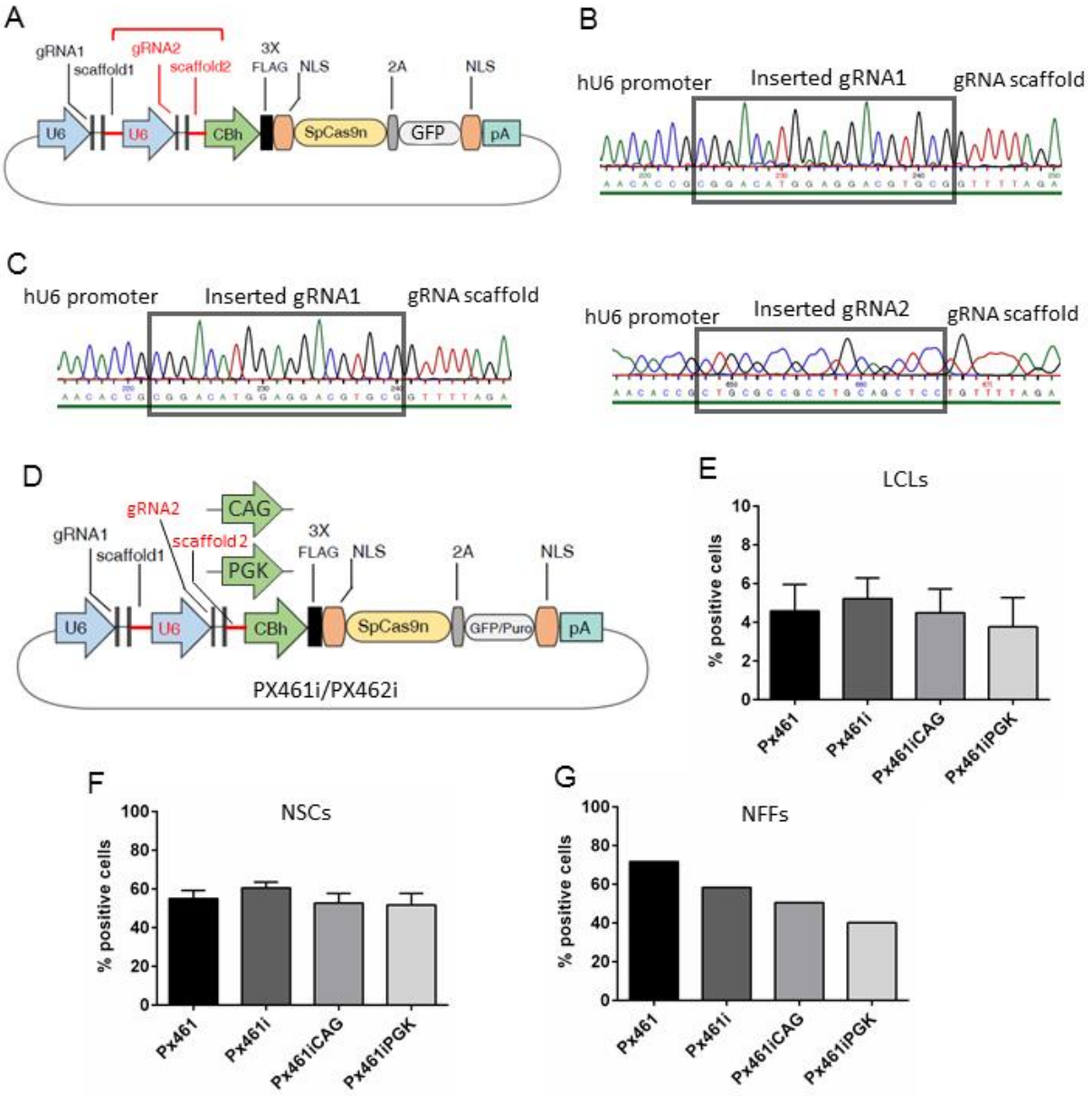

Figure 3.5: Generating CRISPR/Cas9 plasmids to improve Cas9 transfection and expression (A) Cas9-2A-GFP or Puro-expressing plasmids PX461 or PX462 with another gRNA cassette inserted to allow expression of 2 gRNAs from the same plasmid, hence referred to as PX461i or PX462i plasmid. (B) Sanger sequencing showing successful integration of chosen gRNA into PX458 wild type Cas9-GFP plasmid. (C) Sanger sequencing showing successful integration of both chosen gRNA into PX461i nickase plasmid. (D) Double gRNA insert plasmids (PX461i or PX462i) with the promoter than drives Cas9 expression, changed from CBh to a CAG or PGK promoter. (E) Cas9 expression from a single insert Px461, double insert Px461i, double insert Px461i CAG-Cas9 and double insert Px461i PGK-Cas9 plasmids quantified by flow cytometry, 24 hours after transfection of LCLs with the different plasmids (n=3). (F) Cas9 expression from a single insert, double insert, CAG-Cas9 and PGK-Cas9 plasmids quantified by flow cytometry, 24 hours after transfection of NSCs with the different plasmids (n=3). (G) Cas9 expression from a single insert, double insert, CAG-Cas9 and PGK-Cas9 plasmids quantified by flow cytometry, 24 hours after transfection of NFFs with the different plasmids (n=1). All values are represented as mean, error bars show standard error of mean (SEM).

3.3.2 Choosing gRNAs and optimizing transfection into iPSCs

When transfecting with wild type (WT) Cas9, a single gRNA is required. Since the gRNA must be followed by a PAM site (5'NGG in the case of SpCas9), this limits which sites can be chosen as gRNAs. There are several softwares (such as Benchling, E-CRISP, crispr.mit.edu) available online that suggest possible gRNAs with calculated on-target and off-target scores. An ideal gRNA would have high estimated on-target rates and low estimated off-target rates. Cas9 is known to cut 3 base pairs upstream of the PAM site. gRNAs chosen with cut sites closer to the site of change, are expected to show higher editing (*Paquet et al., 2016*) For the generation of the isogenic A3/3 line, a gRNA was used with the cut site only a single base pair upstream of the SNP (Figure 3.6). The gRNA was 17 bp long (as opposed to the traditionally used 20 bp) since shorted gRNAs have been shown to decrease undesired off-target effects (*Fu et al., 2014*). A single stranded oligonucleotide (ssODN) template donor was also designed using Benchling. A 111 bp ssODN symmetrical around the cut site was chosen (Figure 3.6). A silent mutation was inserted in the gRNA region of the ssODN to prevent recognition and recutting of the correctly edited DNA sequence at the target locus by gRNA-Cas9. A silent mutation with the closest codon adaptation index was chosen. However, only for the electroporation optimization experiments (Figs 3.7-3.11), a 20bp version of the same gRNA was used. All ssODNs used, had phosphorothioate ends which extend the lifetime of the ssODN by minimizing nuclease degradation, thus allowing a longer coexistence of Cas9 and donor template in the cell. This is known to increase HDR rates (*Renaud et al., 2016*).

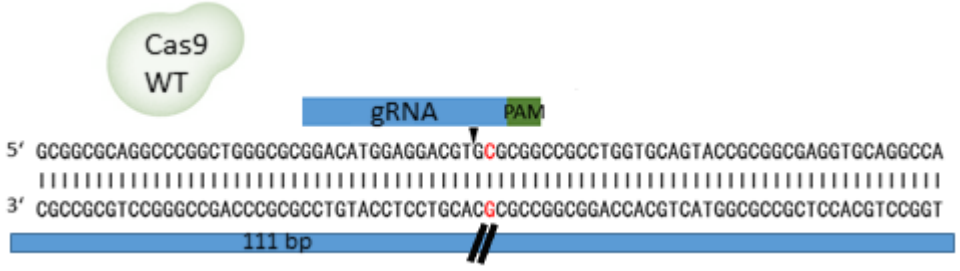

Figure 3.6: gRNA and donor repair sequence chosen for HDR at *APOE4* locus. Schematic representation of the *APOE* locus with the *APOE4* SNP of interest in red. 18 bp gRNA sequence chosen, with the black arrow representing the cut site. PAM site is in green and donor sequence used was a 111 bp oligo donor symmetric on either side of the cut.

3.3.3 Cas9 plasmid and RNP transfection into A4/4 iPSCs

In order to maximize editing by Cas9, transfection efficiencies need to be optimized. At the same time, survival of iPSCs after electroporation needs to be ensured. Thus, A4/4 iPSCs were electroporated with Cas9 WT plasmid, followed by estimation of transfection efficiency and viability. Transfection efficiency was measured by dissociating the cells 24 hours after electroporation, immunostaining against Cas9 using a phycoerythrin (PE)-labelled primary antibody, followed by flow cytometry. A4/4 iPSCs that were not electroporated with Cas9, but underwent the immunostaining procedure served as a negative control for gating the positive cells. Surviving cells were counted, by first gently washing the well of dead cells 24 hours after electroporation, followed by redissociating the cells and performing Trypan Blue exclusion test to label the dead cells blue. Live cells with intact cell membranes actively exclude Trypan Blue. Percentage surviving cells were obtained by calculating the total number of Trypan Blue-negative cells as a percentage of the number of cells electroporated.

Several electroporation parameters were tested, however, they all resulted in a very low percentage of viable cells (Figure 3.7B). For subsequent experiments, 1000V, 30ms, 1p was used for plasmid electroporations since it resulted in better viability than other conditions tested.

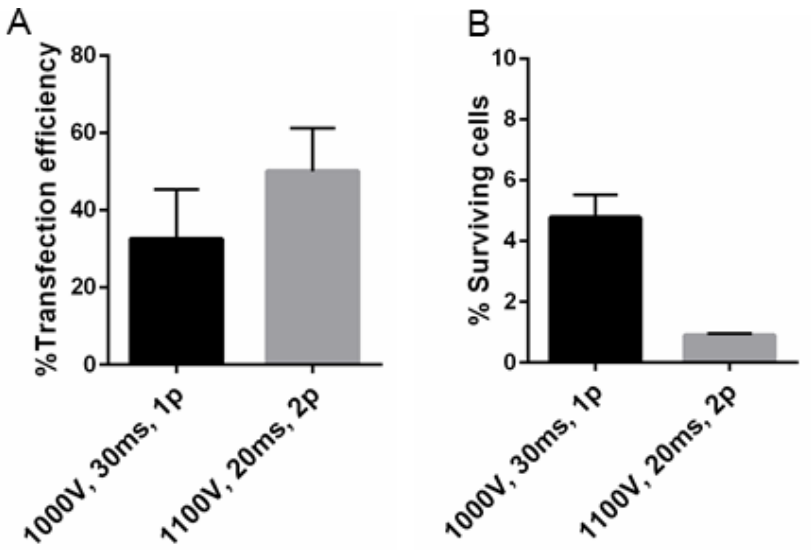

Figure 3.7: Cas9 plasmid transfection into iPS cells. (A) Transfection efficiency of WT Cas9 plasmid (PX458) using two different sets of electroporation parameters. Transfection efficiency was calculated by immunostaining for Cas9, followed by flow sorting (n=2). (B) Surviving cells as a percentage of total cells electroporated, 24 hours after electroporation with two different sets of electroporation parameters. Live cells were counted after Trypan blue staining (n=2). All values are represented as mean, error bars show standard error of mean (SEM).

Since plasmid electroporation resulted in a very low viability and transfection efficiency, Cas9 ribonucleoprotein (RNP) was also tested. Different parameters for Cas9 RNP (Integrated DNA Technologies-IDT) electroporation were tested with and without electroporation enhancer, also supplied by IDT. The electroporation enhancer is a single stranded carrier oligonucleotide computationally designed to be non-homologous to human or mouse genomes and shown to improve electroporation efficiency. A4/4 iPSCs were electroporated with Cas9 RNP (Cas9 protein conjugated to crRNA and gRNA of choice), followed by estimation of transfection efficiency and viability. Transfection efficiency and viability were measured by the same protocol used for plasmid transfections i.e. by immunostaining dissociated cells against Cas9 using a PE-labelled primary antibody, followed by flow cytometry. However, since the RNP is immediately available in the cell, the immunostaining procedure was carried out just 4 hours after transfection. Similarly, A4/4 iPSCs that were not electroporated with Cas9, but underwent the immunostaining procedure served as a negative control for gating the positive cells. As in the case for plasmid electroporation, viability was determined 24 hours after electroporation.

Positive cells were gated in the context of the negative controls, as can be seen in the flow cytometry histograms in Figure 3.8A, which also demonstrates an improvement in transfection efficiency using the electroporation enhancer. Of the different electroporation parameters tested, the 1300V, 30ms, 1 pulse condition was used with electroporation enhancer for all further Cas9 RNP experiments, since it afforded a high level of transfection efficiency while ensuring a sufficient amount of iPSC survival (Figure 3.8 B, C).

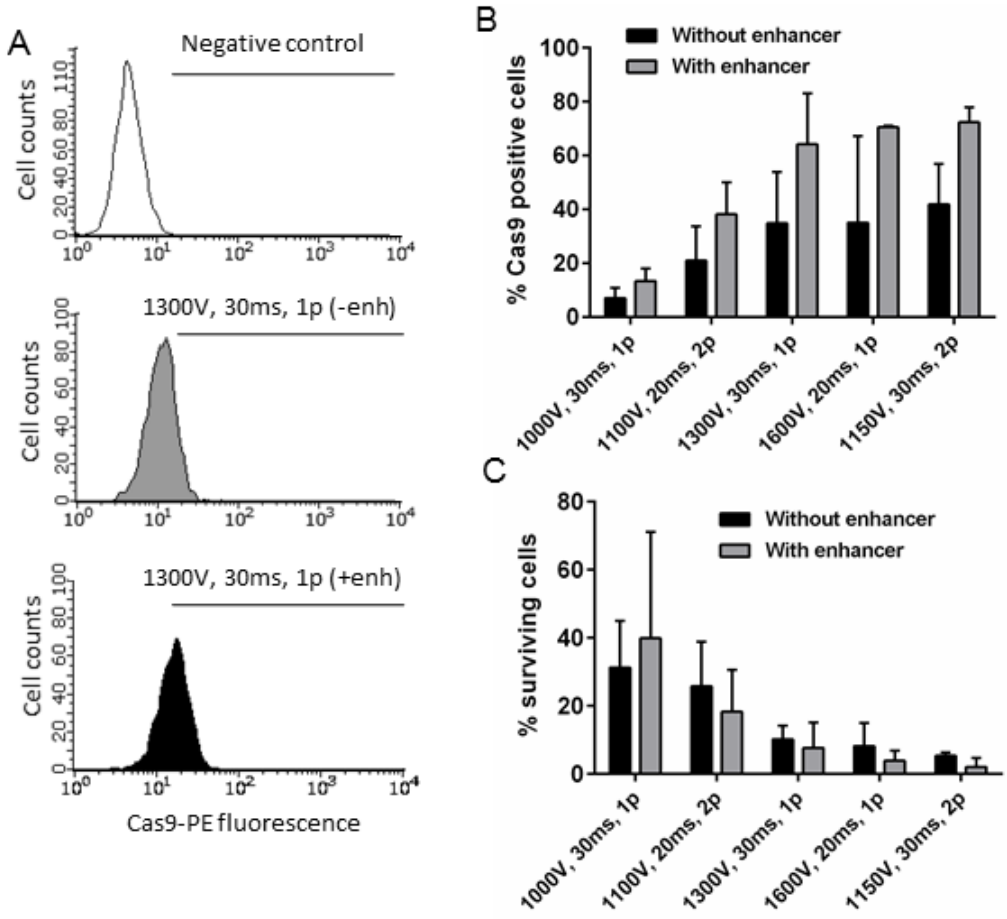

Figure 3.8: Cas9 RNP transfection into iPS cells. (A) Representative histograms of non-electroporated cells (negative control), along with 1300V, 3ms, 1p condition without enhancer (-enh), and with enhancer (+enh). Cells were immunostained for Cas9 4 hours after electroporation and flow cytometry performed. X axis represents fluorescence intensity, Y axis represents cell counts. The straight line represents the gated region for successfully transfected cells. (B) Percentage of Cas9 positive cells obtained 4 h after electroporation, immunostaining for Cas9, followed by flow cytometry. Five different conditions of parameters were tested both with and without electroporation enhancer. (n=3). (C) Surviving cells as a percentage of total cells electroporated, 24 hours after electroporation with with Cas9 RNP, with and without electroporation enhancer. Live cells were counted after Trypan blue staining (n=3). All values are represented as mean, error bars show standard error of mean (SEM).

With the chosen Cas9 RNP electroporation parameters of 1300V, 30 ms, 1 pulse, the transfection efficiency was on an average ~60%. However, the viability of cells after electroporation was below 15%. The amount of Cas9 used per 10µl electroporation tip and per 600,000 cells was 1.83µM, as recommended by the manufacturers (IDT). In an attempt to improve cell viability, while testing if transfection efficiency could be maintained, A4/4 iPSCs were electroporated with reduced amounts of Cas9 (1.83 µM, 1.2 µM, 0.6 µM) at the chosen electroporation parameters of 1300V, 30ms, 1 p in the presence of electroporation enhancer. Transfection efficiency and viability were

tested as described before. However, reducing Cas9 molarities significantly reduced the transfection efficiency without having an effect on the cell survival. Hence, all subsequent experiments were carried out using 1.83 µM Cas9 per 10 µl neon electroporation tip.

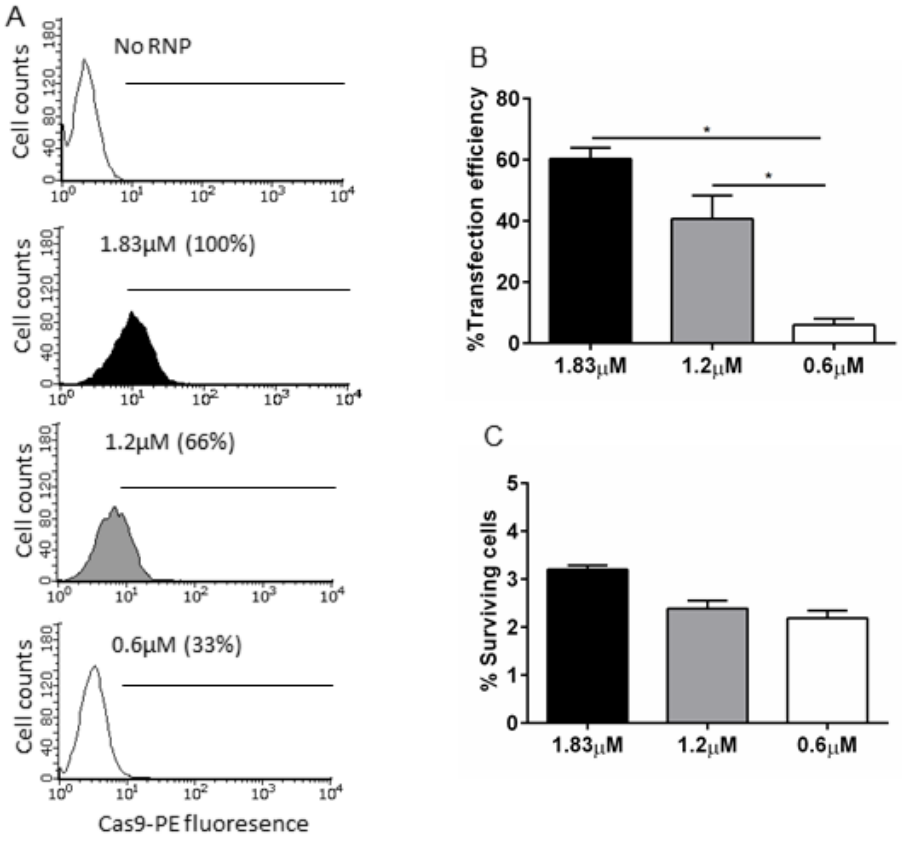

Figure 3.9: Effect of varying Cas9 RNP molarity on transfection efficiency in iPS cells. (A) Representative histograms of non-electroporated cells (no RNP- negative control), compared to varying molarities of Cas9 RNP. Cells were immunostained for Cas9 4 hours after electroporation, followed by flow cytometry. X axis represents Cas9 fluorescence intensity, Y axis represents cell counts. The straight line represents the gated region for positive cells. (B) Transfection efficiency obtained by transfecting A4/4 iPSCs at 3 different Cas9 RNP molarities. (n= 2, * $p < 0.05$, One-way ANOVA, Sidak's multiple comparisons test). (C) Surviving cells as a percentage of total cells electroporated, 24 hours after electroporation with three different molarities of Cas9 RNP. Live cells were counted after Trypan blue staining (n=2). Data are represented as mean ± SEM.

In order to optimize a more precise genome editing protocol in iPSCs, other Cas9 variants were tested to ensure that the same protocols would still be effective. In addition to WT Cas9, HiFi and D10A variants were used. HiFi Cas9 is a rationally engineered variant that also reduces off-target activity while retaining the on-target activity of WT Cas9 (*Vakulskas et al., 2018*). Transfection efficiencies of the three variants were tested 4 hours after electroporation by Cas9 immunostaining and flow cytometry, and did not show any significant differences between the variants. Also, the viability of electroporated cells was not significantly different between the three variants. Notably, cells electroporated without any RNP showed similar levels of viability as RNP-transfected cells, indicating a toxic effect of the electroporation itself, as opposed to an effect of RNP delivery. This is in contrast to results obtained from plasmid transfection, where the viability was strongly reduced upon transfection of plasmid as compared to mock transfected cells (data not shown).

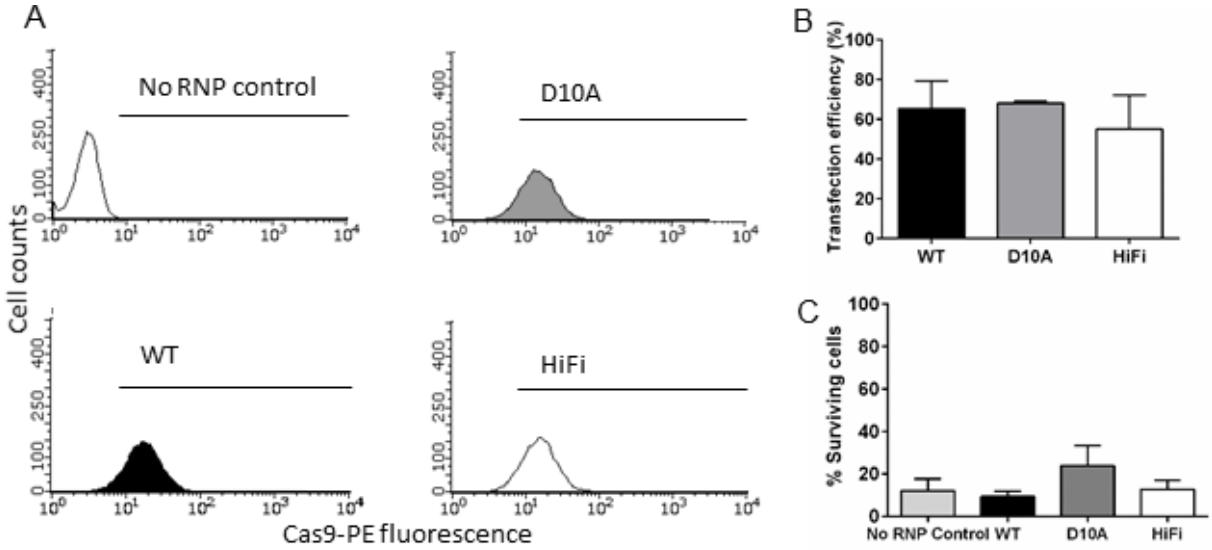

Figure 3.10: Effect of different Cas9 RNP types on transfection efficiency and survival in iPS cells.
(A) Representative histograms of non-electroporated cells (no RNP- negative control), compared to WT, HiFi and D10A Cas9 RNP. Cells were immunostained for Cas9 4 hours after electroporation, followed by flow cytometry. -axis represents Cas9 fluorescence intensity, Y axis represents cell counts. The straight line represents the gated region for positive cells. (B) Transfection efficiency obtained by transfecting A4/4 iPSCs with WT, HiFi and D10A Cas9 RNP (C) Surviving cells as a percentage of total cells electroporated, 24 hours after electroporation with WT, HiFi and D10A Cas9 RNP. Live cells were counted after Trypan blue staining. Data are represented as mean ± SEM. (n= 2, no significant difference by One-way ANOVA, Sidak's multiple comparisons test).

Besides the observed increase in transfection efficiency and viability, RNP-based approaches have the advantage that Cas9 is delivered directly as a protein and is immediately available along with

the ssODN to allow for HDR repair mechanisms of double-stranded breaks. With plasmid transfection, Cas9 must first be expressed and build up in the cell, while the ssODN concentration declines due to degradation by intracellular nucleases. Therefore, the dynamics of RNP and plasmid-derived Cas9 expression were studied in iPS cells. This was done by electroporating A4/4 iPS cells with Cas9 RNP or WT Cas9 plasmid using the conditions optimized in the previous sections, followed by lysing the cells and running the lysates on a polyacrylamide gel. The proteins were transferred onto PVDF membranes and probed for Cas9 as well as α/β tubulin for normalization (Figure 3.11A). Reflecting the lower transfection efficiencies, the Cas9 bands of the plasmid-electroporated cell lysate showed less intensity. Both RNP and plasmid-derived Cas9 decline in expression after 24 hours and in the case of plasmid electroporation, Cas9 expression starts to increase after 12 hours. Thus, regarding the duration of Cas9 availability in the context of off-target activity, these data do not hint that we should preferentially use RNP over plasmid transfection. However, not only duration but also the level of Cas9 could affect off-target activity. In order to compare Cas9 levels per cell, electroporated cells were immunostained for Cas9 followed by fluorescence microscopy. Confirming the transfection efficiency results obtained by flow cytometry, plasmid electroporation resulted in fewer but more intensely Cas9 stained cells, compared to RNP electroporated cells. (Figure 3.11C).

In summary, regarding its higher transfection efficiency and viability along with its immediate availability and lower per-cell expression level, Cas9 RNP seems to be a better approach for successful HDR and increased fidelity when aiming at genome editing in iPSCs.

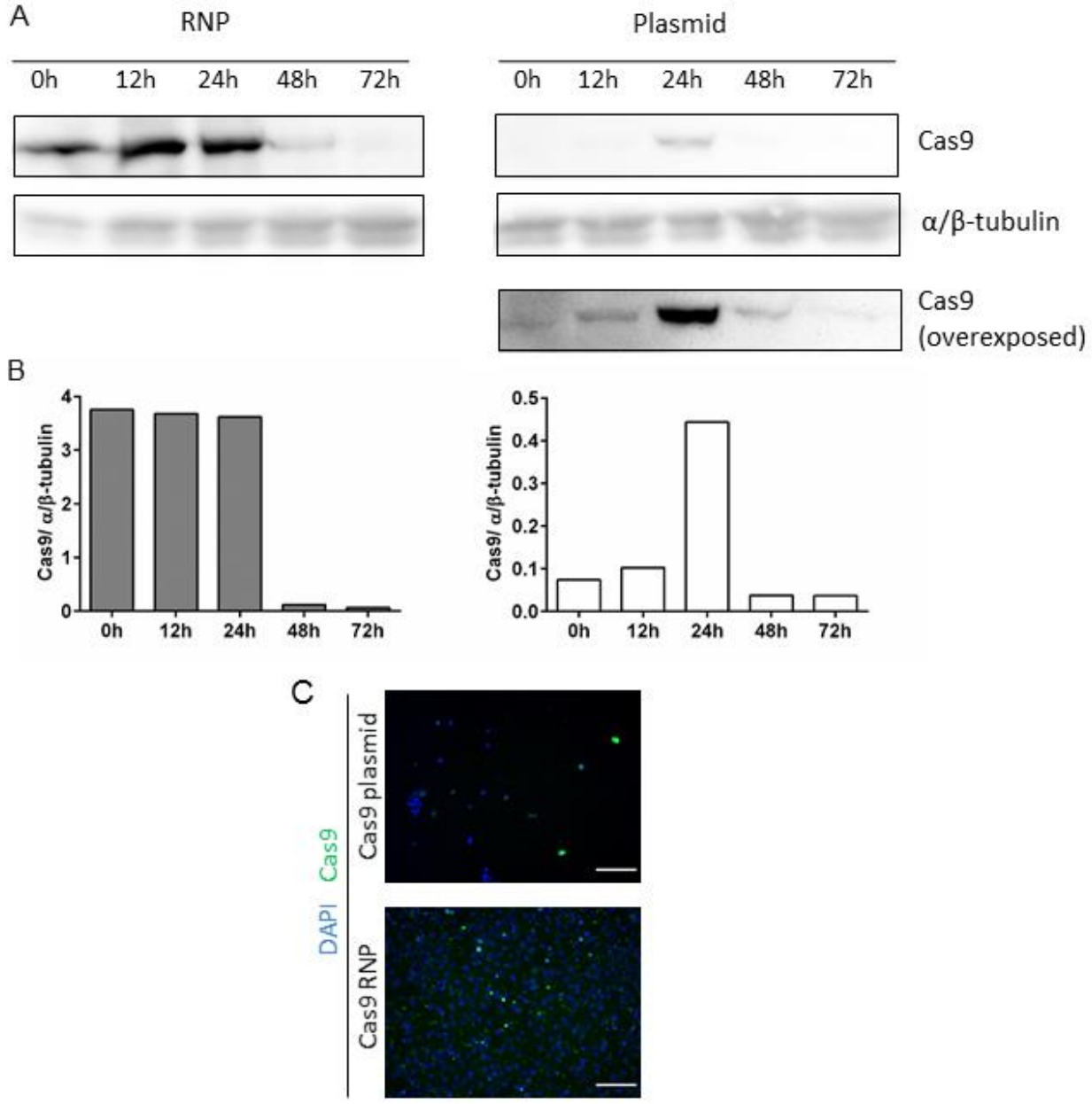

Figure 3.11: Dynamics of RNP and plasmid-derived Cas9 expression in iPSC cells. (A) Representative Western blot depicting the expression of Cas9 in A4/4 iPS cells at 0, 12, 24, 48 and 72 hours after electroporation. An overexposed panel of the plasmid Cas9 blot is also depicted, since plasmid-derived Cas9 amount on the blot was lower. (n=2) (B) Quantification of the immunoblots in (A) representing α/β-tubulin normalized Cas9 expression on the Y axis and time points on the X axis for RNP (left) and plasmid-derived (right) Cas9. (C) iPS cells were immunostained with antibody against Cas9, 24 hours after electroporation with WT Cas9 plasmids (PX458) or Cas9 RNP. Scale bar = 100 μm.

3.3.4 Generation and characterisation of isogenic A3/3 iPS cells

A4/4 iPSCs were electroporated with Cas9-crRNA-tracrRNA complexes and ssODN donor sequences as shown in Figure 3.6. For the first round of genome editing, the cells were sorted for positively transfected cells by FACS, since the tracrRNA was conjugated to ATTO550 fluorescent tag. Clones of sorted cells were obtained as detailed in Section 2.25. From the first round of electroporation and sorting, 2 heterozygous clones were obtained out of 100 clones analyzed. In the second round, one of the two A3/4 clones was electroporated with the same constructs but no sorting was performed. In both rounds, putative correctly edited clones were screened for by performing an RFLP assay from DNA isolated from each of the clones. Therefore, PCR of the *APOE* gene was carried out from genomic DNA followed by digestion with the *HhaI* restriction enzyme (*Hixson et al., 1990*). Each *APOE* allele should yield a characteristic pattern of digested bands (Figure 3.12A). *APOE3* would give rise to a 92 bp digested product, while *APOE3* would show a 72bp and a 19bp band instead. Figure 3.12B shows the bands obtained after RFLP of the parental A4/4 line and an unrelated *APOE3/3* control line, as well as examples of unmodified *APOE4/4* clone, heterozygous *APOE3/4* and homozygous *APOE3/3* clones. Once all the clones were screened by RFLP, Sanger sequencing of the potentially positive clones was performed. Representative sequencing chromatograms of the A4/4 parental line and isogenic A3/4 and A3/3 lines can be seen in Figure 3.12C, where the red asterisk represents the site of change and the black asterisk represents a silent mutation which was inserted into the ssODN to prevent recutting of the gDNA after correction. Next, potential off-target editing was studied. PCR and Sanger sequencing of the top 4 most probable off-target sites (with the highest off-target scores from Benchling off-target prediction) was performed. None of these sites were found to be modified when comparing the parental A4/4 and the isogenic A3/3 line (Figure 3.12D).

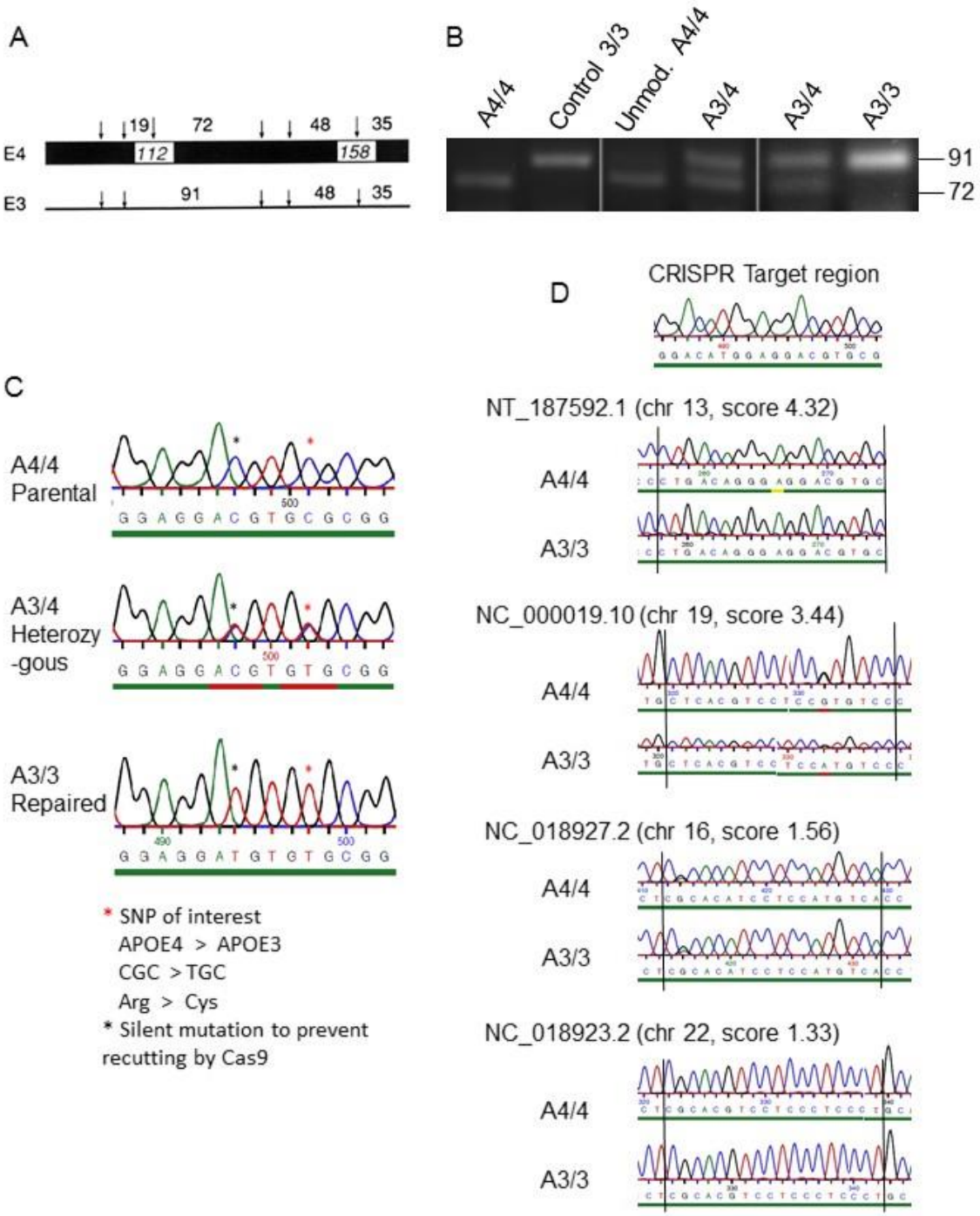

Figure 3.12: Genetic characterization of the derived isogenic iPSC clones, A3/4 and A3/3. (A) RFLP assay to differentiate *APOE3* from *APOE4* alleles: Schematic representation of the *APOE* alleles, with black arrows representing *HhaI* restriction sites (*Hixson et al., 1990*). (B) RFLP products run on an agarose gel showing the 91 and 72 bp bands (which are different between the *APOE3, APOE4* alleles). A4/4 and unrelated *APOE3/3* DNA RFLP products run as reference controls, with some example clones obtained after genome editing. (C) Sanger sequencing of the A4/4 parental and A3/4 and A3/3 isogenic lines. (D) Sequencing chromatograms of the CRISPR target regions (i.e. chosen gRNA site) along with those of the top 4 most likely off-target sites.

To ensure that the A3/3 iPSCs retain their pluripotency after genome editing, the cells were immunostained for pluripotency markers OCT4, SSEA4, SOX2 and TRA1-60, and found to be positive for them all (Figure 3.13A). Their pluripotency was also examined by testing their ability to differentiate to cells of all three germ layers. iPS cells were spontaneously differentiated in serum-containing medium and the resulting population of heterogeneous cells was stained with markers of the three layers: PAX6 (ectoderm), GATA4 (endoderm) and FOXC1 (mesoderm). Some cells of the population stained positively for each of these layers (Figure 3.13C). Since chromosomal truncations and translocations can arise due to improper repair of DSBs generated during genome editing, G-Banding analysis of the isogenic A3/3 and A4/4 iPSC lines was carried out and their karyotypes were found to be normal (46, XX) (Figure 3.13D). As an additional quality control, isogeneity of the A3/3 and A4/4 was confirmed by DNA fingerprinting analysis. PCR for primer sets of D10S1214 and D7S796 was performed to amplify genomic intervals containing variable numbers of tandem repeats. Genomic relatedness between A4/4 and A3/3 lines was ensured by the similar banding pattern obtained as compared to unrelated control lines SZ02 and DF6 (Figure 3.13B).

Taken together, these data show, that genome editing was successfully performed on the A4/4 line without compromising iPSC properties of the A3/3 edited cells.

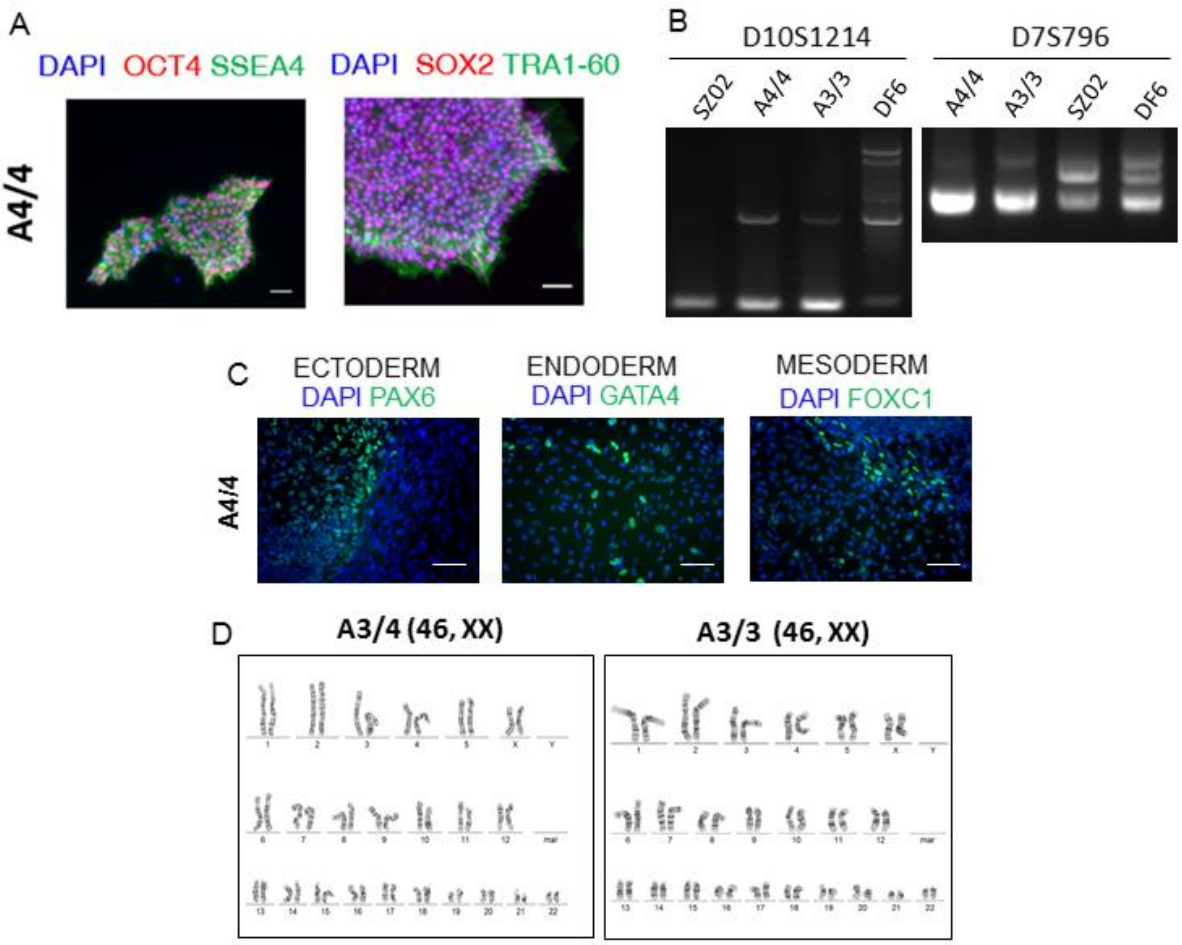

Figure 3.13: Characterisation of A3/3 (A4/4-derived isogenic) iPSC line. (A) A3/3 iPSCs were immunostained for pluripotency markers OCT4, SSEA4, SOX2 and TRA1-60. Nuclei were stained with DAPI (blue). Scale bar = 100 µm. (B) DNA fingerprinting PCR (D10S1214, D7S796) was performed for A4/4 and A3/3 iPSC DNA, showing their genetic relatedness, as opposed to two unrelated iPSC lines SZ02 and DF6. (C) Immunocytochemistry for germ layer markers PAX6 (ectoderm), GATA4 (endoderm) and FOXC1 (mesoderm) performed after spontaneously differentiating iPSCs. Nuclei were stained with DAPI (blue). Scale bar = 100 µm. (D) G-Banding analysis of the derived iPSC lines A3/4 and A3/3 showing a 46, XX karyotype. At least 20 chromosomal spreads were counted and 6 were analyzed.

3.4 Isoform-specific effects of APOE in neurons

3.4.1 Characterisation of iPSC-derived neuronal subtypes

In order to study differences in APOE4 and APOE3-carrying neurons, neural induction of A3/3, A4/4, B3/3 and B4/4 iPSCs was carried out according to the dual SMAD inhibition protocol (*Chambers et al., 2009*) as detailed in Section 2.13.8 using small molecules SB431542 and LDN193189. Cells were then grown as embryoid bodies (EBs) for 2 weeks and then plated on Matrigel coated dishes. 6 weeks after plating, the differentiated neural cultures were immunopurified using an anti-NCAM (neural cell adhesion molecule) antibody to obtain enriched neuronal cultures. Next, the neuronal cultures were characterized by immunostaining to ascertain whether the APOE isoform affected this process of *in vitro* differentiation. It was also necessary to ensure that changes in the APOE-dependent neuronal phenotypes to be studied, are not a result of any inherent differences in the differentiation process and population of neurons itself. A3/3 and A4/4 neurons were thus stained with the pan-neuronal marker MAP2 (microtubule-associated protein 2), which is found abundantly in the neuronal soma and dendrites. Other markers were quantified as a percentage of the total MAP2-positive neurons. These include deep layer cortical markers TBR1 (T-box, brain, 1) and CTIP2 (chicken ovalbumin upstream promoter transcription factor interacting protein 2) and upper layer cortical marker SATB2 (special AT-rich sequence-binding protein 2). GAD67 (glutamic acid decarboxylase 67) was used to identify GABAergic interneurons. The mostly excitatory neuronal population expressed both deep and upper layer cortical markers with a very small percentage of GABAergic cells (Figure 3.14A). Quantification of these markers showed that both A3/3 and A4/4 cells seemed to give rise to similar populations of neurons (Figure 3.14B)

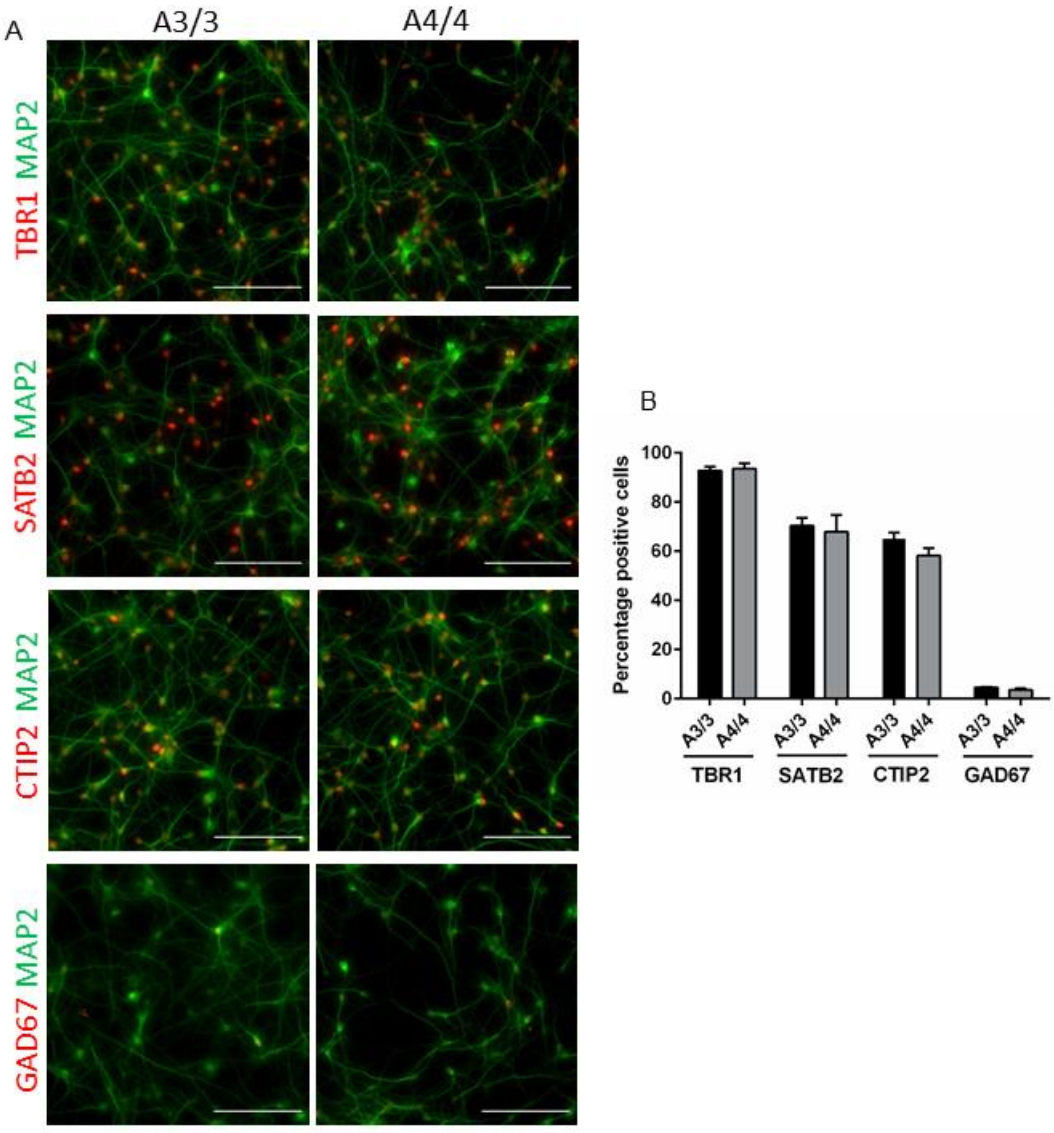

Figure 3.14: Characterisation of A4/4 and A3/3 iPSC-derived neurons. (A) Immunostaining of A3/3 and A4/4 iPSC-derived neurons for the pan neuronal marker MAP2 (green) co-stained with deep layer cortical markers TBR1 and CTIP2, upper layer cortical marker SATB2, and GABAergic interneuron marker GAD67 (red) (n=2). Scale bar = 100 µm. (B) Quantification of immunostaining reveals that both A3/3 and A4/4 iPSC lines give rise to similar populations of neurons. Data are represented as mean ± SEM. (n= 2, no significant difference by One-way ANOVA, Sidak's multiple comparisons test) Data are represented as mean ± SEM.)

3.4.2 Influence of APOE isoforms on amyloid and tau-related pathology in neurons

One of the most well-studied mechanistic hypothesis of AD is the amyloid hypothesis, which postulates that the extracellular accumulation of Aβ protein is the initiating cause of the disease. Aβ is a 37-49 amino acid peptide generated by cleavage of the transmembrane Amyloid Precursor Protein (APP) by 3 enzymes (α-, β- or γ-secretases) (*Zolezzi et al., 2014*). Sequential cleavage of

APP by α-secretase followed by γ-secretase is called non-amyloidogenic processing and yields soluble end products. Here, APP is first cleaved by α-secretase to yield the extracellular sAPPα and intracellular C-terminal fragment α (CTFα). CTFα is further cleaved by γ-secretase to AICD and p3 peptide. On the other hand, the amyloidogenic pathway begins with APP cleavage by the rate-limiting enzyme β-secretase to give extracellular sAPPβ and the membrane-bound CTFβ. CTFβ is further cleaved by γ-secretase to intracellular AICD and extracellular Aβ peptide (Figure 3.15). Aβ peptide of 42 amino acids length (Aβ42) is neurotoxic (*Klein et al., 2006*) and has a tendency to form oligomers, fibrils and plaques (*Burdick et al., 1992*). It is presumed that accumulation of amyloid aggregates leads to hyperphosphorylation and misfolding of the tau protein (*Zheng et al., 2002*), which aggregate to NFT and are also neurotoxic.

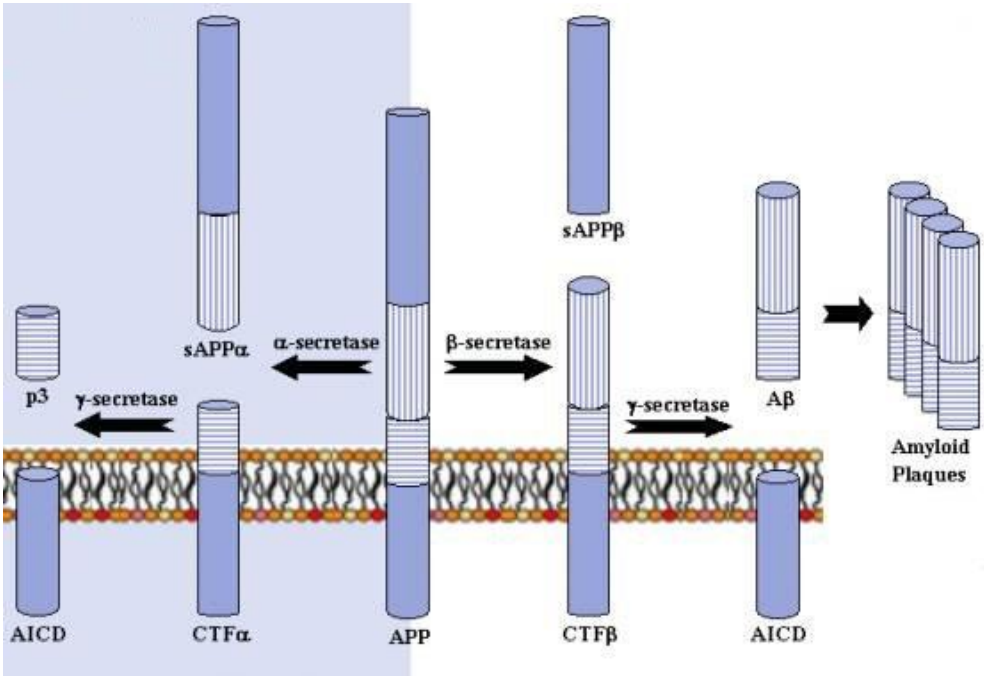

Figure 3.15: APP processing *(Adapted from www.ebi.ac.uk)*

In studying APOE isoform-specific neuronal phenotypes, the Aβ42/40 ratio was measured as it is considered one of the most important diagnostic markers to distinguish AD patients from controls. The first set of experiments were performed in non-isogenic lines. A4/4 patient (Figure 3.16A-Patient) and unrelated APOE3/3 control (Figure 3.16A- Control) neurons were either left untreated, or treated with 10μg/ml recombinant human APOE3 or APOE4 (full length APOE

produced in *E.coli*), or treated with APOE3 or APOE4 astrocyte-conditioned medium (i.e. medium in which APOE4 or APOE3 astrocytes were grown for 72 hours) containing 2ng/ml APOE. The cells were treated this way for 5 days with a media change after 2 days. Three day conditioned medium supernatant from these cells was collected, and Aβ42 and Aβ40 ELISA were performed. Untreated patient and control lines showed no difference in Aβ42/40 ratio. Treatment with recombinant APOE3 or APOE4 did not change the ratio either. However, treatment of APOE4/4 patient neurons with APOE4-containing astrocyte conditioned medium led to a significant increase in the Aβ42/40 ratio. Total levels of either Aβ42, or Aβ40 did not show any significant differences between the conditions (data not shown).

Next, Aβ2/40 ratio measurement was performed with the isogenic pairs A3/3-A4/4 and B3/3-B4/4. B3/3 and B4/4 neurons were also treated with 72 hour-conditioned medium from B3/3 and B4/4 iPSC-derived astrocytes (containing 8.7 ng/ml APOE). The neurons were treated with conditioned medium for a total of 5 days, with a media change in medium after 2 days. Aβ42 and Aβ40 ELISA were performed with 3-day old medium supernatant from these neurons. Again, the Aβ42/40 ratio did not differ significantly between the APOE4/4 and APOE3/3 carriers. However, treatment of B4/4 neurons with B4/4 astrocyte-conditioned medium resulted in a significant increase in the Aβ42/40 ratio (Figure 3.16B). Total levels of either Aβ42, or Aβ40 did not show any significant differences between the conditions (data not shown). As results are consistent in both sets of APOE3–APOE4 comparison, these data indicate that external lipidated APOE4 modulates APP processing by the γ-secretases in neurons with an *APOE4* genotype.

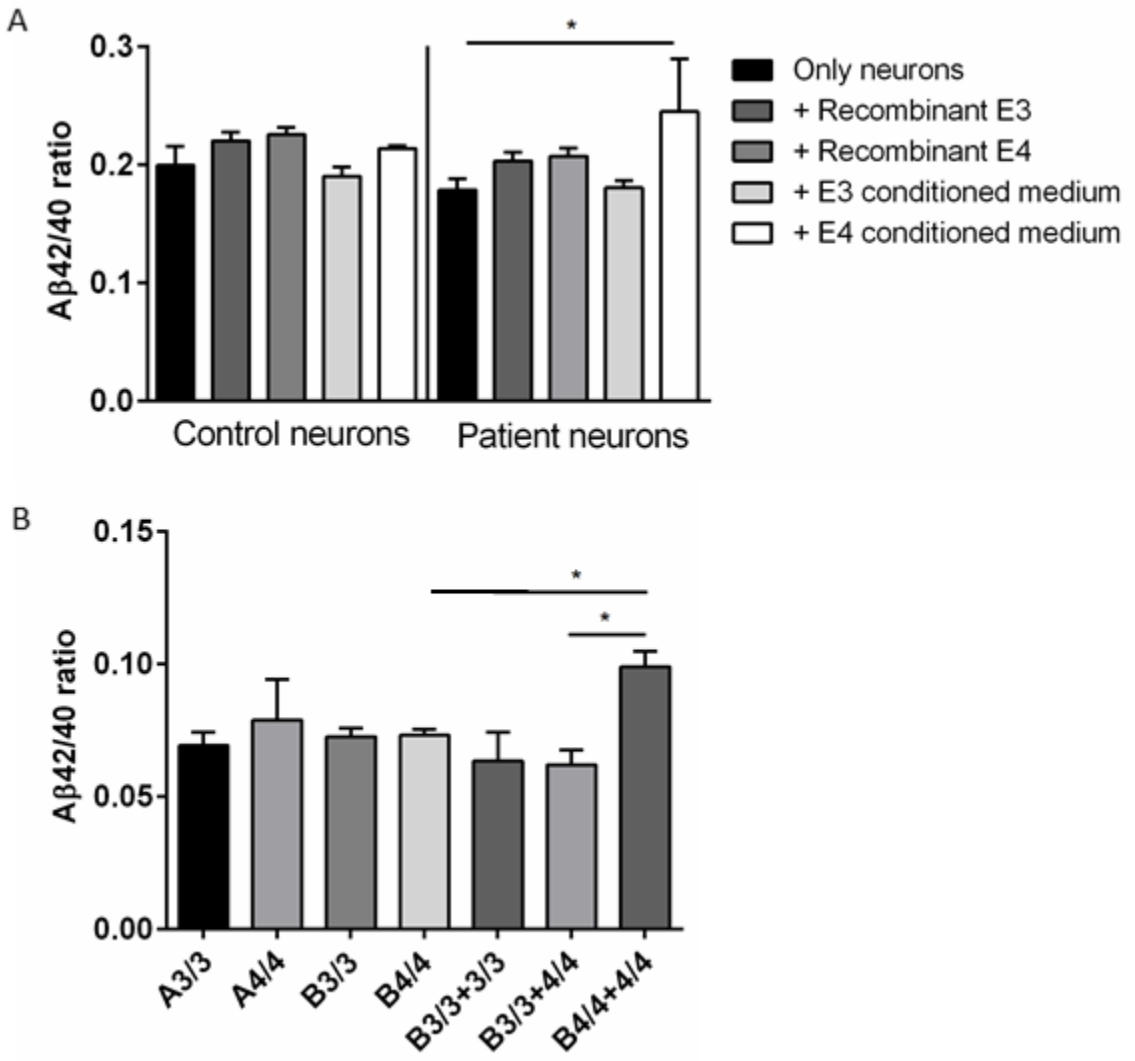

Figure 3.16: Increased Aβ42/40 ratio in APOE4 neurons treated with APOE4 containing medium. (A) Aβ42/40 ratio calculated from ELISAs of 72 hour neuron-conditioned medium of non-isogenic patient and control neurons treated with recombinant APOE3 or APOE4, or APOE3 or APOE4 astrocyte-conditioned medium for 5 days in total. (n= 2 technical replicates, * $p < 0.05$, Kruskal-Wallis test). (B) Aβ42/40 ratio calculated from ELISAs of 72 hour neuron-conditioned medium of isogenic A3/3-A4/4 neurons and B3/3-B4/4 neurons treated with B3/3 or B4/4 astrocyte-conditioned medium for 5 days in total. (n= 2 technical replicates, * $p < 0.05$, One-way ANOVA, Sidak's multiple comparisons test). Data are represented as mean ± SEM.

In addition to amyloid build up, hyperphosphorylation is another important hallmark of AD. Lysates of AraC-treated A3/3, A4/4, B3/3 and B4/4 neurons were prepared two weeks after immunopanning. Western blotting of these lysates was performed using AT8 antibody (targeting tau phosphorylated at both Ser202, Thr205) and PHF1 antibody (targeting tau phosphorylated at both Ser396 and Ser404) which target epitopes containing sites phosphorylated in the AD brain. The AT8 and PHF1 bands were normalized to housekeeping genes α/β-tubulin and GAPDH respectively. The levels of normalized phosphorylated tau (p-tau) was not significantly different between neurons of the two genotypes. However, the APOE4-carrying neurons seem to have a slight tendency of increased phosphorylation at Ser202, Thr205 (AT8) (Figure 3.17A).

Another characteristic of the AD brain is the somatodendritic accumulation of tau. Neurons of the isogenic pair A3/3-A4/4 were immunostained for AT8 and PHF1 and co-stained with pan-neuronal marker MAP2. The A4/4 neurons demonstrated a tendency for greater somatodendritic localization of p-tau, and greater proportion of cells per field demonstrating this localization (Figure 3.17B).

Taken together, classical AD phenotypes were only weakly expressed in APOE4 neurons, showing no effect on amyloidogenesis in the absence of external APOE4. Regarding the fact that neurons only express negligible levels of APOE, it is notable that neurons of the AD genotype already developed first signs of tau pathology at an immature state.

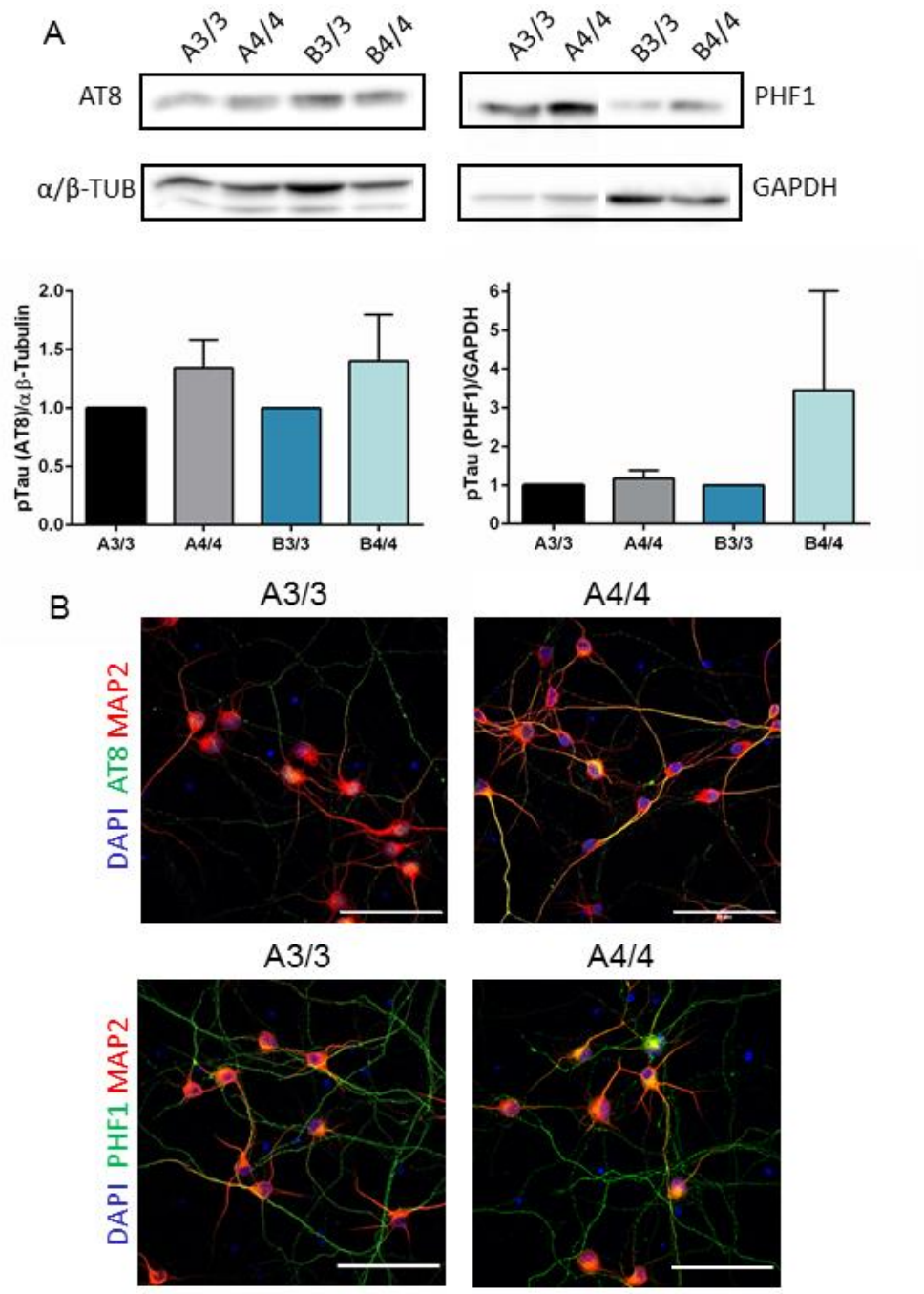

Figure 3.17: Somatodendritic mislocalization of phosphorylated tau. (A) Western blot of isogenic pairs A3/3-A4/4 and B3/3-B4/4 for AT8 (Phospho-tau Ser202, Thr205) and PHF1 and PHF1 (Phospho-tau Ser396, Ser404) normalized to α/β-Tubulin and GAPDH respectively. Quantification of the blots shows that normalized amount of phosphorylated tau (AT8 or PHF1) is not significantly elevated in A4/4 or B4/4. Data are represented as mean ± SEM. (n= 3, no significant difference by One-way ANOVA). (B) Immunostaining of A3/3 and A4/4 neurons for AT8 and PHF1 showed greater tendency for somatodendritic localization of phosphorylated tau in the APOE4 carriers. (n=1). Scale bar = 100 µm.

3.4.3 Influence of APOE isoforms on stress response in neurons

Neuronal cell death is the main pathological outcome of AD and is greatly disruptive to normal brain functioning as post-mitotic neurons are irreplaceable in the brain. Hence, we next tested the response of isogenic pairs of neurons A3/3-A4/4 and B3/3-B4/4 to the induction of oxidative stress. In order to do so, immunopanned and AraC-treated neuronal cultures were redissociated and plated onto glass coverslips at a density of 50,000 cells per 10µl drop size. Two weeks later, the set of control wells was left untreated, while another set of wells was treated for 24 hours with 50 µM hydrogen peroxide along with 5µM ferric chloride to catalyze its decomposition and thus induce the production of reactive oxygen species. The cells were then stained with Calcein Green (a cell permeant dye that marks the live cells with green fluorescence) and Ethidium Homodimer (that marks the dead cells with red fluorescence), as well as Hoechst (to stain nuclei blue-not shown) (Figure 3.18A,C). Quantification of live and dead cells revealed that the stress of redissociation and plating itself induced a significantly greater amount of cell death in A4/4 neurons compared to A3/3. B4/4 also showed an insignificant trend. Upon induction of oxidative stress, both A4/4 and B4/4 showed increased cell death compared to A3/3 and B3/3 respectively, thus suggesting isoform–specific differences in response to oxidative stress (Figure 3.18B, D).

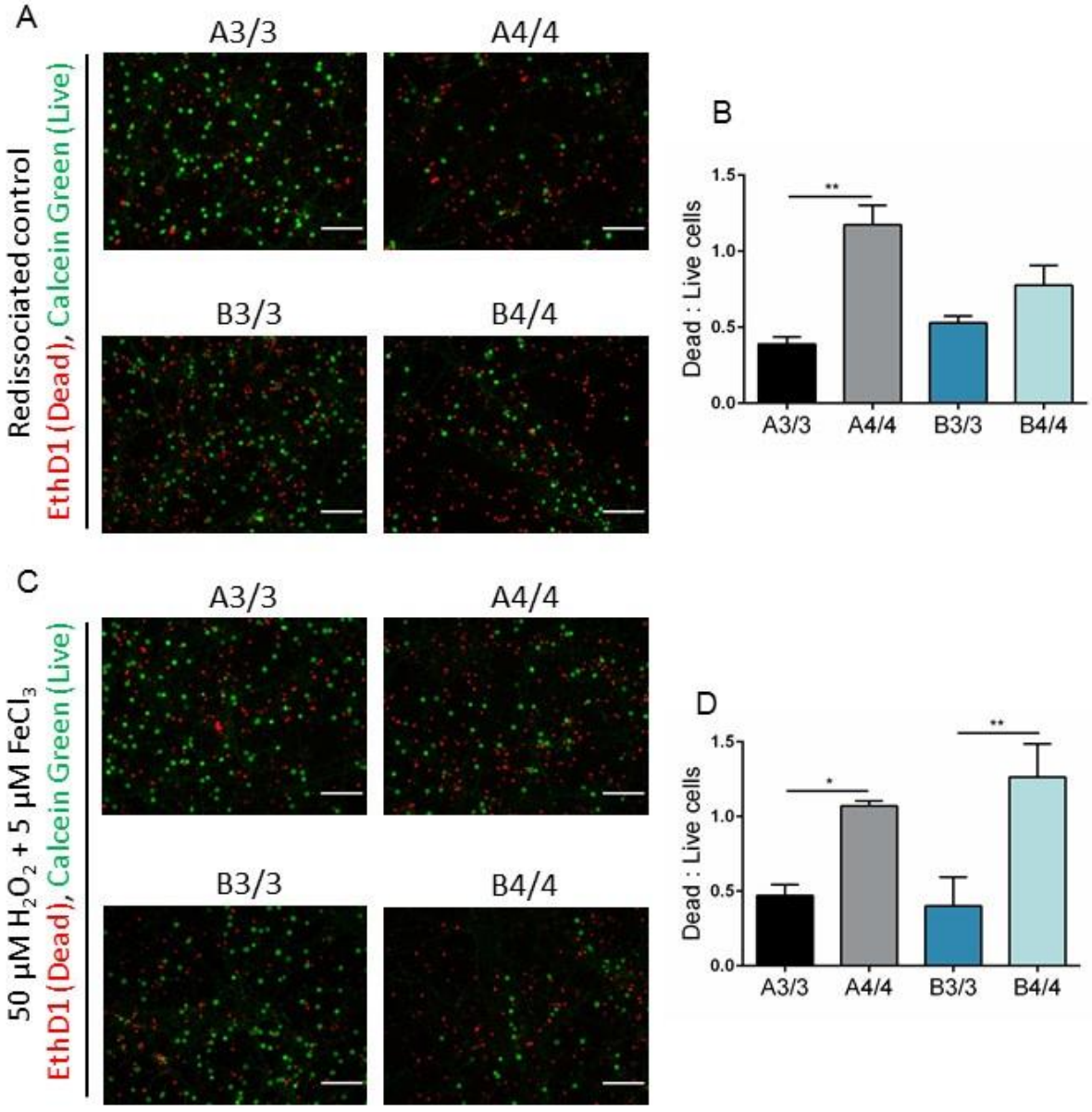

Figure 3.18: APOE isoform-specific stress response and cell death in neurons. Isogenic pairs of neurons A3/3-A4/4 and B3/3-B4/4 were redissociated and plated onto glass coverslips. (A) In the control experiment, cells were left untreated and live-dead staining of the wells was carried out using Calcein Green (to mark live cells) and EthD1 (to mark dead cells). Scale bar = 100 µm. (B) Quantification of live and dead cells reveals that the stress of redissociation resulted in increased cell death in A4/4 cells compared to A3/3. (C) Oxidative stress in neurons was induced by treatment with hydrogen peroxide and ferric chloride, followed by staining with Calcein Green and EthD1. Scale bar = 100 µm. (D) Quantification of live and dead cells shows increased cell death in A4/4 and B4/4 neurons compared to A3/3 and B3/3 neurons respectively. Data are represented as mean ± SEM. (n= 2 technical replicates, * $p < 0.05$, ** $p < 0.01$, *** $p < 0.001$, One-way ANOVA, Sidak's multiple comparisons test).

3.4.4 APOE isoform-specific effects on endosomes and lysosome sizes in neurons

Proper functioning of the endolysosomal system is very crucial to the functioning of a neuron due to its unique morphology. Dysregulation of these compartments is one of the earliest cytopathologies described in AD, specifically endosome enlargement in neurons of the AD brain (*Cataldo et al., 2000*). Several genes imparting susceptibility to AD have been associated with dysfunctions in the endolysosomal system. Significant enrichment in genes involved in endosomal and lysosomal regulation is also seen in APOE4 mice (*Nuriel et al., 2017*). Therefore, A3/3, A4/4, B3/3 and B4/4 neurons were investigated for this early phenotype in a cell autonomous manner and after treatment of B3/3 and B4/4 neurons with B3/3 and B4/4 astrocyte 72-hour conditioned medium containing 8.7 ng/ml APOE. The treatment with conditioned medium was carried out for 5 days, after which the cells were immunostained with antibodies against an endosome marker EEA1 (Early Endosome Antigen 1) and a lysosome marker LAMP2 (Lysosome Associated Membrane Protein 2) (Figure 3.19A, 3.20A). Confocal microscopy images were thresholded using the custom-written image J macro (detailed in Section 2.37) and mean area of EEA1- and LAMP2-positive particles was quantified from the masks (Figure 3.19B, 3.20B). No significant differences were observed in the endosome or lysosome sizes of untreated neurons between both genotypes. However, treatment with B4/4 astrocyte conditioned medium resulted in increased endosome and lysosome sizes in both B3/3 and B4/4 neurons. Notably, the effect was much stronger in APOE4 than APOE3 neurons. Treatment with B3/3 astrocyte conditioned medium did not significantly change the size of endosomes and lysosomes. Again, these data showed, that astrocyte-derived APOE4 is crucial for evoking AD phenotypes in neurons, however the neuronal genotype has a strong impact on effect size.

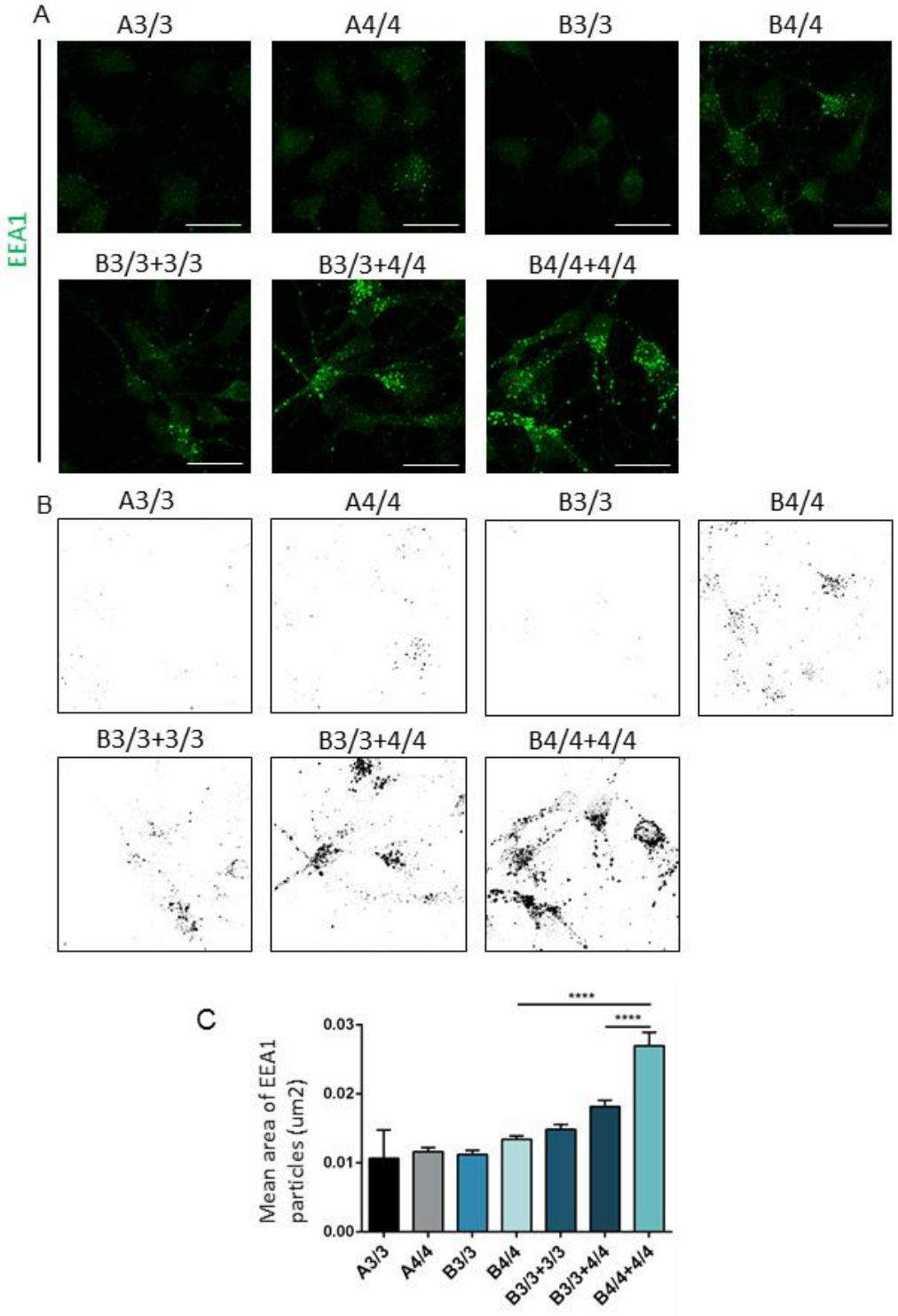

Figure 3.19: APOE isoform-specific effect on endosome size in neurons. (A) Isogenic pairs of neurons A3/3-A4/4 and B3/3-B4/4 were untreated, or treated with B3/3 (APOE3/3) or B4/4 (APOE4/4) astrocyte conditioned medium, followed by immunostaining for early endosome marker EEA1. Scale bar = 50 μm. (B) MaxEntropy threshold was applied to generate a mask in Fiji software. (C) These images were used to quantify the mean area of EEA1 positive particles. B4/4 neurons treated with B4/4 astrocyte conditioned medium showed significantly larger early EEA1-positive puncta compared to B4/4 neurons as well as B3/3 neurons treated with B4/4 astrocyte conditioned medium. Data are represented as mean ± SEM. (n= 2, **** $p < 0.0001$, One-way ANOVA, Sidak's multiple comparisons test).

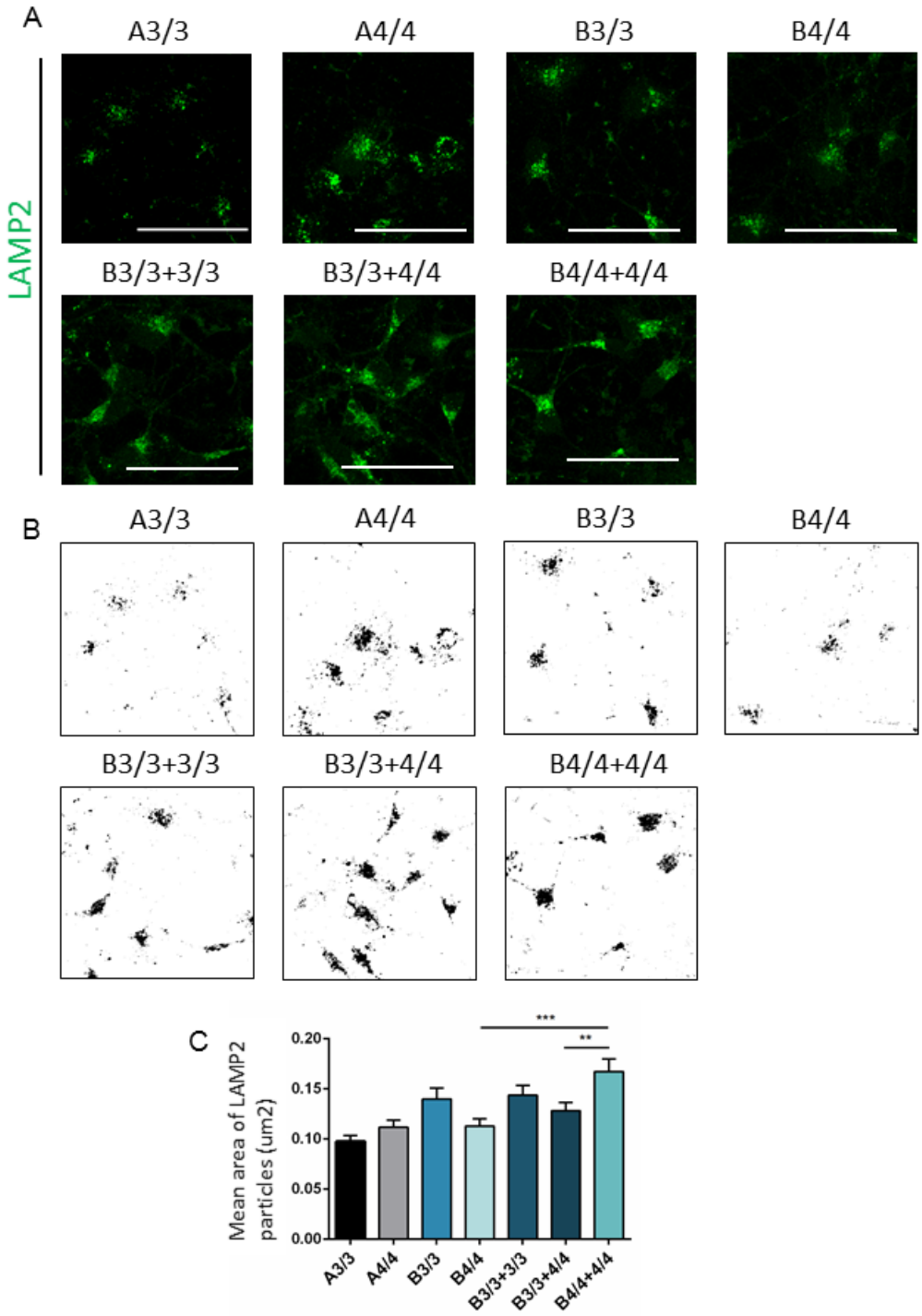

Figure 3.20: APOE isoform-specific effect on lysosome size in neurons. (A) Isogenic pairs of neurons A3/3-A4/4 and B3/3-B4/4 were untreated, or treated with B3/3 (APOE3/3) or B4/4 (APOE4/4) astrocyte conditioned medium, followed by immunostaining for lysosome marker LAMP2. Scale bar = 50 µm. (B) MaxEntropy threshold was applied to generate a mask in Fiji software. (C) These images were used to quantify the mean area of LAMP2 positive particles. B4/4 neurons treated with B4/4 astrocyte conditioned medium showed significantly larger LAMP2-positive punctae compared to B4/4 neurons as well as B3/3 neurons treated with B4/4 astrocyte conditioned medium. Data are represented as mean ± SEM. (n= 2, ** $p < 0.01$, *** $p < 0.001$, One-way ANOVA, Sidak's multiple comparisons test).

3.4.5 APOE isoform-specific effects on mitochondria and ROS in neurons

Mitochondrial dysfunction is known to be a trigger of AD pathophysiology (*Moreira et al., 2010*) and metabolic abnormalities such as impaired glucose metabolism are among the earliest observed dysfunctions in individuals at a high risk for AD (*Reiman et al., 2004*). APOE4 expression resulted in reduced mitochondrial respiratory capacity and reduced expression of mitochondrial complex I, IV and V in neuroblastoma N2A cells and transgenic mouse neurons (*Chen et al., 2011*). As a consequence of mitochondrial dysfunction, increased oxidative stress results in development of other AD hallmarks (*Nunomura et al., 2001*).

In order to study the basal levels of mitochondrial complexes, A3/3 and A4/4 neurons were lysed two weeks after immunopanning and run on a polyacrylamide gel. Western blotting was performed for the mitochondrial complexes and GAPDH as a housekeeping gene (Figure 3.21A). After GAPDH normalization, bands of A4/4 complexes were normalized to those of A3/3. Complexes II and III showed a trend of increased expression and complex IV decreased expression in A4/4 neurons (Figure 3.21B). Next, oxidative stress levels in A3/3, A4/4, B3/3 and B4/4 neurons were measured by performing MitoSOX staining for mitochondrial ROS (reactive oxygen species). Increased MitoSOX fluorescence represents increased levels of ROS. Significant differences were not observed in ROS levels between the 2 genotypes (Figure 3.21C). Similarly, TMRE staining was performed with A3/3 and A4/4 neurons to measure differences in the basal mitochondrial membrane potential. Reduced TMRE fluorescence indicates a reduced mitochondrial membrane potential. No significant differences in mitochondrial membrane potential were observed between A3/3 and A4/4 neurons (Figure 3.21D). In summary, an enhanced expression of some of the mitochondrial complex proteins was observed in APOE4 neurons. Mitochondrial integrity seemed not to be disturbed in these immature neurons of the AD genotype as indicated by membrane potential and ROS measurements.

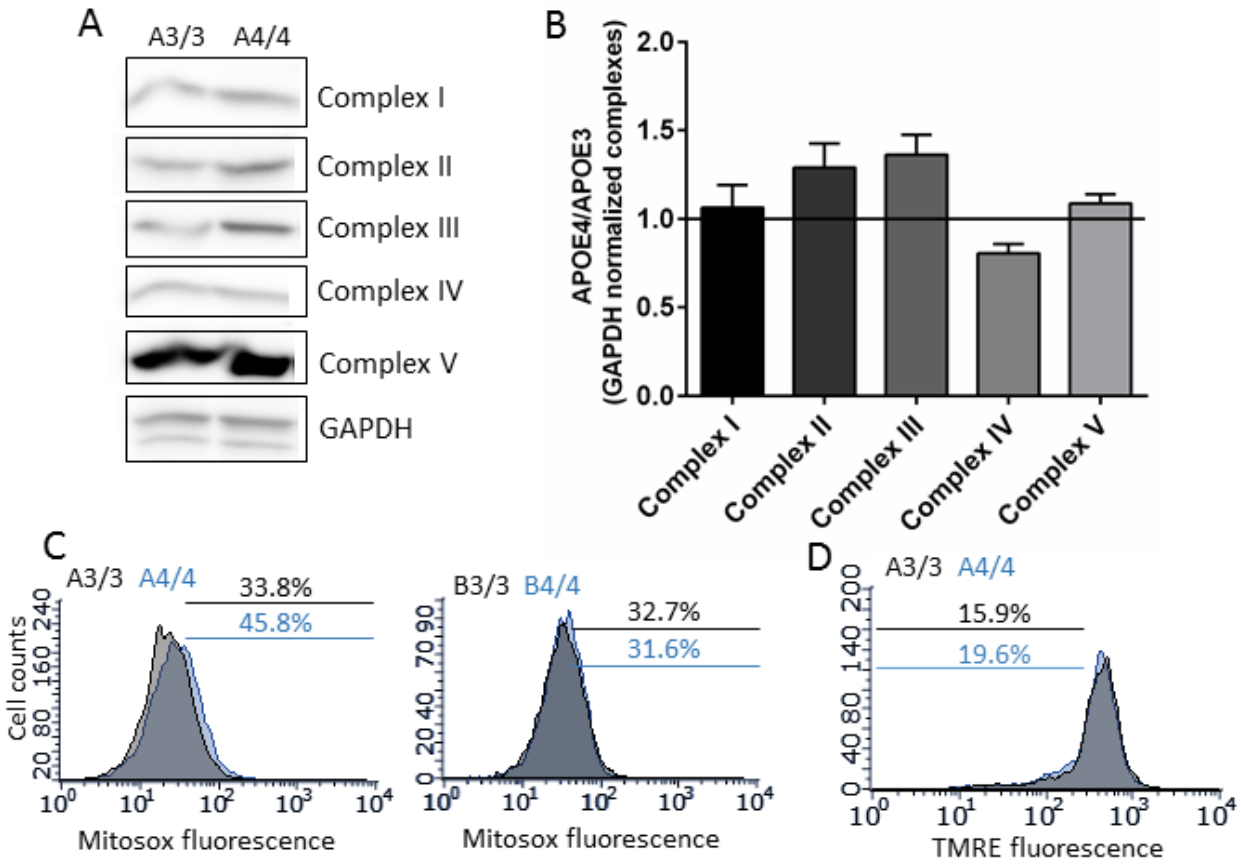

Figure 3.21: APOE isoform-specific effect on mitochondria in neurons. (A) Western blotting of mitochondrial complexes of neurons derived from isogenic lines A3/3 and A4/4, along with housekeeping gene GAPDH. (B) GAPDH normalization of bands from the Western blot followed by deriving ratio of A4/4 bands to A3/3 bands reveals that A4/4 mitochondrial complexes are not significantly different in amount compared to A3/3 (n=3, Unpaired t-test). Data are represented as mean ± SEM. (C) Histograms representing Mitosox staining for mitochondrial ROS in A3/3, A4/4, B3/3 and B4/4 neurons do not show large differences between the two genotypes. (D) Histogram representing TMRE fluorescence for mitochondrial membrane potential in A3/3 and A4/4 do not show much differences (n=2).

3.5 Isoform-specific effects of APOE in astrocytes

3.5.1 Generation of astrocytes from iPSCs and their characterization

In order to study APOE isoform-specific effects of astrocytes, isogenic iPSCs were differentiated to NSCs, then the glial switch was induced to generate astrocyte precursor cells (APCs), followed by terminal differentiation to astrocytes. A3/3, A4/4, B3/3 and B4/4 iPSC differentiation to NSCs was carried out by neural induction through dual SMAD inhibition using small molecules SB431542 and LDN193189. The differentiating cells were then briefly grown in suspension as embryoid bodies (EBs), followed by plating on Matrigel, manual picking of rosettes and then

further expansion in the presence of growth factors bFGF and EGF (Figure 3.22A). In order to confirm the identity of NSCs and ensure uniform differentiation irrespective of *APOE* genotype, the NSCs were immunostained with commonly used neural stem cell markers Nestin and SOX2, along with DAPI to mark the nuclei (Figure 3.22B). Quantification of the A3/3 and A4/4 immunostained cells revealed that nearly all the cells were Nestin and SOX2 positive, irrespective of the *APOE* genotype (Figure 3.22C). Next, growth characteristics of the NSCs were studied by plotting a growth curve for the cell lines. This was done by plating the same numbers of cells of the isogenic lines in several wells. Every alternate day, cells of a sister well were dissociated and Trypan Blue staining was performed to mark the dead cells. The live cells were counted and a growth curve was plotted (Figure 3.22D). Although NSCs from individual A differed from those of individual B, within each isogenic pair, the cell lines had very similar growth curves. The population doubling time was calculated from these growth curves, and no significant difference was observed between isogenic cells of the 2 genotypes (Figure 3.22E).

Next, NSCs were differentiated as neurospheres to astrocyte precursor cells (APCs). In mouse and human *in vivo* neural development, astrocytes are generated from NSCs and radial glia after neuronal differentiation and migration is complete. Also *in vitro*, the gliogenic switch of NSCs, turning from neurogenic to gliogenic stem cells, requires a lot of time. Therefore, astrocyte differentiation protocols tend to be of a long duration, some up to 6 to 8 months long. In this study, a relatively shorter protocol was tested: *Serio et al., 2013* induced the gliogenic switch by culture of NSCs in the presence of LIF and EGF for 3 weeks in suspension, followed by expansion in the presence of EGF and bFGF (Figure 3.23A). The identity of APCs, generated by this protocol, was tested by immunostaining for S100β (a Ca^{2+} binding protein involved in stabilizing the commitment to astrocytic differentiation) and GFAP (glial fibrillary acidic protein), along with DAPI staining for all nuclei. Expression of S100β and GFAP marks the gradual loss of NSC potential and increasing commitment towards the astrocytic lineage. Representative images from B3/3 and B4/4 lines are shown in Figure 3.23B. GFAP positive and S100β positive cells were calculated as a percentage of total DAPI-positive cells. The *Serio et al., 2013* protocol resulted in significantly greater percentage of GFAP positive cells in A3/3, A4/4 and B4/4 APCs as compared to NSCs. Similarly, the protocol resulted in a significantly greater percentage of S100β cells in B3/3 and B4/4 APCs compared to their respective NSCs. Overall expression levels of these

markers along with a highly specific, pan-astrocytic marker ALDH1L1were analyzed by Western blotting lysates of A4/4 NSCs, APCs and terminally differentiated astrocytes (Figure 3.23E). Upon quantification and GAPDH normalization, one can see that GFAP, S100β and ALDH1L1 levels are higher in astrocytes compared to NSCs and APCs. As APOE is not only considered a marker for astrocytes but is also the central protein of interest in this study, it was investigated, whether during astrocyte development, expression of APOE is starting to increase. Western blotting of early and late passage NSCs and APCs shows detectable levels of APOE only in APCs.

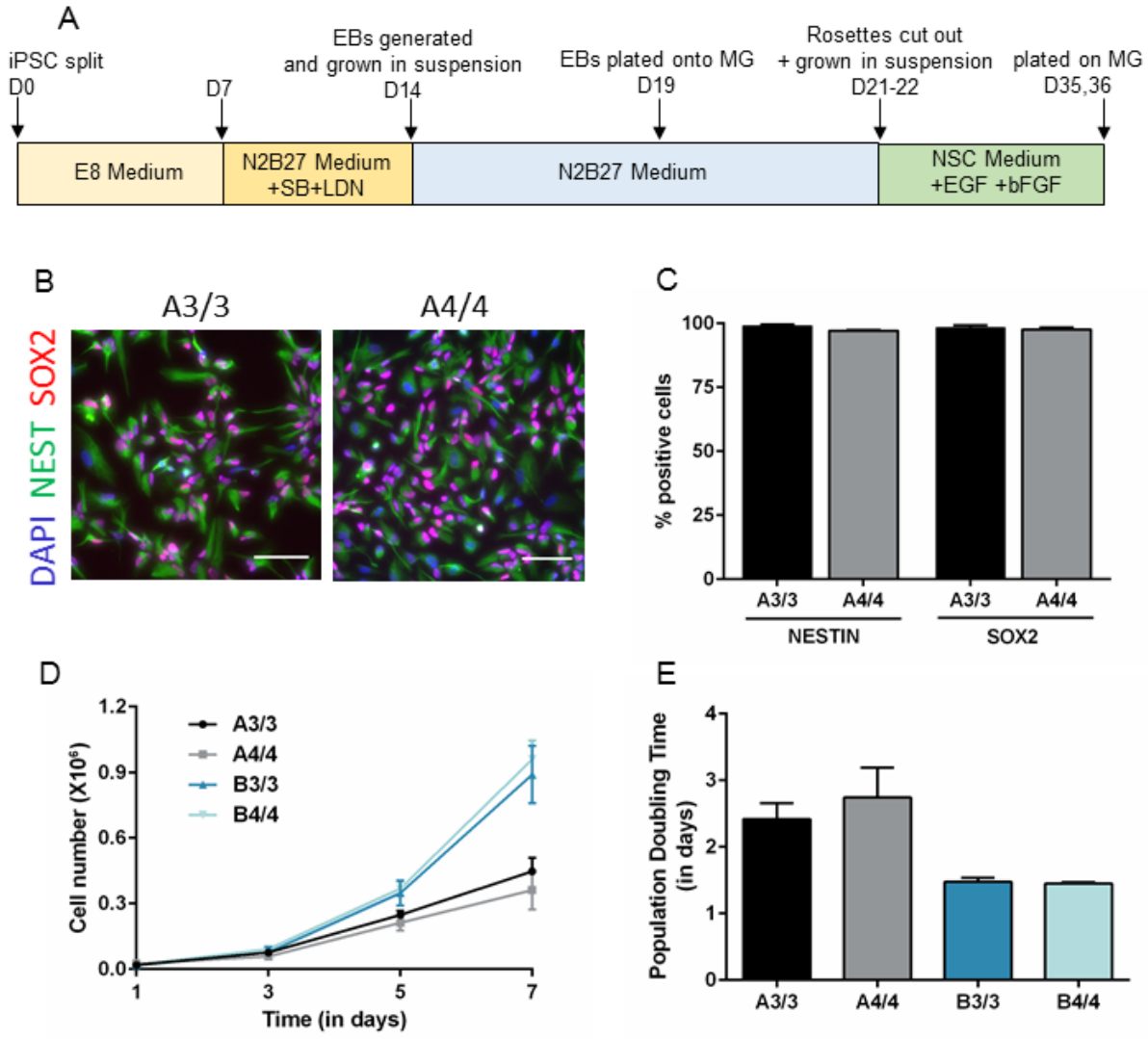

Figure 3.22: Differentiation of NSCs from iPSCs and their characterization. (A) Protocol describing the differentiation of iPSCs to neural stem cells (NSCs). (B) Immunostaining of A3/3 and A4/4 NSCs for typical NSC markers, Nestin (NEST) and SOX2. Nuclei are stained with DAPI. Scale bar = 100 µm. (C) Quantification of marker-positive cells shows that nearly all cells were NESTIN and SOX2 positive in both A3/3 and A4/4 NSCs. (D) Growth curve of A3/3, A4/4, B3/3 and B4/4 NSCs was plotted for 7 days. The growth curve within each isogenic pair looked similar. (E) Population doubling time of the NSCs calculated from the growth curved revealed no signification difference between isogenic counterparts. (n=2, unpaired t-test). Data are represented as mean ± SEM.

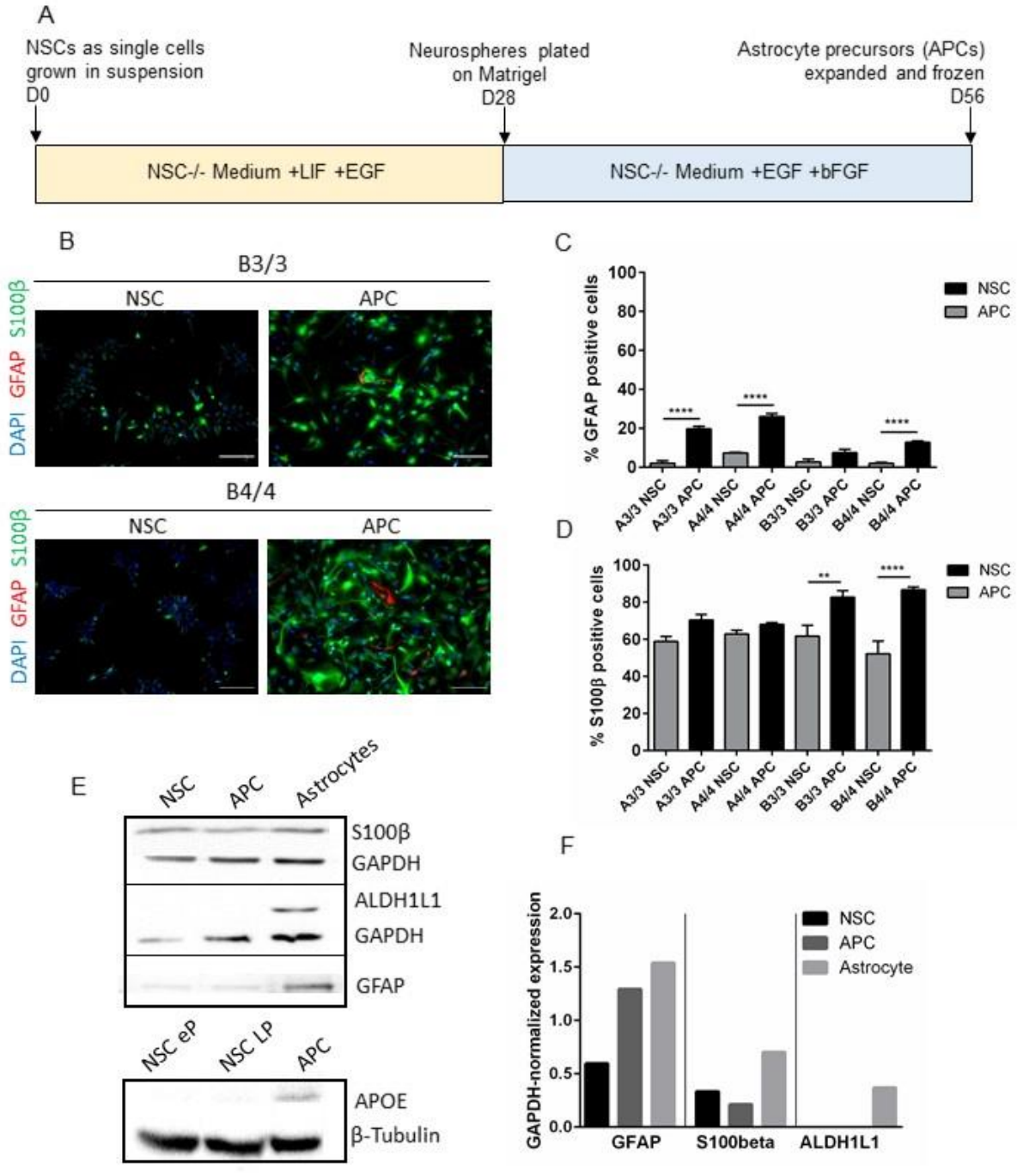

Figure 3.23: Differentiation of astrocyte precursor cells (APCs) from NSCs and their characterization. (A) Protocol describing the differentiation of NSCs to APCs. (B) Representative immunostaining of B3/3 and B4/4 NSCs and APCs for markers defining commitment to astroglial lineage, GFAP and S100β. Nuclei are stained with DAPI. Scale bar = 100 µm. Quantification of marker-positive cells shows that LIF, bFGF and EGF treatment led to significantly greater number of cells (C) expressing GFAP in A3/3, A4/4 and B4/4 APCs, and (D) significantly greater percentage of cells expressing S100β in B3/3 and B4/4 APCs. (n= 3, ** $p < 0.01$, **** $p < 0.0001$, One-way ANOVA, Sidak's multiple comparisons test). Data are represented as mean ± SEM. (E) Western blots of A4/4 iPSC-derived NSCs, APCs, astrocytes for astroglial markers S100β, ALDH1L1, GFAP. APOE expression in APC lysates tends to be greater compared to early (EP) or late passage (LP) NSCs. (F) Quantification of Western blot bands reveals greater expression of GFAP, S100β and ALDH1L1expression in astrocytes compared to NSCs or APCs.

Next, APCs are terminally differentiated to astrocytes by growing in medium containing CNTF for 2 weeks (Figure 3.24A). The key signaling pathway is the STAT1/3 mediated activation of GFAP promoter (*Bonni et al., 1997*). In addition, CTNF is also involved in the PI3K-Akt mediated translocation of NcoR and Olig2 (repressors of astrocytic genes) from the nucleus to the cytoplasm (*Sardi et al., 2006, Setoguchi et al., 2004*). The identity of astrocytes obtained after terminal differentiation was confirmed by staining for typical astrocytic markers S100β, GFAP and GLAST (sodium-dependent glutamate aspartate transporter-a maturity marker of astrocytes involved in clearing glutamate from extracellular space). Cells were also stained with the pan-neuronal marker MAP2 (Figure 3.24B) for calculating the presence of neurons. Quantification of the immunocytochemistry markers confirmed that astrocytes of both genotypes, A3/3 and A4/4 had a similar percentage of cells expressing each of the markers (~55-70% expressing GFAP, ~70-80% expressing S100β, ~60-70% expressing GLAST). 4-8% of cells also expressed MAP2.

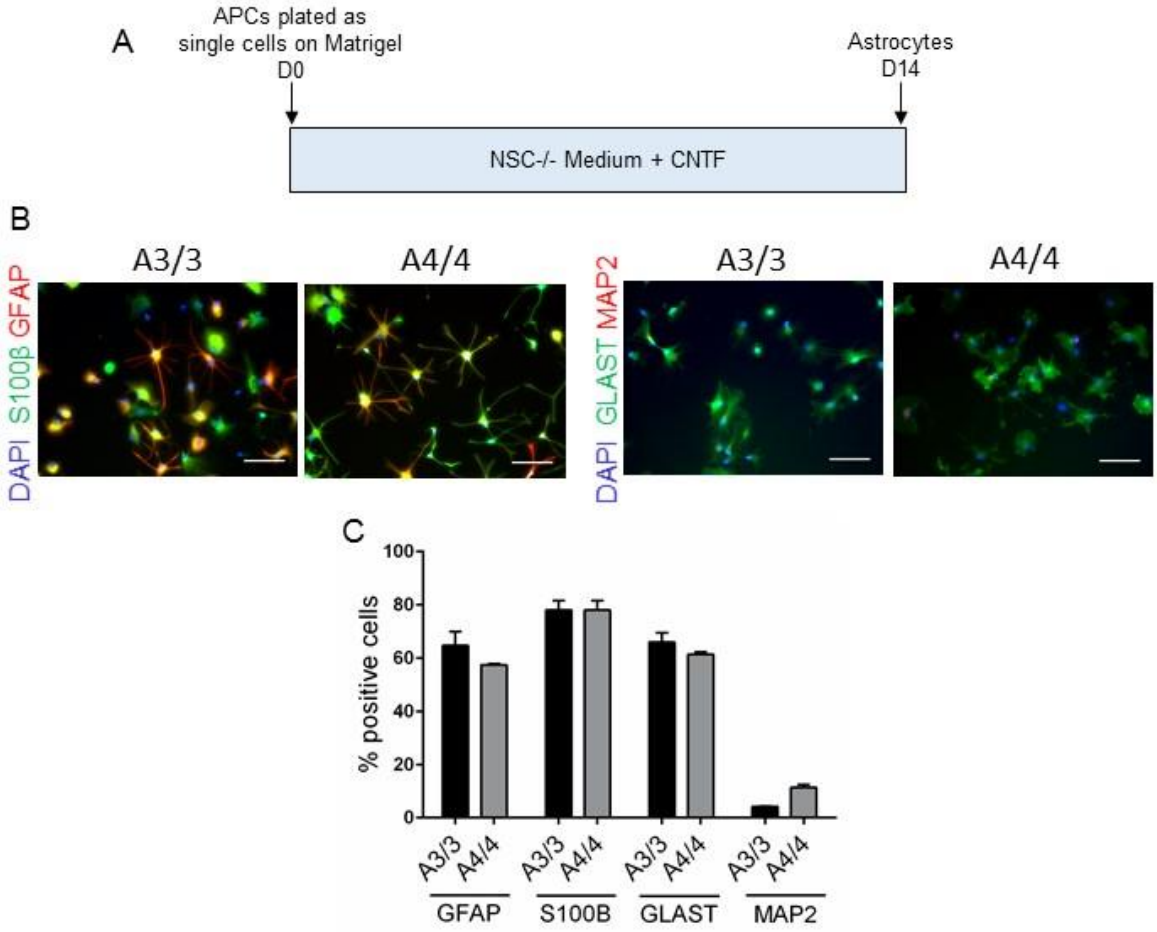

Figure 3.24: Differentiation of astrocytes from APCs and their characterization. (A) Protocol describing the differentiation of APCs to astrocytes. (B) Representative immunostaining of A3/3 and A4/4 astrocytes for typical astrocytic markers GFAP, S100β, GLAST and pan-neuronal marker MAP2. Nuclei were stained with DAPI. Scale bar = 50 µm. (C) Quantification of marker-positive cells shows that the expression of astrocytic markers is not significantly different between A3/3 and A4/4 (n= 3, One-way ANOVA, Sidak's multiple comparisons test). Data are represented as mean ± SEM.

3.5.2 Functional characterization of astrocytes

In order to ensure that astrocytes intended to use for disease modeling in this study, expressed functional properties of terminally differentiated astrocytes, several functional assays were performed. A key function of astrocytes is the clearance of glutamate from extracellular space by glutamate transporters GLAST (EAAT1) and GLT1 (EEAT2). This protects neurons from glutamate overstimulation and excitotoxicity. The glutamate taken up by the astrocytes is converted to glutamine by glutamine synthetase and is transported back to neurons to act as a precursor for GABA and glutamate. To evaluate active uptake of glutamate, a time course experiment was performed where astrocytes were incubated with buffer containing 50 µM L-

glutamate. The buffer was sampled at 30, 60 and 120 minutes and analyzed for depletion of glutamate. The astrocytes demonstrated continued glutamate uptake from 30 to 60 to 120 minutes (Figure 3.25A). Incubating astrocytes with glutamate in the presence of the glutamate transporters inhibitor- L-trans-Pyrrolidine-2,4-dicarboxylic acid (PDC, 1 mM) or using Na^+- free buffer (since glutamate transporter activity is Na^+ dependent) served as additional controls. Again, the remaining glutamate in the extracellular solution was measured, and it was found that the presence of PDC reduced the glutamate uptake ability by ~50-70%, while the absence of Na+ decreased it by ~65-70% (Figure 3.25B).

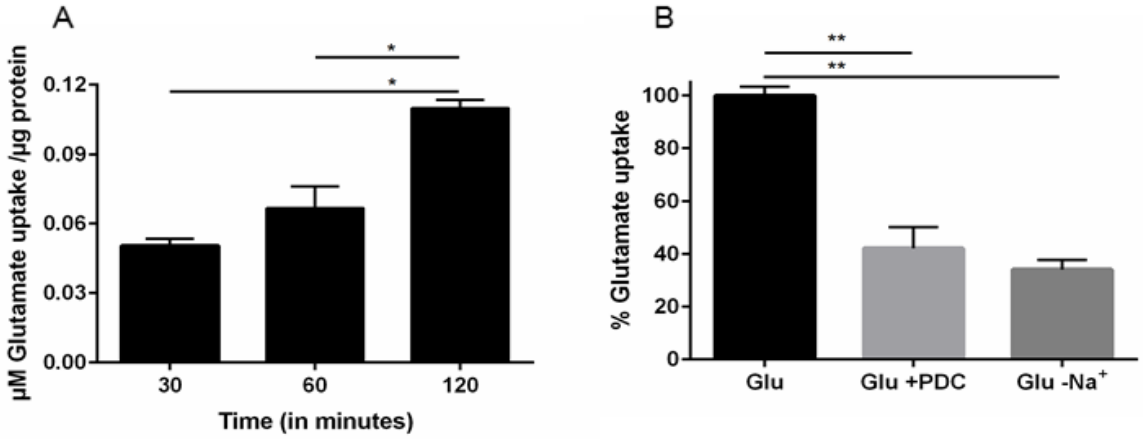

Figure 3.25: L-Glutamate uptake capacity of A4/4 astrocytes. (A) Glutamate uptake capacity of A4/4 astrocytes after incubating cells with 50 µM L-Glutamate for 30 min, 60 min and 120 min respectively, followed by lysis of cells and total protein estimation to normalize glutamate uptake to total protein in the cells. (n= 3, * $p < 0.05$, One-way ANOVA, Sidak's multiple comparisons test). (B) Glutamate uptake of A4/4 astrocytes after 120 min incubation of the cells with 50 µM L-Glutamate, and in the presence of PDC (1mM) or in the absence of Na^+(n= 3, ** $p < 0.01$, One-way ANOVA, Sidak's multiple comparisons test). Data are represented as mean ± SEM.

Intracellular calcium oscillations have been described as a mechanism by which astrocytes respond to stimuli, communicate with each other and conduct intracellular signaling (*Allaman et al., 2011*). Astrocytes have been shown to respond to the synaptic release of glutamate and ATP with increased intracellular calcium. Responsiveness of astrocytes to glutamate can also help to discriminate between a fetal and an adult stage (*Zhang et al., 2016*). Here, calcium oscillations were examined by loading A4/4 astrocytes with calcium binding dye Fluo4. After 2 minutes of time-lapse acquisition of baseline calcium signal, astrocytes were stimulated with 100 µM ATP or 100 µM glutamate and calcium signal was acquired for 4 minutes after this compound addition. Images of the acquisition can be observed in Figure 3.26A,B. Baseline-subtracted ΔF/F of the signal was plotted against time for ATP and glutamate responsiveness (Figure 3.26C, D). All the

cells showing an increase in calcium levels after compound application were counted as responsive cells. ~62-78% cells were responsive to ATP, hinting at the presence of metabotropic purinergic receptors in the astrocytes. Only ~12-26% of the astrocytes were responsive to glutamate, suggesting a differentiation to astrocytic lineage, albeit at a less mature stage (Figure 3.26E).

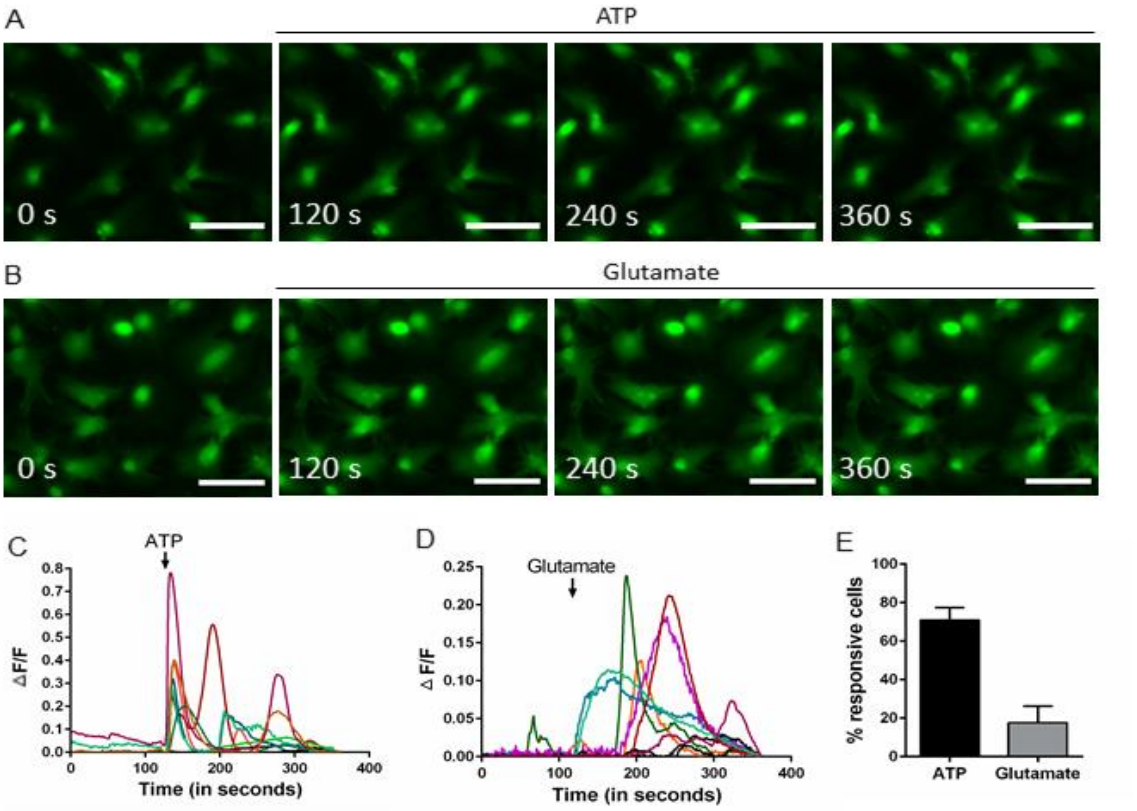

Figure 3.26: Calcium oscillation in A4/4 astrocytes. Fluo4-loaded A4/4 astrocytes at 0, 120, 240 and 360 seconds of calcium imaging. Cells were stimulated with (A) 100µM of ATP or (B) 100µM of L-Glutamate at 120 seconds. Scale bar = 50 µM. Change in fluorescence intensity over time compared to initial intensity (ΔF/F) plotted for (C) ATP and (D) Glutamate stimulation of astrocytes. (E) Comparison of percentage of total cells responsive to ATP and Glutamate (n= 2; 3 technical replicates). Data are represented as mean ± SD.

Astrocytes in response to injury, inflammation or infection, turn reactive. This includes a change in size and morphology accompanied by a secretion of inflammatory mediators like chemokines, cytokines and prostaglandins. Astrocyte-derived cytokines and chemokines can play both neurotoxic and neuroprotective roles in neurological diseases like AD. Chemokines aid in inducing the infiltration of monocytes and lymphocytes through the blood–brain barrier into the brain. Here, a 48 hour treatment of astrocytes with 50 ng/ml TNFα was used to induce gliosis, and medium was collected. Antibody-coated beads with specific fluorescence intensities were used to capture specific chemokines and then subjected to flow cytometry against a set of standards. The levels of

chemokines were compared between TFNα treated and untreated samples. The TNFα- treated astrocytes showed a significant increase in CCL5, CXCL8, CXCL9 and CXCL10, but not CCL2 levels (Figure 3.27A, B, C, D, E).

In order to confirm the relevance of these astrocytes to study APOE-related phenotypes and to prepare APOE-containing astrocyte-conditioned medium, 72-hour conditioned medium was collected from astrocytes 3, 10 and 17 days after CNTF treatment was completed. The amount of APOE in the medium was measured by ELISA and normalized to the amount of total protein in the lysate of cells from which medium was collected. This showed a trend for increased APOE secretion with time (Figure 3.28), thus being in line with the observation that APOE expression increases with astrocyte maturation (*Sloan et al., 2017*).

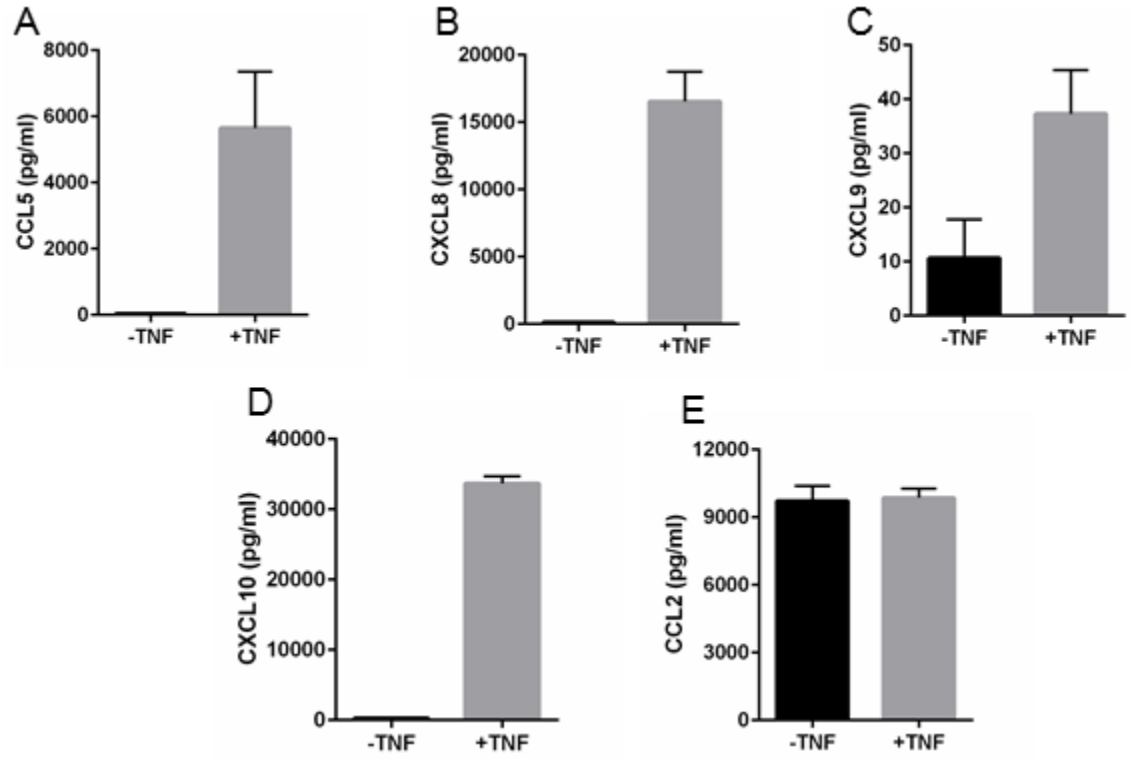

Figure 3.27: A4/4 astrocyte response to inflammatory stimuli. Treatment of astrocytes with 50 ng/ml TNFα followed by measurement of (A) CCL5, (B) CXCL8, (C) CXCL9, (D) CXCL10 and (E) CCL2 secreted by the astrocytes. (n= 3, * $p < 0.05$, ** $p < 0.01$, **** $p < 0.0001$, unpaired t-test).

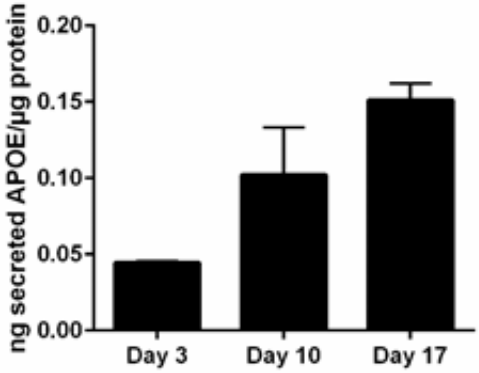

Figure 3.28: APOE expression increases with astrocyte maturation: Amount of APOE in 72-hour astrocyte conditioned medium collected at Day 3, 10 and 17 after CNTF treatment was measured by ELISA and normalized to total protein in the cell lysates. There seemed to be a trend for increasing APOE secretion with time. (n=2, * $p < 0.05$, One-way ANOVA, Sidak's multiple comparisons test). Data are represented as mean ± SEM.

3.5.3 APOE isoform-specific effects on endosomes and lysosome sizes in astrocytes

Dysregulation of the endolysosomal system is one of the earliest pathologies described in AD, with preclinical APOE4 carriers demonstrating enlarged endosomes in neurons (*Cataldo et al., 2000*). However, the cell-autonomous effects of APOE4 on the endolysosomal system of astrocytes are relatively less studied. Therefore, we first tested for endosome sizes in APCs i.e. before terminal differentiation to astrocytes. From the secreted APOE quantification of early terminally differentiated astrocytes (Figure 3.28), we can infer that cells at the astrocyte progenitor stage produce relatively little APOE. A3/3, A4/4, B3/3 and B4/4 APCs were immunostained with antibodies against an endosome marker EEA1 (Early Endosome Antigen 1) (Figure 3.29A). After images were acquired, they were thresholded (Figure 3.29B) and the mean area of EEA1-positive particles was quantified from the masks derived thereof. At this stage, no significant differences were observed in the endosome sizes of APCs of different genotypes, however, B4/4 APCs had a tendency for slightly enlarged endosomes.

When terminally differentiated astrocytes of the two isogenic pairs were similarly immunostained for endosomal marker EEA1 (Figure 3.30A) and lysosomal marker LAMP2 (Figure 3.31A), significant differences were observed in vesicle sizes. A4/4 and B4/4 astrocytes had significantly larger endosomes (Figure 3.30C) as well as lysosomes (Figure 3.31C) compared to A3/3 and B3/3

astrocytes respectively, thus demonstrating a cell-autonomous, APOE4-isoform specific effect on endosomes and lysosomes in astrocytes.

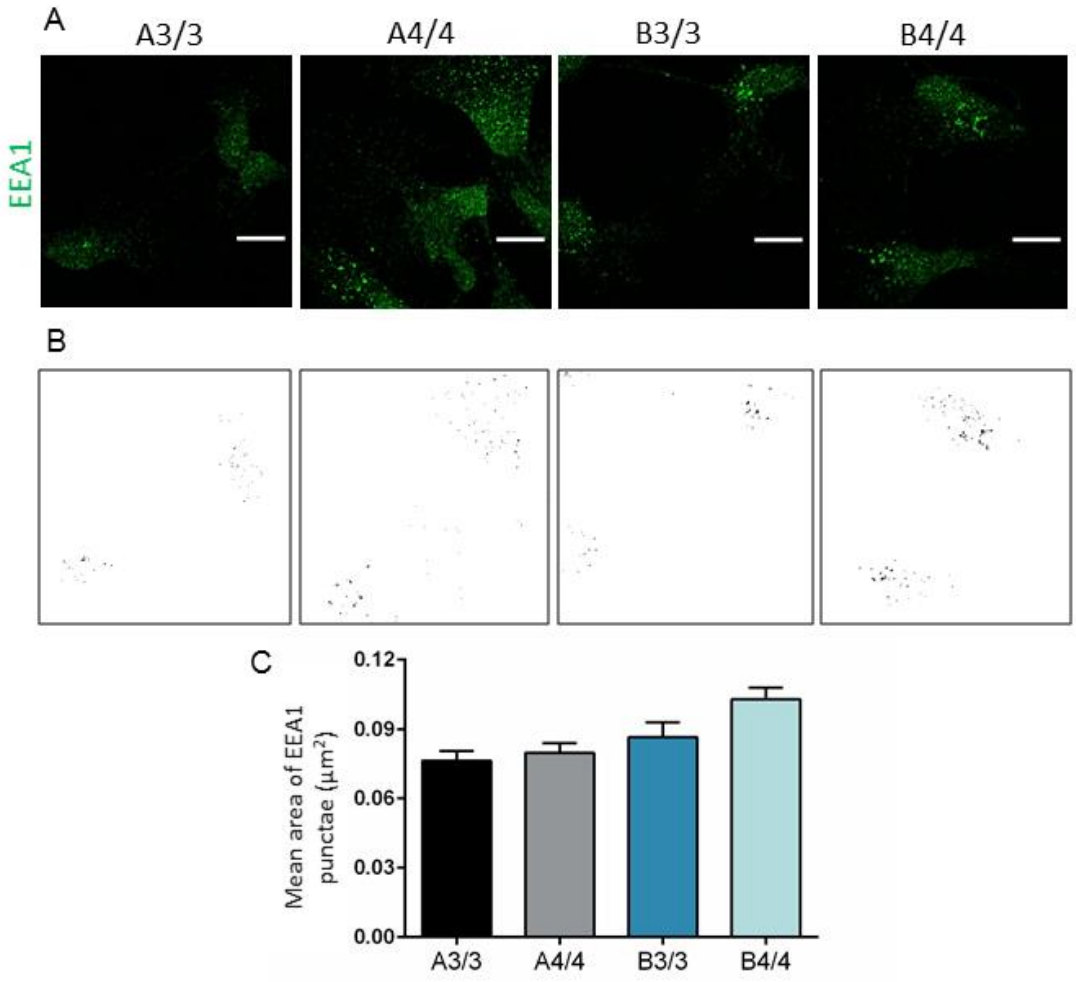

Figure 3.29: APOE isoform-specific effect on endosome size in APCs. (A) Isogenic pairs of APCs A3/3-A4/4 and B3/3-B4/4 APCs were immunostained for early endosome marker EEA1. Scale bar = 10 µm. (B) Images after applying MaxEntropy threshold using Fiji software. (C) Thresholded images were used for generating a mask to quantify the mean area of EEA1-positive particles. B4/4 APCs showed a tendency for larger EEA1-positive puncta compared to B3/3 APCs (n= 2 technical replicates, one-way ANOVA, Sidak's multiple comparisons test). Data are represented as mean ± SEM.

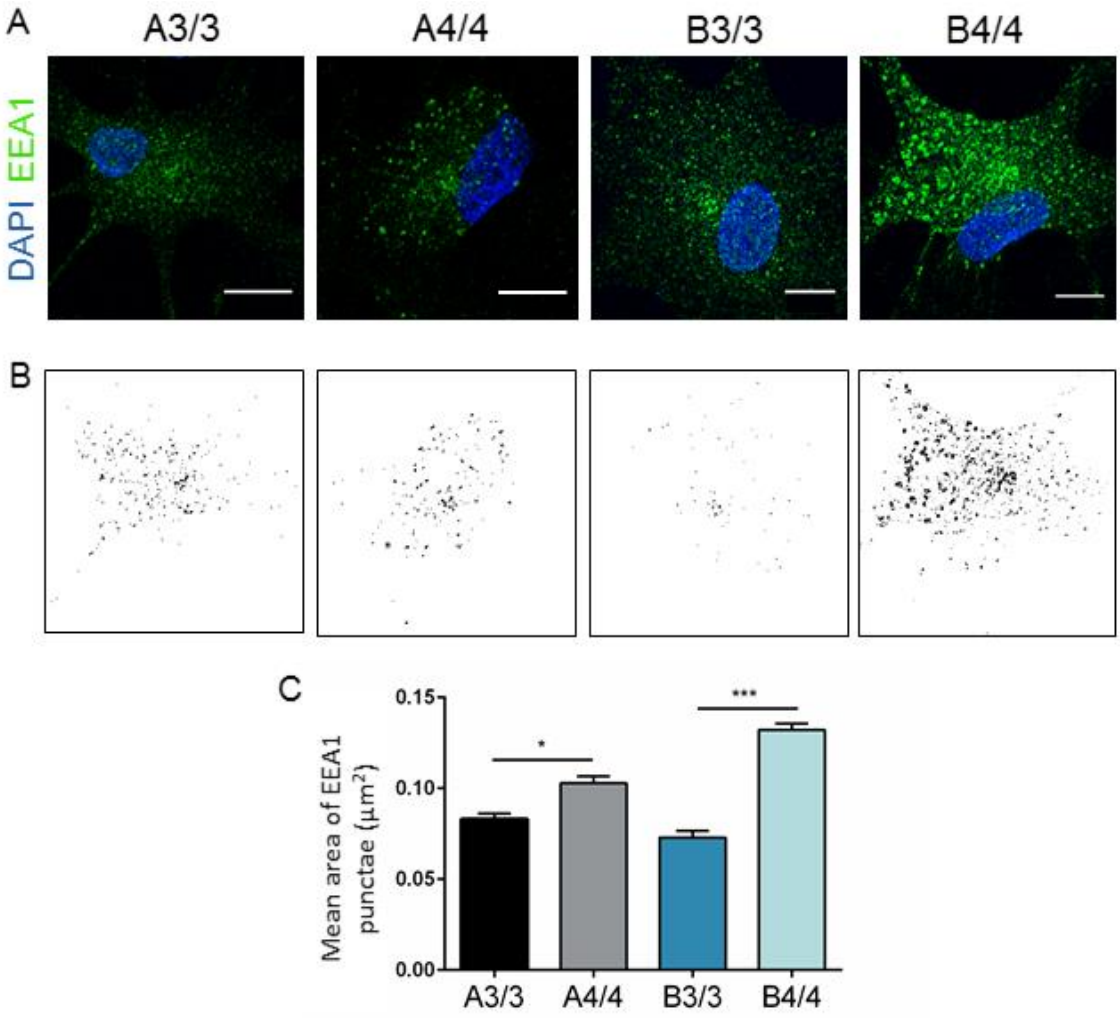

Figure 3.30: APOE isoform-specific effect on endosome size in astrocytes. (A) Isogenic pairs of astrocytes A3/3-A4/4 and B3/3-B4/4 were immunostained for early endosome marker EEA1. Scale bar = 10 µm. (B) Images after applying MaxEntropy threshold using Fiji software. (C) Thresholded images were used to generate a mask for quantifying the mean area of EEA1-positive particles. A4/4 and B4/4 astrocytes showed significantly larger EEA1-positive puncta compared to A3/3 and B3/3 astrocytes respectively (n= 3, * $p < 0.05$, *** $p < 0.001$, one-way ANOVA, Sidak's multiple comparisons test). Data are represented as mean ± SEM.

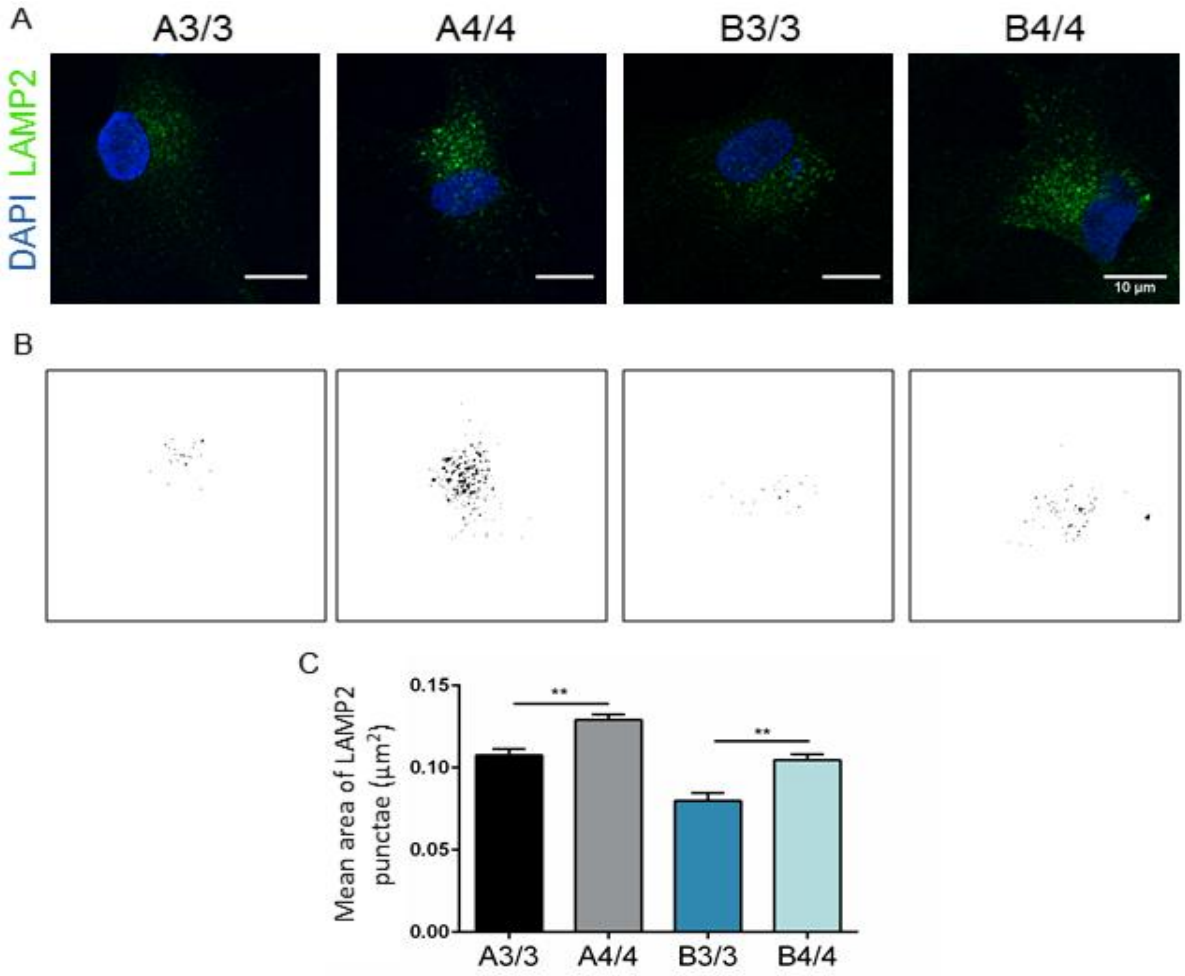

Figure 3.31: APOE isoform-specific effect on lysosome size in astrocytes. (A) Isogenic pairs of astrocytes A3/3-A4/4 and B3/3-B4/4 were immunostained for lysosome marker LAMP2. Scale bar = 10 µm. (B) Images after applying MaxEntropy threshold using Fiji software. (C) Thresholded images were used to generate a mask for quantifying the mean area of LAMP2-positive particles. A4/4 and B4/4 astrocytes showed significantly larger LAMP2-positive puncta compared to A3/3 and B3/3 astrocytes respectively (n= 2, ** $p < 0.01$, one-way ANOVA, Sidak's multiple comparisons test). Data are represented as mean ± SEM.

3.5.4 APOE isoform-specific effects on astrocytic metabolic function and mitochondria

Although the widespread effects of APOE4 on cell metabolism and related disruptions in the mitochondrial respiratory chain have been described in mouse neuronal and neuroblastoma cells (Orr et al., 2019), there is a dearth of research on the APOE4-related effects on the metabolism of the cells that produce APOE themselves, the astrocytes. Here, we performed measurements of metabolic parameters of isogenic astrocytes A3/3-A4/4 and B3/3-B4/4 to figure out the contributions of the APOE isoform. The Seahorse XF96 assay was used to measure the extracellular acidification rate (ECAR) which in a glucose-free medium represents the non-glycolytic acidification rate. Subsequent addition of glucose allows to quantify the basal glycolysis rate and addition of the ATP synthase inhibitor oligomycin was used to quantify the glycolytic capacity of astrocytes. Figure 3.32A shows ECAR plotted against time for the isogenic astrocytes. Both A4/4 and B4/4 showed a tendency for reduced basal glycolysis rates and glycolytic capacity as seen in Figure 3.32B, C. Similarly, the Seahorse XF96 assay was also used to measure the oxygen consumption rate (OCR) of astrocytes after sequential addition of oligomycin, electron transport chain uncoupling agent FCCP and complex I/III inhibitors antimycin A/rotenone (Figure 3.33A). Basal respiration is measured in glucose containing medium. Application of oligomycin allows to quantify ATP production. By subsequent applications of electron transport chain uncoupling agent FCCP and complex I/III inhibitors antimycin A/rotenone the maximal respiration rate can be quantified. Again, both A4/4 and B4/4 showed significantly reduced levels of basal respiration and ATP production compared to A3/3 and B3/3 respectively. B4/4 also showed significantly reduced maximal respiration rates and there was a tendency for reduced maximal respiration in A4/4. Thus, a clear APOE4 isoform-specific effect on energy metabolism could be observed in astrocytes.

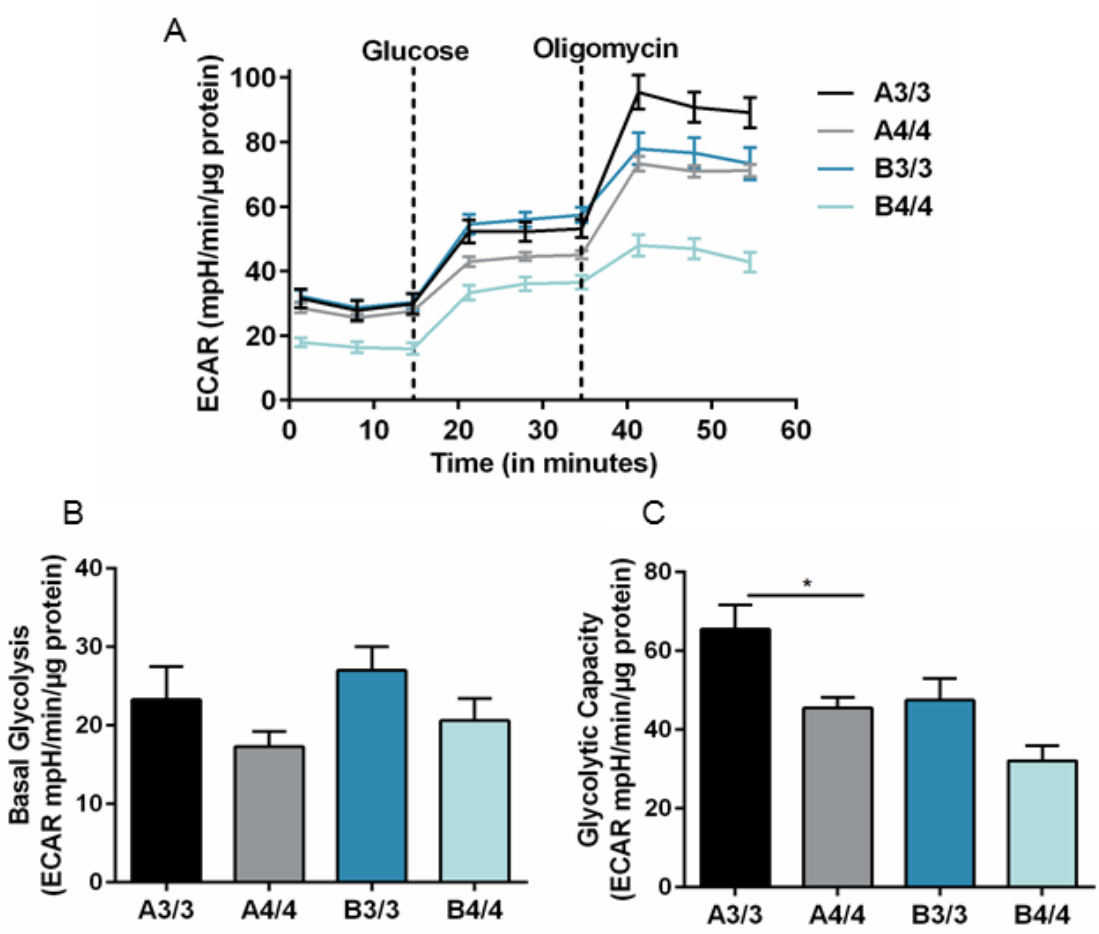

Figure 3.32: APOE isoform-specific effect on glycolysis in astrocytes. (A) Seahorse XF96 measurements were performed and ECAR (extracellular acidification rate) was assessed as a measure for glycolysis rate in A3/3, A4/4, B3/3 and B4/4 astrocytes. (B) Basal glycolysis rate had a tendency to be reduced in A4/4 and B4/4 astrocytes, whereas (C) Glycolytic capacity extrapolated from the ECAR measurements showed a significant reduction in A4/4 and a weak reduction in B4/4 astrocytes. (n=2, 12 technical replicates, * $p < 0.05$, One way ANOVA, Sidak's multiple comparisons test). Data are represented as mean ± SD.

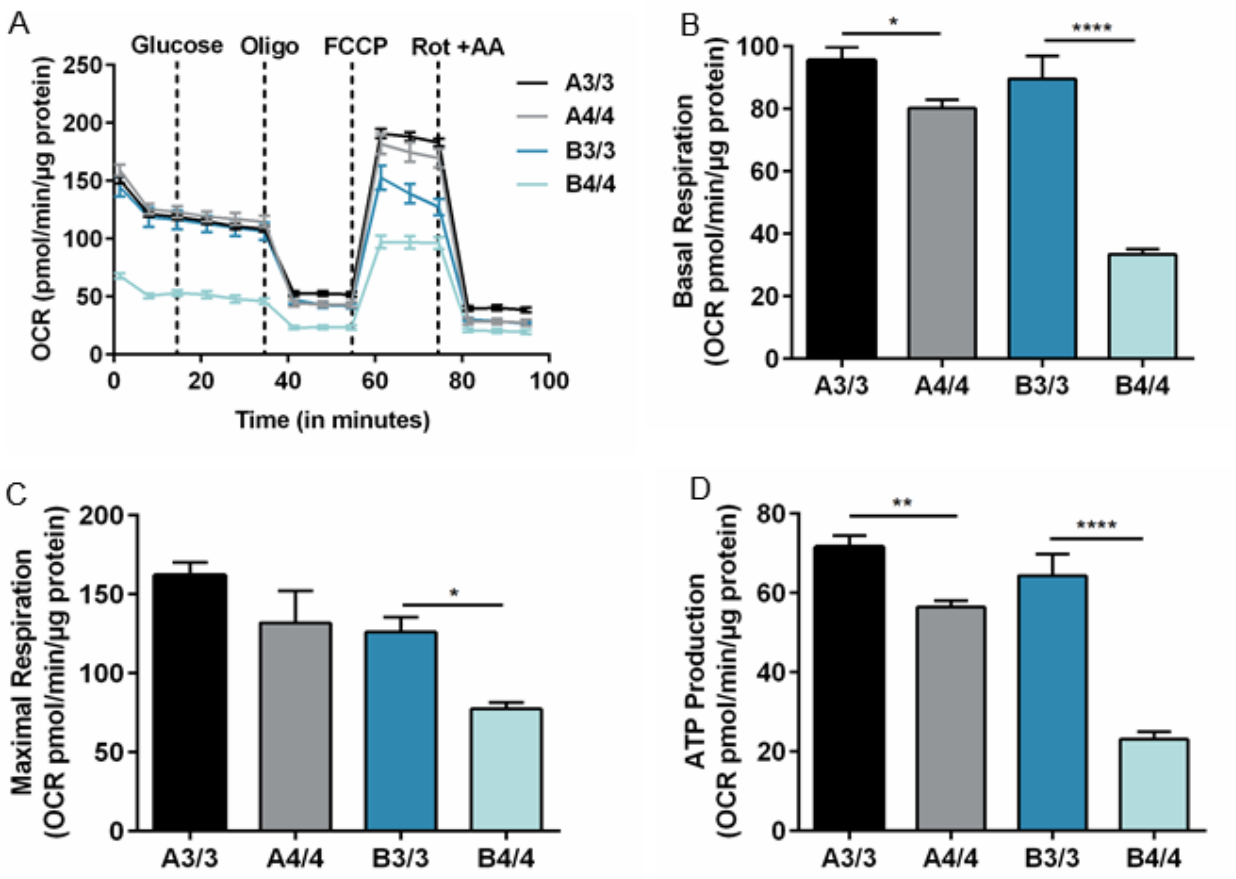

Figure 3.33: APOE isoform-specific effect on mitochondrial respiration in astrocytes. (A) Seahorse XF96 measurements were performed and OCR (oxygen consumption rate) was assessed as a measure for mitochondrial respiration in A3/3, A4/4, B3/3 and B4/4 astrocytes. (B) Basal respiration rate, (C) Maximal respiration and (D) ATP production extrapolated from the OCR measurements showed a significant reduction in A4/4 and B4/4 astrocytes. (n=2, 12 technical replicates, * $p < 0.05$, ** $p < 0.01$, **** $p < 0.0001$, One way ANOVA, Sidak's multiple comparisons). Data are represented as mean ± SD.

Since significant differences were observed in oxidative respiration and ATP production, basal levels of electron transport chain complexes were determined in terminally differentiated astrocytes from A3/3, A4/4, B3/3 and B4/4. The astrocytes were lysed and lysates were run on a polyacrylamide gel. Western blotting for mitochondrial complexes and housekeeping gene GAPDH were performed (Figure 3.34A). The bands of the different complexes were normalized to GAPDH and relative levels between different genotypes compared. Complex I (NADH dehydrogenase) and Complex III ($CoHQ_2$-cytochrome c reductase) showed a significant reduction in B4/4 astrocytes and a trend for reduction in A4/4 astrocytes compared to B3/3 and A3/3 astrocytes respectively (Figure 3.34B, D). Complex II (succinate dehydrogenase) showed a significant reduction in B4/4 and Complex IV (cytochrome c oxidase) showed a significant

reduction in A4/4 astrocytes compared to B3/3 and A3/3 astrocytes respectively (Figure 3.34C, E). Further, both A4/4 and B4/4 astrocytes showed significantly reduced levels of Complex V (ATP synthase) compared to A3/3 and B3/3 astrocytes respectively (Figure 3.34F). These protein expression data thus further support the differences seen in respiration and ATP production between the two genotypes.

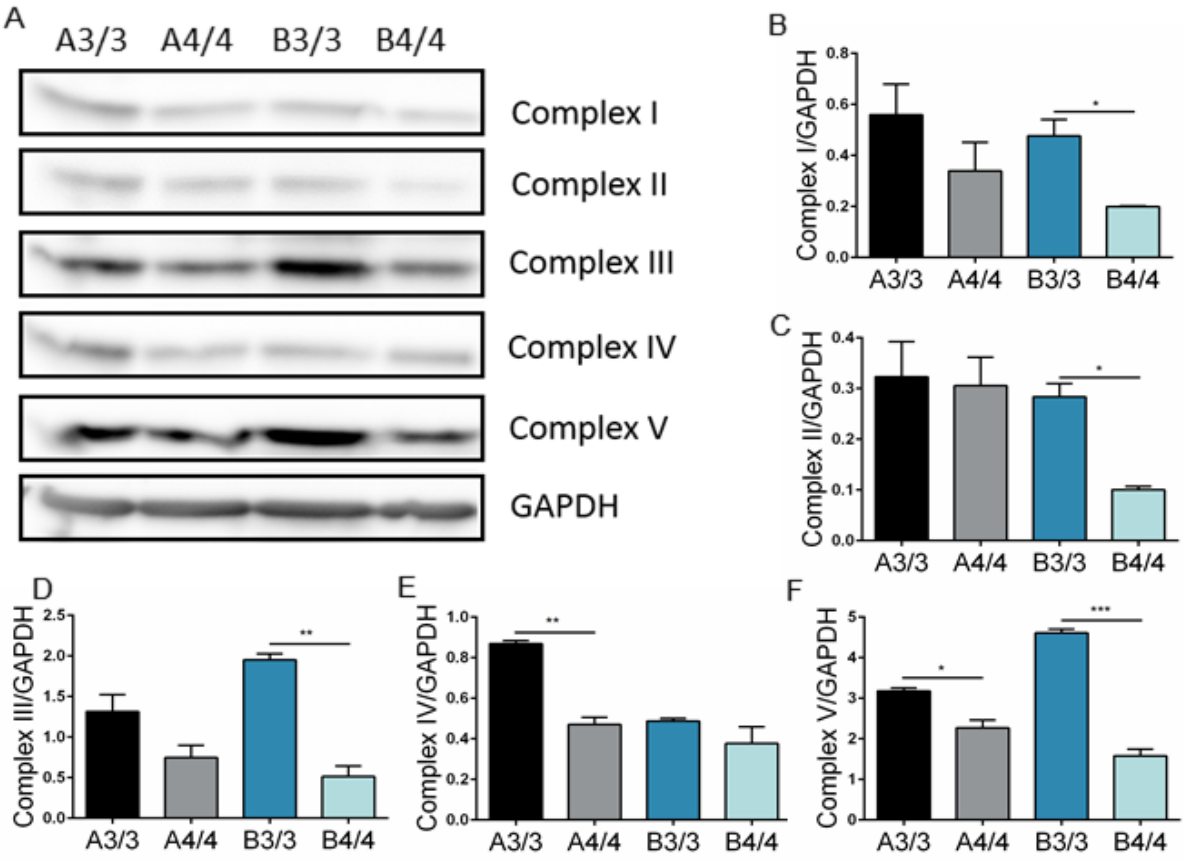

Figure 3.34: APOE isoform-specific effect on mitochondrial complexes in astrocytes. (A) Representative Western blots of mitochondrial complexes of astrocytes derived from isogenic pairs of lines A3/3-A4/4 and B3/3-B4/4, along with housekeeping gene GAPDH. GAPDH normalization of bands from the Western blot was performed for (B) Complex I, (C) Complex II, (D) Complex III, (E) Complex IV and (F) Complex V. (n=3, * $p < 0.05$, ** $p < 0.01$, *** $p < 0.001$, One way ANOVA, Sidak's multiple comparisons). Data are represented as mean ± SEM.

Complexes I and III are known to be the main sites of reactive superoxide (ROS) production by electron leakage. Due to their electron transfer mechanisms, these complexes are more prone to electron leak even under physiological conditions (Musatov and Robinson, 2012). Since both Complexes I and III were significantly reduced in B4/4 and a trend for reduced amounts was also seen in A4/4, measurement of mitochondrial reactive oxygen species (ROS) was performed. This

was done by staining mitochondrial ROS with MitoSOX dye which is a live cell-permeable fluorescent dye that localizes to the mitochondria and shows increased emission at 580 nm when oxidized by superoxides. Thus, a higher fluorescence intensity represents a higher amount of mitochondrial ROS levels. Representative histograms obtained upon flow cytometry of MitoSOX-stained A3/3, A4/4, B3/3 and B4/4 astrocytes can be seen in Figure 3.35A. The percentage of cells with increased levels of ROS is higher in A4/4 and B4/4 astrocytes. This is corroborated by the significantly higher median MitoSOX intensity of B4/4 as compared to B3/3 astrocytes (Figure 3.35B). A4/4 astrocytes show a trend for increased ROS just as they show a trend for reduced Complex I and III.

In conclusion, these data on glycolysis and mitochondrial function indicate that astrocytes of the *APOE4* genotype show severely compromised metabolic capacities already at an early developmental state, which might have drastic consequences for neurons relying on energy supply from this specific glial cell type.

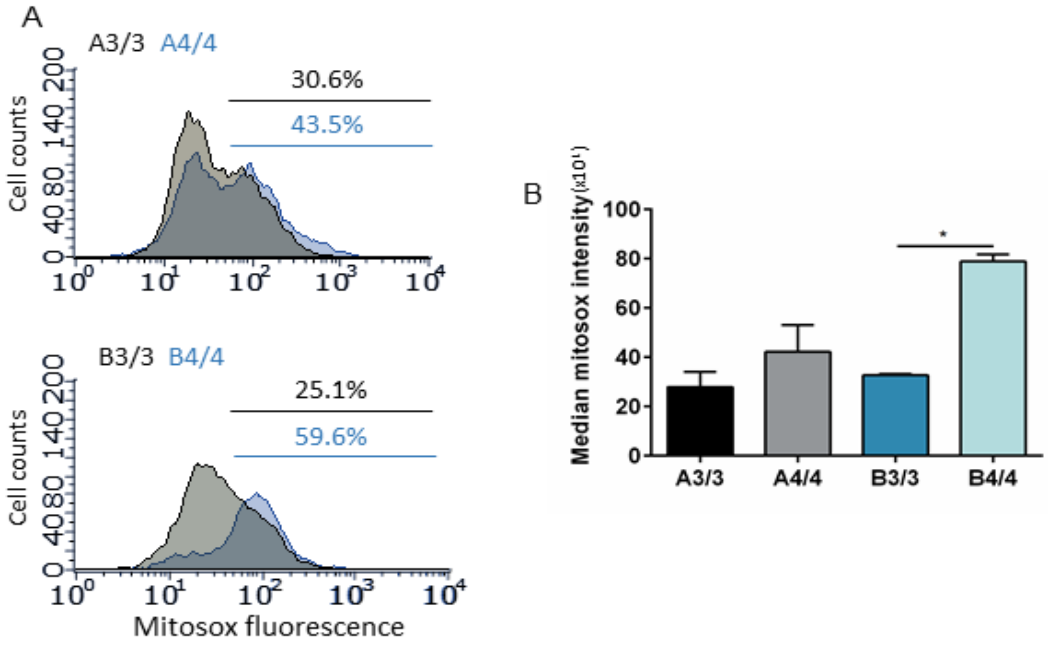

Figure 3.35: APOE isoform-specific effect on oxidative stress in astrocytes. (A) Representative histograms of MitoSox staining for mitochondrial ROS in A3/3, A4/4, B3/3 and B4/4 astrocytes show a larger percentage of cells with high mitochondrial ROS in A4/4 and B4/4 astrocytes. (B) Median fluorescence intensities (± SEM) were calculated from the flow cytometry data. It revealed a trend for higher median MitoSox intensities in A4/4 and B4/4 compared to A3/3 and B3/3 respectively. (n=3 * $p < 0.05$, One way ANOVA, Sidak's multiple comparisons).

4. Discussion

4.1 Patient-derived iPS cells as disease models

Alzheimer's Disease (AD) remains the leading ageing-related neurodegenerative disorder, and one without a cure. Current treatments for AD only deal with providing symptomatic relief. This is not due to lack of trying. One of the reasons a cure has evaded scientists for so long has been the use of non-physiological or insufficient models, both for studying the molecular basis of the disease, and for drug screening. For many years, AD-related cellular research was performed using either human or mouse non-neuronal or neuroblastoma cells. The bulk of the research however, was performed using mouse models that overexpressed human familial AD (FAD) susceptibility genes (such as *PSEN1*). This form of the disease that manifests before the age of 65, however, is rare, and seen in less than 5% of patients. The more common sporadic form of the disease (SAD) occurring commonly after the age of 65, remains underrepresented in research. Additionally, some groups have shown that SAD cases and SAD-susceptibility genes do not change the levels of Aβ40 or 42 (*Israel et al., 2012; Kondo et al., 2013*) or do not specifically alter the Aβ42/40 ratio (*Bali et al., 2012),* which serve as key markers of AD. Thus, they suggest that while symptoms and pathology in FAD and SAD cases may be similar, SAD susceptibility genes probably contribute to AD though distinct early mechanisms (*Bali et al., 2012*). Due to the aforementioned reasons, a more physiological, human neural cell-based model to study SAD susceptibility genes and their human-specific effects remains the need of the hour. Thus, the development of human iPSCs from adult somatic cells in 2007 (*Takahashi et al., 2007*) was a turning point in generating patient-specific models. This circumvents the accessibility issues of human brain tissue as well as the ethical issues of using human embryonic stem cells. iPSCs can also be propagated, banked and differentiated to practically any other cell type of the body. Some of the earliest studies to model AD using iPS cells used FAD cells or cells with mutations in FAD genes like *PSEN1* (*Yagi et al., 2011*). The recapitulation of typical AD markers served as an important proof-of concept for the utility of iPSC-based AD models.

In order to study the isoform-specific role of the susceptibility gene *APOE* in AD, the first goal of this study was to generate and characterize a bank of iPS cells from individuals with different

APOE genotypes (pathogenic *APOE4*-carrying or neutral *APOE3*-carrying homozygotes or heterozygotes) and different disease backgrounds (AD patients, or young undiagnosed 'controls'). The generation of iPSCs from somatic cells requires the expression of reprogramming pluripotency factors. The earliest reprogramming protocols used retroviruses and lentiviruses to deliver these factors, which reprogrammed the cells with 0.01-0.02% efficiency in 25-30 days (*Takahashi et al., 2007; Yu et al., 2007*). However, a key concern with using integrating viruses is the possibility of insertional mutagenesis due to the random insertion of the provirus in the human genome. There is also the issue of reactivation of the oncogenic reprogramming factor c-Myc itself, which may cause tumorigenecity. Therefore, footprint-free methods like delivering the reprogramming cocktail as mRNA or protein, were developed (*Zhou et al., 2009; Warren et al., 2010*). However, these protocols suffer from technical challenges like ensuring sufficient levels of mRNA or protein levels and require repeated transfections over 10-20 days.

Therefore, the method of choice used for this study was the transient expression of the reprogramming factors as episomal plasmids. The expression of the OSKM reprogramming factors coupled with EBNA/OriP-based plasmids ensured expression over longer periods, without integration, thus providing clinically-approved iPSCs in 22-25 days. The use of a xeno-free defined medium and feeder-free protocol (*Chen et al., 2011*) ensured a reproducible method that could also be used for translational studies. Once iPSCs were obtained and propagated to Passage 7-8, PCR was performed from their total DNA for episomal plasmid backbone elements OriP and EBNA1. The absence of these elements proved that the reprogramming process was successful in switching on the endogenous transcription factors of the cell and that pluripotent state is being maintained without exogenous factor expression.

The first step towards the goal of iPSC generation from somatic cells was the optimization of the delivery of aforementioned episomal plasmids to the somatic cells. Electroporation, which has successfully been used in several cell types, is described as the delivery of protein or nucleic acid cargo through pores in the cell membrane, formed by the rearrangement of lipids and water under the effect of an electrical field (*Shi et al., 2018*). However, achieving an efficient protocol for different cell types using the Neon electroporation device required tweaking of parameters like electrical pulse strength and duration as well as number of pulses. This is because a one-size-fits-

all approach does not work for transfecting different cell types. In the case of electroporation, differences in electroporation behavior can be attributed to cell type differences in shape, size, cytoskeleton and membrane fluidity (*Kandušer et al., 2009*).

Using electroporation protocols optimized for fibroblasts, lymphoblastoid cells and neural stem cells, iPS cells were generated. However, the efficiency of reprogramming was only about 0.01% i.e. only 1 cell per 10000 was completely reprogrammed. This low efficiency can be attributed to the stochastic nature of reprogramming, which occurs in a step-wise manner. The early phase of reprogramming which includes the suppression of somatic gene expression and mesenchymal-to-epithelial transformation is encouraged by a specific stoichiometry of OCT3/4 high expression and SOX2 low expression. The late phase and stable pluripotency, on the other hand, which includes expression of late pluripotency factors, requires a balanced 1:1:1:1 expression of the OSKM factors (*Takahashi et al., 2016*). Immunostaining of OSKM-electroporated LCLs for OCT4 and SOX2 showed various different expression states, hinting towards a large population of incompletely reprogrammed cells. HDAC inhibitor sodium butyrate was thus used to enhance reprogramming by hastening epigenetic changes associated with the reprogramming process (*Zhang et al., 2014*).

The iPSC field is still relatively new and developing and so, once the iPSC lines are generated, it is necessary to thoroughly validate their identity and pluripotency status. The gold standard for pluripotency in the past has been the teratoma assay, where putative stem cells are implanted into an immunocompromised mouse and observed for their development into a teratoma (a disorganized mass of cells comprised of cells from all three germ layers). However, there has been a recent shift towards the use of *in vitro* assays since these are easily scalable and do not involve the sacrifice of laboratory animals (*Buta et al., 2013*). All the cells lines generated had typical embryonic stem cell-like morphology (small, round with a large nucleus forming flat colonies) and were immunostained for typical nuclear (OCT4, SOX2) and surface (SSEA4, TRA1-60) pluripotency markers. Cells used for genome editing were also analyzed for their ability to differentiate into cell types of all three germ layers by allowing them to undergo spontaneous differentiation as embryoid bodies, followed by immunostaining for markers of the three germ layers. Although this method is not quantitative in demonstrating a preference for the development

of the stem cells into one or the other germ layers, it is a widely accepted method to confirm the developmental capacity of the cells being analyzed. Large scale studies of human ES and iPS cells have confirmed that the reprogramming process, to some extent, and the long term culture of human stem cells has been associated with recurrent karyotypic abnormalities. These include aneuploidy of chromosomes 12, 8, 17 and 20 (*Spiets et al., 2008; Draper et al., 2004; Taapken et al., 2011; International Stem Cell Initiative et al., 2011*). Thus, continuous monitoring of the genomic integrity of iPSC lines is important. Using a fast and inexpensive method like karyotyping, followed by chromosome counting as well as G-banding, karyotypic integrity of all the generated iPSC lines was demonstrated. Comprehensive methods like the unbiased global gene expression profiling test PluriTest (to compare with a large database of pluripotent cells) and comparative genome hybridization assay (to identify DNA microanomalies) can be considered when expanding the bank in order to distribute cells for research purposes.

4.2 A CRISPR/Cas9 approach to generating isogenic iPSCs

The use of iPSC technology has been transformative in the study of monoallelic diseases and for the past several years, disease modelling studies utilized age and sex-matched controls to compare against the cases. However, small phenotypic differences that arise while comparing cases and controls may be due to the variation in their genetic background, as opposed to only due to a difference in the SNP of interest. This problem is exacerbated when trying to model polygenic diseases like AD, where many factors affect the phenotype. So far, GWAS studies have recognized over 20 AD-associated genomic loci (*Jansen et al., 2019*). Therefore, a large number of patient and control lines is necessary to offset individual-dependent phenotype variabilities. This problem can be circumvented by generating isogenic controls by genome editing. Isogenic cell lines differ from each other at only one specific locus of study. Therefore, the second goal of this study was to generate isogenic iPSC lines from the *APOE4* homozygous A4/4 patient line using CRISPR/Cas9.

In addition to generating an *APOE3/3*-carrying isogenic control (A3/3) for the A4/4 patient line, the differentiation to neural cells and phenotypic comparison also included a pair of isogenic iPS cell lines ordered from the European Bank of Induced Pluripotent Stem Cells (EBiSC). These were generated from an 18-years old non-diseased *APOE3/4* individual from which *APOE3/3* and

APOE4/4 homozygotic lines were generated (B3/3 and B4/4 respectively) (*Schmid et al., 2019*). Genome editing tools co-opt the cell's DNA repair machinery by making double stranded breaks (DSB) in the DNA. Upon encountering a DSB, the cell can repair it by the error-prone non homologous end joining (NHEJ) pathway which leads to knockouts, or the more precise homology directed repair (HDR) which leads to precise modifications like specific substitutions, insertions or deletions in the presence of exogenous DNA that acts as the template for repair. Since *APOE3* and *APOE4* differ at a single base pair, a precise nucleotide substitution was required.

Our tool of choice for this purpose was the CRISPR/Cas9 system. It comprises of a Cas9 nuclease complexed to a CRISPR RNA (crRNA), which comprises the guide RNA or gRNA (a customizable nucleotide sequence that guides the Cas9 to the desired site of DSB generation) and a tracrRNA (which is involved in the maturation of the crRNA). The only requirement for choosing a gRNA is that its target DNA must be preceded by a PAM site (5'NGG in this case). Binding of this entire complex to the site of interest leads to a DSB. Along with this complex, a donor sequence containing the change of interest is also delivered to the cell. The donor sequence may be in the form of a plasmid, which is used for larger insertions, or in the form of a single stranded oligonucleotide donor (ssODN) which are preferred for point mutations. ssODNs are typically 100-200 bp long with at least 40 bp of homology on either side of the SNP (*Byrne et al., 2015, Ran et al., 2013*). The CRISPR/Cas9 system was used in this study since the efficiency of HDR is comparable in hiPSC when CRISPR/Cas9 or TALEN (another popular genome editing tool) are used (*Yang et al., 2013*). The advantage of using a CRISPR/Cas9 approach is that they are able to bind to and modify hypermethylated sequences while TALENs are not. However, an important point to consider while using CRISPR/Cas9 is that the gRNAs are mismatch-tolerant to some extent, which means that they bind to sequences similar to the site of interest and can create DSB and thus, knockouts at these 'off-target' sites. The probability of an off-target depends on the number and succession of mismatched nucleotides. For e.g. mismatches in high GC content gRNA sequences or at the 5' end are more likely to be tolerated (*Hsu et al., 2014; Hu et al., 2014*). Hence, it was important to choose gRNA carefully and use a protocol that maximizes HDR while minimizing off-targets in hiPSCs. While hiPSCs are cells that can retain their pluripotency and genomic integrity through the genome editing process, the intrinsic inefficiency of HDR in human pluripotent cells has made this process difficult (Zwaka & Thomson, 2003). Additionally, their

intractability to transfection, low single cell survival rates and low survival after sorting and screening, makes their precise editing inconsistent and inefficient. The efficiency of single nucleotide substitution therefore ranges anywhere from 0.2 to 8% in human PSCs (*Yang et al., 2016; Miyaoka et al., 2016*) and is often corrupted by additional indels in the corrected regions (*Inui et al., 2014*). Therefore, a protocol for transfection, genome editing and screening of hiPSCs that reliably yields relatively high levels of HDR is the need of the hour.

The intention of the study was to systematically compare the effect of different (a) Cas9 nuclease types, (b) gRNA-to-DSB distances, (c) symmetric or asymmetric ssODNs and (d) target or non-target strand ssODNs on off-target rates and precise HDR rates by using deep sequencing methods. This work is currently ongoing and so the results presented in this thesis only deal with standardizing an efficient protocol to generate the isogenic A3/3 line from the A4/4 line. The first step in the protocol was the sequencing of the *APOE* locus of the A4/4 cell line. The gRNA and ssODN were designed based on this sequence. This was done to ensure minimum divergence between the cell's *APOE* locus and the donor template since *Elliot et al., 1998* showed that greater than 2% divergence in these sequences leads to a decrease in HDR-mediated repair. The gRNA site was chosen such that the DSB would be just a single base pair away from the SNP of interest, since *Paquet et al, 2016* have shown that the shorter the DSB-SNP distance is, the greater the mutation's incorporation rate. ssODN used was 111 bp long and symmetric on both sides of the DSB. *Richardson et al., 2016* optimized an asymmetric ssODN against the non-target strand that resulted in higher HDR rates, due to early release of the non-target strand of DNA after resection by Cas9. However, our earlier Cas9 transfection of neural stem cells (NSCs) using a Cas9 plasmid and an asymmetric donor resulted in only frameshift mutations/deletions. Therefore, as recommended by *Ran et al., 2013*, we relied on symmetric ssODNs (with at least 40 bp homology on both sides of the DSB) to increase HDR rates. The Cas9 plasmid toolkit was expanded by the generation of a single multiplexing Cas9 nickase plasmid that would permit delivery of both gRNAs from the same plasmid. This plasmid would be useful when aiming for a high transfection efficiency of both gRNAs while desiring low off-target rates, when using a Cas9 nickase.

For generation of isogenic clones, however, Cas9 was delivered as a ribonucleoprotein (RNP) since degradation of the protein after delivery is quick which leads to a dramatic reduction in off-

targets (*Kim et al., 2014*). *Liang et al., 2015* confirmed up to 28-fold lower off-targets at some sites compared to Cas9 plasmid delivery. *Merkle et al., 2015* have also associated Cas9 plasmid transfection with unwanted off-targets. Regarding the HDR rate, *Kim et al., 2014* highlighted another advantage. They performed a Western blot analysis of lysates collected at different time points after Cas9 RNP or plasmid transfection. These confirmed the immediate Cas9 presence after RNP transfection and its reduction after 24 hours, allowing co-existence of Cas9 and the quickly degrading ssODN in the cell, which may lead to the demonstrated increase in precise HDR. *Kim et al., 2014* also report that RNP transfection is less stressful for human embryonic stem cells with two-fold more colonies being produced by RNP transfection compared to plasmid transfection. These results were confirmed in our study, where after testing several different electroporation conditions, we observed that while transfection efficiencies were comparable between plasmid and RNP transfection, the survival rate was much higher in RNP transfected cells. One of the RNP types used, the high fidelity 'HiFi' Cas9, was rationally engineered by introducing a point mutation R691A, to retain high on-target editing while reducing off-target activity (*Vakulskas et al., 2018*). When optimizing transfection protocols, the survival rates for plasmid transfection were found to be very low and ultimately, the 1000V condition was used since it afforded slightly better viability. Cells transfected with RNP tolerated slightly higher voltages and the 1300V condition was chosen as it afforded a fairly high level of transfection efficiency with a sufficient amount of viability. Co-transfecting with the electroporation enhancer (an IDT® proprietary single-stranded oligonucleotide) consistently showed a trend for increased transfection efficiency.

Meanwhile, in order to adapt the protocol to different needs and allow an eventual systematic comparison of off-target and on-target editing between different Cas9 types, a comparison of wild type, HiFi and D10A nickase Cas9 using the same protocol was carried. As expected, no significant differences in transfection efficiency and survival could be observed. As the manufacturer-recommended protocol for Cas9 HiFi RNP of 1.83 µM lead to low survival after transfection, we next tested Cas9 amounts at 1/3rd and 2/3rd of the recommended amount. This attempt lead to a reduction in transfection efficiency, as one might expect, but without any improvement in survival. Therefore, to improve HDR rates, we applied other modifications to the protocol that have been recommended in recent literature, starting with the design of the ssODN. Chemically modified ssODNs were used where phosphodiester bonds at both ends were replaced by phosphorothioate

bonds, which increase its intracellular exonuclease resistance and cellular half-life. *Renaud et al., 2016* reported higher knock-in rates in rodent embryos and osteosarcoma-derived U2OS cells using phosphorothioate modified ssODNs. Additionally, instead of a typical 20bp gRNA, an 18 bp long gRNA was used instead. *Fu et al., 2014* found that using 17-18 bp 'truncated' gRNAs can decrease unwanted off-target modifications by 5000-fold or more. The strength of this effect may be target-dependent however. After transfection, small molecules SCR7 and RS-1 were applied to the cells for 24 hours. SCR7 suppresses DNA Ligase IV, a key enzyme involved in the NHEJ pathway which leads to an increase in HDR by 19-fold in epithelial and melanoma cell lines (*Maruyama et al., 2015*) and by 4-5 fold in HEK cells (*Chu et al., 2015*). RS-1 is known to activate the protein RAD-51 which is involved in the search for homology during HDR as well as strand exchange (*Baumann et al., 1998*). It has been shown to improve HDR rates by 3-6 fold in human osteosarcoma cells (*Pinder et al., 2015*) and by 2-5 fold in rabbit embryos. Several studies have reported that the reason HDR is a relatively rare event, is because NHEJ takes place throughout the cell cycle, while HDR pathway is restricted to the S/G2 phase. Arresting or synchronizing cells at the G2 phase before transfection by using nocodazole, has led to a 6-fold increase in HDR in pluripotent stem cells (*Yang et al., 2016*) and a 38% increase using HEK293T cells and embryonic stem cells. However, *Kallas et al., 2011* have found that nocodazole leads to apoptosis in hESCs and may cause an irreversible loss of pluripotency marker expression.

In order to avoid these toxic effects, instead of synchronizing cells chemically, we always passaged the iPS cells at a specific density 72 hours before the intended electroporation. This ensured that the cells were in an active growth phase at the time of transfection. While this method is crude and not chemically controlled, it led to very similar populations and densities of cells every time. 24 hours after electroporation with the optimized electroporation conditions, cells were sorted using the ATT0550 dye-tagged tracrRNA to enrich for cells that received the crRNA-tracrRNA-Cas9 RNP complex. The positively sorted population was extremely high (~95%), which is not in line with the data obtained from Cas9-ICC (~60%), indicating unspecific cellular binding of the ATT0550 dye. Redissociation of cells in PBS containing 1% BSA while sorting seemed to improve the survival of iPS cells after FACS. Up to 10,000 cells were sorted into a 10 cm Matrigel-coated dish containing TESR medium + ROCK inhibitor, to increase iPSC viability. This helped to improve the single cell survival of iPSCs as compared to culturing them as single cells in wells

of a 96-well plate. The long duration of ROCK inhibitor treatment briefly changed the morphology of the iPSCs, which reverted back to normal upon ROCK inhibitor removal. Care was taken to ensure that the small single colonies did not merge and the ones that did, were marked and not included in the screening. The final step in the gene editing workflow was screening the positive clones for allele conversion to *APOE3*. Manually picked iPSC clonal colonies were first passaged onto 96-well plates and subsequently plated onto 2 24-well plates for expansion and DNA extraction. For screening, a simple RFLP-based assay was used. In the first round of transfection and screenings, 2 out of 100 clones picked were identified by restriction fragment length as *APOE3*/*APOE4* heterozygotes. This was further confirmed by Sanger sequencing, yielding a ~1% HDR hit rate. In the second round of transfections and screening, cells were redissociated for plating at clonal densities 24 hours after transfection without FACS, due to the issue of unspecific ATT0550 signals observed before. 1 clone out of the 50 picked was found and confirmed to be *APOE3/3* homozygous, again yielding a 1% rate of precise HDR modification. The similar HDR rate might be due to the high transfection rates, thus rendering the FACS step in the workflow unnecessary. The A3/3 line obtained by genome editing was characterized for its pluripotency markers, karyotype and ability for trilineage differentiation, confirming that the genome editing process did not change its pluripotency ability or chromosomal integrity. Sanger sequencing was performed for the top 5 most likely off-target sites predicted by the Benchling software, confirming that there were no modifications at these sites. Since hiPSCs are stable cells with genetically intact checkpoints, one would expect fewer off-targets to accumulate compared to what has been observed in cancer cells (Hockemeyer and Jaenisch, 2016). Confirming off-target and on-target editing efficiency using an unbiased deep sequencing approach like GuideSeq would strengthen the study. Additionally, it could help to further optimize the protocol by comparing on-target rates across different gRNA, ssODN design and Cas9 nuclease types. Testing the same protocol with other gene loci would also help to improve reliability and reproducibility of the protocol.

4.3 Differentiation and characterization of iPSC-derived neural cells

Most models of neurodegenerative diseases like AD for the past several decades have been animal models or non-neuronal cells due to inaccessibility of human brain tissue. Although these models have taught us a great deal about the mechanisms of AD, none of the treatments developed by using these models have passed clinical trials. Therefore, the reprogramming of somatic cells to

iPSCs and their subsequent differentiation to neurons came as a major breakthrough for personalized medicine and disease modelling. Now, disease mechanisms could be studied in human cell types that are affected in the disease in question. In the case of AD, hippocampal and entorhinal cortex neurons are affected in the disease, but with disease progression, the most widespread areas of damage are in the frontal and temporo-parietal cortex region. Therefore, studies attempting to model AD have done so with cortical neurons (*Kondo et al., 2013; Shi et al., 2012*) or basal forebrain cholinergic neurons (*Duan et al., 2014).* Less-defined neuronal cultures (MAP2-expressing cells) have been used by others (*Israel et al., 2012; Yagi et al., 2011; Liu et al., 2014, Dashinimaev et al.,* 2016).

For neuronal differentiation we applied the *Chambers et al., 2009* protocol to generate dorsal forebrain neurons by dual SMAD inhibition, using SB431542 (to block TGFβ) and LDN193189 (to inhibit the BMP pathway). After this initial differentiation, cells were grown as embryoid bodies that after plating on Matrigel, gave rise to neuroepithelial cells, that further gave rise to heterogeneous cultures. The heterogeneous culture was enriched for neural cells but likely contained some non-neuronal cells as well (*Nieweg et al., 2015*). After 8 weeks of *in vitro* differentiation, the mixed cultures were dissociated and immunopurified using the protocol established in *Nieweg et al., 2015*. Immunopanning is the process of selecting or depleting a particular cell type from a population of cells by incubating cell suspensions on a dish coated with immobilized antibodies. Neural cell adhesion molecule (NCAM) antibody VIN-IS-53 was used to isolate immature neurons expressing NCAM at a high level. *Nieweg et al., 2015* report that NCAM immunopanning gives rise to neuron-enriched cultures that were 95% positive for the pan-neuronal marker found abundantly in soma and dendrites, microtubule associated protein 2 (MAP2), compared to 28.1 ±20.6% MAP2-positive cells in the heterogeneous and variable non-immunopanned population.

The enriched neuronal culture was characterized by immunostaining for markers of different cortical layers. The MAP2–positive postmitotic neurons were positive mainly for early-born neuron markers (TBR1, CTIP2), but also for upper layer markers like SATB2. *Srinivasan et al., 2012* have shown that up to 20-30% of upper layer neurons may be positive also for TBR1. The neurons were therefore, a mixture of glutamatergic upper and deep layer cortical neurons with an

unsurprisingly low amount of GAD67-positive GABAergic neurons. Following the immunopanning, the cells were also treated with AraC for 5 days to kill remaining proliferating NSCs. *Nieweg et al., 2015* showed functionally active neurons 8 weeks after immunopurification that generated action potentials upon depolarizing current injections. Since most *in vitro* neuronal differentiation protocols show variability in differentiation efficiency between cell lines (*Hu et al., 2010*), it was important to show the robustness of the protocol we used, as well as to ensure that any subsequent phenotypic differences in the isogenic pair arise due to the genotype rather than variability in the differentiation protocol. This was done by comparing the immunostaining for cortical markers between the A3/3 and A4/4 lines which showed reproducibility between experiments and no significant differences between the two different genotypes.

It is widely accepted that iPSC differentiation gives rise to immature neurons representing the neonatal stage (*Mariani et al., 2012; Nicholas et al., 2013*). Therefore, using these neurons to model AD which is a neurodegenerative, ageing-related disorder is challenging. While penetrant familial AD mutations start to show disease-related phenotypes even in these young neurons, the same may not be true of sporadic AD models. Since maturation of these neurons in culture takes a very long time, it may be necessary in some cases to stress the cells in order to 'accelerate' ageing and trigger a disease phenotype. These stresses are designed to reflect changes that may occur in an ageing brain such as decrease in brain pH (*Forester et al., 2010*) or accumulation of reactive oxygen species (ROS) (*Balaban et al., 2005*). Another approach that has been used involves repressing or activating genes which are key regulators in the ageing process (such as progerin) that lead to an exaggerated ageing phenotype (*Miller et al., 2013*). With increasing focus on modelling sporadic and ageing-related illnesses, there is likely to be greater focus on effectively representing 'aged' neural cells *in vitro*.

Over the last few decades, as the understanding of AD pathology as well as normal astrocyte functions has deepened, there is increasingly greater interest in the role of astrocytes in pathological conditions. Since astrocytes have been shown to have diverse functions in maintaining brain homeostasis such as in neurotransmitter recycling, antioxidant supply, neuroinflammation etc. i.e. pathways that go awry in AD, this has necessitated the development of more physiologically relevant models to study these functions in AD. For several decades, glioma

cell lines were used for studying astrocyte functions and screening, however, biological relevance of these cells is questionable since *Auvergne et al., 2013* uncovered substantial transcriptional differences between normal and glioma-derived glial progenitor cells. Studies focusing on astrocyte functions in AD were performed using transgenic rodent astrocytes. However, recent studies have highlighted crucial differences between human and rodent astrocytes including in their size, complexity, synaptic coverage, Ca^{+2} wave propagation (*Oberheim et al., 2006*), glutamate responses (*Oberheim et al., 2009*) and transcriptomic profiles (*Zhang et al., 2016*). Since the development of iPSC technology, several protocols have been developed for their differentiation to various neuronal subtypes, however, the progress in their differentiation to astrocytes has been relatively limited due to limited understanding of stage-specific astrocyte markers. Early protocols for differentiation to and maintenance of astrocytes were performed in serum-containing medium since serum is rich in the required growth factors and trace elements. However, batch-to-batch variation of serum and frequent contamination was a concern. Additionally, *Foo et al., 2011* have shown the gene expression profile of serum-cultured astrocytes to be a mixture of reactive and developing astrocytes. A concern with more recent serum-free protocols has been the duration of culture time. *In vivo*, since astrogliogenesis follows neurogenesis, *in vitro* protocols developed based on those developmental cues tend to be of a fairly long duration (*Krencik et al., 2011*: 120 days). Other protocols that aimed to shorten the protocol (to 35-42 days) have had variable success in maturation and yield of astrocytes (55% (*Mormone et al., 2014*); 70% (*Shaltouki et al., 2013*)). Therefore, keeping these concerns in mind, we adapted a modified version of the *Serio et al., 2013* protocol that showed 90% GFAP-positive cells using a 49-day protocol.

The first step of our adapted protocol was neural induction of the iPSCs by dual SMAD inhibition (*Chambers et al., 2009*) followed by culturing the neural rosettes to yield neural stem cells (NSCs). Almost 100% of the resultant cells were positive for neural stem cells markers SOX2 and Nestin for both APOE3/3 and APOE4/4 lines, showing no significant differences in ability to undergo neural induction. Calculation of population doubling time, however, revealed that the A and B lines (which were derived from different individuals) had different growth rates, although here too, 3/3 and 4/4 isogenic pairs for each cell line had similar growth rates. Thus, this hinted at a

possible individual-specific difference in growth rates, further validating the need for isogenic lines in disease modelling.

The next step in the generation of astrocytes involves a shift from neurogenic NSCs to gliogenic ones. This switch involves chromatin remodeling and GFAP promoter demethylation and can be brought about by prolonged cultivation of NSCs in culture. However, this switch can also be induced by other methods, such as by triggering progliogenic signaling pathways. Culturing NSCs with LIF and EGF for 6 weeks lead to the induction and enrichment of astrocyte progenitors (APCs) in culture (*Viki et al., 2003; Fukuda et al., 2007*), evidenced by an increase in the percentage of cells expressing GFAP and S100β, both commonly used astrocyte markers. Once the switch to APCs has occurred, proneural genes are downregulated, astrocytic genes are demethylated and are thus sensitive to be acted upon by CNTF. CNTF treatment leads to activation of the JAK/STAT pathway, STAT translocation from cytoplasm to nucleus and binding to GFAP promoter region and leading to its transcription (*Rajan et al., 1998*). This terminal differentiation to astrocytes was validated by expression of GFAP, S100B, ALDH1L1 (a highly specific pan-astrocytic marker and folate metabolizing enzyme) and GLAST (a marker known to be involved in neuronal migration and glutamate uptake, and shown to be present only in glial cells (*Ullensvang et al., 1997*)). Here too, the percentage of cells expressing the different astrocytic markers was similar for both 3/3 and 4/4 astrocytes.

A shortage of consistent stage-specific markers for human astrocytes makes it imperative to characterize them by assessing different astrocytic functions. Also, since a relatively short differentiation protocol was used, confirming their functional relevance for the study was all the more important. A key function of astrocytes is the removal of excess glutamate from the extracellular environment, thus helping to maintain synaptic signaling. It also helps to avoid glutamate excitotoxicity, which has been hypothesized as a mechanism of AD-related neuronal death. Glutamate uptake by astrocytes is mainly performed by 2 excitatory amino acid transporters: EAAT1 (GLAST) and EAAT2 (GLT-1) in a sodium and potassium dependent manner. We evaluated active glutamate uptake by performing a time course experiment where astrocytes were incubated with glutamate. With increasing time (30, 60, 120 min) amount of glutamate taken up by the astrocytes increased. The specificity of this uptake could be proven by blocking the uptake

using PDC, a specific glutamate transporter inhibitor or in the absence of sodium, thus proving that the differentiated astrocytes contained functional glutamate transporters. A key mechanism of astrocytic communication with each other as well as performing intracellular signaling is through calcium oscillations. Astrocytes express a large number of metabotropic receptors which modulate intracellular calcium levels based on external stimuli thus allowing chemical excitability. Glutamate and ATP were applied to the differentiated astrocytes to elicit a calcium response. While some cells responded to ATP as well as glutamate, a larger percentage of cells were responsive to ATP, thus confirming the presence of purinergic receptors on these astrocytes. Since a smaller percentage of cells show glutamate responsiveness, one can surmise that the cells are more fetal in nature since *Zhang et al., 2016* suggested that glutamate responsiveness is acquired by human astrocytes only after mid-gestation. Astrocytes are important players in neuroinflammation, and reactive astrocytes have been found to be associated with amyloid plaques (*Perez-Nievas et al., 2018*). In response to TNFα or IL-6 secretion by microglia, astrocytes turn reactive, due to the expression of pattern-recognition receptors on their surface. Once active, astrocytes secrete chemokines that recruit lymphocytes to travel into the brain and neutralize the infection. Upon treating the differentiated astrocytes with TNFα for 48 hours, we could see an upregulation in the expression of CCL5, CXCL8, CXCL9 and CXCL10, as has already been reported in human primary astrocytes (*Hariharan et al., 2014*). However, high levels of CCL2 could already be found in the untreated cells and upon TNFα treatment, this value did not change. This could be due to the NF-κB-mediated upregulation of CCL2 during astrocyte differentiation, as described by *Lawrence et al., 2016* using human-derived fetal brain progenitors. Lastly, since this study focuses on APOE, a lipoprotein enriched in the transcriptome of astrocytes (*Cahoy et al., 2008*), it was necessary to test if these astrocytes produce and secrete APOE. After CNTF terminal differentiation, 72-hour astrocyte-conditioned medium was collected at different time points and evaluated by APOE ELISA. With increasing time from day 3 to day 17, the APOE amount secreted by these astrocytes in the surrounding medium increased. *Lundin et al., 2018* reported a significant increase in the APOE amount secreted by astrocytes as compared to NSCs, thus hinting that our cells continue to undergo differentiation/maturation even several days after CNTF treatment is completed. Thus, this model system provided functionally active and biologically relevant astrocytes to study early isoform-specific effects of APOE.

4.4 Isoform-specific effects of APOE4 in human iPSC-derived neurons

Apolipoprotein E (APOE) is a lipoprotein primarily involved in the transport of lipids, cholesterol and fat soluble vitamins. It exists in three isoforms imparting different amount of risk to AD: APOE2 (protective), APOE3 (wild type) and APOE4 (increased disease susceptibility). It is produced in the brain mainly by astrocytes and microglia while neurons express APOE receptors such as LRP1, APOER2, LDLR (*Holtzman et al., 2012*). Neurons may express APOE in response to stress or injury (*Boschert et al., 1999; Mahley et al., 2016*). *APOE4* is the strongest known genetic risk factor for sporadic AD with an odds ratio of ~4, compared to other AD susceptibility genes with odds ratios between 1.1 and 1.3 (*Lambert et al., 2013*). There are several hypotheses for how APOE4 imparts this strong susceptibility to the disease, some of them Aβ-dependent and some Aβ-independent. This includes the observation that APOE4 is less efficient at transporting cholesterol than APOE2 or APOE3 (*Rapp et al., 2006*). Thus, while a young brain may have compensatory mechanisms to cope with inefficient cholesterol transport, an aging brain with its increased need for neuronal repair, may not. Similarly, reduced Aβ clearance and increased Aβ aggregation seen in an APOE4 brain (*Holtzman et al., 2000; Castellano et al*., 2011) leads to an accumulation of Aβ with increasing age. However, structural changes in the APOE4 brain such as cortical thinning (*Espeseth et al., 2008*) and reduced hippocampal volumes (*O'Dwyer et al., 2012*) are seen in individuals as young as 20 years old. In order to improve chances of developing a successful drug, greater attention needs to be paid to pathways affected early in the disease such as endolysosomal (*Cataldo et al., 1997*) and metabolic abnormalities (*Reiman et al., 2004*). APOE, being a lipoprotein, is not a very druggable target and for this reason also, there needs to be greater research into the pathways through which APOE4 mediates its toxic effects.

We first tested if the isogenic APOE neurons could be used to study key pathological hallmarks of AD that appear with ageing. This included abnormal hyperphosphorylation of the microtubule associated protein tau that is seen in the AD brain. Hyperphosphorylation eventually leads to tau aggregation and neurofibrillary tangle (NFT) formation. While Aβ is widely believed to be the initiator of AD pathology, Aβ aggregates correlate poorly with tissue loss or cognitive symptoms (*Josephs et al., 2008*). On the other hand, tau phosphorylation and accumulation correlate strongly with disease symptoms (*Arriagada et al., 1992*). APOE4 carriers are found to have higher tau as

well as phosphorylated tau levels (*Vemuri et al., 2010*). Furthermore, mislocalisation of phosphorylated tau to the soma and dendrites is also observed in patients and mediates synaptic dysfunction (*Thies et al., 2007; Hoover et al., 2010*). These results have been replicated by *Bennett et al., 2013* using 3xTG-APOE4 mouse model where greater tau accumulation as well as somatodendritic mislocalisation have been observed.

We performed a Western blot of A3/3 and A4/4 neuronal lysates 2 weeks after immunopanning using the AT8 antibody (targeting tau phosphorylated at both Ser202, Thr205) and PHF1 antibody (targeting tau phosphorylated at both Ser396 and Ser404). These are the epitopes normally hyperphosphorylated in the AD brain. There seemed to be a trend for increased hyperphosphorylation in the APOE4-carrying neurons compared to the APOE3 neurons, but this difference was not significant. Additionally, the amounts of phosphorylated tau were quite variable between replicates. Since tau phosphorylation is associated with neuronal differentiation (*Brion et al., 1994*), the variability could be a result of neuronal differentiation variation between replicates and perhaps using more mature neurons at a later stage would help to avoid the variability. These results are in line with recent studies showing increased tau phosphorylation in neurons derived from APOE4/4 iPSCs (*Wang et al., 2018, Wadhwani et al., 2019, Lin et al., 2018*). Moreover, upon immunostaining A3/3 and A4/4 neurons with AT8 and PHF1 antibodies, we did observe a somatodendritic mislocalization of phosphorylated tau, similar to the observations in *Wang et al., 2018*. Notably, this mislocalization of p-tau was unaccompanied by changes in the Aβ42/40 ratio. This result agrees with *Shi et al., 2017*, who report higher tau levels and somatodendritic compartmentalization of tau in P301s mice (tauopathy model) on an APOE4 background. They also observe that the mislocalization is an Aβ-pathology independent event.

The second key hallmark of AD we focused on, was Aβ pathology, particularly the Aβ42/Aβ40 ratio. Aβ42 and Aβ40 represent the 42 and 40 amino acid fragments formed after proteolysis of the integral membrane protein Amyloid Precursor Protein (APP). The Aβ42 fragment has a greater tendency to aggregate and form oligomers, fibrils and plaques (*Burdick et al., 1992*). APP when processed by the non-amyloidogenic pathway of α-secretase followed by γ-secretase cleavage leads to the formation of non-toxic AICD and p3 peptides. When processed by the amyloidogenic pathway of β-secretase followed by γ-secretase cleavage leads to the formation of Aβ peptides of

various lengths. The Aβ42/Aβ40 concentration ratio has a strong diagnostic performance in distinguishing non-AD from AD patients (*Lewczuk et al., 2015*).

We performed an ELISA for Aβ40 and Aβ42 from medium that had been conditioned by A4/4 patient and non-related APOE3/3 control neurons for 72 hours. The Aβ42/Aβ40 ratio did not differ between APOE3/3 and APOE4/4 neurons. This observation was replicated using isogenic pairs of A3/3-A4/4 and B3/3-B4/4 neurons. These results were not surprising, since studies using AD brain tissue have reported that levels of soluble and insoluble Aβ42 are higher in familial AD as compared to sporadic AD (*Shepherd et al., 2009*). Using RNAi to silence several sporadic or late onset AD genes, *Bali et al, 2012* reported no significant differences in the Aβ42/Aβ40 ratio and suggest that although familial and sporadic AD are clinically similar, they may possibly have different underlying molecular causes. They did not rule out the possibility that vulnerability to Aβ-mediated toxicity imparted by sporadic AD genes may occur late in the disease. Other studies using iPSC-derived neurons also report that sporadic AD neurons do not always show differences in the Aβ42/Aβ40 ratio, while showing other pathologies like increased levels of ROS *(Kondo et al., 2013*) or vulnerability to excitotoxicity (*Duan et al., 2014*). Two of the afore mentioned iPSC studies (*Lin et al., 2018 and Wadhwani et al., 2019*) also did not observe significant differences in Aβ42/Aβ40 ratio between induced neurons derived from isogenic APOE3 and APOE4 iPSC lines.

We observed a significant increase in the Aβ42/Aβ40 ratio only from APOE4/4 neurons which were treated for 5 days with APOE4-containing conditioned medium derived from APOE4/4 astrocytes. This result could be seen in A4/4 patient neurons treated with unrelated APOE4 astrocyte-conditioned medium. The result could also be replicated using isogenic cell lines i.e. B4/4 neurons treated with B4/4 astrocyte-conditioned medium. The conditioned media contained APOE at a concentration of ~9 ng/ml. This concentration was similar to the mean concentration of recoverable APOE in the hippocampal interstitial fluid measured by *Ulrich et al., 2013* to be ~10 ng/ml. It is interesting to note that treating APOE3/3 neurons with APOE4/4-containing medium did not lead to an increase in the Aβ42/Aβ40 ratio. This suggests that an intersection of changes in neurons and astrocytes mediated by APOE4 is necessary to see an Aβ-related phenotype. It is also important to note that treating APOE3/3 or APOE4/4 neurons with recombinant APOE3 or APOE4 did not change the Aβ42/Aβ40 ratio. This could be due to the state

in which APOE physiologically exists in the brain. Astrocytes secrete APOE as truly lipidated particles, whereas recombinant APOE particles produced by overexpression in non-physiological cells types like HEK cells are non-lipidated and are mostly just aggregates *(LaDu et al., 2006*).

The role of APOE4 in AD has often been attributed to its ability to increase aggregation of Aβ (*Castano et al., 1995*) and reduce its clearance from the brain (*Castellano et al., 2011*). Very few studies have focused on its role in increasing production of Aβ from APP. In rat neuroblastoma cells, *Ye et al., 2005* describe increased APP internalization and Aβ production in the presence of APOE4. This effect was mediated by the APOE receptor LRP1 and an increased retention time and colocalisation of APP and the β-secretase within early endosomes. APOE is internalized by binding to one of its key receptors LRP1, which has a rapid endocytosis rate compared to APP (*Cam et al., 2005*). LRP1 interacts with APP through the adaptor protein FE65 which binds to the NPxY motifs within both receptors (*Trommsdorff et al., 1998; Pietrzik et al., 2004*), thus causing APP to internalize along with LRP1. Proteolytic processing of APP occurs along this pathway where α-secretase (ADAM10), primarily found at the plasma membrane, competes with β-secretase (BACE1) found in the acidic environs of endosomes and the trans-golgi network (TGN). Therefore, exogenous astrocyte-secreted APOE4 leads to production of Aβ peptides by increasing simultaneous localization of APP and BACE1 in the endosomes, as also reported by *Vincent et al., 2001*. Even though the Aβ42/Aβ40 ratio was changed in the presence of external APOE4, we did not observe a significant increase in the Aβ level, hinting at changes in the mode of function of the γ-secretase. This could be due to a direct interaction with APOE, altered γ-secretase trafficking or environmental changes in the cellular compartment, where cleavage takes place. γ-secretase was found to cleave APP both at the cell surface and in the endosomal compartment.

The endolysosomal system consists of a network of progressively acidic vesicles that internalize trophic factors, nutrients and receptors. The internalized materials are trafficked to various destinations: they may be recycled back to the surface or modified by the actions of enzymes found in the vesicles or they may be degraded. Through this system consisting of early, recycling and late endosomes and lysosomes, the neuron can control the processing and abundance of receptors found on the cell surface. Endosomal enlargement was one of the earliest pathologies seen in the sporadic AD brain by *Cataldo et al., 1997*. On an average, 2.5- fold greater endosomal volume per

pyramidal neuron was seen even before the appearance of amyloid pathology. Enlarged endosomes were also present to a greater degree in the brains of APOE4 carriers at a preclinical stage while they were not found in familial AD brains at advanced stages (*Cataldo et al., 2000*). Complementing this study, *Nuriel et al., 2017* found that APOE4 expression leads to dysregulation of several endolysosomal pathway genes in APOE targeted replacement mice. To observe endosomes in the isogenic neurons, we immunostained them with early endosome antigen 1 (EEA1) and found no difference in endosome sizes between neurons of different APOE genotypes alone. However, treatment of B4/4 neurons with B4/4 astrocyte-conditioned medium lead to a significant enlargement of endosomes. Again, this effect was not seen with B3/3 neurons treated with B4/4 astrocyte-conditioned medium. This result correlated well with the pattern we saw in Aβ42/Aβ40 ratios, indicating a direct link between both phenotypes. Enlarged endosomes may result from the difference in the intracellular trafficking properties of APOE3 and APOE4. Following endocytosis, APOE3 is readily cycled back to the surface while APOE4 remains trapped in the endosomes leading to increased endosomal fusion and reduced trafficking (*Li et al., 2012*).

After early and late endosomes, the next compartment in the ELS are lysosomes. They are more acidic (pH 4.5-5) and receive material from the endocytic or autophagic pathway for degradation by proteases, phosphatases and lipases. *Cataldo et al., 1995; 1996* demonstrated an upregulation in acid hydrolase synthesis as well as 2 to 7–fold increases in the number of lysosomes in the AD brain. We immunostained the isogenic pairs of neurons with the lysosome marker LAMP2 and did not observe a significant difference in the mean area of lysosomes. Similar to the endosomal staining, treatment of B4/4 neurons with B4/4 astrocyte-conditioned medium resulted in significantly larger lysosomes. Enlarged lysosomes could be a result of a buildup of endocytic substrates. *Nixon, 2017* describe enlarged lysosomes in AD to be dysfunctional which become autolysosomes and lipofuscin granules as hydrolysis by lysosomal enzymes declines. Lysosomes are the site for Aβ and βCTF degradation, which is also a function APOE4 is known to impair (*Jiang et al., 2008*). In addition, *Cataldo et al., 1997* identified lysosomal hydrolases Cathepsin B and Cathepsin D in most early endosomes in sporadic AD brains. These hydrolases have been shown to have β- and γ-secretase properties. Therefore, it would be also interesting to test for altered Cathepsin trafficking to endosomes in the neurons isogenic for APOE, since this could also lead to increased Aβ production.

Loss of neurons is the main pathological outcome of AD. Since neurons are post-mitotic and largely irreplaceable, preventing loss of these cells is important to ensure normal function. *Duan et al., 2014* reported increased susceptibility to glutamate-induced cell death in iPSC-derived cholinergic neurons from an APOE3/4 sporadic AD patient. *Wadhwani et al., 2019* used isogenic neurons to demonstrate greater cell death in response to ionomycin-induced cytotoxicity in APOE4 neurons as compared to APOE3 neurons. Since aging is one of the greatest risk factors for sporadic AD and aging is also accompanied by increased oxidative stress (*Liguori et al., 2018*), we replated the isogenic pairs of neurons on glass coverslips and treated them with hydrogen peroxide and ferric chloride to induce the production of reactive oxygen species. The dissociation and plating of neurons was stressful enough to cause a vulnerability in APOE4 neurons. Further induction of oxidative stress demonstrated that APOE4 neurons have a greater susceptibility to cell death as compared to APOE3 neurons. These results suggest that a cell death response to oxidative stress is an important mechanism in AD pathology, although the mechanism for this is not clear yet.

4.5 Endosomal and metabolic compromise in human iPSC-derived APOE4/4 astrocytes

Several hypothesis used to explain AD pathology hypothesize neurons to be the originators of the disease. The strongest genetic risk factor for AD, APOE, is produced only by astrocytes and microglia in a healthy brain. These hypotheses also ignore the key role of astrocytes in maintaining brain homeostasis. Therefore, it becomes important to study the cell-autonomous effect of APOE4 on astrocytes.

As mentioned above, enlarged endosomes were found in the brains of APOE4 carriers at a preclinical stage (*Cataldo et al., 2000*). In our isogenic lines, APOE4/4 APCs had a tendency for enlarged endosomes, however, the difference was not significant. Whereas terminally differentiated astrocytes showed significantly enlarged endosomes and lysosomes in the APOE4/4 lines. This could be because, we don't expect cells at the progenitor stage to express as much APOE as a terminally differentiated astrocytes. Due to the neurocentric view of AD, an enlarged endosome phenotype at early stages of the disease has yet only been described for affected neurons (*Lin et al., 2018; Cataldo et al., 2000*). The single amino acid difference between APOE3 and APOE4 increases the isoelectric point of APOE4 to coincide with the pH of endosomes (~pH 6.5).

This causes APOE4 to unfold into a 'molten globule' conformation and aggregate when they enter the acidic environment of an endosome (*Xian et al., 2018*). A key function of the increasingly acidic pH gradient through the endolysosomal vesicles is the dissociation of ligands from their receptors and the cycling back of receptors to the surface. As the APOE4 aggregates in the endosomes, it is believed to sequester internalized receptors along with it. Trapping of Aβ receptor LRP1 in endosomes of APOE4 astrocytes leads to reduced LRP1 availability on the surface and a reduced Aβ clearance (*Prasad and Rao 2018*). This could have far-reaching consequences, since APOE4 downregulates the levels of other growth factor and neurotransmitter receptors like VEGF, NMDA and Insulin (*Safieh et al., 2019*).

Another one of the earliest changes that takes place in the AD brain is the impairment of glucose metabolism that arises decades before any other pathological phenotype (*Reiman et al., 2004*). Cerebral hypometabolism has been confirmed by FDG PET studies in middle aged (*Reiman et al., 2010*) and young (20-30 years old) APOE4 carriers (*Reiman et al., 2014*) as compared to age-matched non-carriers in parts of the brain affected in AD. It, thus, becomes important to examine the role of astrocytes in glucose hypometabolism as they are the cells that use up to 85% of the glucose in the brain. They sense changes in synaptic activity, and accordingly modulate cerebral blood flow (*Magistretti et al., 2006*), as well as control glucose entry into the brain at the intraparenchymal capillaries through their endfeet. Through glycolysis, they convert glucose to lactate and release it into extracellular space where it is taken up by neurons as their key source of energy.

We performed the Seahorse assay with the isogenic pairs of astrocytes and observed a strong tendency for reduced glycolysis in APOE4/4 astrocytes. There was a significant reduction in glycolytic capacity in APOE4/4 astrocytes. It also revealed a significant reduction in basal respiration and ATP production in APOE4/4 astrocytes. This reduction in glycolysis and mitochondrial respiration correlates well with the endosomal enlargement also seen in APOE4/4 astrocytes. *Zhao et al., 2017* used mouse primary neurons to describe the interaction of APOE4 with insulin receptor leading to its entrapment in endosomes. This, in, turn, compromised insulin receptor trafficking and insulin-stimulated glycolysis and mitochondrial respiration. This observation is supported by impaired brain insulin signaling upon conditional deletion of the

APOE receptor LRP1 (*Liu et al., 2015*). Although not tested yet, we anticipate a reduction in lactate production by the APOE4/4 astrocytes as a result of glycolysis impairment, as has been described for hiPSC-derived PSEN1 DE9 astrocytes (*Oksanen et al., 2017*). Since rat studies have shown that transport of astrocyte-released lactate to neurons is essential for long-term memory formation (*Suzuki et al., 2011*), APOE4-mediated reduction of glycolysis could be critical for dementia in AD. Postmortem AD brain studies have revealed reduced levels of astrocyte GLUT1 and neuronal GLUT3 (both responsible for uptake of glucose) (*Simpson et al., 1994*). However, it remains to be tested in our model if a reduction in GLUT1-mediated uptake is responsible for glycolysis impairment. With aging, the strongest risk factor for sporadic AD, the glycolysis rate of astrocytes is decreased (*Yao et al., 2011*). Therefore, a lifelong glycolysis compromise due to APOE4 would lead to a metabolic crisis in neurons that would come to a head with aging.

AD brains have been reported to have reduced levels of mitochondrial Complex IV (cytochrome c oxidase) (*Parker et al., 1994*). This phenomenon was also observed in fibroblasts from AD patients (*Cardoso et al., 1994*). In order to ascertain if reduced mitochondrial complexes was the reason behind the observed reduction in mitochondrial respiration and ATP production in APOE4 astrocytes, we performed a Western blot for mitochondrial complexes. Complex V (ATP synthetase was significantly reduced in APOE4/4 compared to APOE3/3 astrocytes. The other complexes were all significantly reduced in the APOE4/4 astrocytes of one of the isogenic pairs and often showed a strong trend for reduction in the other pair. *Nakamura et al., 2009* reported that expression of APOE4 in neuroblastoma cells leads to its cleavage by proteases and the fragments then go on to bind with components of Complex III and Complex IV and impair their function. However, the mechanism is much less clear in astrocytes where such APOE proteolysis has not been described. These results stand in sharp contrast to the *Chen et al., 2011* study. They reported a decrease in all mitochondrial complexes in neurons cultured from mice that only expressed APOE4 in the neurons, whereas no significant differences were seen in the level of mitochondrial complexes from astrocyte cultures from mice that showed astrocyte-specific expression of APOE4. It still remains to be tested if this was a species-specific effect. Since APOE also has transcription factor-like functions (*Theendakara et al., 2016*), it still remains to be determined whether the reduction of electron transport chain complexes in our model system was at a pre-or post-translational level.

Oxidative stress is hypothesized to play a critical role in AD and is shown to arise before Aβ pathology (*Nunomura et al., 2001*). Since we saw a reduction in APOE4/4 astrocytes of Complexes I and III which are considered the main sites of superoxide production by electron leakage, mitochondrial reactive oxygen species (ROS) measurement was performed in the isogenic astrocytes. Greater ROS levels were observed in APOE4/4 astrocytes. *Oksanen et al., 2017* also observed increased ROS production in tandem with decreased lactate secretion in PS1 astrocytes. Since mitochondrial DNA lacks histones (*Shokolenko et al., 2017*), it is easily attacked by ROS and could lead to further mitochondrial damage and electron transport chain defects.

In summary, this study describes the generation and characterization of isogenic physiologically relevant iPSC-derived neural cells that can be employed for sporadic Alzheimer's disease modeling and discovery studies. The model was utilized to highlight early pathologies in AD that are relatively less studied, such as metabolic and endolysosomal defects in APOE4/4 astrocytes. The protocols developed here for reprogramming, genome editing and differentiation can be applied to modelling other diseases.

5. References:

Allaman, I., Bélanger, M., & Magistretti, P. J. (2011). Astrocyte–neuron metabolic relationships: for better and for worse. *Trends in neurosciences*, *34*(2), 76-87.

Arriagada, P. V., Growdon, J. H., Hedley-Whyte, E. T., & Hyman, B. T. (1992). Neurofibrillary tangles but not senile plaques parallel duration and severity of Alzheimer's disease. *Neurology*, *42*(3), 631-631.

Augustinack, J. C., Schneider, A., Mandelkow, E. M., & Hyman, B. T. (2002). Specific tau phosphorylation sites correlate with severity of neuronal cytopathology in Alzheimer's disease. *Acta neuropathologica*, *103*(1), 26-35.

Auvergne, R. M., Sim, F. J., Wang, S., Chandler-Militello, D., Burch, J., Al Fanek, Y., ... & Johnson, M. (2013). Transcriptional differences between normal and glioma-derived glial progenitor cells identify a core set of dysregulated genes. *Cell reports*, *3*(6), 2127-2141.

Balaban, R. S., Nemoto, S., & Finkel, T. (2005). Mitochondria, oxidants, and aging. *cell*, *120*(4), 483-495.

Bali, J., Gheinani, A. H., Zurbriggen, S., & Rajendran, L. (2012). Role of genes linked to sporadic Alzheimer's disease risk in the production of β-amyloid peptides. *Proceedings of the National Academy of Sciences*, *109*(38), 15307-15311.

Baumann, P., & West, S. C. (1998). Role of the human RAD51 protein in homologous recombination and double-stranded-break repair. *Trends in biochemical sciences*, *23*(7), 247-251.

Bennett, R. E., Esparza, T. J., Lewis, H. A., Kim, E., Mac Donald, C. L., Sullivan, P. M., & Brody, D. L. (2013). Human Apolipoprotein E4 worsens acute axonal pathology but not amyloid-β immunoreactivity after traumatic brain injury in 3× TG-AD mice. *Journal of Neuropathology & Experimental Neurology*, *72*(5), 396-403.

Bertram, L., Lill, C. M., & Tanzi, R. E. (2010). The genetics of Alzheimer disease: back to the future. *Neuron*, *68*(2), 270-281.

Bigl, M., Brückner, M. K., Arendt, T., Bigl, V., & Eschrich, K. (1999). Activities of key glycolytic enzymes in the brains of patients with Alzheimer's disease. *Journal of neural transmission*, *106*(5-6), 499-511.

Bobba, A., Amadoro, G., Valenti, D., Corsetti, V., Lassandro, R., & Atlante, A. (2013). Mitochondrial respiratory chain Complexes I and IV are impaired by β-amyloid via direct interaction and through Complex I-dependent ROS production, respectively. *Mitochondrion*, *13*(4), 298-311.

Boch, J., Scholze, H., Schornack, S., Landgraf, A., Hahn, S., Kay, S., ... & Bonas, U. (2009). Breaking the code of DNA binding specificity of TAL-type III effectors. *Science*, *326*(5959), 1509-1512.

Boschert, U., Merlo-Pich, E., Higgins, G., Roses, A. D., & Catsicas, S. (1999). Apolipoprotein E expression by neurons surviving excitotoxic stress. *Neurobiology of disease*, *6*(6), 508-514.

Brion, J. P., Octave, J. N., & Couck, A. M. (1994). Distribution of the phosphorylated microtubule-associated protein tau in developing cortical neurons. *Neuroscience*, *63*(3), 895-909.

Burdick, D., Soreghan, B., Kwon, M., Kosmoski, J., Knauer, M., Henschen, A., ... & Glabe, C. (1992). Assembly and aggregation properties of synthetic Alzheimer's A4/beta amyloid peptide analogs. *Journal of Biological Chemistry*, *267*(1), 546-554.

Buta, C., David, R., Dressel, R., Emgård, M., Fuchs, C., Gross, U., ... & Mikkers, H. (2013). Reconsidering pluripotency tests: do we still need teratoma assays?. *Stem cell research*, *11*(1), 552-562.

Byrne, S. M., & Church, G. M. (2015). CRISPR-mediated gene targeting of human induced pluripotent stem cells. *Current protocols in stem cell biology*, *35*(1), 5A-8.

Cahoy, J. D., Emery, B., Kaushal, A., Foo, L. C., Zamanian, J. L., Christopherson, K. S., ... & Thompson, W. J. (2008). A transcriptome database for astrocytes, neurons, and oligodendrocytes: a new resource for understanding brain development and function. *Journal of Neuroscience*, *28*(1), 264-278.

Cam J. A., Zerbinatti C. V., Li Y., Bu G. (2005). Rapid endocytosis of the low density lipoprotein receptor-related protein modulates cell surface distribution and processing of the β-amyloid precursor protein. *J. Biol. Chem.* 280 15464–15470

Cardoso SM, Proenca MT, Santos S, Santana I, Oliveira CR. Cytochrome c oxidase is decreased in Alzheimer's disease platelets. Neurobiol Aging. 2004;25(1):105–110

Castano, E. M., Prelli, F., Wisniewski, T., Golabek, A., Kumar, R. A., Soto, C., & Frangione, B. (1995). Fibrillogenesis in Alzheimer's disease of amyloid β peptides and apolipoprotein E. *Biochemical Journal*, *306*(2), 599-604.

Castellano, J. M., Kim, J., Stewart, F. R., Jiang, H., DeMattos, R. B., Patterson, B. W., ... & Goate, A. M. (2011). Human apoE isoforms differentially regulate brain amyloid-β peptide clearance. *Science translational medicine*, *3*(89), 89ra57-89ra57.

Cataldo, A. M., Barnett, J. L., Berman, S. A., Li, J., Quarless, S., Bursztajn, S., ... & Nixon, R. A. (1995). Gene expression and cellular content of cathepsin D in Alzheimer's disease brain: evidence for early up-regulation of the endosomal-lysosomal system. *Neuron*, *14*(3), 671-680.

Cataldo, A. M., Barnett, J. L., Pieroni, C., & Nixon, R. A. (1997). Increased neuronal endocytosis and protease delivery to early endosomes in sporadic Alzheimer's disease: neuropathologic evidence for a mechanism of increased β-amyloidogenesis. *Journal of Neuroscience*, *17*(16), 6142-6151.

Cataldo, A. M., Hamilton, D. J., Barnett, J. L., Paskevich, P. A., & Nixon, R. A. (1996). Properties of the endosomal-lysosomal system in the human central nervous system: disturbances mark most neurons in populations at risk to degenerate in Alzheimer's disease. *Journal of Neuroscience*, *16*(1), 186-199.

Cataldo, A. M., Peterhoff, C. M., Troncoso, J. C., Gomez-Isla, T., Hyman, B. T., & Nixon, R. A. (2000). Endocytic pathway abnormalities precede amyloid β deposition in sporadic Alzheimer's disease and Down syndrome: differential effects of APOE genotype and presenilin mutations. *The American journal of pathology*, *157*(1), 277-286.

Chambers, S. M., Fasano, C. A., Papapetrou, E. P., Tomishima, M., Sadelain, M., & Studer, L. (2009). Highly efficient neural conversion of human ES and iPS cells by dual inhibition of SMAD signaling. *Nature biotechnology*, *27*(3), 275.

Chapman, J. R., Taylor, M. R., & Boulton, S. J. (2012). Playing the end game: DNA double-strand break repair pathway choice. *Molecular cell*, *47*(4), 497-510.

Chen, G., Gulbranson, D. R., Hou, Z., Bolin, J. M., Ruotti, V., Probasco, M. D., ... & Wagner, R. (2011). Chemically defined conditions for human iPSC derivation and culture. *Nature methods*, *8*(5), 424.

Chen, H. K., Ji, Z. S., Dodson, S. E., Miranda, R. D., Rosenblum, C. I., Reynolds, I. J., ... & Mahley, R. W. (2011). Apolipoprotein E4 domain interaction mediates detrimental effects on mitochondria and is a potential therapeutic target for Alzheimer disease. *Journal of Biological Chemistry*, *286*(7), 5215-5221.

Choi, H. W., Kim, J. S., Choi, S., Hong, Y. J., Kim, M. J., Seo, H. G., & Do, J. T. (2014). Neural stem cells differentiated from iPS cells spontaneously regain pluripotency. *Stem cells*, *32*(10), 2596-2604.

Chouliaras, L., Rutten, B. P., Kenis, G., Peerbooms, O., Visser, P. J., Verhey, F., ... & van den Hove, D. L. (2010). Epigenetic regulation in the pathophysiology of Alzheimer's disease. *Progress in neurobiology*, *90*(4), 498-510.

Chu, V. T., Weber, T., Wefers, B., Wurst, W., Sander, S., Rajewsky, K., & Kühn, R. (2015). Increasing the efficiency of homology-directed repair for CRISPR-Cas9-induced precise gene editing in mammalian cells. *Nature biotechnology*, *33*(5), 543.

Chu, V. T., Weber, T., Wefers, B., Wurst, W., Sander, S., Rajewsky, K., & Kühn, R. (2015). Increasing the efficiency of homology-directed repair for CRISPR-Cas9-induced precise gene editing in mammalian cells. *Nature biotechnology*, *33*(5), 543.

Chung, W. S., Verghese, P. B., Chakraborty, C., Joung, J., Hyman, B. T., Ulrich, J. D., ... & Barres, B. A. (2016). Novel allele-dependent role for APOE in controlling the rate of synapse pruning by astrocytes. *Proceedings of the National Academy of Sciences*, *113*(36), 10186-10191.

Chung-ha, O. D., Kim, K. Y., Bushong, E. A., Mills, E. A., Boassa, D., Shih, T., ... & Nguyen, J. V. (2014). Transcellular degradation of axonal mitochondria. *Proceedings of the National Academy of Sciences*, *111*(26), 9633-9638.

Cong, L., Ran, F. A., Cox, D., Lin, S., Barretto, R., & Habib, N. Multiplex genome engineering using CRISPR. *Cas systems*, *332*, 819-823.

Corder, E. H., Saunders, A. M., Strittmatter, W. J., Schmechel, D. E., Gaskell, P. C., Small, G., ... & Pericak-Vance, M. A. (1993). Gene dose of apolipoprotein E type 4 allele and the risk of Alzheimer's disease in late onset families. *Science*, *261*(5123), 921-923.

Craig, L. A., Hong, N. S., & McDonald, R. J. (2011). Revisiting the cholinergic hypothesis in the development of Alzheimer's disease. *Neuroscience & Biobehavioral Reviews*, *35*(6), 1397-1409.

Dang, C. V. (2012). MYC on the path to cancer. *Cell*, *149*(1), 22-35.

Dashinimaev, E. B., Artyuhov, A. S., Bolshakov, A. P., Vorotelyak, E. A., & Vasiliev, A. V. (2017). Neurons derived from induced pluripotent stem cells of patients with Down syndrome reproduce early stages of Alzheimer's disease type pathology in vitro. *Journal of Alzheimer's Disease*, *56*(2), 835-847.

De Vivo, L., Melone, M., Rothstein, J. D., & Conti, F. (2010). GLT-1 promoter activity in astrocytes and neurons of mouse hippocampus and somatic sensory cortex. *Frontiers in neuroanatomy*, *3*, 31.

Dean, D. C., Jerskey, B. A., Chen, K., Protas, H., Thiyyagura, P., Roontiva, A., ... & Siniard, A. L. (2014). Brain differences in infants at differential genetic risk for late-onset Alzheimer disease: a cross-sectional imaging study. *JAMA neurology*, *71*(1), 11-22.

Deneen, B., Ho, R., Lukaszewicz, A., Hochstim, C. J., Gronostajski, R. M., & Anderson, D. J. (2006). The transcription factor NFIA controls the onset of gliogenesis in the developing spinal cord. *Neuron*, *52*(6), 953-968.

DeVos, S. L., Corjuc, B. T., Commins, C., Dujardin, S., Bannon, R. N., Corjuc, D., ... & Dooley, P. M. (2018). Tau reduction in the presence of amyloid-β prevents tau pathology and neuronal death in vivo. Brain, 141(7), 2194-2212.

Diecke, S., Jung, S. M., Lee, J., & Ju, J. H. (2014). Recent technological updates and clinical applications of induced pluripotent stem cells. *The Korean journal of internal medicine*, *29*(5), 547.

Draper, J. S., Smith, K., Gokhale, P., Moore, H. D., Maltby, E., Johnson, J., ... & Andrews, P. W. (2004). Recurrent gain of chromosomes 17q and 12 in cultured human embryonic stem cells. *Nature biotechnology*, *22*(1), 53.

Du, F., Yu, Q., Chen, A., Chen, D., & Yan, S. S. (2018). Astrocytes attenuate mitochondrial dysfunctions in human dopaminergic neurons derived from iPSC. *Stem cell reports*, *10*(2), 366-374.

Duan, L., Bhattacharyya, B. J., Belmadani, A., Pan, L., Miller, R. J., & Kessler, J. A. (2014). Stem cell derived basal forebrain cholinergic neurons from Alzheimer's disease patients are more susceptible to cell death. *Molecular neurodegeneration*, *9*(1), 3.

Elkabetz, Y., Panagiotakos, G., Al Shamy, G., Socci, N. D., Tabar, V., & Studer, L. (2008). Human ES cell-derived neural rosettes reveal a functionally distinct early neural stem cell stage. *Genes & development*, *22*(2), 152-165.

Elliott, B., Richardson, C., Winderbaum, J., Nickoloff, J. A., & Jasin, M. (1998). Gene conversion tracts from double-strand break repair in mammalian cells. *Molecular and cellular biology*, *18*(1), 93-101.

Elliott, B., Richardson, C., Winderbaum, J., Nickoloff, J. A., & Jasin, M. (1998). Gene conversion tracts from double-strand break repair in mammalian cells. *Molecular and cellular biology*, *18*(1), 93-101.

Emdad, L., D'Souza, S. L., Kothari, H. P., Qadeer, Z. A., & Germano, I. M. (2011). Efficient differentiation of human embryonic and induced pluripotent stem cells into functional astrocytes. *Stem cells and development*, *21*(3), 404-410.

Espeseth, T., Westlye, L. T., Fjell, A. M., Walhovd, K. B., Rootwelt, H., & Reinvang, I. (2008). Accelerated age-related cortical thinning in healthy carriers of apolipoprotein E ε4. *Neurobiology of aging*, *29*(3), 329-340.

Farrer, L. A., Cupples, L. A., Haines, J. L., Hyman, B., Kukull, W. A., Mayeux, R., ... & Van Duijn, C. M. (1997). Effects of age, sex, and ethnicity on the association between apolipoprotein E genotype and Alzheimer disease: a meta-analysis. *Jama*, *278*(16), 1349-1356.

Federation, A. J., Bradner, J. E., & Meissner, A. (2014). The use of small molecules in somatic-cell reprogramming. Trends in cell biology, 24(3), 179-187.

Fillenz, M. (2005). The role of lactate in brain metabolism. *Neurochemistry international*, *47*(6), 413-417.

Foo, L. C., Allen, N. J., Bushong, E. A., Ventura, P. B., Chung, W. S., Zhou, L., ... & Barres, B. A. (2011). Development of a method for the purification and culture of rodent astrocytes. *Neuron*, *71*(5), 799-811.

Forester, B. P., Berlow, Y. A., Harper, D. G., Jensen, J. E., Lange, N., Froimowitz, M. P., ... & Cohen, B. M. (2010). Age-related changes in brain energetics and phospholipid metabolism. *NMR in Biomedicine*, *23*(3), 242-250.

Fu, W., Shi, D., Westaway, D., & Jhamandas, J. H. (2015). Bioenergetic mechanisms in astrocytes may contribute to amyloid plaque deposition and toxicity. *Journal of Biological Chemistry*, *290*(20), 12504-12513.

Fu, Y., Sander, J. D., Reyon, D., Cascio, V. M., & Joung, J. K. (2014). Improving CRISPR-Cas nuclease specificity using truncated guide RNAs. *Nature biotechnology*, *32*(3), 279.

Fukuda, S., Abematsu, M., Mori, H., Yanagisawa, M., Kagawa, T., Nakashima, K., ... & Taga, T. (2007). Potentiation of astrogliogenesis by STAT3-mediated activation of bone morphogenetic protein-Smad signaling in neural stem cells. *Molecular and cellular biology*, *27*(13), 4931-4937.

Guerreiro, R., Wojtas, A., Bras, J., Carrasquillo, M., Rogaeva, E., Majounie, E., ... & Hazrati, L. (2013). TREM2 variants in Alzheimer's disease. *New England Journal of Medicine*, *368*(2), 117-127.

Guo, T., Feng, Y. L., Xiao, J. J., Liu, Q., Sun, X. N., Xiang, J. F., ... & Dong, M. M. (2018). Harnessing accurate non-homologous end joining for efficient precise deletion in CRISPR/Cas9-mediated genome editing. *Genome biology*, *19*(1), 170.

Gurdon, J. B. (1962). The developmental capacity of nuclei taken from intestinal epithelium cells of feeding tadpoles. *Development*, *10*(4), 622-640.

Han, X., Chen, M., Wang, F., Windrem, M., Wang, S., Shanz, S., ... & Silva, A. J. (2013). Forebrain engraftment by human glial progenitor cells enhances synaptic plasticity and learning in adult mice. *Cell stem cell*, *12*(3), 342-353.

Hartlage-Rübsamen, M., Zeitschel, U., Apelt, J., Gärtner, U., Franke, H., Stahl, T., ... & Roßner, S. (2003). Astrocytic expression of the Alzheimer's disease β-secretase (BACE1) is stimulus-dependent. *Glia*, *41*(2), 169-179.

Hauser, P. S., Narayanaswami, V., & Ryan, R. O. (2011). Apolipoprotein E: from lipid transport to neurobiology. *Progress in lipid research*, *50*(1), 62-74.

Herrero-Mendez, A., Almeida, A., Fernández, E., Maestre, C., Moncada, S., & Bolaños, J. P. (2009). The bioenergetic and antioxidant status of neurons is controlled by continuous degradation of a key glycolytic enzyme by APC/C–Cdh1. *Nature cell biology*, *11*(6), 747.

Hippius, H., & Neundörfer, G. (2003). The discovery of Alzheimer's disease. *Dialogues in clinical neuroscience*, *5*(1), 101.

Hixson, J. E., & Vernier, D. T. (1990). Restriction isotyping of human apolipoprotein E by gene amplification and cleavage with HhaI. *Journal of lipid research*, *31*(3), 545-548.

Hockemeyer, D., & Jaenisch, R. (2016). Induced pluripotent stem cells meet genome editing. *Cell stem cell*, *18*(5), 573-586.

Hockemeyer, D., Soldner, F., Beard, C., Gao, Q., Mitalipova, M., DeKelver, R. C., ... & Meng, X. (2009). Efficient targeting of expressed and silent genes in human ESCs and iPSCs using zinc-finger nucleases. *Nature biotechnology*, *27*(9), 851.

Hoe, H. S., Freeman, J., & Rebeck, G. W. (2006). Apolipoprotein E decreases tau kinases and phospho-tau levels in primary neurons. *Molecular neurodegeneration*, *1*(1), 18.

Holmes, C., Cunningham, C., Zotova, E., Woolford, J., Dean, C., Kerr, S. U., ... & Perry, V. H. (2009). Systemic inflammation and disease progression in Alzheimer disease. *Neurology*, *73*(10), 768-774.

Holtzman, D. M., Bales, K. R., Tenkova, T., Fagan, A. M., Parsadanian, M., Sartorius, L. J., ... & Paul, S. M. (2000). Apolipoprotein E isoform-dependent amyloid deposition and neuritic degeneration in a mouse model of Alzheimer's disease. *Proceedings of the National Academy of Sciences*, *97*(6), 2892-2897.

Holtzman, D. M., Bales, K. R., Tenkova, T., Fagan, A. M., Parsadanian, M., Sartorius, L. J., ... & Paul, S. M. (2000). Apolipoprotein E isoform-dependent amyloid deposition and neuritic degeneration in a mouse model of Alzheimer's disease. *Proceedings of the National Academy of Sciences*, *97*(6), 2892-2897.

Holtzman, D. M., Herz, J., & Bu, G. (2012). Apolipoprotein E and apolipoprotein E receptors: normal biology and roles in Alzheimer disease. *Cold Spring Harbor perspectives in medicine*, *2*(3), a006312.

Hong, S., & Song, M. R. (2014). STAT3 but not STAT1 is required for astrocyte differentiation. *PLoS One*, *9*(1), e86851.

Hoover, B. R., Reed, M. N., Su, J., Penrod, R. D., Kotilinek, L. A., Grant, M. K., ... & Ashe, K. H. (2010). Tau mislocalization to dendritic spines mediates synaptic dysfunction independently of neurodegeneration. *Neuron*, *68*(6), 1067-1081.

Hoover, B. R., Reed, M. N., Su, J., Penrod, R. D., Kotilinek, L. A., Grant, M. K., ... & Ashe, K. H. (2010). Tau mislocalization to dendritic spines mediates synaptic dysfunction independently of neurodegeneration. *Neuron*, *68*(6), 1067-1081.

Hsu, P. D., Scott, D. A., Weinstein, J. A., Ran, F. A., Konermann, S., Agarwala, V., ... & Cradick, T. J. (2013). DNA targeting specificity of RNA-guided Cas9 nucleases. *Nature biotechnology*, *31*(9), 827.

Hsu, P. D., Lander, E. S., & Zhang, F. (2014). Development and applications of CRISPR-Cas9 for genome engineering. Cell, 157(6), 1262-1278.

Hu, B. Y., Weick, J. P., Yu, J., Ma, L. X., Zhang, X. Q., Thomson, J. A., & Zhang, S. C. (2010). Neural differentiation of human induced pluripotent stem cells follows developmental principles but with variable potency. *Proceedings of the National Academy of Sciences*, *107*(9), 4335-4340.

Hu, J., Lei, Y., Wong, W. K., Liu, S., Lee, K. C., He, X., ... & Peng, X. (2014). Direct activation of human and mouse Oct4 genes using engineered TALE and Cas9 transcription factors. Nucleic acids research, 42(7), 4375-4390.

Inui, M., Miyado, M., Igarashi, M., Tamano, M., Kubo, A., Yamashita, S., ... & Takada, S. (2014). Rapid generation of mouse models with defined point mutations by the CRISPR/Cas9 system. *Scientific reports*, *4*, 5396.

Israel, M. A., Yuan, S. H., Bardy, C., Reyna, S. M., Mu, Y., Herrera, C., ... & Carson, C. T. (2012). Probing sporadic and familial Alzheimer's disease using induced pluripotent stem cells. *Nature*, *482*(7384), 216.

Jansen, I. E., Savage, J. E., Watanabe, K., Bryois, J., Williams, D. M., Steinberg, S., ... & Voyle, N. (2019). Genome-wide meta-analysis identifies new loci and functional pathways influencing Alzheimer's disease risk.

Jiang, Q., Lee, C. D., Mandrekar, S., Wilkinson, B., Cramer, P., Zelcer, N., ... & Richardson, J. C. (2008). ApoE promotes the proteolytic degradation of Aβ. *Neuron*, *58*(5), 681-693.

Jinek, M., Chylinski, K., Fonfara, I., Hauer, M., Doudna, J. A., & Charpentier, E. (2012). A programmable dual-RNA–guided DNA endonuclease in adaptive bacterial immunity. *science*, *337*(6096), 816-821.

Jones, V. C., Atkinson-Dell, R., Verkhratsky, A., & Mohamet, L. (2017). Aberrant iPSC-derived human astrocytes in Alzheimer's disease. *Cell death & disease*, *8*(3), e2696.

Josephs, K. A., Whitwell, J. L., Ahmed, Z., Shiung, M. M., Weigand, S. D., Knopman, D. S., ... & Jack Jr, C. R. (2008). β-amyloid burden is not associated with rates of brain atrophy. *Annals of neurology*, *63*(2), 204-212.

Jürgensen, S., & Ferreira, S. T. (2010). Nicotinic receptors, amyloid-β, and synaptic failure in Alzheimer's disease. *Journal of molecular neuroscience*, *40*(1-2), 221-229.

Kallas, A., Pook, M., Maimets, M., Zimmermann, K., & Maimets, T. (2011). Nocodazole treatment decreases expression of pluripotency markers Nanog and Oct4 in human embryonic stem cells. *PLoS One*, *6*(4), e19114.

Kandušer, M., & Miklavčič, D. (2009). Electroporation in biological cell and tissue: an overview. In *Electrotechnologies for extraction from food plants and biomaterials* (pp. 1-37). Springer, New York, NY.

Kayed, R., & Lasagna-Reeves, C. A. (2013). Molecular mechanisms of amyloid oligomers toxicity. Journal of Alzheimer's Disease, 33(s1), S67-S78.

Keene, C. D., Cudaback, E., Li, X., Montine, K. S., & Montine, T. J. (2011). Apolipoprotein E isoforms and regulation of the innate immune response in brain of patients with Alzheimer's disease. *Current opinion in neurobiology*, *21*(6), 920-928.

Kilian, J. G., Hsu, H. W., Mata, K., Wolf, F. W., & Kitazawa, M. (2017). Astrocyte transport of glutamate and neuronal activity reciprocally modulate tau pathology in Drosophila. *Neuroscience*, *348*, 191-200.

Kim, H., Yoo, J., Shin, J., Chang, Y., Jung, J., Jo, D. G., ... & Kim, J. (2017). Modelling APOE ε3/4 allele-associated sporadic Alzheimer's disease in an induced neuron. *Brain*, *140*(8), 2193-2209.

Kim, S., Kim, D., & Cho, S. W. Highly efficient RNA-guided genome editing in human cells via.

Kim, S., Kim, D., Cho, S. W., Kim, J., & Kim, J. S. (2014). Highly efficient RNA-guided genome editing in human cells via delivery of purified Cas9 ribonucleoproteins. *Genome research*, *24*(6), 1012-1019.

Klein, R. C., Mace, B. E., Moore, S. D., & Sullivan, P. M. (2010). Progressive loss of synaptic integrity in human apolipoprotein E4 targeted replacement mice and attenuation by apolipoprotein E2. *Neuroscience*, *171*(4), 1265-1272.

Knouff, C., Hinsdale, M. E., Mezdour, H., Altenburg, M. K., Watanabe, M., Quarfordt, S. H., ... & Maeda, N. (1999). Apo E structure determines VLDL clearance and atherosclerosis risk in mice. *The Journal of clinical investigation*, *103*(11), 1579-1586.

Kofuji, P., & Newman, E. A. (2004). Potassium buffering in the central nervous system. *Neuroscience*, *129*(4), 1043-1054.

Kondo, T., Asai, M., Tsukita, K., Kutoku, Y., Ohsawa, Y., Sunada, Y., ... & Takahashi, K. (2013). Modeling Alzheimer's disease with iPSCs reveals stress phenotypes associated with intracellular Aβ and differential drug responsiveness. *Cell stem cell*, *12*(4), 487-496.

Korwek, K. M., Trotter, J. H., LaDu, M. J., Sullivan, P. M., & Weeber, E. J. (2009). ApoE isoform-dependent changes in hippocampal synaptic function. *Molecular neurodegeneration*, *4*(1), 21.

Krencik, R., & Zhang, S. C. (2011). Directed differentiation of functional astroglial subtypes from human pluripotent stem cells. *Nature protocols*, *6*(11), 1710.

Krencik, R., Weick, J. P., Liu, Y., Zhang, Z. J., & Zhang, S. C. (2011). Specification of transplantable astroglial subtypes from human pluripotent stem cells. *Nature biotechnology*, *29*(6), 528.

Kuntz, I. D., Weisgraber, K. H., & Mahley, R. W. (2005). Apolipoprotein (apo) E4 enhances amyloid peptide production in cultured neuronal cells: ApoE structure as a potential therapeutic target. *PNAS*, *102*(51).

LaDu, M. J., Stine, W. B., Narita, M., Getz, G. S., Reardon, C. A., & Bu, G. (2006). Self-assembly of HEK cell-secreted ApoE particles resembles ApoE enrichment of lipoproteins as a ligand for the LDL receptor-related protein. *Biochemistry*, *45*(2), 381-390.

Lambert, J. C., Ibrahim-Verbaas, C. A., Harold, D., Naj, A. C., Sims, R., Bellenguez, C., ... & Grenier-Boley, B. (2013). Meta-analysis of 74,046 individuals identifies 11 new susceptibility loci for Alzheimer's disease. *Nature genetics*, *45*(12), 1452.

Lewczuk, P., Mroczko, B., Fagan, A., & Kornhuber, J. (2015). Biomarkers of Alzheimer's disease and mild cognitive impairment: a current perspective. *Advances in medical sciences*, *60*(1), 76-82.

Li, J., Kanekiyo, T., Shinohara, M., Zhang, Y., LaDu, M. J., Xu, H., & Bu, G. (2012). Differential regulation of amyloid-β endocytic trafficking and lysosomal degradation by apolipoprotein E isoforms. *Journal of Biological Chemistry*, *287*(53), 44593-44601.

Li, R., Liang, J., Ni, S., Zhou, T., Qing, X., Li, H., ... & Qin, B. (2010). A mesenchymal-to-epithelial transition initiates and is required for the nuclear reprogramming of mouse fibroblasts. *Cell stem cell*, *7*(1), 51-63.

Li, R., Lindholm, K., Yang, L. B., Yue, X., Citron, M., Yan, R., ... & Wong, P. (2004). Amyloid β peptide load is correlated with increased β-secretase activity in sporadic Alzheimer's disease patients. *Proceedings of the National Academy of Sciences*, *101*(10), 3632-3637.

Liang, P., Xu, Y., Zhang, X., Ding, C., Huang, R., Zhang, Z., ... & Sun, Y. (2015). CRISPR/Cas9-mediated gene editing in human tripronuclear zygotes. *Protein & cell*, *6*(5), 363-372.

Liguori, C., Mercuri, N. B., Nuccetelli, M., Izzi, F., Bernardini, S., & Placidi, F. (2018). Cerebrospinal Fluid Orexin Levels and Nocturnal Sleep Disruption in Alzheimer's Disease Patients Showing Neuropsychiatric Symptoms. *Journal of Alzheimer's Disease*, (Preprint), 1-7.

Lin, Y. T., Seo, J., Gao, F., Feldman, H. M., Wen, H. L., Penney, J., ... & Rueda, R. (2018). APOE4 causes widespread molecular and cellular alterations associated with Alzheimer's disease phenotypes in human iPSC-derived brain cell types. *Neuron*, *98*(6), 1141-1154.

Liu, D. S., Pan, X. D., Zhang, J., Shen, H., Collins, N. C., Cole, A. M., ... & Tai, L. M. (2015). APOE4 enhances age-dependent decline in cognitive function by down-regulating an NMDA receptor pathway in EFAD-Tg mice. *Molecular neurodegeneration*, *10*(1), 7.

Liu, Q., Huang, Y., Xue, F., Simard, A., DeChon, J., Li, G., ... & Hu, G. (2009). A novel nicotinic acetylcholine receptor subtype in basal forebrain cholinergic neurons with high sensitivity to amyloid peptides. *Journal of Neuroscience*, *29*(4), 918-929.

Lund P. L-Glutamine and L-Glutamate: UV-Method with Glutaminase and Glutamate Dehydrogenase. Methods of Enzymatic Analysis. 8. 357-363 1986.

Lund, R. J., Närvä, E., & Lahesmaa, R. (2012). Genetic and epigenetic stability of human pluripotent stem cells. *Nature Reviews Genetics*, *13*(10), 732.

Lund, R. J., Nikula, T., Rahkonen, N., Närvä, E., Baker, D., Harrison, N., ... & Lahesmaa, R. (2012). High-throughput karyotyping of human pluripotent stem cells. *Stem cell research*, *9*(3), 192-195.

Lundin, A., Delsing, L., Clausen, M., Ricchiuto, P., Sanchez, J., Sabirsh, A., ... & Hicks, R. (2018). Human iPS-derived astroglia from a stable neural precursor state show improved functionality compared with conventional astrocytic models. *Stem cell reports*, *10*(3), 1030-1045.

Magistretti, P. J. (2006). Neuron–glia metabolic coupling and plasticity. *Journal of Experimental Biology*, *209*(12), 2304-2311.

Mahley, R. W. (2016). Apolipoprotein E: from cardiovascular disease to neurodegenerative disorders. *Journal of molecular medicine*, *94*(7), 739-746.

Mahley, R. W., Weisgraber, K. H., & Huang, Y. (2006). Apolipoprotein E4: a causative factor and therapeutic target in neuropathology, including Alzheimer's disease. *Proceedings of the National Academy of Sciences*, *103*(15), 5644-5651.

Mali, P., Chou, B. K., Yen, J., Ye, Z., Zou, J., Dowey, S., ... & Yusa, K. (2010). Butyrate greatly enhances derivation of human induced pluripotent stem cells by promoting epigenetic remodeling and the expression of pluripotency-associated genes. *Stem cells*, *28*(4), 713-720.

Mann, K. M., Thorngate, F. E., Katoh-Fukui, Y., Hamanaka, H., Williams, D. L., Fujita, S., & Lamb, B. T. (2004). Independent effects of APOE on cholesterol metabolism and brain Aβ levels in an Alzheimer disease mouse model. *Human molecular genetics*, *13*(17), 1959-1968.

Mariani, J., Simonini, M. V., Palejev, D., Tomasini, L., Coppola, G., Szekely, A. M., ... & Vaccarino, F. M. (2012). Modeling human cortical development in vitro using induced pluripotent stem cells. *Proceedings of the National Academy of Sciences*, *109*(31), 12770-12775.

Martinez-Hernandez, A., Bell, K. P., & Norenberg, M. D. (1977). Glutamine synthetase: glial localization in brain. *Science*, *195*(4284), 1356-1358.

Maruyama, T., Dougan, S. K., Truttmann, M. C., Bilate, A. M., Ingram, J. R., & Ploegh, H. L. (2015). Increasing the efficiency of precise genome editing with CRISPR-Cas9 by inhibition of nonhomologous end joining. *Nature biotechnology*, *33*(5), 538.

Matos, M., Augusto, E., Machado, N. J., dos Santos-Rodrigues, A., Cunha, R. A., & Agostinho, P. (2012). Astrocytic adenosine A 2A receptors control the amyloid-β peptide-induced decrease of glutamate uptake. *Journal of Alzheimer's Disease*, *31*(3), 555-567.

Mawuenyega, K. G., Sigurdson, W., Ovod, V., Munsell, L., Kasten, T., Morris, J. C., ... & Bateman, R. J. (2010). Decreased clearance of CNS β-amyloid in Alzheimer's disease. *Science*, *330*(6012), 1774-1774.

Merkle, F. T., Neuhausser, W. M., Santos, D., Valen, E., Gagnon, J. A., Maas, K., ... & Eggan, K. (2015). Efficient CRISPR-Cas9-mediated generation of knockin human pluripotent stem cells lacking undesired mutations at the targeted locus. *Cell reports*, *11*(6), 875-883.

Merlini, M., Meyer, E. P., Ulmann-Schuler, A., & Nitsch, R. M. (2011). Vascular β-amyloid and early astrocyte alterations impair cerebrovascular function and cerebral metabolism in transgenic arcAβ mice. *Acta neuropathologica*, *122*(3), 293-311.

Miller, J. C., Tan, S., Qiao, G., Barlow, K. A., Wang, J., Xia, D. F., ... & Dulay, G. P. (2011). A TALE nuclease architecture for efficient genome editing. *Nature biotechnology*, *29*(2), 143.

Miller, J. D., Ganat, Y. M., Kishinevsky, S., Bowman, R. L., Liu, B., Tu, E. Y., ... & Taldone, T. (2013). Human iPSC-based modeling of late-onset disease via progerin-induced aging. *Cell stem cell*, *13*(6), 691-705.

Miller, S. J. (2018). Astrocyte heterogeneity in the adult central nervous system. Frontiers in cellular neuroscience, 12, 401.

Miyaoka, Y., Berman, J. R., Cooper, S. B., Mayerl, S. J., Chan, A. H., Zhang, B., ... & Conklin, B. R. (2016). Systematic quantification of HDR and NHEJ reveals effects of locus, nuclease, and cell type on genome-editing. *Scientific reports*, *6*, 23549.

Miyata, M., & Smith, J. D. (1996). Apolipoprotein E allele–specific antioxidant activity and effects on cytotoxicity by oxidative insults and β–amyloid peptides. *Nature genetics*, *14*(1), 55.

Moreira, P. I., Carvalho, C., Zhu, X., Smith, M. A., & Perry, G. (2010). Mitochondrial dysfunction is a trigger of Alzheimer's disease pathophysiology. *Biochimica et Biophysica Acta (BBA)-Molecular Basis of Disease*, *1802*(1), 2-10.

Mormone, E., D'Sousa, S., Alexeeva, V., Bederson, M. M., & Germano, I. M. (2014). "Footprint-free" human induced pluripotent stem cell-derived astrocytes for in vivo cell-based therapy. *Stem cells and development*, *23*(21), 2626-2636.

Morris, M., Maeda, S., Vossel, K., & Mucke, L. (2011). The many faces of tau. *Neuron*, *70*(3), 410-426.

Morrison, S. J., Perez, S. E., Qiao, Z., Verdi, J. M., Hicks, C., Weinmaster, G., & Anderson, D. J. (2000). Transient Notch activation initiates an irreversible switch from neurogenesis to gliogenesis by neural crest stem cells. Cell, 101(5), 499-510.

Musatov, A., & Robinson, N. C. (2012). Susceptibility of mitochondrial electron-transport complexes to oxidative damage. Focus on cytochrome c oxidase. Free radical research, 46(11), 1313-1326.

Nakamura, T., Watanabe, A., Fujino, T., Hosono, T., & Michikawa, M. (2009). Apolipoprotein E4 (1–272) fragment is associated with mitochondrial proteins and affects mitochondrial function in neuronal cells. *Molecular neurodegeneration*, *4*(1), 35.

Nakamura, T., Watanabe, A., Fujino, T., Hosono, T., & Michikawa, M. (2009). Apolipoprotein E4 (1–272) fragment is associated with mitochondrial proteins and affects mitochondrial function in neuronal cells. Molecular neurodegeneration, 4(1), 35.

Namihira, M., Kohyama, J., Semi, K., Sanosaka, T., Deneen, B., Taga, T., & Nakashima, K. (2009). Committed neuronal precursors confer astrocytic potential on residual neural precursor cells. Developmental cell, 16(2), 245-255.

Nicholas, C. R., Chen, J., Tang, Y., Southwell, D. G., Chalmers, N., Vogt, D., ... & Sasai, Y. (2013). Functional maturation of hPSC-derived forebrain interneurons requires an extended timeline and mimics human neural development. *Cell stem cell*, *12*(5), 573-586.

Nieweg, K., Andreyeva, A., Van Stegen, B., Tanriöver, G., & Gottmann, K. (2015). Alzheimer's disease-related amyloid-β induces synaptotoxicity in human iPS cell-derived neurons. *Cell death & disease*, *6*(4), e1709.

Nixon, R. A. (2017). Amyloid precursor protein and endosomal–lysosomal dysfunction in Alzheimer's disease: inseparable partners in a multifactorial disease. *The FASEB Journal*, *31*(7), 2729-2743.

Noctor, S. C., Flint, A. C., Weissman, T. A., Dammerman, R. S., & Kriegstein, A. R. (2001). Neurons derived from radial glial cells establish radial units in neocortex. *Nature*, *409*(6821), 714.

Nunomura, A., Moreira, P. I., Lee, H. G., Zhu, X., Castellani, R. J., Smith, M. A., & Perry, G. (2007). Neuronal death and survival under oxidative stress in Alzheimer and Parkinson diseases. *CNS & Neurological Disorders-Drug Targets (Formerly Current Drug Targets-CNS & Neurological Disorders)*, *6*(6), 411-423.

Nunomura, A., Perry, G., Aliev, G., Hirai, K., Takeda, A., Balraj, E. K., ... & Chiba, S. (2001). Oxidative damage is the earliest event in Alzheimer disease. *Journal of Neuropathology & Experimental Neurology*, *60*(8), 759-767.

Nuriel, T., Peng, K. Y., Ashok, A., Dillman, A. A., Figueroa, H. Y., Apuzzo, J., ... & Duff, K. E. (2017). The endosomal–lysosomal pathway is dysregulated by APOE4 expression in vivo. *Frontiers in Neuroscience*, *11*, 702.

Oberheim, N. A., Takano, T., Han, X., He, W., Lin, J. H., Wang, F., ... & Ransom, B. R. (2009). Uniquely hominid features of adult human astrocytes. *Journal of Neuroscience*, *29*(10), 3276-3287.

Oberheim, N. A., Wang, X., Goldman, S., & Nedergaard, M. (2006). Astrocytic complexity distinguishes the human brain. *Trends in neurosciences*, *29*(10), 547-553.

O'Dwyer, L., Lamberton, F., Matura, S., Tanner, C., Scheibe, M., Miller, J., ... & Hampel, H. (2012). Reduced hippocampal volume in healthy young ApoE4 carriers: an MRI study. *PloS one*, *7*(11), e48895.

Okita, K., Matsumura, Y., Sato, Y., Okada, A., Morizane, A., Okamoto, S., ... & Shibata, T. (2011). A more efficient method to generate integration-free human iPS cells. *Nature methods*, *8*(5), 409.

Oksanen, M., Petersen, A. J., Naumenko, N., Puttonen, K., Lehtonen, Š., Olivé, M. G., ... & Rinne, J. O. (2017). PSEN1 mutant iPSC-derived model reveals severe astrocyte pathology in Alzheimer's disease. *Stem cell reports*, *9*(6), 1885-1897.

Panopoulos, A. D., Yanes, O., Ruiz, S., Kida, Y. S., Diep, D., Tautenhahn, R., ... & Berggren, W. T. (2012). The metabolome of induced pluripotent stem cells reveals metabolic changes occurring in somatic cell reprogramming. *Cell research*, *22*(1), 168.

Papapetrou, E. P., Tomishima, M. J., Chambers, S. M., Mica, Y., Reed, E., Menon, J., ... & Sadelain, M. (2009). Stoichiometric and temporal requirements of Oct4, Sox2, Klf4, and c-Myc expression for efficient human iPSC induction and differentiation. *Proceedings of the National Academy of Sciences*, *106*(31), 12759-12764.

Paquet, D., Kwart, D., Chen, A., Sproul, A., Jacob, S., Teo, S., ... & Tessier-Lavigne, M. (2016). Efficient introduction of specific homozygous and heterozygous mutations using CRISPR/Cas9. *Nature*, *533*(7601), 125.

Parker, W. D., Mahr, N. J., Filley, C. M., Parks, J. K., Hughes, D., Young, D. A., & Cullum, C. M. (1994). Reduced platelet cytochrome c oxidase activity in Alzheimer's disease. *Neurology*, *44*(6), 1086-1086.

Perez-Nievas, B. G., & Serrano-Pozo, A. (2018). Deciphering the astrocyte reaction in Alzheimer's disease. *Frontiers in aging neuroscience*, *10*.

Pietrzik, C. U., Yoon, I. S., Jaeger, S., Busse, T., Weggen, S., & Koo, E. H. (2004). FE65 constitutes the functional link between the low-density lipoprotein receptor-related protein and the amyloid precursor protein. *Journal of Neuroscience*, *24*(17), 4259-4265.

Pinder, J., Salsman, J., & Dellaire, G. (2015). Nuclear domain 'knock-in'screen for the evaluation and identification of small molecule enhancers of CRISPR-based genome editing. *Nucleic acids research*, *43*(19), 9379-9392.

Polo, J. M., Anderssen, E., Walsh, R. M., Schwarz, B. A., Nefzger, C. M., Lim, S. M., ... & Bar-Nur, O. (2012). A molecular roadmap of reprogramming somatic cells into iPS cells. *Cell*, *151*(7), 1617-1632.

Prasad, H., & Rao, R. (2018). Amyloid clearance defect in ApoE4 astrocytes is reversed by epigenetic correction of endosomal pH. *Proceedings of the National Academy of Sciences*, *115*(28), E6640-E6649.

Qiu, C., & Fratiglioni, L. (2018). Aging without dementia is achievable: current evidence from epidemiological research. *Journal of Alzheimer's Disease*, *62*(3), 933-942. Qiu, C., & Fratiglioni, L. (2018). Aging without dementia is achievable: current evidence from epidemiological research. *Journal of Alzheimer's Disease*, *62*(3), 933-942.

Rajan, P., & McKay, R. D. (1998). Multiple routes to astrocytic differentiation in the CNS. *Journal of Neuroscience*, *18*(10), 3620-3629.

Ran, F. A., Hsu, P. D., Wright, J., Agarwala, V., Scott, D. A., & Zhang, F. (2013). Genome engineering using the CRISPR-Cas9 system. *Nature protocols*, *8*(11), 2281.

Rapp, A., Gmeiner, B., & Hüttinger, M. (2006). Implication of apoE isoforms in cholesterol metabolism by primary rat hippocampal neurons and astrocytes. *Biochimie*, *88*(5), 473-483.

Reiman, E. M., Chen, K., Alexander, G. E., Caselli, R. J., Bandy, D., Osborne, D., ... & Hardy, J. (2004). Functional brain abnormalities in young adults at genetic risk for late-onset Alzheimer's dementia. *Proceedings of the National Academy of Sciences*, *101*(1), 284-289.

Reiman, E. M., Chen, K., Langbaum, J. B., Lee, W., Reschke, C., Bandy, D., ... & Caselli, R. J. (2010). Higher serum total cholesterol levels in late middle age are associated with glucose hypometabolism in brain regions affected by Alzheimer's disease and normal aging. *Neuroimage*, *49*(1), 169-176.

Reiman, E. M., Chen, K., Liu, X., Bandy, D., Yu, M., Lee, W., ... & Alexander, G. E. (2009). Fibrillar amyloid-β burden in cognitively normal people at 3 levels of genetic risk for Alzheimer's disease. *Proceedings of the National Academy of Sciences*, *106*(16), 6820-6825.

Reitz, C., Brayne, C., & Mayeux, R. (2011). Epidemiology of Alzheimer disease. *Nature Reviews Neurology*, *7*(3), 137.

Renaud, J. B., Boix, C., Charpentier, M., De Cian, A., Cochennec, J., Duvernois-Berthet, E., ... & Cherifi, Y. (2016). Improved genome editing efficiency and flexibility using modified oligonucleotides with TALEN and CRISPR-Cas9 nucleases. *Cell reports*, *14*(9), 2263-2272.

Richardson, C. D., Ray, G. J., DeWitt, M. A., Curie, G. L., & Corn, J. E. (2016). Enhancing homology-directed genome editing by catalytically active and inactive CRISPR-Cas9 using asymmetric donor DNA. *Nature biotechnology*, *34*(3), 339.

Roberson, E. D., Scearce-Levie, K., Palop, J. J., Yan, F., Cheng, I. H., Wu, T., ... & Mucke, L. (2007). Reducing endogenous tau ameliorates amyloid ß-induced deficits in an Alzheimer's disease mouse model. *Science*, *316*(5825), 750-754.

Roßner, S., Apelt, J., Schliebs, R., Perez-Polo, J. R., & Bigl, V. (2001). Neuronal and glial β-secretase (BACE) protein expression in transgenic Tg2576 mice with amyloid plaque pathology. *Journal of neuroscience research*, *64*(5), 437-446.

Rouet, P., Smih, F., & Jasin, M. (1994). Expression of a site-specific endonuclease stimulates homologous recombination in mammalian cells. *Proceedings of the National Academy of Sciences*, *91*(13), 6064-6068.

Rouet, P., Smih, F., & Jasin, M. (1994). Introduction of double-strand breaks into the genome of mouse cells by expression of a rare-cutting endonuclease. *Molecular and cellular biology*, *14*(12), 8096-8106.

Roybon, L., Lamas, N. J., Garcia-Diaz, A., Yang, E. J., Sattler, R., Jackson-Lewis, V., ... & Wichterle, H. (2013). Human stem cell-derived spinal cord astrocytes with defined mature or reactive phenotypes. *Cell reports*, *4*(5), 1035-1048.

Safieh, M., Korczyn, A. D., & Michaelson, D. M. (2019). ApoE4: an emerging therapeutic target for Alzheimer's disease. *BMC medicine*, *17*(1), 64.

Sagar, S. M., Sharp, F. R., & Swanson, R. A. (1987). The regional distribution of glycogen in rat brain fixed by microwave irradiation. *Brain research*, *417*(1), 172-174.

Sardi, S. P., Murtie, J., Koirala, S., Patten, B. A., & Corfas, G. (2006). Presenilin-dependent ErbB4 nuclear signaling regulates the timing of astrogenesis in the developing brain. *Cell*, *127*(1), 185-197.

Schaeffer, E. L., Figueiro, M., & Gattaz, W. F. (2011). Insights into Alzheimer disease pathogenesis from studies in transgenic animal models. Clinics, 66, 45-54.

Schmid, B., Prehn, K. R., Nimsanor, N., Garcia, B. I. A., Poulsen, U., Jørring, I., ... & Muddashetty, R. (2019). Generation of a set of isogenic, gene-edited iPSC lines homozygous for all main APOE variants and an APOE knock-out line. Stem cell research, 34, 101349.

Serio, A., Bilican, B., Barmada, S. J., Ando, D. M., Zhao, C., Siller, R., ... & Carrasco, M. A. (2013). Astrocyte pathology and the absence of non-cell autonomy in an induced pluripotent stem cell model of TDP-43 proteinopathy. *Proceedings of the National Academy of Sciences*, *110*(12), 4697-4702.

Setoguchi, T., & Kondo, T. (2004). Nuclear export of OLIG2 in neural stem cells is essential for ciliary neurotrophic factor–induced astrocyte differentiation. *The Journal of cell biology*, *166*(7), 963-968.

Shaltouki, A., Peng, J., Liu, Q., Rao, M. S., & Zeng, X. (2013). Efficient generation of astrocytes from human pluripotent stem cells in defined conditions. *Stem cells*, *31*(5), 941-952.

Shepherd, C., McCann, H., & Halliday, G. M. (2009). Variations in the neuropathology of familial Alzheimer's disease. *Acta neuropathologica*, *118*(1), 37-52.

Shi, J., Ma, Y., Zhu, J., Chen, Y., Sun, Y., Yao, Y., ... & Xie, J. (2018). A review on electroporation-based intracellular delivery. *Molecules*, *23*(11), 3044.

Shi, Y., Kirwan, P., Smith, J., MacLean, G., Orkin, S. H., & Livesey, F. J. (2012). A human stem cell model of early Alzheimer's disease pathology in Down syndrome. *Science translational medicine*, *4*(124), 124ra29-124ra29.

Shi, Y., Yamada, K., Liddelow, S. A., Smith, S. T., Zhao, L., Luo, W., ... & Gallardo, G. (2017). ApoE4 markedly exacerbates tau-mediated neurodegeneration in a mouse model of tauopathy. *Nature*, *549*(7673), 523.

Shokolenko, I. N., Wilson, G. L., & Alexeyev, M. F. (2016). The "fast" and the "slow" modes of mitochondrial DNA degradation. Mitochondrial DNA Part A, 27(1), 490-498.

Sild, M., & Ruthazer, E. S. (2011). Radial glia: progenitor, pathway, and partner. *The Neuroscientist*, *17*(3), 288-302.

Simard, M., & Nedergaard, M. (2004). The neurobiology of glia in the context of water and ion homeostasis. *Neuroscience*, *129*(4), 877-896.

Simonovitch, S., Schmukler, E., Bespalko, A., Iram, T., Frenkel, D., Holtzman, D. M., ... & Pinkas-Kramarski, R. (2016). Impaired autophagy in APOE4 astrocytes. *Journal of Alzheimer's Disease*, *51*(3), 915-927.

Simpson, I. A., Chundu, K. R., Davies-Hill, T., Honer, W. G., & Davies, P. (1994). Decreased concentrations of GLUT1 and GLUT3 glucose transporters in the brains of patients with Alzheimer's disease. *Annals of Neurology: Official Journal of the American Neurological Association and the Child Neurology Society*, *35*(5), 546-551.

Simpson, J. E., Ince, P. G., Lace, G., Forster, G., Shaw, P. J., Matthews, F., ... & Wharton, S. B. (2010). Astrocyte phenotype in relation to Alzheimer-type pathology in the ageing brain. *Neurobiology of aging*, *31*(4), 578-590.

Smith, C., Gore, A., Yan, W., Abalde-Atristain, L., Li, Z., He, C., ... & Ye, Z. (2014). Whole-genome sequencing analysis reveals high specificity of CRISPR/Cas9 and TALEN-based genome editing in human iPSCs. *Cell stem cell*, *15*(1), 12-13.

Sofroniew, M. V. (2009). Molecular dissection of reactive astrogliosis and glial scar formation. *Trends in neurosciences*, *32*(12), 638-647.

Song, J., Yang, D., Xu, J., Zhu, T., Chen, Y. E., & Zhang, J. (2016). RS-1 enhances CRISPR/Cas9-and TALEN-mediated knock-in efficiency. *Nature communications*, *7*, 10548.

Sotiropoulos, I., Galas, M. C., Silva, J. M., Skoulakis, E., Wegmann, S., Maina, M. B., ... & Spillantini, M. G. (2017). Atypical, non-standard functions of the microtubule associated Tau protein. Acta neuropathologica communications, 5(1), 91.

Srinivasan, K., Leone, D. P., Bateson, R. K., Dobreva, G., Kohwi, Y., Kohwi-Shigematsu, T., ... & McConnell, S. K. (2012). A network of genetic repression and derepression specifies projection fates in the developing neocortex. *Proceedings of the National Academy of Sciences*, *109*(47), 19071-19078.

Sullivan, P. M., Mezdour, H., Aratani, Y., Knouff, C., Najib, J., Reddick, R. L., ... & Maeda, N. (1997). Targeted replacement of the mouse apolipoprotein E gene with the common human APOE3 allele enhances diet-induced hypercholesterolemia and atherosclerosis. *Journal of Biological Chemistry*, *272*(29), 17972-17980.

Sullivan, P. M., Mezdour, H., Quarfordt, S. H., & Maeda, N. (1998). Type III hyperlipoproteinemia and spontaneous atherosclerosis in mice resulting from gene replacement of mouse Apoe with human Apoe* 2. *The Journal of clinical investigation*, *102*(1), 130-135.

Suzuki, A., Stern, S. A., Bozdagi, O., Huntley, G. W., Walker, R. H., Magistretti, P. J., & Alberini, C. M. (2011). Astrocyte-neuron lactate transport is required for long-term memory formation. *Cell*, *144*(5), 810-823.

Swomley, A. M., & Butterfield, D. A. (2015). Oxidative stress in Alzheimer disease and mild cognitive impairment: evidence from human data provided by redox proteomics. *Archives of toxicology*, *89*(10), 1669-1680.

Szekely, C. A., Breitner, J. C., Fitzpatrick, A. L., Rea, T. D., Psaty, B. M., Kuller, L. H., & Zandi, P. P. (2008). NSAID use and dementia risk in the Cardiovascular Health Study*: Role of APOE and NSAID type. *Neurology*, *70*(1), 17-24.

Taapken, S. M., Nisler, B. S., Newton, M. A., Sampsell-Barron, T. L., Leonhard, K. A., McIntire, E. M., & Montgomery, K. D. (2011). Karyotypic abnormalities in human induced pluripotent stem cells and embryonic stem cells. *Nature biotechnology*, *29*(4), 313.

Takahashi, K., & Yamanaka, S. (2006). Induction of pluripotent stem cells from mouse embryonic and adult fibroblast cultures by defined factors. *cell*, *126*(4), 663-676.

Takahashi, K., Tanabe, K., Ohnuki, M., Narita, M., Ichisaka, T., Tomoda, K., & Yamanaka, S. (2007). Induction of pluripotent stem cells from adult human fibroblasts by defined factors. *cell*, *131*(5), 861-872.

Talantova, M., Sanz-Blasco, S., Zhang, X., Xia, P., Akhtar, M. W., Okamoto, S. I., ... & Kang, Y. J. (2013). Aβ induces astrocytic glutamate release, extrasynaptic NMDA receptor activation, and synaptic loss. *Proceedings of the National Academy of Sciences*, *110*(27), E2518-E2527.

Tebas, P., Stein, D., Tang, W. W., Frank, I., Wang, S. Q., Lee, G., ... & Holmes, M. C. (2014). Gene editing of CCR5 in autologous CD4 T cells of persons infected with HIV. *New England Journal of Medicine*, *370*(10), 901-910.

Texidó, L., Martín-Satué, M., Alberdi, E., Solsona, C., & Matute, C. (2011). Amyloid β peptide oligomers directly activate NMDA receptors. *Cell calcium*, *49*(3), 184-190.

Theendakara, V., Peters-Libeu, C. A., Spilman, P., Poksay, K. S., Bredesen, D. E., & Rao, R. V. (2016). Direct transcriptional effects of apolipoprotein E. *Journal of Neuroscience*, *36*(3), 685-700.

Thies, E., & Mandelkow, E. M. (2007). Missorting of tau in neurons causes degeneration of synapses that can be rescued by the kinase MARK2/Par-1. *Journal of Neuroscience*, *27*(11), 2896-2907.

Tombaugh, T. N., & McIntyre, N. J. (1992). The mini-mental state examination: a comprehensive review. *Journal of the American Geriatrics Society*, *40*(9), 922-935.

Tyzack, G., Lakatos, A., & Patani, R. (2016). Human stem cell-derived astrocytes: specification and relevance for neurological disorders. *Current stem cell reports*, *2*(3), 236-247.

Ullensvang, K., Lehre, K. P., Storm-Mathisen, J., & Danbolt, N. C. (1997). Differential developmental expression of the two rat brain glutamate transporter proteins GLAST and GLT. *European Journal of Neuroscience*, *9*(8), 1646-1655.

Ulrich, J. D., Burchett, J. M., Restivo, J. L., Schuler, D. R., Verghese, P. B., Mahan, T. E., ... & Holtzman, D. M. (2013). In vivo measurement of apolipoprotein E from the brain interstitial fluid using microdialysis. *Molecular neurodegeneration*, *8*(1), 13.

Vakulskas, C. A., Dever, D. P., Rettig, G. R., Turk, R., Jacobi, A. M., Collingwood, M. A., ... & Lee, C. M. (2018). A high-fidelity Cas9 mutant delivered as a ribonucleoprotein complex enables efficient gene editing in human hematopoietic stem and progenitor cells. *Nature medicine*, *24*(8), 1216.

Vemuri, P., Wiste, H. J., Weigand, S. D., Knopman, D. S., Shaw, L. M., Trojanowski, J. Q., ... & Alzheimer's Disease Neuroimaging Initiative. (2010). Effect of apolipoprotein E on biomarkers of amyloid load and neuronal pathology in Alzheimer disease. *Annals of neurology*, *67*(3), 308-316.

Villemagne, V. L., Pike, K. E., Chételat, G., Ellis, K. A., Mulligan, R. S., Bourgeat, P., ... & Martins, R. (2011). Longitudinal assessment of Aβ and cognition in aging and Alzheimer disease. *Annals of neurology*, *69*(1), 181-192.

Vincent, B., & Smith, J. D. (2001). Astrocytes down-regulate neuronal β-amyloid precursor protein expression and modify its processing in an apolipoprotein E isoform-specific manner. *European Journal of Neuroscience*, *14*(2), 256-266.

Voloboueva, L. A., Suh, S. W., Swanson, R. A., & Giffard, R. G. (2007). Inhibition of mitochondrial function in astrocytes: implications for neuroprotection. *Journal of neurochemistry*, *102*(4), 1383-1394.

Wadhwani, A. R., Affaneh, A., Van Gulden, S., & Kessler, J. A. (2019). Neuronal apolipoprotein E4 increases cell death and phosphorylated tau release in alzheimer disease. *Annals of neurology*, *85*(5), 726-739.

Wang, C., Najm, R., Xu, Q., Jeong, D. E., Walker, D., Balestra, M. E., ... & Miller, B. L. (2018). Gain of toxic apolipoprotein E4 effects in human iPSC-derived neurons is ameliorated by a small-molecule structure corrector. *Nature medicine*, *24*(5), 647.

Wang, T., Birsoy, K., Hughes, N. W., Krupczak, K. M., Post, Y., Wei, J. J., ... & Sabatini, D. M. (2015). Identification and characterization of essential genes in the human genome. *Science*, *350*(6264), 1096-1101.

Warren, L., Manos, P. D., Ahfeldt, T., Loh, Y. H., Li, H., Lau, F., ... & Daley, G. Q. (2010). Highly efficient reprogramming to pluripotency and directed differentiation of human cells with synthetic modified mRNA. *Cell stem cell*, *7*(5), 618-630.

Wilmut, I., Schnieke, A. E., McWhir, J., Kind, A. J., & Campbell, K. H. (1997). Viable offspring derived from fetal and adult mammalian cells. *Nature*, *385*(6619), 810.

Wyss-Coray, T., Loike, J. D., Brionne, T. C., Lu, E., Anankov, R., Yan, F., ... & Husemann, J. (2003). Adult mouse astrocytes degrade amyloid-β in vitro and in situ. *Nature medicine*, *9*(4), 453.

Xian, X., Pohlkamp, T., Durakoglugil, M. S., Wong, C. H., Beck, J. K., Lane-Donovan, C., ... & Herz, J. (2018). Reversal of ApoE4-induced recycling block as a novel prevention approach for Alzheimer's disease. *Elife*, *7*, e40048.

Yagi, T., Ito, D., Okada, Y., Akamatsu, W., Nihei, Y., Yoshizaki, T., ... & Suzuki, N. (2011). Modeling familial Alzheimer's disease with induced pluripotent stem cells. *Human molecular genetics*, *20*(23), 4530-4539.

Yang, H., Wang, H., Shivalila, C. S., Cheng, A. W., Shi, L., & Jaenisch, R. (2013). One-step generation of mice carrying reporter and conditional alleles by CRISPR/Cas-mediated genome engineering. *Cell*, *154*(6), 1370-1379.

Yang, K., Guo, R., & Xu, D. (2016). Non-homologous end joining: advances and frontiers. *Acta biochimica et biophysica Sinica*, *48*(7), 632-640.

Yang, W., Tu, Z., Sun, Q., & Li, X. J. (2016). CRISPR/Cas9: implications for modeling and therapy of neurodegenerative diseases. *Frontiers in molecular neuroscience*, *9*, 30.

Yao, J., Du, H., Yan, S., Fang, F., Wang, C., Lue, L. F., ... & Chen, J. X. (2011). Inhibition of amyloid-β (Aβ) peptide-binding alcohol dehydrogenase-Aβ interaction reduces Aβ accumulation and improves mitochondrial function in a mouse model of Alzheimer's disease. *Journal of Neuroscience*, *31*(6), 2313-2320.

Ye, S., Huang, Y., Müllendorff, K., Dong, L., Giedt, G., Meng, E. C., ... & Mahley, R. W. (2005). Apolipoprotein (apo) E4 enhances amyloid β peptide production in cultured neuronal cells: ApoE structure as a potential therapeutic target. *Proceedings of the National Academy of Sciences*, *102*(51), 18700-18705.

Yu, D. X., Di Giorgio, F. P., Yao, J., Marchetto, M. C., Brennand, K., Wright, R., ... & Silberman, P. (2014). Modeling hippocampal neurogenesis using human pluripotent stem cells. Stem cell reports, 2(3), 295-310.

Yu, J. T., Tan, L., & Hardy, J. (2014). Apolipoprotein E in Alzheimer's disease: an update. *Annual review of neuroscience*, *37*, 79-100.

Yu, J., Vodyanik, M. A., Smuga-Otto, K., Antosiewicz-Bourget, J., Frane, J. L., Tian, S., ... & Slukvin, I. I. (2007). Induced pluripotent stem cell lines derived from human somatic cells. *science*, *318*(5858), 1917-1920.

Yun, S. W., Lannert, H., & Hoyer, S. (2000). Chronic exposure to low-level lead impairs learning ability during aging and energy metabolism in aged rat brain. *Archives of gerontology and geriatrics*, *30*(3), 199-213.

Zhang, S. C., Wernig, M., Duncan, I. D., Brüstle, O., & Thomson, J. A. (2001). In vitro differentiation of transplantable neural precursors from human embryonic stem cells. *Nature biotechnology*, *19*(12), 1129.

Zhang, Y., Sloan, S. A., Clarke, L. E., Caneda, C., Plaza, C. A., Blumenthal, P. D., ... & Duncan III, J. A. (2016). Purification and characterization of progenitor and mature human astrocytes reveals transcriptional and functional differences with mouse. *Neuron*, *89*(1), 37-53.

Zhang, Z., Xiang, D., & Wu, W. S. (2014). Sodium Butyrate Facilitates Reprogramming by Derepressing OCT4 Transactivity at the Promoter of Embryonic Stem Cell–Specific miR-302/367 Cluster. *Cellular reprogramming*, *16*(2), 130-139.

Zhao, J., Davis, M. D., Martens, Y. A., Shinohara, M., Graff-Radford, N. R., Younkin, S. G., ... & Bu, G. (2017). APOE ε4/ε4 diminishes neurotrophic function of human iPSC-derived astrocytes. *Human molecular genetics*, *26*(14), 2690-2700.

Zhao, J., O'Connor, T., & Vassar, R. (2011). The contribution of activated astrocytes to Aβ production: implications for Alzheimer's disease pathogenesis. *Journal of neuroinflammation*, *8*(1), 150.

Zhao, N., Liu, C. C., Van Ingelgom, A. J., Martens, Y. A., Linares, C., Knight, J. A., ... & Bu, G. (2017). Apolipoprotein E4 impairs neuronal insulin signaling by trapping insulin receptor in the endosomes. *Neuron*, *96*(1), 115-129.

Zhao, N., Liu, C. C., Van Ingelgom, A. J., Martens, Y. A., Linares, C., Knight, J. A., ... & Bu, G. (2017). Apolipoprotein E4 impairs neuronal insulin signaling by trapping insulin receptor in the endosomes. *Neuron*, *96*(1), 115-129.

Zheng, W. H., Bastianetto, S., Mennicken, F., Ma, W., & Kar, S. (2002). Amyloid β peptide induces tau phosphorylation and loss of cholinergic neurons in rat primary septal cultures. *Neuroscience*, *115*(1), 201-211.

Zheng, W. H., Bastianetto, S., Mennicken, F., Ma, W., & Kar, S. (2002). Amyloid β peptide induces tau phosphorylation and loss of cholinergic neurons in rat primary septal cultures. *Neuroscience*, *115*(1), 201-211.

Zhong, N., & Weisgraber, K. H. (2009). Understanding the association of apolipoprotein E4 with Alzheimer disease: clues from its structure. *Journal of Biological Chemistry*, *284*(10), 6027-6031.

Zhou, W., & Freed, C. R. (2009). Adenoviral gene delivery can reprogram human fibroblasts to induced pluripotent stem cells. *Stem cells*, *27*(11), 2667-2674.

Zolezzi, J. M., Bastías-Candia, S., Santos, M. J., & Inestrosa, N. C. (2014). Alzheimer's disease: relevant molecular and physiopathological events affecting amyloid-β brain balance and the putative role of PPARs. *Frontiers in aging neuroscience*, *6*, 176.

Zuris, J. A., Thompson, D. B., Shu, Y., Guilinger, J. P., Bessen, J. L., Hu, J. H., ... & Liu, D. R. (2015). Cationic lipid-mediated delivery of proteins enables efficient protein-based genome editing in vitro and in vivo. *Nature biotechnology*, *33*(1), 73.

Zwaka, T. P., & Thomson, J. A. (2003). Homologous recombination in human embryonic stem cells. *Nature biotechnology*, *21*(3), 319.

6. Abbreviations

2DG	2-Deoxy-D-Glucose
ABCA7	ATP-binding cassette sub-family A member 7
AD	Alzheimer's Diseases
AICD	Amyloid precursor protein Intracellular Cytoplasmic/C-terminal Domain
APC	Astrocyte progenitor cells
APOE	Apolipoprotein E
APP	Amyloid precursor protein
AraC	Arabinofuranosyl cytidine
ATP	Adenosine triphosphate
BACE1	Beta-secretase 1 precursor
BCA	Bicinchoninic assay
BDNF	Brain derived neurotrophic factor
BIN1	Bridging integrator 1
BMP	Bone Morphogenetic Proteins
CBh	Hybrid CBA promoter
CD44	Cluster of differentiation 44
CDR	Clinical dementia rating
CLU	Clusterin
CNTF	Ciliary neurotrophic factor
COX	Cytochrome C oxidase
CRISPR	Clustered regularly interspaced short palindromic repeats
CTF	C-terminal fragment
CTIP2	Chicken ovalbumin upstream promoter transcription factor-interacting protein 2
DMEM	Dulbecco's Modified Eagle Medium
DMSO	Dimethyl sulfoxide
DSB	Double stranded break
EAAT	Excitatory amino acid transporters
EB	Embryoid body
ECAR	Extracellular acidification rate

EEA1	Early endosome antigen 1
ELS	Endolysosomal system
EOAD	Early onset Alzheimer's disease
ESC	Embryonic stem cells
ETC	Electron transport chain
FACS	Fluorescence activated cell sorting
FAD	Familial Alzheimer's disease
FCCP	Carbonyl cyanide-p-trifluoromethoxyphenylhydrazone
FGF	Fibroblast growth factor
fMRI	Functional magnetic resonance imaging
FOXC1	Forkhead box C1
GABA	Gamma-Aminobutyric acid
GAD67	Glutamic acid decarboxylase
GAPDH	Glyceraldehyde 3-phosphate dehydrogenase
GFAP	Glial fibrillary acidic protein
GFP	Green fluorescent protein
GLAST	Glutamate Aspartate Transporter 1
GLT	Glutamate transporter 1
GLUT	Glucose transporter
GSH	Glutathione
GSK3	Glycogen synthase kinase 3
GSSG	Glutathione disulfide
GWAS	Genomewide association studies
HDR	Homology directed repair
HEK	Human embryonic kidney cells
IL-6	Interleukin-6
iPSC	Induced pluripotent stem cells
KLF4	Krüppel-like factor 4
LAMP2	Lysosome-associated membrane protein 2
LCL	Lymphoblastoid cell lin
LDLR	Low-Density Lipoprotein Receptor

LIF	Leukemia inhibitory factor
LRP1	Low density lipoprotein receptor-related protein 1
MAP2	Microtubule-associated protein 2
MCI	Mild cognitive impairment
MMSE	Mini mental state examination
NADPH	Nicotinamide-adenine dinucleotide phosphate
NCAM	Neural cell adhesion molecule
NEAA	Non-essential amino acids
NFF	Normal human fetal fibroblast
NFT	Neurofibrillary tangles
NHEJ	Non-homology end joining
NMDA	N-methyl-D-aspartate
NPC	Neural progenitor cells
NSC	Neural stem cells
OCR	Oxygen consumption rate
OCT3/4	Octamer-binding transcription factor 4
OTE	Off target effects
PAGE	Polyacrylamide gel electrophoresis
PAX6	Paired box protein 6
PBS	Phosphate buffered saline
PE	Phycoerythrin
PET	Positron emission tomography
PFA	Paraformaldehyde
PFKFB3	6-Phosphofructo-2-Kinase/Fructose-2,6-Biphosphatase 3
PGK	3-phosphoglycerate kinase
PICALM	Phosphatidylinositol Binding Clathrin Assembly Protein
PSEN	Presenilin
PVDF	Polyvinylidene fluoride
RFLP	Restriction fragment length polymorphism
RNP	Ribonucleoprotein
RNS	Reactive nitrogen species

ROCK	Rho-associated, coiled-coil containing protein kinase
ROS	Reactive oxygen species
RS-1	RAD51-stimulatory compound
RT	Room temperature
SAD	Sodium butyrate
SATB2	Special AT-rich sequence-binding protein 2
SB	Sodium butyrate
SCNT	Somatic cell nuclear transfer
SDS	Sodium dodecyl sulphate
SNP	Single nucleotide polymorphism
SORL1	Sortilin Related Receptor 1
SOX2	SRY-Box 2
SSN	Site specific nucleases
ssODN	Single stranded oligonucleotide
TALEN	Transcription activator-like effector nucleases
TBR1	T-Box, Brain 1
TBST	Tris-buffered saline with Tween 20
TGN	Trans-golgi network
TIDE	Tracking of Indels by Decomposition
TNFα	Tumour Necrosis Factor alpha
TREM2	Triggering receptor expressed on myeloid cells 2
WT	Wild type
ZFN	Zinc finger nucleases

7. List of figures

8. Acknowledgments

There are a number of people to whom I am deeply indebted for their encouragement and support during my PhD. First, I would like to extend my sincere gratitude to my mentor, Prof. Katja Nieweg for her enthusiastic support and invaluable scientific insight. I greatly appreciate the opportunity to work on this project and learn the ins and outs of scientific research with her.

Sincere thanks to my second supervisor, Prof. Amalia Dolga for her kind support and for always being just a phone call away. I would like to thank Profs. Carsten Culmsee, Moritz Bünermann, Jens Kockskämper and Cornelius Krasel for discussions and suggestions. Thanks to Dominic for help with the confocal microscopy and Matthias for the ImageJ macros.

I am grateful to my colleague and friend Gaye for her warmth. It made a lot of the difficult times, easier. Pretty and Marlene as well, I thank for their friendship and helpful discussions. Many thanks to dear Alwina for her invaluable help with the cell culture and delicious apple cake to mark all the happy moments. Many thanks to students Laila, Leena, Nadia and many others for bringing fun and energy to the lab.

Deepest gratitude to Emma for her friendship, incredible resourcefulness and always providing a helping hand and a warm smile. Special thanks to Jelena, Goutham, Olga, Sandra, Susanne, Lena, Malena, Ina, Anja, Michael, Nadja, Volker, Birgit and all other colleagues at the BPC.

To all my dear friends, near and far- Radhika, Shehjar, Krithika, Srikar, Amit, Utkarsh, Joshi, Selvam- thank you for all the motivating conversations.

To Saikat- heartfelt thanks for your help through every step of this journey, and for your calmness to perfectly counterbalance my chaos. I could not have done this without you.

To Bhaiyya, thank you for inspiring me with your persistence and integrity every day.
Finally, Ammi and Abbu, your unconditional love and support takes me through every difficult moment in life. Words are not enough. Thank you.